Synthesis of value-added Nitrogen-based products through advanced electrocatalytic systems

Marcelo Eduardo Chávez Blanco

Doctoral Thesis

Synthesis of value-added Nitrogen-based products through advanced electrocatalytic systems

Marcelo Eduardo Chavez Blanco

UNIVERSITAT DE BARCELONA

Synthesis of value-added Nitrogen-based products through advanced electrocatalytic systems

Memòria presentada per optar al Grau de Doctor per la Universitat de Barcelona

Programa de Doctorat en Enginyeria i Ciències Aplicades

Marcelo Eduardo Chavez Blanco

Directors: Prof. Joan Ramon Morante, Dr. Sebastian Murcia Lopez

Tutor: Dr. Julià Vidrier López

Facultat de Física

UNIVERSITAT DE BARCELONA

Marcelo Eduardo Chavez Blanco

Enginyer Químic per la *Universidad Nacional de Asunción*

Màster Universitari en Enginyeria Química per la Universitat de Barcelona

Juliol 2024

ACKNOWLEDGMENTS

Index

ABSTRACT

The transition towards a sustainable and carbon-neutral economy is crucial due to the escalating concerns over excessive greenhouse gas emissions, climate change, and the need for effective utilization of renewable energy sources. The continued reliance on fossil fuels has led to a significant increase in CO_2 and other greenhouse gases, contributing to global warming and severe climate change impacts. To mitigate these effects, it is imperative to develop sustainable energy systems that can harness and store renewable energy efficiently. This thesis explores the synthesis of value-added nitrogen-based products, particularly ammonia, through advanced electrocatalytic systems, addressing the urgent need for sustainable ammonia production pivotal for agriculture, industry, and as a potential energy carrier.

The Power-to-X concept involves converting renewable electricity into carbon-neutral synthetic fuels and chemicals, such as hydrogen, synthetic natural gas, liquid fuels, and ammonia, which can be stored and utilized as energy carriers. Electrocatalysis contributes to Power-to-X technologies by enabling the efficient conversion of electrical energy into chemical bonds, thus providing a sustainable method to store and transport renewable energy. Electrochemical processes are particularly advantageous due to their low environmental impact, mild operational conditions, and compatibility with renewable energy sources.

Chapter 3 investigates the synergistic effects of combining Cu and Ti-based materials as electrocatalysts for the electrochemical reduction of nitrate to ammonia. The study demonstrates that the integration of Cu_2O-Cu nanocubes on Ti substrates significantly enhances catalytic performance, leading to higher yields and selectivity of NH_3. Detailed kinetic insights reveal that the improved activity is due to better adsorption and activation of nitrate ions, facilitated by efficient electron transfer and intermediate stabilization.

Chapter 4 evaluates the energy efficiency and scalability of flow-cell configurations in ammonia electrogeneration. By optimizing the flow-cell design and operational parameters, the research demonstrates substantial improvements in energy efficiency, with the tandem system combining Cu-based and TiO_2-based catalysts achieving high faradaic efficiency and selectivity. Energy efficiency calculations indicate that the optimized configuration is economically viable for large-scale applications. The feasibility of large-scale implementation

of these flow-cell systems presents a promising pathway for integrating sustainable ammonia production into industrial processes.

Chapter 5 explores the impact of lithium enrichment on hydrogen evolution reactions during nitrate electroreduction. The incorporation of lithium into mixed nickel oxide and tin oxide catalysts effectively limits the evolution of hydrogen, enhancing the selectivity towards nitrate conversion, and providing insights about catalyst doping for future works.

Overall, this thesis contributes to the field of sustainable chemistry by presenting innovative electrocatalytic strategies for ammonia synthesis. The research findings highlight the potential of Cu and Ti-based catalysts, the advantages of flow-cell configurations, and the beneficial effects of lithium enrichment, paving the way for more efficient and environmentally friendly ammonia synthesis technologies.

RESUM

La transició cap a una economia sostenible i neutral en carboni és crucial a degut a les preocupacions creixents sobre les emissions excessives de gasos d'efecte hivernacle, el canvi climàtic i la necessitat d'un ús efectiu de les fonts d'energia renovable. La continuada dependència dels combustibles fòssils ha comportat un augment significatiu del CO_2 i d'altres gasos d'efecte hivernacle, contribuint a l'escalfament global i a greus impactes del canvi climàtic. Per mitigar aquests efectes, és imprescindible desenvolupar sistemes energètics sostenibles que puguin capturar i emmagatzemar energia renovable de manera eficient. Aquesta tesi explora la síntesi de productes nitrogenats de valor afegit, especialment amoníac, mitjançant sistemes electrocatalítics avançats, abordant la urgent necessitat d'una producció sostenible d'amoníac essencial per a l'agricultura, la indústria i com a potencial portador d'energia.

El concepte *Power-to-X* implica convertir l'electricitat renovable en combustibles sintètics i productes químics neutres en carboni, com ara hidrogen, gas natural sintètic, combustibles líquids i amoníac, que poden ser emmagatzemats i utilitzats com a portadors d'energia. L'electrocatàlisi contribueix a les tecnologies Power-to-X permetent la conversió eficient d'energia elèctrica en enllaços químics, proporcionant així un mètode sostenible per emmagatzemar i transportar energia renovable. Els processos electroquímics són particularment avantatjosos per el seu baix impacte ambiental, unes condicions operatives suaus i la seva compatibilitat amb fonts d'energia renovable.

El Capítol 3 investiga els efectes sinèrgics de la combinació de materials basats en Cu i Ti com a electrocatalitzadors per a la reducció electroquímica del nitrat a amoníac. L'estudi demostra que la integració de nanocubs de Cu_2O-Cu en substrats de Ti millora significativament el rendiment catalític, conduint a majors rendiments i selectivitat de NH3. Informacions cinètiques detallades revelen que l'activitat millorada es deu a una millor adsorció i activació dels ions nitrat, facilitada per una transferència d'electrons eficient i la estabilització dels compostos intermèdis.

El Capítol 4 avalua l'eficiència energètica i l'escalabilitat de les configuracions de cel·les de flux en l'electrogeneració d'amoníac. Optimitzant el disseny de la cel·la de flux i els paràmetres

operatius, la investigació demostra millores substancials en l'eficiència energètica, amb el sistema en *tandem* que combina catalitzadors basats en Cu i TiO2, assolint alta eficiència faradaica i selectivitat. Els càlculs d'eficiència energètica indiquen que la configuració optimitzada és econòmicament viable per a aplicacions a gran escala. La viabilitat de la implementació a gran escala d'aquests sistemes de cel·la de flux presenta una via prometedora per integrar la producció sostenible d'amoníac en processos industrials.

El Capítol 5 explora l'impacte de l'enriquiment en liti en les reaccions d'evolució d'hidrogen durant la reducció electroquímica de nitrat. La incorporació de liti en catalitzadors d'òxid de níquel i d'òxid d'estany mixts limita efectivament l'evolució d'hidrogen, millorant la selectivitat cap a la conversió de nitrat i proporcionant informació sobre el dopatge de catalitzadors per a futurs treballs.

En general, aquesta tesi contribueix al camp de la química sostenible presentant estratègies electroanalítiques innovadores per a la síntesi d'amoníac. Els resultats de la investigació destaquen el potencial dels catalitzadors basats en Cu i Ti, els avantatges de les configuracions de cel·la de flux i els efectes beneficiosos de l'enriquiment en liti, obrint camí cap a tecnologies de síntesi d'amoníac més eficients i respectuoses amb el medi ambient.

LIST OF ABBREVIATIONS.

AEM: Anion Exchange Membrane

BPM: Bipolar Membrane

CA: Chronoamperometry

CE: Counter Electrode

CEM: Cation Exchange Membrane

CP: Chronopotentiometry

CV: Cyclic Voltammetry

ECSA: Electrochemical Surface Area

EC: Electrochemical / Energy Consumption

EDX: Energy Dispersive X-ray Spectroscopy

EIS: Electrochemical Impedance Spectroscopy

FE: Faradaic Efficiency

GC: Gas Chromatography

HER: Hydrogen Evolution Reaction

HR-TEM: High-Resolution Transmission Electron Microscopy

IC: Ion Chromatography

LSV: Linear Sweep Voltammetry

NO$_3^-$RR: Nitrate Reduction Reaction

OCV: Open Circuit Voltage

PED: Pulsed Electrodeposition

PEIS: Potentiostatic Electrochemical Impedance Spectroscopy

PLAL: Pulsed Laser Ablation in Liquids

RDE: Rotating Disk Electrode

RDS: Rate-Determining Step

RE: Reference Electrode

RHE: Reversible Hydrogen Electrode

SE: Selectivity Efficiency

SEM: Scanning Electron Microscopy

SHE: Standard Hydrogen Electrode

WE: Working Electrode

XPS: X-ray Photoelectron Spectroscopy

XRD: X-ray Diffraction

Chapter 1

Introduction

CHAPTER 1 GENERAL INTRODUCTION.

1.1. Research context.

Ammonia, a compound conformed by nitrogen (N_2) and hydrogen (H_2) with the formula NH_3, has been a central component in the development of modern agriculture and industry. Its role extends from ancient practices to modern applications, marking its significance over centuries. In our days, the rapid increase in energy demand, along with the changes associated with greenhouse gas emissions, requires the support of alternative energy systems that can help to meet this demand. The following sections have the objective of providing an overview of the challenges that motivated the investigation of electrochemical generation of NH_3 as a free-carbon energy source, together with the state of the art of the actual technology to finally define the scope of this thesis.

1.1.1. Energy sources and greenhouse gas emissions.

The energy sector, encompassing generation, distribution, and consumption, has significantly expanded due to exponential population and economic growth since the Industrial Revolution [1]. The urban population has surged from 746 million in the mid-20th century to 8 billion in 2024, with projections reaching 9.8 billion by 2050 [2]. This rapid growth places immense pressure on each component of the energy sector.

One of the key indicators of this pressure is the rising electricity demand. According to the International Energy Agency (IEA), global electricity demand increased by nearly 2.4% in 2022, though this growth slowed to 2.2% in 2023 [3]. This trend underscores the challenges in meeting the energy needs of a rapidly expanding population and urbanizing world. However, with the increasing electricity demand, there are significant implications for CO_2 emissions. The IEA also reports that global energy-related CO_2 emissions rose by 1.1% in 2023, increasing by 410 million tons (Mt) to a record high of 37.4 billion tons (Gt). This compares to a 1.3% increase in 2022, where emissions grew by 490 Mt, with over 65% of this rise attributed to coal [4]. These values highlight an ongoing strain on both energy resources and the environment, emphasizing the urgent need for sustainable solutions.

In addressing these challenges, low-carbon energy sources, including renewables (wind, solar, hydroelectric) and nuclear, are projected to account for 46% of the world's electricity generation by the end of 2026, up from 39% in 2023 according to projections of the IEA [3]. Although renewable energy is growing impressively in many parts of the world, it is still insufficient to achieve net-zero emissions by mid-century [4] and other alternatives must be addressed. **Figure 1.1** represents the

evolution of energy consumption by sources [1], [4], [5] illustrating the shifts and trends within the energy sector over time.
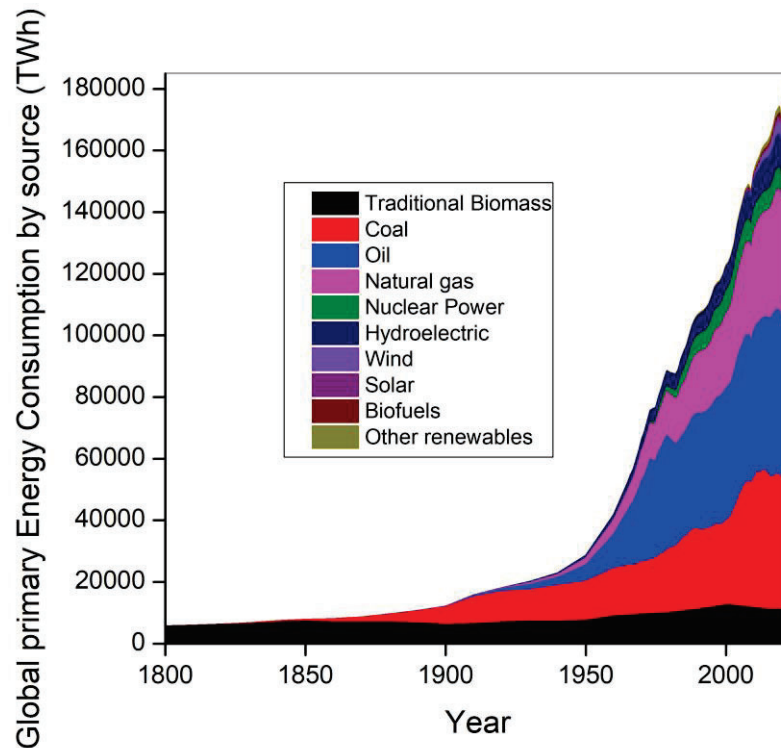
Figure 1.1 Evolution of energy demand distributed by source in the period 1800 to 2022. Data obtained from the International Energy Agency.

During the last three decades, many studies have pointed that the greenhouse gas emissions affect the planet's climate [5], with the major contribution of CO_2 concentration in the atmosphere directly connected to an increase in the average global temperature[6]–[8]. In turn, this increase has been correlated to numerous effects on the ecosystems. The correlation between traditional energy systems, CO_2 emissions, and the increase in average temperature has captured global attention. This led to the 2015 Paris Agreement, where 195 countries committed to reducing CO_2 emissions. The goal is to keep global temperatures below 2°C above pre-industrial levels, striving for a 1.5°C limit [9], [10].

Recognizing that economic growth requires increased energy consumption underscores the urgency of transitioning to sustainable energy sources. It is crucial to address the negative impacts of traditional energy systems on our climate and ecosystems to responsibly and sustainably meet rising global energy demands and follow the international agreements.

1.1.2. Transforming energy systems.

To help mitigate global climate change and achieve the objectives of international agreements, global energy demand should be covered with a secure, affordable, and reliable energy supply that ensures reduced greenhouse gas emissions [11], [12]. Meeting global energy demand in as sustainable way will require both increased energy efficiency of existing carbon-based technologies, and a shift to others that can be close the net-zero emissions[13], [14]. By Integrating renewable energy into these traditional systems contributes to a more sustainable energy supply, reducing the consumption of non-renewable energy and consequently lowering the emission of greenhouse gases [14].

In 2022, the total greenhouse gas emissions of the European Union (EU); excluding land use, land-use change, and forestry, and international aviation; decreased by 2.4% compared to 2021. This reduction continues the 30-year descending trend of emissions in the EU. Among several reasons, this reduction in CO_2 emissions was possible by the implementation of renewable energy sources, with a record high of around 60 Gigawatts of wind and solar installations according to a REPORT FROM THE COMMISSION TO THE EUROPEAN PARLIAMENT AND THE COUNCIL EU Climate Action Progress Report 2023[15].

In the specific case of Spain, during 2022 the main sources of renewable energy were wind, solar, biofuel and waste, and hydroelectric power, making up 56.4% of the country's total energy production (**Figure 1.2**). These sources generally avoid air, land, or water pollution and emit low CO_2 (including nuclear power), with reduced costs due to technological advances. However, their intermittency, dependency on climate conditions, and storage challenges demand alternatives. For instance, potential solutions include developing chemical energy storage technologies, such as converting CO_2 to hydrocarbons and producing nitrogen-energy carriers like NH_3.
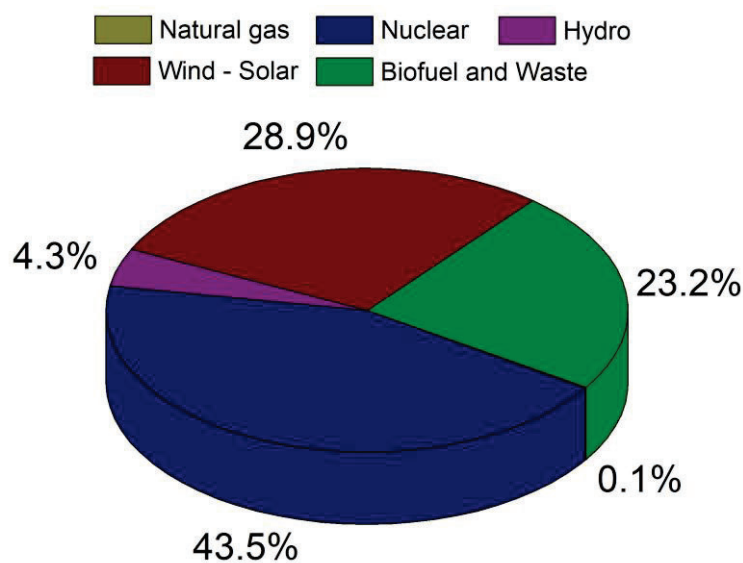
Figure 1.2 Sources of energy in Spain in 2022. Data obtained from World Energy Statistics and Balances, IEA.

1.1.3.   Powering new technologies.

As previously mentioned, the intermittency of renewable energy sources necessitates alternatives to smooth the instability of its production. This intermittency sometimes leads to periods where excess energy (specifically electric energy) cannot be consumed immediately and is lost. For this reason, chemical energy storage systems can utilize the surplus electricity from renewable power plants to drive chemical or electrochemical reactions, producing several types of energy carriers. This method captures energy that might otherwise be wasted.

The current competitive prices of renewable energy present a significant opportunity to transform sectors requiring chemicals such as H_2, alcohols, and other energy carriers. However, using excess renewable energy for chemical storage is only the first stage of this transformation. The second stage involves the full production of chemical energy carriers using renewable energy. This approach, known as Power-to-X, converts renewable electricity into carbon-neutral synthetic fuels, such as H_2, synthetic natural gas, liquid fuels, or synthetic energy carriers[16]. Power-to-X also addresses environmental problems by transforming certain pollutants such as CO_2, nitrogen oxides and oxyanions among others, into valuable compounds and energy carriers into a circular economy context[17].

Electrochemical processes are included into Power-to-X technologies and can contribute mitigating the impact of pollutants and add economic value to clean energy use[18]. **Figure 1.3** schematically represents this concept.
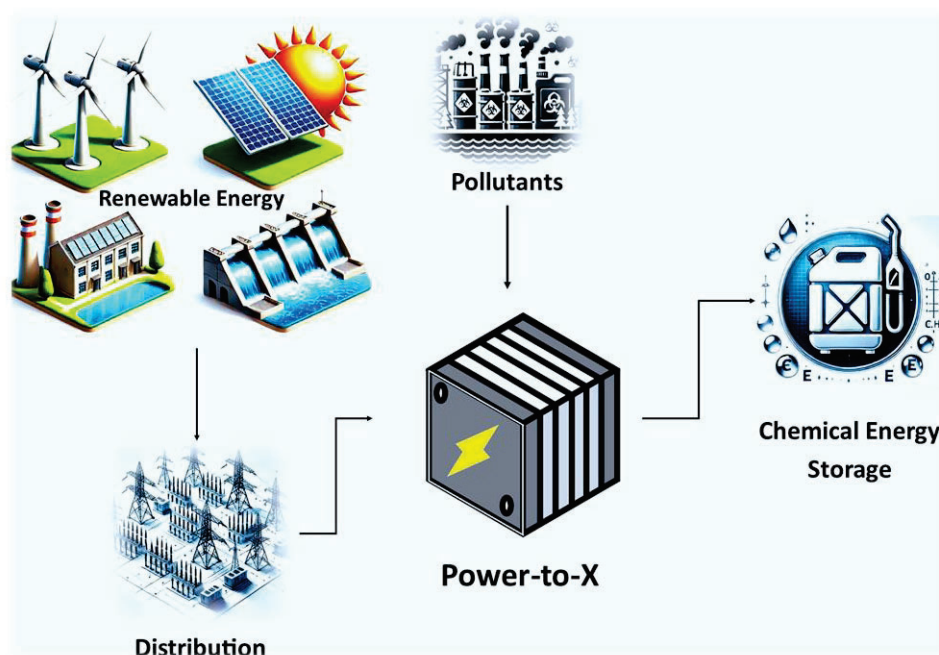
Figure 1.3 Power-to-X concept for converting electricity into carbon-neutral synthetic fuels, such as H_2, synthetic natural gas, liquid fuels, or synthetic energy carriers.

1.1.4. Electrochemical processes for the future.

Electrochemical processes have a low environmental impact, typically operate under mild conditions, and are well-suited to be coupled with renewable electricity sources for decarbonization [19]. This allows electrical energy to be stored in the chemical bonds of various substances, including H_2, alcohols, and others.

Among these substances, H_2 has attracted special attention as a high-energy dense fuel/energy carrier (gravimetric energy density: 143 MJ·kg^{-1}) and an environmentally friendly alternative to fossil fuels[20] when it is produced using renewable energy sources (green-H_2)[21]. Its use in the transportation and electricity sectors can significantly reduce carbon emissions. Additionally, its compatibility with the actual natural gas infrastructure makes H_2 an attractive option for the future [22].

Although hydrogen's high gravimetric energy density makes it a promising energy carrier for weight-sensitive applications, its low volumetric energy density presents challenges for storage and transportation (refer to **Figure 1.4**). Storing H_2 as compressed gas is inefficient because of its lightest molecular weight and very low density, with 1 kg of gas occupying over 11 m³ at room temperature and atmospheric pressure. To be viable for large-scale storage, the storage density must be increased, which increases risk factors such as heat, pressure, and process complexity. To understand this, compressed gas storage systems require storage compartments and compressors, and large amounts of gaseous H_2 are typically stored at pressures not exceeding 100 bar above ground and 200 bar underground. Even at 100 bar and 20°C, hydrogen gas density is only about 7.8 kg·m³, leading to large storage volumes and high investment costs. On the contrary, liquefying H_2 increases its density significantly, with saturated liquid hydrogen at 1 bar having a density of 70 kg·m³. While this high density is advantageous for transporting, the liquefaction process is energy-intensive due to its low boiling point (−250°C at 1 bar) and the need for precooling with liquid nitrogen [23]. This makes the storage of liquid hydrogen as well costly and complex. To harness the benefits of hydrogen's gravimetric energy density while addressing the issues related to volumetric energy density, ongoing efforts focus improving hydrogen storage methods and system efficiency as will see next.

An alternative to storing H_2 as a final product is to store it as NH_3, which has a higher **volumetric energy density** of about 12.7 MJ·L^{-1} compared to hydrogen's 10.1 MJ·L^{-1} [1] (both in liquid forms). NH_3 can be easily liquefied by increasing the pressure to about 10 bar at room temperature or by cooling it to -33°C at 1 bar. Additionally, NH_3 is safer and easier to store and transport due to its low vapor pressure and high boiling point [25], [26], all this with the advantage of being compatible with existing infrastructure.

Figure 1.4 plots the volumetric energy density vs. the gravimetric energy density of some common energy carriers. Although NH_3 shows the lowest gravimetric energy density among the compounds in the figure, it is the only non-carbon energy carrier of the group besides hydrogen.

Building up on the advantages of having NH_3, it is worth exploring into the available methods for producing it using renewable energy sources. In the next sections we will introduce important aspects of NH_3 as an alternative energy/hydrogen carrier and in the industry as commodity.
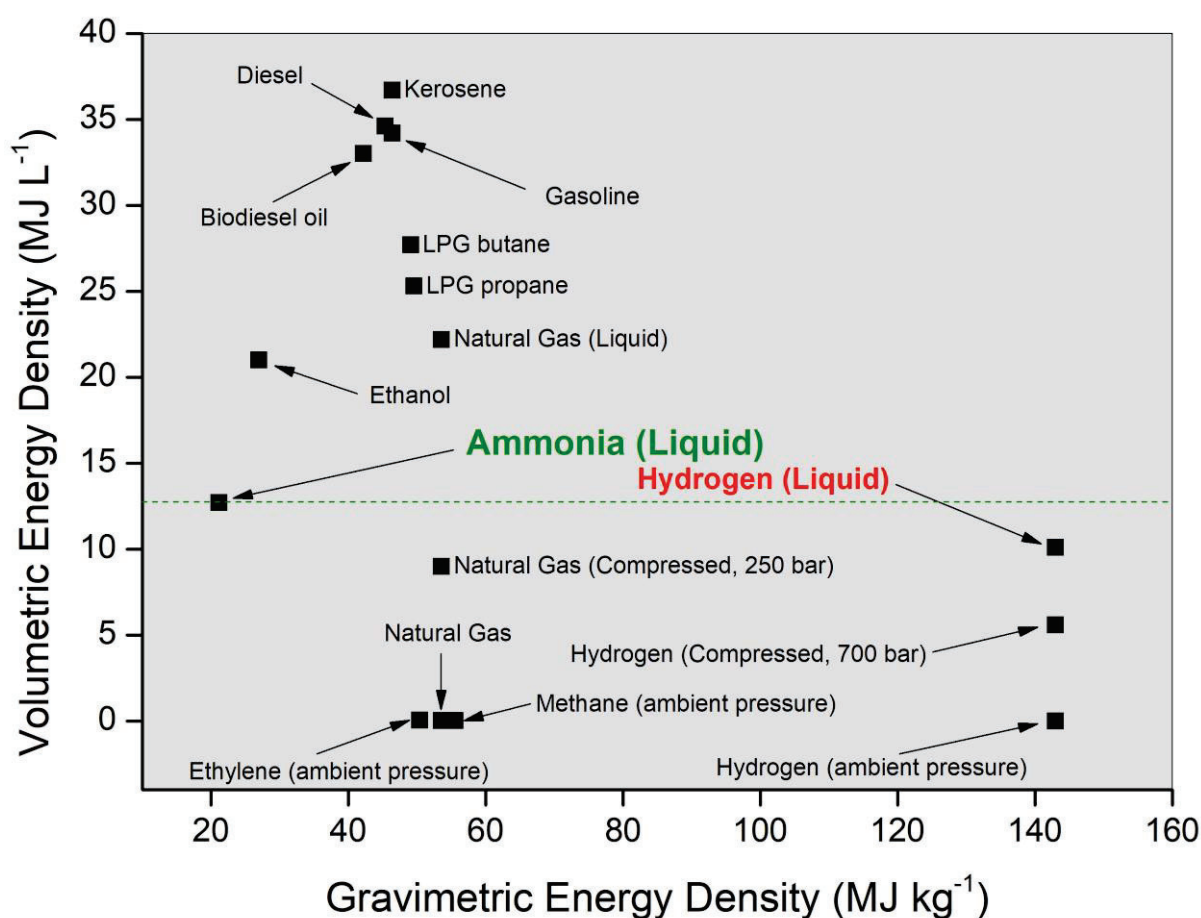
Figure 1.4 Energy density vs specific energy of common fuels. Data obtained from [24], [25], [27], [28]

1.1.5. Ammonia in the past, present and future. Generation of NH_3 and CO_2 emissions.

Ammonia or nitrogen trihydride is a colorless, poisonous gas with a strong nervous odor. It occurs in nature, primarily by anaerobic decay of plants and animal matter. Some plants, mainly legumes, in combination with rhizobia bacteria use atmospheric nitrogen to produce NH_3.
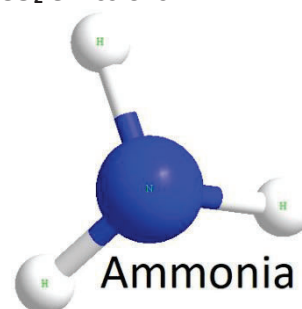
Historically, NH_3 has an extended variety of uses, including very early civilizations that utilized ammonium chloride (NH_4Cl) in dyeing and metallurgy. It was isolated in the 18th century by the chemists Joseph Black, Peter Woulfe, Carl Wilhem Scheele, and Joseph Priestley in 1785 and Claude Louis Berthollet determined its elemental composition.

In our days, the use of NH_3 is extensive, particularly in agriculture, where it is crucial for fertilizer production (around 70% of the total amount[29]). These compounds are the main source of nitrogen (a macronutrient) used for plants to grow, being this way essential for food production (**Table 1.1**).

N-based fertilizer	N% by weight	Precursors
NH_3	82%	H_2, N_2
Urea – $CO(NH_2)_2$	46%	NH_3, carbon dioxide (CO_2)
Ammonium nitrate – NH_4NO_3	34%	Nitric acid (HNO_3), NH_3
Calcium ammonium nitrate – $Ca(NO_3)_2(NH_4)_2$	27%	Calcium carbonate ($CaCO_3$), NH_4NO_3, H_2O
Urea ammonium nitrate – $H_2ONH_3HNO_3CO(NH_2)_2$	30%	NH_3, NO_3, $CO(NH_2)_2$, H_2O
Diammonium phosphate – $(NH_4)_2HPO_4$	18%	NH_3, phosphoric acid (H_3PO_4)
Monoammonium phosphate – $(NH_4)H_2PO_4$	11%	NH_3, phosphoric acid (H_3PO_4)
Ammonium sulphate – NH_4SO_4	21%	NH_3, sulfuric acid (H_2SO_4)

Table 1.1 Nitrogen content of typical NH_3-derivative fertilizers. Represented from Table 1.1 from reference [30]

Along with fertilizers production, NH_3 plays a crucial role in various industrial processes, where approximately 30% of global demand is for a range of industrial applications, including plastics, explosives, pharmaceutical products among others, and as well a role in refrigeration and wastewater treatment processes[30], [31].

Although NH_3 production is currently massive, its synthetic generation at industrial scale was not possible until the second decade of the 20th century [32]. This was due that N_2 molecule is extremely stable as consequence of strong triple bond, which has a bond-dissociation energy of approx. 941 $kJ \cdot mol^{-1}$ [33]. Breaking this bond requires a large activation energy, making difficult to conduct the reaction under mild conditions of pressure and temperature. For this reason, when Fritz Haber and Carl Bosch introduced the **Haber-Bosch process (H-B)** pointed a complete change of paradigm of NH_3 production. This industrial process revolutionized agriculture by enabling the mass production of NH_3 from atmospheric N_2 and H_2 gas under high pressure and temperature, using an iron (Fe) and later a ruthenium (Ru) catalyst. This innovation provided an abundant source of NH_3-based fertilizers, addressing the global food shortages and catalyzed NH_3 transformative impact.
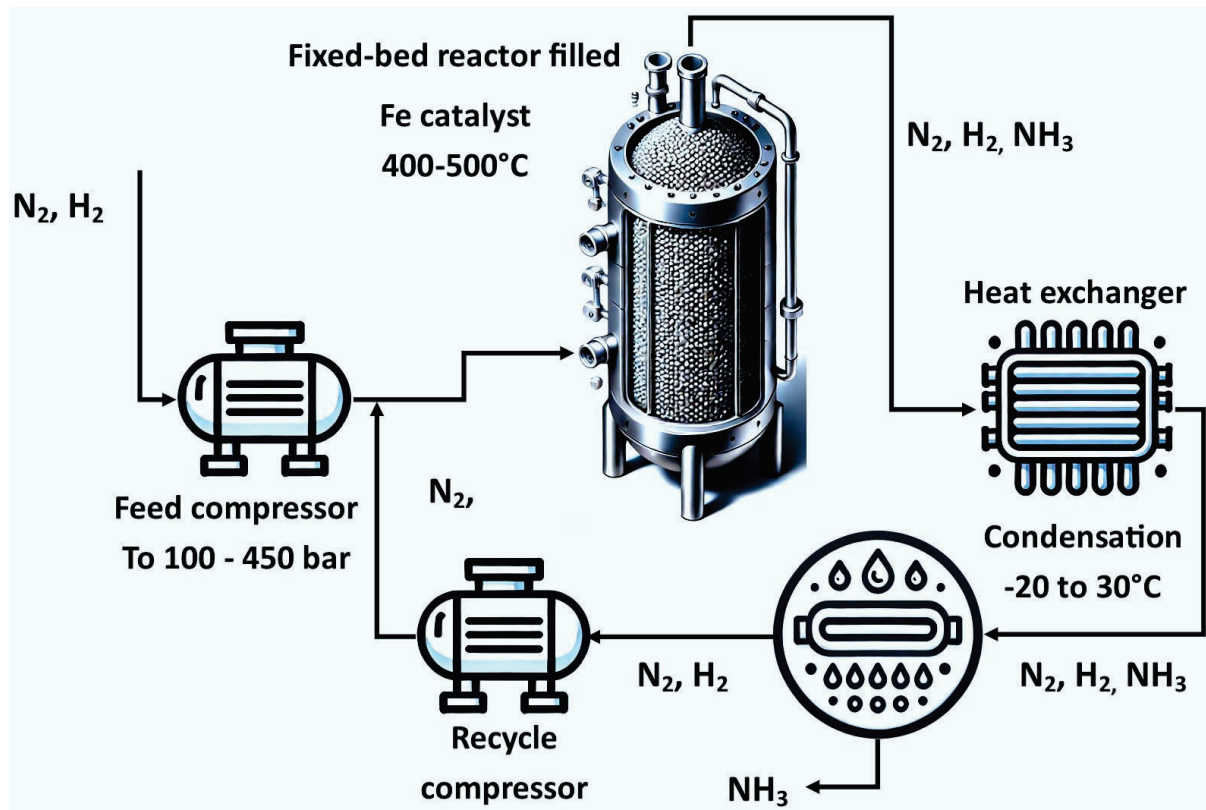
Figure 1.5 Schematic diagram of *Haber-Bosch process. Inspired from reference* [32].

In the H-B process (schematically represented in **Figure 1.5**) the system is supplied with H_2, typically produced from methane through Steam Methane Reforming (SMR), and N_2, which completes the gas mixture. This gas mixture is then compressed to pressures of 100 to 450 bars and fed into the Fe or Ru fixed-bed reactor operating at temperatures between 400 and 500°C. Only about 15-20% of the feed gas is converted to NH_3. The reactor effluent is then cooled to ambient temperature to condense the NH_3 and the remaining gas is recycled back into the bed reactor.

The H-B process faces some important drawbacks:

(1) Energy intensive: H-B requires high temperatures (400 - 500°C) and pressures (100 – 450 bar) to synthesize NH_3[34], making it highly energy-intensive. This energy is typically supplied by non-renewable energy sources consuming 1 % to 2 % of the global energy supply annually[35]. **(2) Greenhouse gas Emissions:** The H_2 required for the H-B process is primarily produced via SMR, which emits a global average of 2.9-ton carbon dioxide (CO_2) per ton NH_3[36], resulting in one of the major contributors to global carbon emissions. **(3) Scalability Issues and dependence on fossil fuels:** The process is designed for large-scale production, which limits its flexibility and makes it less suitable for

decentralized or small-scale applications. Along with this, the process is not well suited for batch operation, making it difficult to integrate with renewable energy sources[37].

In the future, NH_3 is set to play a significant role in various alternative sectors to those mentioned due to its potential as an energy/hydrogen carrier. This includes its use in internal combustion engines and gas turbines, etc. Additionally, the concept of green-NH_3 (produced with zero or net-zero emissions) positions it as an active participant in the decarbonization of the global energy system expected for 2050[38].

Figure 1.6 illustrates the demand for NH_3 in 2020, expressed in Mton of nitrogen, and provides a perspective on future demand of the global energy system, considering both Sustainable and Net-Zero scenarios[30]. Notably, in the ideal Net-Zero-emissions scenario, it is expected that around 50% of the total NH_3 demand will come from its use as an energy carrier.
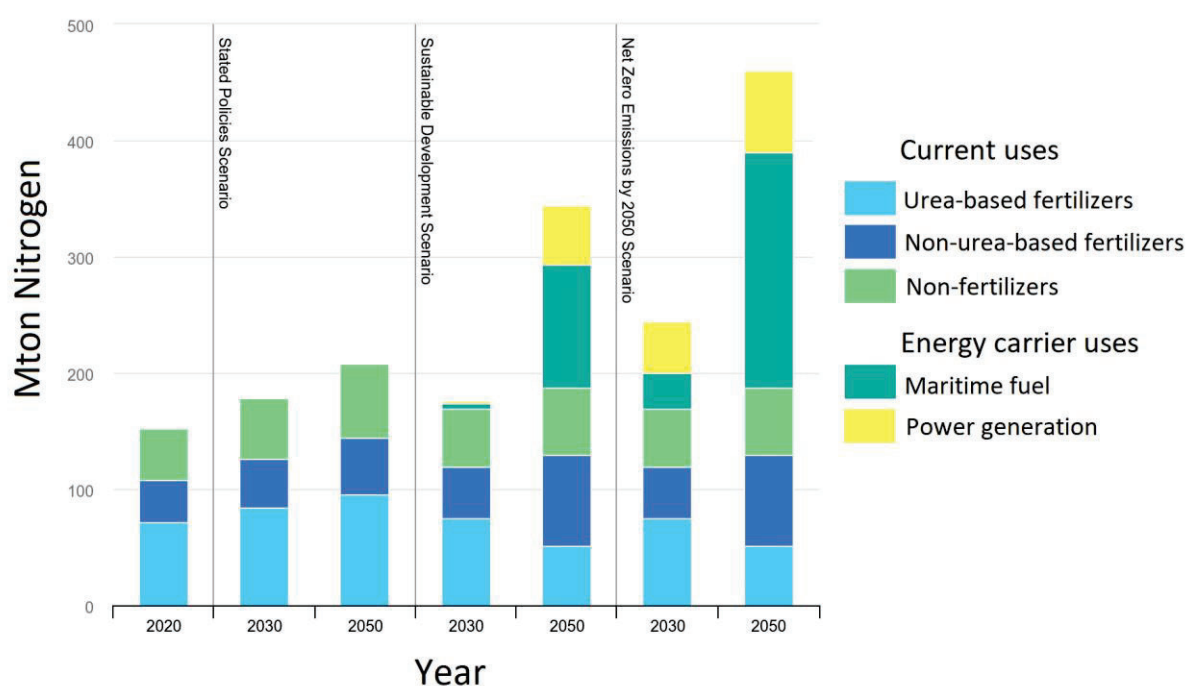
Figure 1.6 Actual and future demand of NH_3 expressed in Mton of Nitrogen. This is a work derived by Marcelo Chavez from IEA material and Marcelo Chavez is solely liable and responsible for this derived work. The derived work is not endorsed by the IEA in any manner. Source[30].

1.1.6. Generation of NH₃ and CO₂ emissions.

The current technology used for NH_3 production generates about 450 Mton of CO_2 annually (about 1.3% of global CO_2 emissions) and consumes 1–2% of the total global energy production according to the IEA. This is because about 22% of its production is coal-powered, which duplicates the amount of emitted CO_2 if compared with natural gas-based production[30].
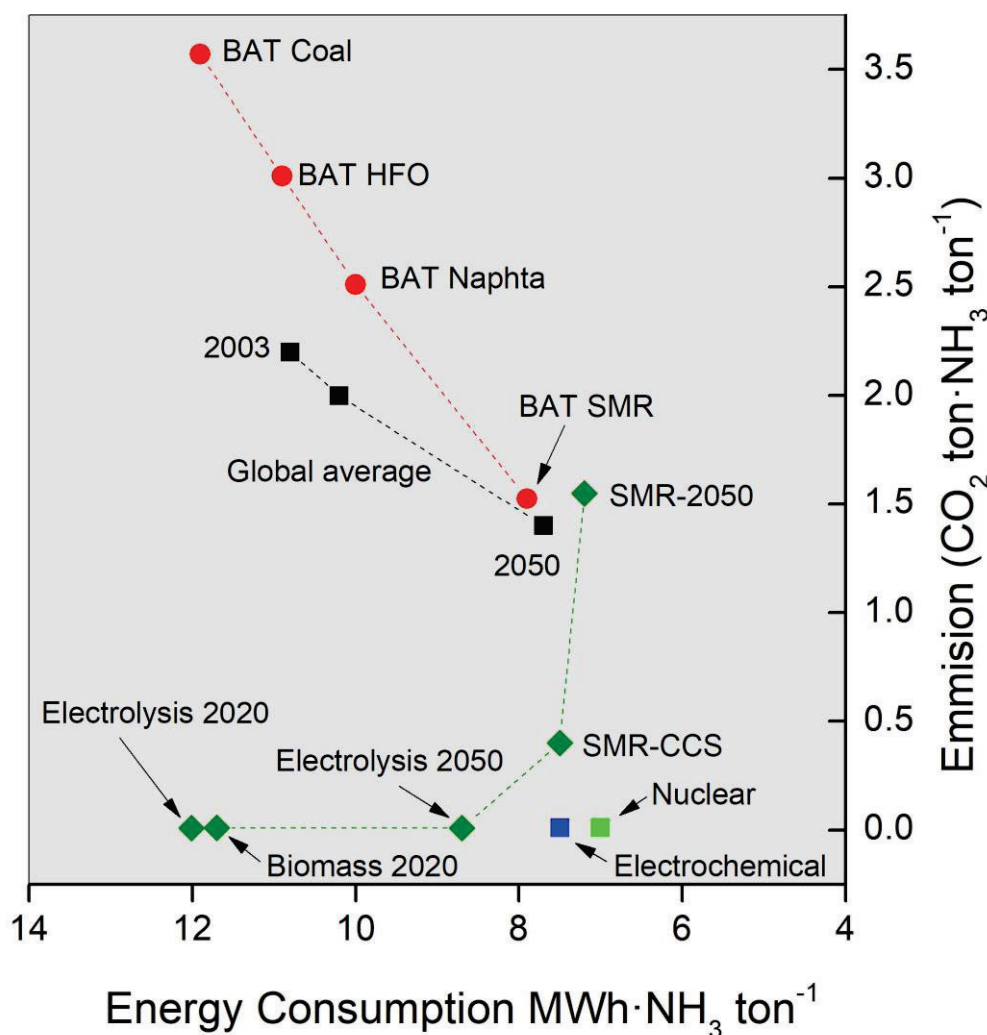
Figure 1.7 Evolution of CO₂ emissions for NH₃ technologies from 2000 to 2050. Adapted from[39]. BAT - Best Available Technology. CCS - Captured and Stored Carbon. HFO – Heavy Fuel Oil.

Figure 1.7 illustrates the current and expected evolution of energy consumption and associated CO_2 emissions for NH_3 technologies from 2000 to 2050. Among current processes, the coal-based H-B process has a high energy requirement of about 12 MWh per ton of NH_3[39]. Progressive system developments, including the replacement of the coal-based H-B process with the Best Available

Technology (BAT) using Heavy Fuel Oil (HFO), Naphtha, and SMR show improved system efficiencies. The BAT-SMR process has shown a significantly reduced carbon footprint (1.5 tons CO_2 per ton of NH_3) and improved energy efficiency (8 MWh per ton of NH_3), making it the most efficient H-B plant in operation. In contrast, NH_3 production via direct electrolysis, despite its low CO_2 emissions, still shows a high energy consumption (12 MWh per ton of NH_3) compared to the current BAT-SMR process. However, by 2050, it is anticipated that NH_3 production from direct electrolysis will achieve improved system efficiency (with approx. zero-CO_2 emissions and around 8.5 MWh per ton of NH_3 of energy consumption), and with nuclear-powered NH_3 synthesis expected to offer the most efficient technology.

Without the improvement in efficiency and the transition from the coal based H-B processes, as well as from fossil fuels to renewable energy sources and better technologies, emissions will keep growing joined to the increased demand of NH_3, already situated as the second most consumed commodity among industrial chemicals[40].

In the previous sections, we mentioned that electrocatalysis is an integral part of the Power-to-X concept. Notably, the technology referred to as "Electrochemical" in **Figure 1.7** corresponds to the direct electrocatalytic generation of NH_3 from N_2. This promising ongoing development process aims to achieve the full electroreduction of the N_2 molecule to NH_3 using water or other sources of hydrogen under milder conditions than the H-B process. In the next section, we will discuss this technology in more detail.

1.2. N_2 electrochemical fixation for producing NH_3. What is the problem here?

The energy-intensive nature, complexity, and environmental impact of the H-B process drive the search for alternatives that enable the reaction of N_2 and H_2 under milder conditions. In this context, advancements in sustainable chemistry have explored the aqueous electrochemical reduction of N_2 (eN_2RR) as a promising alternative. The eN_2RR employs electrocatalysis to convert N_2 to NH_3 or to the protonated ammonium (NH_4^+) under ambient conditions, promising a sustainable solution with lower energy requirements and a reduced carbon footprint. The eN_2RR involves the direct reduction of N_2 gas to NH_3 using electrical energy (e$^-$) and H_2O as the source of protons (H$^+$). The overall reaction is represented in **Equation 1.1.**

$$N_2 + 8H^+ + 6e^- \rightarrow 2NH_4^+ \qquad \text{(U°= 0.275 vs Standard Hydrogen Electrode)} \qquad 1.1$$

$$2H^+ + 2e^- \rightarrow H_2 \qquad \text{(U°= 0.000 vs Standard Hydrogen Electrode)} \qquad 1.2$$
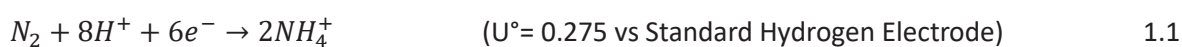
As presented in **Figure 1.8** eN$_2$RR can follow several direct and indirect reaction mechanisms. Direct NH$_3$ synthesis follows dissociative and associative pathways, differentiated by either direct dissociation of the triple bond of N$_2$ or by protonation of the adsorbed N$_2$ molecule, respectively. The H-B process corresponds to a dissociative pathway, which requires high input energy of 941 kJ·mol^{-1}, and involves the hydrogenation of dissociated nitrogen using H$_2$. In the case of the associative pathway, it involves a six proton-coupled electron transfer steps, keeping the N−N bond intact initially and then divided into associative alternating and associative distal pathways[41]. In the alternating pathway, hydrogenation occurs on both nitrogen atoms simultaneously, while in the distal pathway, it occurs sequentially, with the first ammonia molecule being released before the second nitrogen is protonated. Additionally, the Mars–van Krevelen (MvK) mechanism which occurs on transition metal nitrides[42].
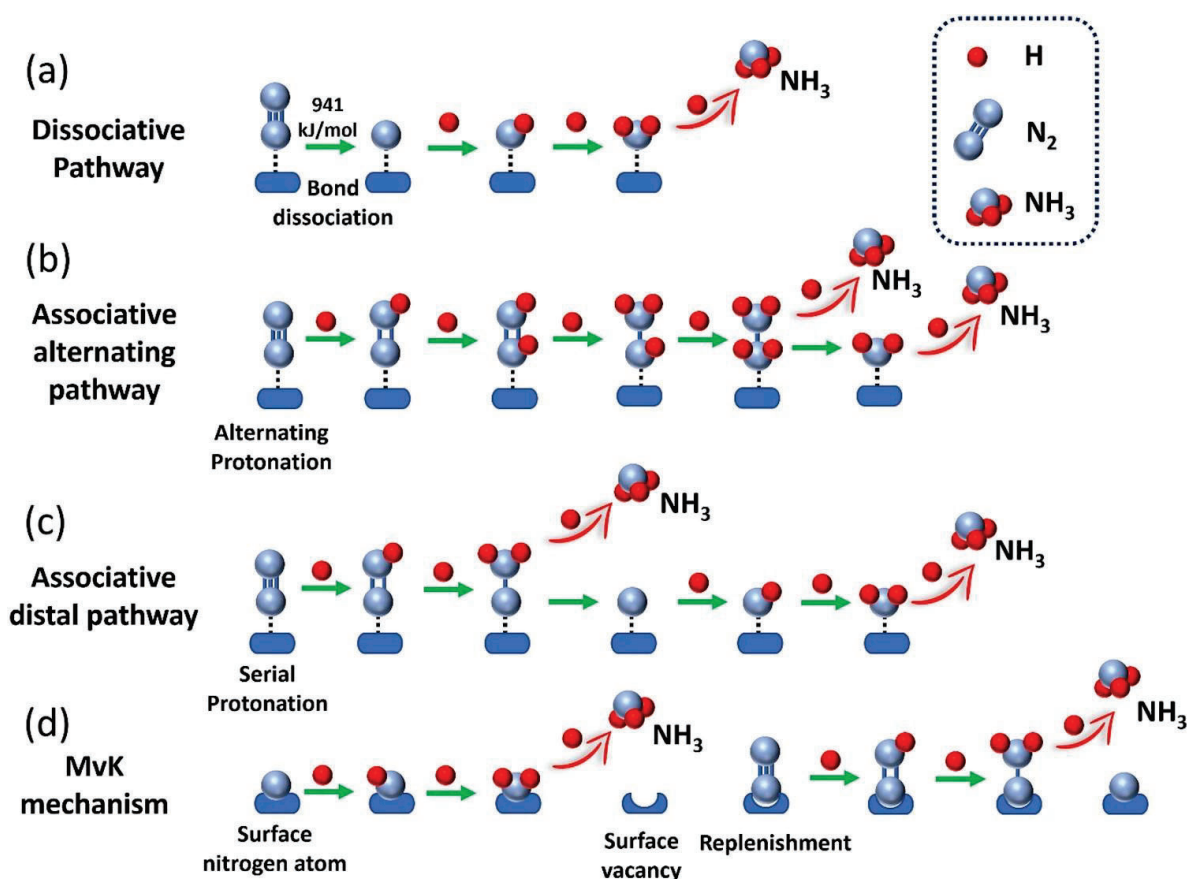
Figure 1.8 NH$_3$ synthesis mechanisms. Reprinted from source[43].

Although eN$_2$RR represents as a very promising technology for producing NH$_3$, it still faces several limitations that confines the technology at laboratory scale. One major challenge is the already mentioned high stability of the triple bond in the N$_2$ molecule, which is of the most inert diatomic molecules that adds complexity to electrochemical reductions[33].

In addition to the bond stability, a second limitation is found in the very low solubility of the molecule in water base electrolytes. The solubility of N_2 in water at normal conditions is approx. 20 mg·L^{-1}, a very low value that derives in mass transport limitations that restrict the rate at which N_2 can be supplied to the catalyst surface for reduction[44]. Enhancing the solubility of N_2 or improving mass transport within the electrolyte can help mitigate this issue. Approaches such as using gas-diffusion electrodes (GDE) or designing electrolytes that have better N_2 solubility are actively under research. Another significant limitation inherent to aqueous electrolysis is that eN_2RR has a standard reduction potential very close to that of the hydrogen evolution reaction (HER)[44]. Additionally, eN_2RR is kinetically more complex than HER. While HER only requires the reduction of two protons (**Equation 1.2**), eN_2RR involves the adsorption and splitting of N_2, followed by its reaction with six or eight protons to produce NH_3 or ammonium (NH_4^+), respectively[45].

Another significant challenge is the absence of an effective catalyst that combines selectivity, high catalytic activity, and stability under operational conditions. Designing such materials is complex, as many catalysts suffer from poisoning and degradation due to reaction intermediates and by-products[33].

All these factors combined directly impact the efficiency of the eN_2RR process. However, in the recent years, research efforts have been succeeded in overcoming many of the mentioned challenges. Several types of electrocatalyst have shown excellent results in terms of current efficiency, reaching values close to 70% for the direct eN_2RR[46] but maintaining low productivities.

1.3. NO_3^- and NO_2^- as pollutants and as a nitrogen source.

NO_3^- and NO_2^- are nitrogen oxyanions with oxidations stages of 5+ and 3+ respectively. They are key components of the nitrogen cycle, also essential for agricultural productivity and environmental health. However, the extensive use of nitrogen-based fertilizers has led to significant nitrate pollution, which poses threats to both ecosystems and human health[47], [48]. In the specific case of the EU, the average NO_3^- concentration in groundwaters did not change significantly from 2000 to 2021 despite the changes in legislation. In fact, it has not been reduced the number of groundwater monitoring stations with NO_3^- concentrations greater than 50 mg·L^{-1} (or 50 ppm). **Figure 1.9** shows the NO_3^- concentrations in groundwater for the period 2016 – 2019, classifying the type of water by concentration of the pollutant. All EU-27 countries had some groundwaters with reported NO_3^- concentrations above the maximum allowable of 50 ppm of NO_3^-. At present, there are several physical and chemical treatment methods on the market, such as electrodialysis, reverse osmosis, ion

exchange, and others which can be used only to collect NO_3^- from wastewater resulting in the accumulation of high-concentration NO_3^- brines for after treatment [17]. For instance, finding a route for NO_3^- and NO_2^- reconversion to N_2, or to value-added products such NH_3, is highly desirable. NO_3^- electrochemical reduction (NO_3^-RR) along with its complementary NO_2^-RR to NH_3 have recently became trend research, pointing to be an alternative to eN_2RR given its dual-benefit solution: it removes the harmful NO_3^-/NO_2^- ions from water sources and produces valuable NH_3 offering at the same time, the option of being powered by renewable energy sources. As is the case of N_2 reduction, NO_3^-RR involves complex pathways where a total of eight electrons are required for the complete reduction to NH_3. Details of the pathways and conditions have been studied during the last years, giving an overview of the key factors governing the reaction that will be presented in the further sections.
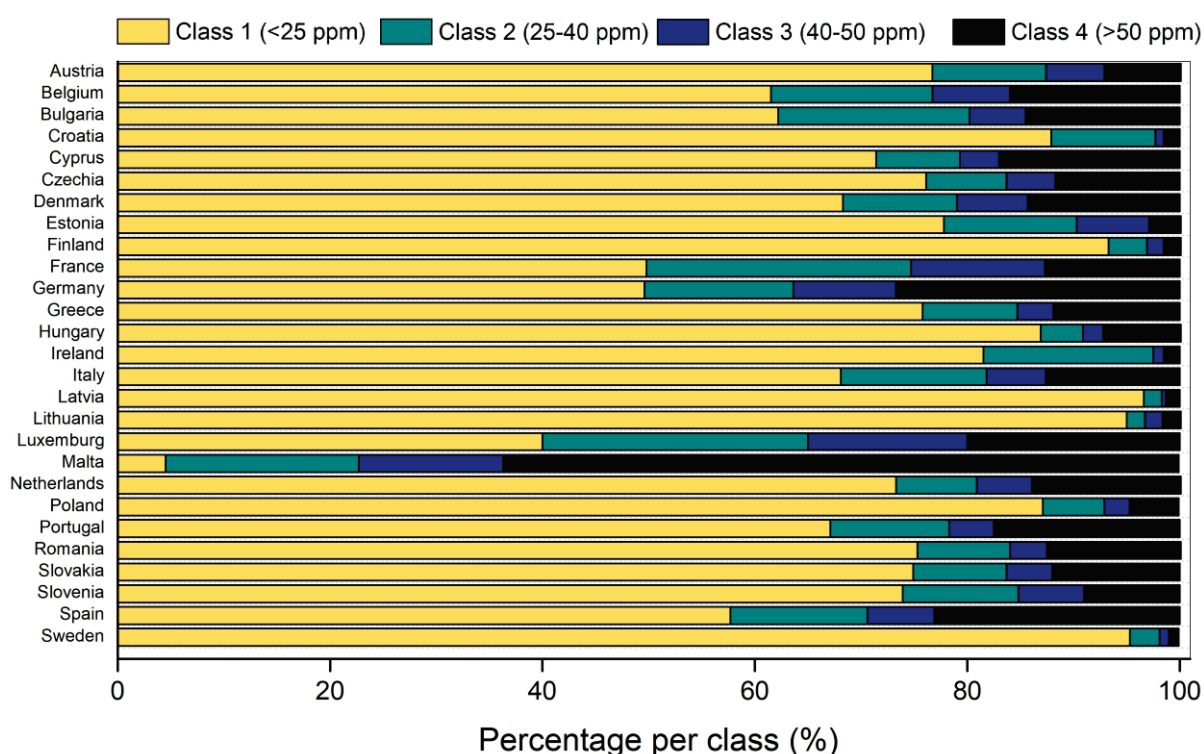
Figure 1.9 NO_3^- in Groundwater - Nitrates Directive reporting period 7 (2016-2019) from the European Environment Agency (EEA). Class 1 represents concentrations that are below 25 ppm, Class 2 from 25 to 40 ppm, class 3 from 40 to 50 ppm and Class 4 >50 ppm maximum allowable concentration.

1.4. NO₃⁻RR to NH₃. An opportunity for restoring the nitrogen cycle.

The NO_3RR has both a lower bond energy of $N - O$ (204 kJ·mol⁻¹) and a higher theoretical reduction reaction potential (0.69 V vs. RHE), compared with eN_2RR, ensuring a high selectivity due to the distant reduction potential to the competing HER[49]. This represents a thermodynamical advantage which allows a reachable route for NH_3 electrogeneration under mild conditions. Based on the previous

mentioned considerations, NO_3^-RR to NH_3 provides a promising solution for restoring the balance of the global nitrogen cycle along with the application of the circular economy mentioned above. However, calculations performed at molecular level has concluded that a slow NO_3^- reduction kinetics can be expected, due to the high energy of the lowest unoccupied molecular π^* orbital of NO_3^- molecules, resulting in a high activation energy. This has been experimentally corroborated during the study of the reaction with several materials. Therefore, the slow kinetics of the reaction is an intrinsic property of the reaction to be taken into account[50].
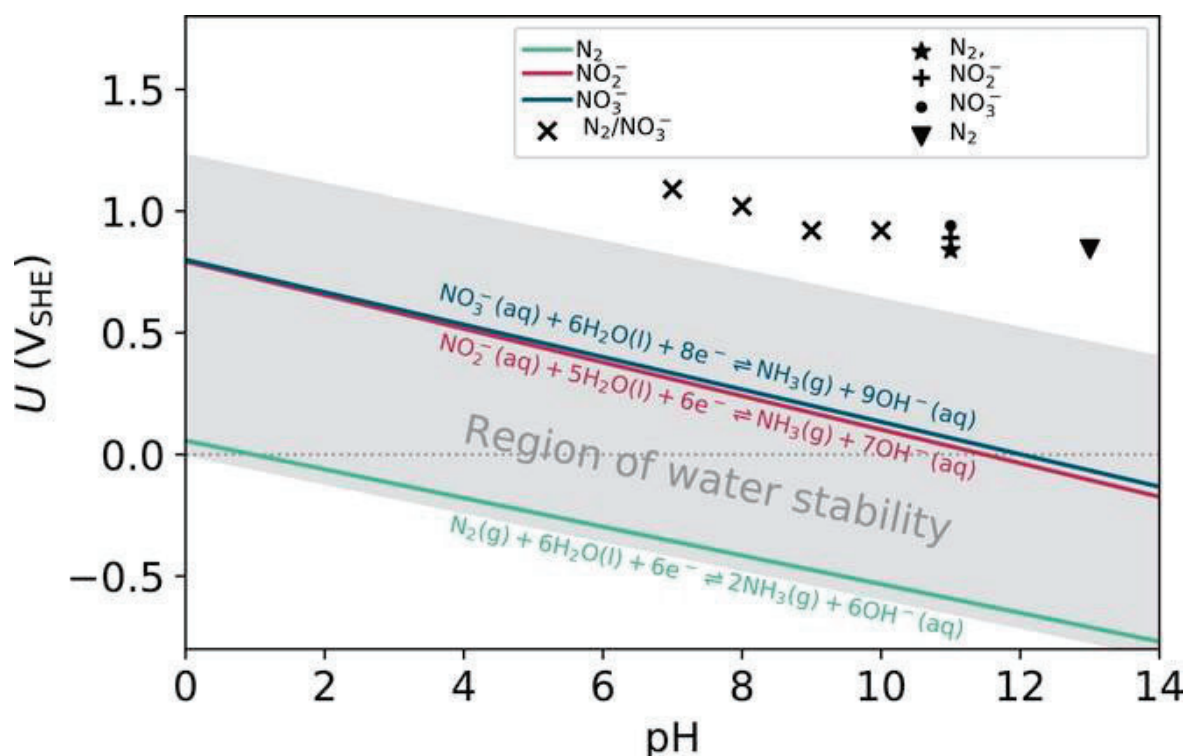
Figure 1.10 NO₃⁻ Pourbaix diagram. Reprinted from reference [51].

There is wide pH range where NO_3^-RR to NH_3 can be conducted (**Figure 1.10**), with dependance on the specific catalyst or other operative conditions. Studies have been carried out from extreme and moderate acidic conditions[52], [53], neutral[54], [55] to highly alkaline conditions[56], [57]. The HER is pH-dependent[58]. For instance, this reaction competes for the active sites of the catalyst with the NO_3^-RR. Although is not in all cases, current efficiencies of HER are normally higher in acid pH than in alkaline and consequently can reduce the overall efficiency towards NH_3. This because of the high availability of protons (H^+) in the solution. In contrast, as it will be discussed in the next section of reaction mechanisms, when NH_3^-RR is conducted in acidic media, several steps are proton-coupled electron transfer reactions, consuming H^+ and producing OH^- ions during the process[59]. This produces an increase of pH along the progress of the reaction modifying the initial conditions. For

electrode materials optimized for operating under acidic conditions, alkalinization of the electrolyte could limit efficiency and conducts to the generation of byproducts (nitrogen oxides – NO, N_2O, NO_2) or to deactivation of active sites given morphological changes or oxidation state. For electrolysis conducted in alkaline media, the reduction of NO_3^- ions to NH_3 with 100% of current efficiency has been demonstrated even in the absence of H^+ as source of hydrogen[60], [61]. pH fluctuation and effects still require further studies; however, it seems clear that the optimal pH has a strong dependency on the catalyst to be utilized for the reaction.

1.4.1. NO$_3^-$RR to NH$_3$ reaction pathways.

Under alkaline conditions, NO_3^-RR to NH_3 is conducted to a series of electron transfer reactions that occur in the presence of hydroxide ions (OH$^-$). The process is strongly influenced by the pH environment, which affects both reaction kinetics and stability of intermediates (**Figure 1.11**).
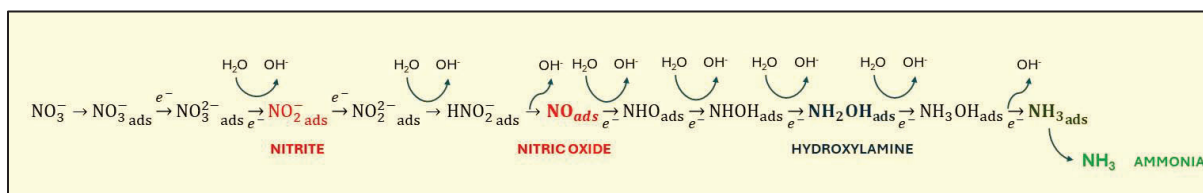
Figure 1.11 NO$_3^-$RR to NH$_3$ when alkaline conditions are applied.

This pathway involves stepwise electron transfer, converting NO_3^- to NO_2^-, then to nitric oxide (NO), hydroxylamine (NH_2OH), and finally to NH_3[62]–[65]:

$$NO_3^- + * \rightarrow *NO_3^- \qquad \textbf{(Adsorption of NO}_3^- \textbf{ to an active site *)} \qquad 1.3$$

$$*NO_3^- + 1e^- \rightarrow *NO_3^{2-} \qquad\qquad 1.4$$

$$*NO_3^{2-} + H_2O \rightarrow *HNO_3^- + OH^- \qquad\qquad 1.5$$

$$*HNO_3^- + 1e^- \rightarrow *\textcolor{red}{\textbf{NO}_2^-} + OH^- \qquad\qquad 1.6$$

1.3 to 1.6 reactions correspond to the **RDS** of the overall NO_3^-RR, this was corroborated by several authors which in general terms attributes the formation of NO_2^- intermediate as the limiting step.

$$*\textcolor{red}{\textbf{NO}_2^-} + 1e^- \rightarrow *NO_2^{2-} \qquad\qquad 1.7$$

$$*NO_2^{2-} + H_2O \rightarrow *HNO_2^- + OH^- \qquad\qquad 1.8$$

$$*HNO_2^- \rightarrow *\textcolor{red}{\textbf{NO}} + OH^- \qquad\qquad 1.9$$

Steps 1.7 to 1.9 correspond to the formation of nitric oxide, which is the second meta-stable intermediate, from where other products can be formed.

$$* \boldsymbol{NO} + 1e^- \rightarrow * NO^-$$ 1.10

$$* NO^- + H_2O \rightarrow * NHO + OH^-$$ 1.11

$$* NHO + 1e^- \rightarrow * NHO^-$$ 1.12

$$* NHO^- + H_2O \rightarrow NHOH + OH^-$$ 1.13

$$* NHOH + 1e^- \rightarrow * NHOH^-$$ 1.14

$$* NHOH^- + H_2O \rightarrow * \boldsymbol{NH_2OH} + OH^-$$ 1.15
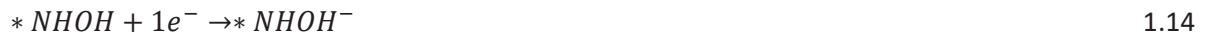
Steps 1.10 to 1.15 correspond to the formation of hydroxylamine as one of the potential reaction products. Experimental conditions can be adapted to conduct the reaction on this direction.

$$* \boldsymbol{NH_2OH} + 1e^- \rightarrow * NH_2OH^-$$ 1.16

$$* NH_2OH^- + H_2O \rightarrow * NH_3OH + OH^-$$ 1.17

$$* NH_3OH + 1e^- \rightarrow * NH_3 + OH^-$$ 1.18

$$* NH_3 \rightarrow \boldsymbol{NH_3} + *$$ 1.19

Steps 1.16 to 1.19 correspond to the final reduction of NH_2OH to NH_3.

The full reaction at **alkaline conditions** is summarized in **Equation 1.20.**

$$\boldsymbol{NO_3^- + 6H_2O + 8e^- \rightarrow NH_3 + 9OH^-}$$ 1.20

1.4.2. NO₃⁻RR to NH₃ under acidic conditions.

Under acidic conditions the high concentration of H^+ in the solution corresponds to the source of hydrogen atoms that form NH_3. The HER can be favored by the massive presence of protons in solution. Similar to the alkaline pathway, this one involves a stepwise electron transfer, converting NO_3^- to NO_2^- (RDS), a further formation of $*NO$, $*NH_2OH$ intermediates, and finally the reduction to NH_3 (**Figure 1.12**).
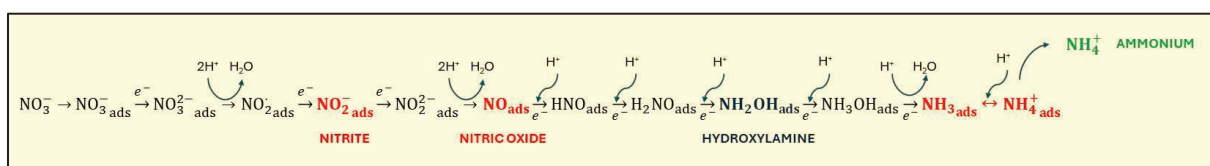
Figure 1.12 NO₃⁻RR to NH₃ when acidic conditions are applied.

The pathway is summarized in steps 1.21 to 1.26[2].

$$NO_3^- + * \rightarrow * NO_3^-$$ 1.21

$$* NO_3^- + 2H^+ + 2e^- \rightarrow \textcolor{red}{* \mathbf{NO_2^-}} + H_2O$$ 1.22

$$* NO_2^- + 5H^+ + 4e^- \rightarrow \textcolor{red}{* \mathbf{NH_2OH}} + H_2O$$ 1.23

$$* NH_2OH + 2H^+ + 2e^- \rightarrow * \mathbf{NH_3} + H_2O$$ 1.24

$$* NH_3 \rightarrow \textcolor{green}{\mathbf{NH_3}} + *$$ 1.25
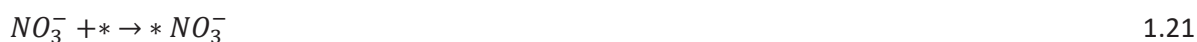
The full reaction at **acidic conditions** is the **Equation 1.26**.

$$\mathbf{NO_3^- + 9H^+ + 8e^- \rightarrow NH_3 + 3H_2O}$$ 1.26

1.4.3. Conditions affecting the NO$_3^-$RR to NH$_3$.

The NO$_3^-$RR to NH$_3$ is influenced by several conditions that affect the reaction's efficiency, selectivity, and overall performance. In this section, we analyze some key conditions that impact the process.

(a)   Concentration of NO$_3^-$:

The initial concentration of NO$_3^-$ influences both the kinetic and current efficiencies of NO$_3^-$RR to NH$_3$. Higher concentrations can lead to increased current densities, however, may also conduct to side-reactions. An optimal concentration of nitrate ensures there is enough reactant at the active sites while minimizing mass transport limitations, essential for maintaining high efficiency. At lower concentrations, the process may suffer due to limited availability of NO$_3^-$ ions. For nitrate concentrations less than 1M, direct reduction mechanisms are favored, whereas concentrations greater than 1M, particularly in the presence of nitrite, tend to support indirect reduction mechanisms. Additionally, in alkaline conditions, the abundance of OH- ions helps stabilize intermediates and enhance electron transfer, promoting the direct reduction pathway.

It is crucial to consider the initial concentration of the nitrate electrolyte when evaluating conversion or faradaic efficiency, as this affects the mass transfer rate in the solution and the coverage of nitrate on the electrode surface. At higher concentrations, the reaction rate is largely dependent on the availability of effective active sites. In contrast, at lower concentrations, the efficiency is more influenced by the transport of nitrate to the catalyst surface.

Given the broad applications and compatibility of nitrate reduction catalysts, a thorough investigation into varying initial nitrate concentrations is recommended to optimize performance and efficiency.

(b)   **Working electrode potential (U_W).**

The applied electrode potential influences the reduction steps and the overall reaction pathway. Each reduction step (NO_3^- to NO_2^-, NO_2^- to NO, NO to NH_2OH, and NH_2OH to NH_3) requires specific potentials to proceed efficiently[67]. This U_W must be sufficient to drive these reductions while avoiding excessive overpotentials that could lead to side reactions, particularly the HER. Understanding this, the standard reduction potentials (U^0) for NO_3^-RR to NH_3 based on thermodynamic simulation for both acidic and alkaline extreme conditions are[51]:

$$NO_3^- + 9H^+ + 8e^- \rightarrow NH_3 + 3H_2O \qquad\qquad U^0_{pH=0} = 0.799\ V\ vs\ SHE$$

$$NO_3^- + 6H_2O + 8e^- \rightarrow NH_3 + 9OH^- \qquad\qquad U^0_{pH=14} = -0.132\ V\ vs\ SHE$$

Figure 1.13 shows the variation of Faradaic Efficiency and current density at different applied potentials for a series of electrodes. In most cases, the range of applied potentials forms a volcano shape with a peak, indicating the optimal applied potential for that electrode and process among the various parameters.
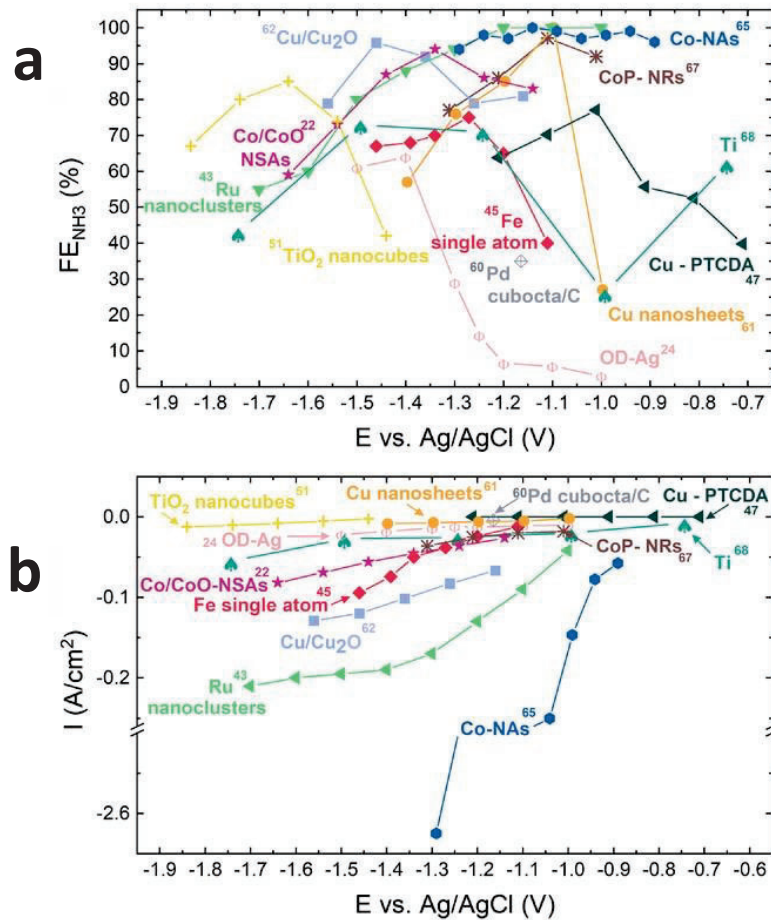
Figure 1.13 Influence of the applied potential in a) Faradaic Efficiency to NH$_3$ and b) NH$_3$ Partial current density. Reprinted from reference [68].

1.4.4. Electrocatalyst surface and State-of-the-art electrocatalysts for NO_3^-RR to NH_3.

Along with the pH, NO_3^- concentration and U_W, the electrocatalytic surface strongly affects both efficiency and selectivity to NH_3 during the reaction. Factors such as adsorption, activation, and intermediate stabilization are directly correlated with the identity of the active sites within the catalyst. Transition metals (TM) or d-band metal group is the more extensively studied group in electrocatalysis. The name of the group is given due that the d-orbital is the outer most filled with electrons orbital. These d-orbitals are normally semi filled, which allow them to both donate and accept electrons easily from other molecules and conduct reactions through more energetically favorable intermediate states. For instance, TM-based catalysts, particularly those involving Cu combined with other metals like Ti, V, Cr, Mn, Fe, and Co, have been extensively reported for NO_3^-RR to NH_3 due to their ability to lower the activation energy for NO_3^- dissociation and subsequent reduction steps. A probe of this is the dissociative – associative mechanism, recently proposed by X. Zheng e.al[62]. According with this study the NO_3^- undergoes initial bond breaking (dissociation) followed by the hydrogenation (association), highlighting the importance of the catalytic surface in breaking the N-O bond before hydrogenation. Cu-base combined with other TM used as models for the study exhibit low limiting potentials, making them efficient for NO_3^-RR. As depicted in **Figure 1.13** most of the recent catalysts used for NO_3^-RR to NH_3 are TM-based (with exception of the last group of non-metallic). However it is interesting to highlight the work presented by X. Deng et al.[69], where using a catalyst based on Co nanoarrays reached and impressive partial current density of approx. 2 $A \cdot cm^{-2}$ towards NH_3, almost 6 times higher than the next (CoP NAs/CFC) included in the figure.

Another important group to highlight is the TM-compound catalysts, including TM-Oxides and their combinations. These materials are characterized by their variable oxidation states and proven catalytic activity for NH_3 electrogeneration. Similar to pure TM, the d-orbitals in TM-composites can participate in the donation and back-donation of electrons, which is essential for weakening the N-O bond and facilitating the water dissociation process (a source of hydrogen). Additionally, surface defects, such as oxygen vacancies (OV) can be created in TM-compounds like oxides (CuO or TiO_2 catalysts). These defects create active sites that significantly enhance NO_3^- reduction by providing specific active sites for NO_3^- adsorption and activation[70], [71]. Density Functional Theory (DFT) calculations have shown that the presence of these defects can reduce the activation energy of intermediate species and improve the overall reaction kinetics[72]. Many of these TM-compounds are depicted in **Figure 1.13**. However, despite the high faradaic efficiency demonstrated by most TM-compounds included, the partial current densities towards NH_3 are lower than 100 $mA \cdot cm^{-2}$ for all components of the group. This is because most of them are oxides with lower conductivity than their respective pure metal components.
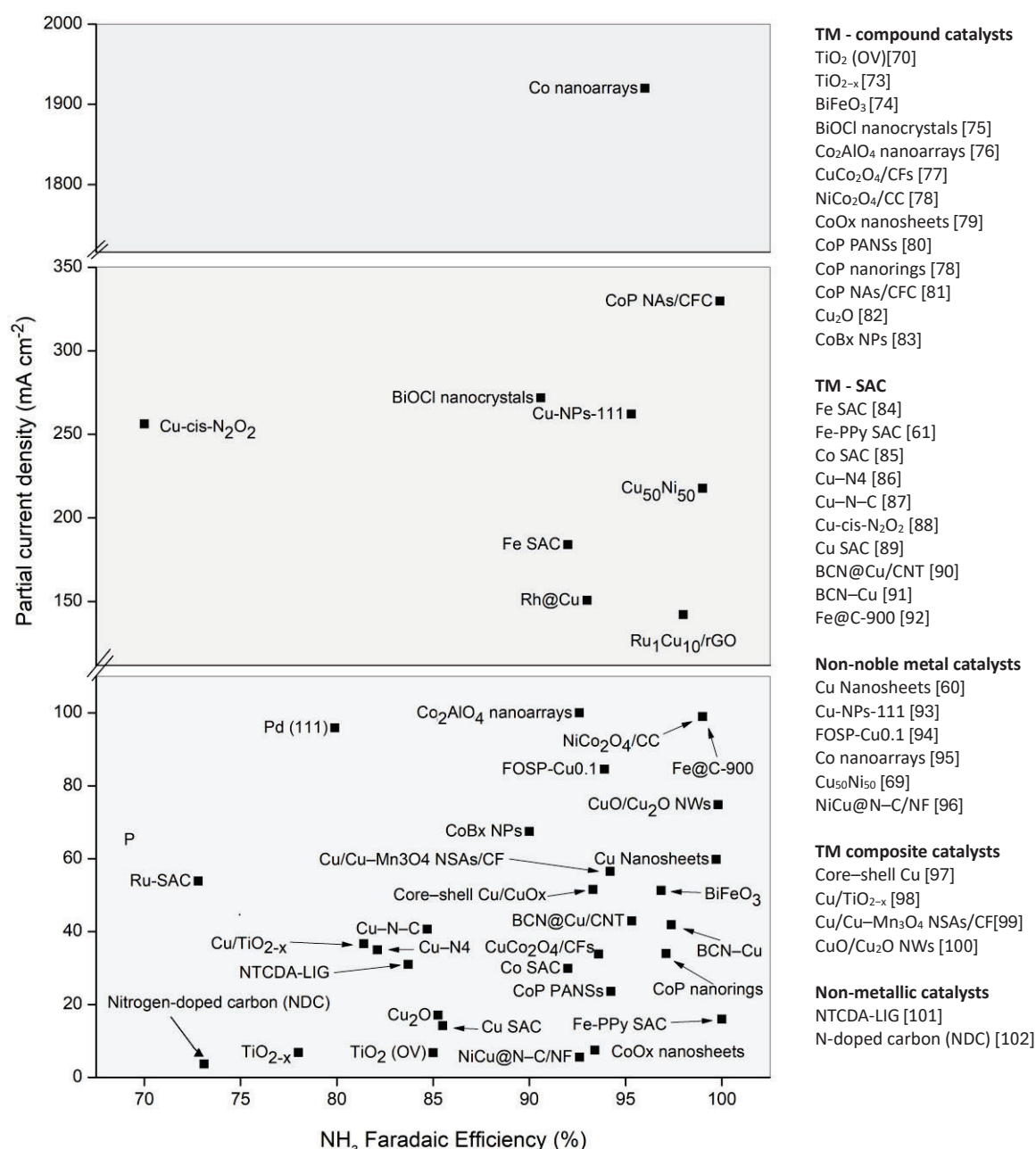
Figure 1.14 NH₃ Partial current density vs NH₃ Faradaic Efficiency of Recent catalyst used for NO₃⁻RR to NH₃.

In the recent years Single-atom catalysts (SACs) have emerged as very functionalized catalysts and the application in NO₃RR to NH₃ is extensive. These type catalysts are composed by isolated metal atoms dispersed on a support material combining the advantages of single and composite catalysts. The surface properties of SACs, including the electronic structure and coordination environment can be finely tuned by the support material, which also influences the catalytic activity[103]. SACs demonstrate exceptional selectivity for NH₃ production due to their well-defined active sites. The precise coordination environment around the single metal minimizes generation of byproducts such as nitrogen oxides (NO_x) and nitrogen gas. During recent years SAC based on Cu and Fe were utilized

for NH_3 electrogeneration, highlighting the work performed by W.-D. Zhang et al.[84], which utilizing a Fe-SAC reached faradaic efficiencies higher than 90% towards NH_3 and an important enhance in partial current density towards NH_3 (>170 mA·cm^{-2}).

Figure 1.13 illustrates some state-of-the-art materials used in recent years for NH_3 electrogeneration from NO_3^-. The figure aims to showcase the recent advancements in terms of partial current density for different groups of materials, including TM, TM-composites, and composites, along with pure metals and non-metallic catalysts. In recent years, the faradaic efficiency towards NH_3 has reached values close to 100% for many materials. However, other parameters, such as **productivity** (linked to the partial current) and **energy efficiency**, still require improvement and **motivated this work** which aims to situate electrogenerated NH_3 from NO_3^- as a viable alternative to alleviate the effects caused by the extensive use of the Haber-Bosch process.

1.5. Thesis scope

Aiming for a carbon-neutral economy and the integration of renewable electricity into the energy system, new technologies are being developed to convert electrical renewable energy into chemical energy. This doctoral thesis focuses on the experimental investigation of the electrochemical reduction of nitrate and nitrite to value-added ammonia. The emphasis is placed on the cathodic reaction, while the anodic reaction (water oxidation) is outside the scope of this thesis. The primary goal is to enhance efficiency towards value-added chemicals as final energy carriers, requiring the development of a system that can operate efficiently and maintain stability over extended periods.

Chapter 1 introduces the project, highlighting the significance of ammonia and the current state of nitrate electroreduction research. **Chapter 2** describes the principles and methods of characterization and analysis used throughout the project. **Chapter 3** explores the combination of materials with different properties to optimize the conversion of nitrate to ammonia. **Chapter 4** examines the energy efficiency of various electrochemical cell configurations. **Chapter 5** investigates the impact of lithium enrichment on hydrogen evolution during nitrate electroreduction. Finally, **Chapter 6** summarizes the findings and provides an outlook for future research and development in this field.

1.6.   General Objectives:

Development of Electrochemical Systems for Ammonia Production from Nitrates:

To develop of advanced electrochemical systems for the generation of nitrogen-based energy carriers from nitrate as a simulated pollutant of water. This involves creating highly active and stable electrocatalysts to enhance the efficiency and selectivity of the ammonia production process.

- **Exploration and Development of Cu and Ti-based Electrocatalytic Materials:**

  To explore and develop electrocatalytic materials based on copper (Cu) and titanium (Ti) that can be integrated into electrochemical systems. This includes investigating the properties and performance of these materials to improve catalytic activity and stability.

- **Mechanistic and Kinetic Processes of nitrate to ammonia electroreduction:**

  To investigate and understand the mechanistic and kinetic processes involved in the electrochemical reduction of nitrate to ammonia. This includes studying the reaction pathways, intermediate species, and factors affecting the reaction rates and selectivity.

- **Integration of Electrocatalysts into Electrocatalytic Systems:**

  To integrate these electrocatalysts into electrocatalytic h-cell and flow-cell systems by optimizing the operative conditions. The goal is to maximize the production of ammonia-energy carriers under various reaction environments.

- **Optimization of Electrochemical Systems for Energy Efficiency and Scalability:**

  To optimize the integrated electrocatalytic systems in terms of energy efficiency and scalability. This includes evaluating and improving the systems to viable parameters for scaling-up ammonia production with minimal energy consumption and environmental impact.

- **Iteration and Enhancement of Electrocatalytic Systems:**

  To continuously iterate and enhance the optimized electrocatalytic systems, focusing on improving material properties and catalytic performance. This involves ongoing development to ensure sustained efficiency, stability, and selectivity in the production of ammonia and other nitrogen-based compounds with reducing competitive reactions such as HER.

1.7. Bibliography.

[1] R. Gahlot and M. Garg, *The Effect of Energy Consumption on Economic Growth: a Scientometric Analysis*, J. Knowl. Econ., no. 0123456789, May 2024, doi: 10.1007/s13132-024-02048-y.

[2] World Population Prospects 2022, no. 9. 2022.

[3] International Energy Agency, *Electricity 2024 Analysis and forecast to 2026*, pp. 1–170, 2023, https://www.iea.org/news/global-coal-demand-expected-to-decline-in-coming-years.

[4] International Energy Agency, *CO_2 Emissions in 2023*. Int. Energy Agency, vol. 24, p. 22, 2023.

[5] S. A. Montzka, E. J. Dlugokencky, and J. H. Butler, *Non-CO_2 greenhouse gases and climate change*, Nature, vol. 476, no. 7358, pp. 43–50, Aug. 2011, doi: 10.1038

[6] N. P. Gillett, *Warming proportional to cumulative carbon emissions not explained by heat and carbon sharing mixing processes,*" Nat. Commun., vol. 14, no. 1, p. 6466, Oct. 2023, doi: 10.1038/s41467-023-42111-x.

[7] B. Ekwurzel, J. Boneham, M. Dalton, R. Heede, R.J. Mera, M.R. Allen, P.C. Frumhoff, *The rise in global atmospheric CO2, surface temperature, and sea level from emissions traced to major carbon producers*, Clim. Change, vol. 144, no. 4, pp. 579–590, Oct. 2017, doi: 10.1007/s10584-017-1978-0.

[8] L. A. Gil-Alana and M. Monge, "*Global CO_2 emissions and global temperatures: Are they related,*" Int. J. Climatol., vol. 40, no. 15, pp. 6603–6611, Dec. 2020, doi: 10.1002/joc.6601.

[9] M. Meinshausen, N. Meinshausen, W. Hare, S. Raper, K. Frieler, R. Knutti, D. Frame, M. Allen, Greenhouse-gas emission targets for limiting global warming to 2 degrees C, Nature, vol. 458, no. 7242, pp. 1158–62, Apr. 2009, doi: 10.1038/nature08017.

[10] S. K. Allen et al., *Climate Change 2014 Synthesis Report Summary for Policymakers*, vol. 9781107025, Cambridge University Press, 2014, pp. 3–22.

[11] E. Schmid, B. Knopf, and A. Pechan, *Putting an energy system transformation into practice: The case of the German Energiewende*, Energy Res. Soc. Sci., vol. 11, pp. 263–275, 2016, doi: 10.1016/j.erss.2015.11.002.

[12] F. Ausfelder and K. Wagemann, *Power-to-Fuels: E-Fuels as an Important Option for a Climate-Friendly Mobility of the Future*, Chemie-Ingenieur-Technik, vol. 92, no. 1–2, pp. 21–30, 2020, doi: 10.1002/cite.201900180.

[13] N. S. Lewis and D. G. Nocera, *Powering the planet: chemical challenges in solar energy utilization*, Proc. Natl. Acad. Sci. U. S. A., vol. 103, no. 43, pp. 15729–35, Oct. 2006, doi: 10.1073/pnas.0603395103.

[14] F. Ausfelder, C. Beilmann, M. Bertau et al., *Energy Storage as Part of a Secure Energy Supply*, ChemBioEng Rev., vol. 4, no. 3, pp. 144–210, Jun. 2017, doi: 10.1002/cben.201700004.

[15] C. Action, REPORT FROM THE COMMISSION TO THE EUROPEAN PARLIAMENT AND THE COUNCIL EU Climate Action Progress Report 2023.

[16] S. R. Foit, I. C. Vinke, L. G. J. de Haart, and R. Eichel, *Power-to-Syngas: An Enabling Technology for the Transition of the Energy System?*, Angew. Chem. Int. Ed. Engl., vol. 56, no. 20, pp. 5402–5411, May 2017, doi: 10.1002/anie.201607552.

[17] D. Hidalgo, J. M. Martín-Marroquín, and F. Corona, *A multi-waste management concept as a basis towards a circular economy model*, Renew. Sustain. Energy Rev., vol. 111, no. December 2018, pp. 481–489, Sep. 2019, doi: 10.1016/j.rser.2019.05.048.

[18]   A. R. Dahiru, A. Vuokila, and M. Huuhtanen, *Recent development in Power-to-X: Part I - A review on techno-economic analysis*, J. Energy Storage, vol. 56, no. PA, p. 105861, Dec. 2022, doi: 10.1016/j.est.2022.105861.

[19]   R. Xia, S. Overa, and F. Jiao, *Emerging Electrochemical Processes to Decarbonize the Chemical Industry*, JACS Au, vol. 2, no. 5, pp. 1054–1070, May 2022, doi: 10.1021/jacsau.2c00138.

[20]   C. Tarhan and M. A. Çil, *A study on hydrogen, the clean energy of the future: Hydrogen storage methods*, J. Energy Storage, vol. 40, no. May, p. 102676, 2021, doi: 10.1016/j.est.2021.102676.

[21]   E. L. Carlson, K. Pickford, and H. Nyga-Łukaszewska, *Green hydrogen and an evolving concept of energy security: Challenges and comparisons*, Renew. Energy, vol. 219, no. P1, p. 119410, Dec. 2023, doi: 10.1016/j.renene.2023.119410.

[22]   European Union Agency for the Cooperation of Energy Regulations, *Transporting Pure Hydrogen by Repurposing Existing Gas Infrastructure: Overview of existing studies and reflections on the conditions for repurposing*, Report, no. July, pp. 1–23, 2021.

[23]   U. S. Meda, N. Bhat, A. Pandey, K. N. Subramanya, and M. A. Lourdu Antony Raj, *Challenges associated with hydrogen storage systems due to the hydrogen embrittlement of high strength steels*, Int. J. Hydrogen Energy, vol. 48, no. 47, pp. 17894–17913, Jun. 2023, doi: 10.1016/j.ijhydene.2023.01.292.

[24]   N. Ma, W. Zhao, W. Wang, X. Li, and H. Zhou, *Large scale of green hydrogen storage: Opportunities and challenges*, Int. J. Hydrogen Energy, vol. 50, pp. 379–396, Jan. 2024, doi: 10.1016/j.ijhydene.2023.09.021.

[25]   S. Chatterjee, R. K. Parsapur, and K.-W. Huang, *Limitations of Ammonia as a Hydrogen Energy Carrier for the Transportation Sector*, ACS Energy Lett., vol. 6, no. 12, pp. 4390–4394, Dec. 2021, doi: 10.1021/acsenergylett.1c02189.

[26]   M. Aziz, A. T. Wijayanta, and A. B. D. Nandiyanto, *Ammonia as Effective Hydrogen Storage: A Review on Production, Storage and Utilization*, Energies, vol. 13, no. 12, p. 3062, Jun. 2020, doi: 10.3390/en13123062.

[27]   B. C. Tashie-Lewis and S. G. Nnabuife, *Hydrogen Production, Distribution, Storage and Power Conversion in a Hydrogen Economy - A Technology Review*, Chem. Eng. J. Adv., vol. 8, no. August, p. 100172, Nov. 2021, doi: 10.1016/j.ceja.2021.100172.

[28]   K. Ogura, *Electrochemical reduction of carbon dioxide to ethylene: Mechanistic approach*, J. CO_2 Util., vol. 1, pp. 43–49, Jun. 2013, doi: 10.1016/j.jcou.2013.03.003.

[29]   D. Erdemir and I. Dincer, *A perspective on the use of ammonia as a clean fuel: Challenges and solutions*, Int. J. Energy Res., vol. 45, no. 4, pp. 4827–4834, 2021, doi: 10.1002/er.6232.

[30]   Organisation for Economic Co-operation and Development, *Ammonia Technology Roadmap*. 2021.

[31]   P. Mayer, A. Ramirez, G. Pezzella, B. Winter, S. Sarathy, J. Gascon, and A. Bardow, *Blue and green ammonia production: A techno-economic and life cycle assessment perspective*, iScience, vol. 26, no. 8, 2023, doi: 10.1016/j.isci.2023.107389.

[32]   K. H. R. Rouwenhorst, F. Jardali, A. Bogaerts, and L. Lefferts, *From the Birkeland–Eyde process towards energy-efficient plasma-based NO_X synthesis*: *a techno-economic analysis*, Energy Environ. Sci., vol. 14, no. 5, pp. 2520–2534, 2021, doi: 10.1039/D0EE03763J.

[33]   X. Wang, J. Yang, M. Salla, S. Xi, Y. Yang, M. Li, F. Zhang, M. Zhu, S. Huang, S. Huang, Y. Zhang, and Q. Wan, *Redox-Mediated Ambient Electrolytic Nitrogen Reduction for Hydrazine and Ammonia Generation*, Angew. Chemie, vol. 133, no. 34, pp. 18869–18875, Aug. 2021, doi: 10.1002/ange.202105536.

[34]   S. Zhang, Y. Zhao, R. Shi, G. I. N. Waterhouse, and T. Zhang, *Photocatalytic ammonia synthesis: Recent progress and future*, EnergyChem, vol. 1, no. 2, p. 100013, Sep. 2019, doi: 10.1016/j.enchem.2019.100013.

[35]   J. W. Erisman, M. A. Sutton, J. Galloway, Z. Klimont, and W. Winiwarter, *How a century of ammonia synthesis changed the world*, Nat. Geosci., vol. 1, no. 10, pp. 636–639, Oct. 2008, doi: 10.1038/ngeo325.

[36]   C. Smith, A. K. Hill, and L. Torrente-Murciano, *Current and future role of Haber-Bosch ammonia in a carbon-free energy landscape*, Energy Environ. Sci., vol. 13, no. 2, pp. 331–344, 2020, doi: 10.1039/c9ee02873k.

[37]   M. Wang, A. Khan, I. Mohsin, J. Wicks, A. Ip, K. Sumon, C. Dinh, E. Sargent, I. Gates, and Md. Kibria, *Can sustainable ammonia synthesis pathways compete with fossil-fuel based Haber–Bosch processes?*, Energy Environ. Sci., vol. 14, no. 5, pp. 2535–2548, 2021, doi: 10.1039/D0EE03808C.

[38]   A. Valera-Medina, H. Xiao, M. Owen-Jones, W. I. F. David, and P. J. Bowen, *Ammonia for power*, Prog. Energy Combust. Sci., vol. 69, pp. 63–102, 2018, doi: 10.1016/j.pecs.2018.07.001.

[39]   G. Soloveichik, *ARPA-E REFUEL Program: Distributed Production of Ammonia and its Conversion to Energy REFUEL: sustainable fuels as energy vector*, 2019.

[40]   S. Ghavam, M. Vahdati, I. A. G. Wilson, and P. Styring, *Sustainable Ammonia Production Processes*, Front. Energy Res., vol. 9, no. March, pp. 1–19, Mar. 2021, doi: 10.3389/fenrg.2021.580808.

[41]   N. Cherkasov, A. O. Ibhadon, and P. Fitzpatrick, *A review of the existing and alternative methods for greener nitrogen fixation*, Chem. Eng. Process. Process Intensif., vol. 90, pp. 24–33, Apr. 2015, doi: 10.1016/j.cep.2015.02.004.

[42]   C. D. Zeinalipour-Yazdi, J. S. J. Hargreaves, and C. R. A. Catlow, *Nitrogen Activation in a Mars-van Krevelen Mechanism for Ammonia Synthesis on Co_3Mo_3N*, J. Phys. Chem. C, vol. 119, no. 51, pp. 28368–28376, 2015, doi: 10.1021/acs.jpcc.5b06811.

[43]   S. C. Jesudass, S. Surendran, J.Y. Kim, T. An, G. Janani, T. Kim, J.K. Kim, and U. Sim, *Pathways of the Electrochemical Nitrogen Reduction Reaction: From Ammonia Synthesis to Metal-N_2 Batteries*," Electrochem. Energy Rev., vol. 6, no. 1, p. 27, Dec. 2023, doi: 10.1007/s41918-023-00186-6.

[44]   W. Li, K. Li, Y. Ye, Y. Zhang, Y. Liu, G. Wang, C. Liang, H. Zhang, and H. Zhao, *Efficient electrocatalytic nitrogen reduction to ammonia with aqueous silver nanodots*, Commun. Chem., vol. 4, no. 1, p. 10, Jan. 2021, doi: 10.1038/s42004-021-00449-7.

[45]   Y. J. Jang and K.-S. Choi, *Enabling electrochemical N_2 reduction to NH_3 in the low overpotential region using non-noble metal Bi electrodes via surface composition modification*, J. Mater. Chem. A, vol. 8, no. 27, pp. 13842–13851, 2020, doi: 10.1039/D0TA02550J.

[46]   R. Zhao, H. Xie, L. Chang, X. Zhang, X. Zhu, X. Tong, X. Wang, Y. Luo, P. Wei, Z. Wang, and X. Sun, *Recent progress in the electrochemical ammonia synthesis under ambient conditions*, EnergyChem, vol. 1, no. 2, p. 100011, Sep. 2019, doi: 10.1016/j.enchem.2019.100011.

[47]   A. H. Mahvi, J. Nouri, A. A. Babaei, and R. Nabizadeh, *Agricultural activities impact on groundwater nitrate pollution*, Int. J. Environ. Sci. Technol., vol. 2, no. 1, pp. 41–47, Mar. 2005, doi: 10.1007/BF03325856.

[48]   E. Abascal, L. Gómez-Coma, I. Ortiz, and A. Ortiz, *Global diagnosis of nitrate pollution in groundwater and review of removal technologies*, Sci. Total Environ., vol. 810, p. 152233, Mar. 2022, doi: 10.1016/j.scitotenv.2021.152233.

[49]   X. Zheng, Y. Yan, X. Li, Y. Liu, and Y. Yao, *Theoretical insights into dissociative-associative mechanism for enhanced electrochemical nitrate reduction to ammonia*, J. Hazard. Mater., vol. 446, no. 3, p. 130679, Mar. 2023, doi: 10.1016/j.jhazmat.2022.130679.

[50]   D. De, E. E. Kalu, P. P. Tarjan, and J. D. Englehardt, *Kinetic Studies of the Electrochemical Treatment of Nitrate and Nitrite Ions on Iridium-Modified Carbon Fiber Electrodes*, Chem. Eng. Technol., vol. 27, no. 1, pp. 56–64, Jan. 2004, doi: 10.1002/ceat.200401832.

[51]   R. M. Choueiri, S. W. Tatarchuk, A. Klinkova, and L. D. Chen, *Mechanism of ammonia oxidation to dinitrogen, nitrite, and nitrate on β-Ni(OH)$_2$ from first-principles simulations*, Electrochem. Sci. Adv., vol. 2, no. 6, pp. 1–10, 2022, doi: 10.1002/elsa.202100142.

[52]   J.M. McEnaney, S. Blair, A.C. Nielander, J.A Schwalbe, D.M. Koshy, M. Cargnello, T.F. Jaramillo, *Electrolyte engineering for efficient electrochemical nitrate reduction to ammonia on a titanium electrode*. ACS Sustain. Chem. Eng. 8, 2672–2681 (2020). https://doi.org/10.1021/acssuschemeng.9b05983

[53]   R. Zhang, C. Li, H. Cui, Y. Wang, S. Zhang, P. Li, Y. Hou, Y. Guo, G. Liang, Z. Huang, C. Peng, and C. Zhi, *Electrochemical nitrate reduction in acid enables high-efficiency ammonia synthesis and high-voltage pollutes-based fuel cells*, Nat. Commun., vol. 14, no. 1, p. 8036, Dec. 2023, doi: 10.1038/s41467-023-43897-6.

[54]   B. Li, P. Xue, M. Qiao, Y. Tang, and D. Zhu, *Cu doping in FeP enabling efficient electrochemical nitrate reduction to ammonia in neutral media*, Chem. Commun., vol. 59, no. 91, pp. 13611–13614, 2023, doi: 10.1039/D3CC04775J.

[55]   X.H. Wang, Z.M. Wang, Q.L. Hong, Z.N. Zhang, F. Shi, D.S. Li, S.N. Li, and Y. Chen, *Oxygen-Vacancy-Rich Cu$_2$O Hollow Nanocubes for Nitrate Electroreduction Reaction to Ammonia in a Neutral Electrolyte*, Inorg. Chem., vol. 61, no. 39, pp. 15678–15685, Oct. 2022, doi: 10.1021/acs.inorgchem.2c02716.

[56]   M. E. Chavez, M. Biset-Peiró, S. Murcia-López, and J. R. Morante, *Cu$_2$O–Cu@Titanium Surface with Synergistic Performance for Nitrate-to-Ammonia Electrochemical Reduction*, ACS Sustain. Chem. Eng., vol. 11, no. 9, pp. 3633–3643, Mar. 2023, doi: 10.1021/acssuschemeng.2c05885.

[57]   L. Fang, S. Wang, C. Song, S. Lu, X. Yang, X. Qi, and H. Liu, *Boosting nitrate electroreduction to ammonia via in situ generated stacking faults in oxide-derived copper*, Chem. Eng. J., vol. 446, no. P4, p. 137341, 2022, doi: 10.1016/j.cej.2022.137341.

[58]   A. J. B. Larry and L. R. Faulkner, *ELECTROCHEMICAL METHODS*, in BIOS Instant Notes in Analytical Chemistry, Taylor & Francis, 2002, pp. 71–75.

[59]   G. Cioncoloni, I. Roger, P. Wheatley, C. Wilson, R. Morris, S. Sproules, and M.D. Symes, *Proton-Coupled Electron Transfer Enhances the Electrocatalytic Reduction of Nitrite to NO in a Bioinspired Copper Complex*, ACS Catal., vol. 8, no. 6, pp. 5070–5084, Jun. 2018, doi: 10.1021/acscatal.8b00361.

[60]   T. Wu, X. Kong, S. Tong, Y. Chen, J. Liu, Y. Tang, X. Yang, Y. Chen, and P. Wan, *Self-supported Cu nanosheets derived from CuCl-CuO for highly efficient electrochemical degradation of NO$_3^-$,*" Appl. Surf. Sci., vol. 489, no. May, pp. 321–329, Sep. 2019, doi: 10.1016/j.apsusc.2019.05.358.

[61]   P. Li, Z. Jin, Z. Fang, and G. Yu, *A single-site iron catalyst with preoccupied active centers that achieves selective ammonia electrosynthesis from nitrate*, Energy Environ. Sci., vol. 14, no. 6, pp. 3522–3531, 2021, doi: 10.1039/d1ee00545f.

[62]   X. Zheng, Y. Yan, X. Li, Y. Liu, and Y. Yao, *Theoretical insights into dissociative-associative mechanism for enhanced electrochemical nitrate reduction to ammonia*, J. Hazard. Mater., vol. 446, no. 3, p. 130679, Mar. 2023, doi: 10.1016/j.jhazmat.2022.130679.

[63]   Y. Wu, K.K. Lu, and L.H. Xu, *Progress and prospects of electrochemical reduction of nitrate to restore the nitrogen cycle*, J. Mater. Chem. A, vol. 11, no. 33, pp. 17392–17417, 2023, doi: 10.1039/D3TA01592K.

[64]   X. He, H. Liu, W. Zhao, J. Mu, and B. Liu, *Recent progress on cathode material regulation for electrochemical nitrate reduction to ammonia*, Sep. Purif. Technol., vol. 329, no. September 2023, p. 125129, 2024, doi: 10.1016/j.seppur.2023.125129.

[65]   D. Liu, L. Qiao, S. Peng, H. Bai, C. Liu, W. Ip, K.H. Lo, H. Liu, K.W. Ng, S. Wang, X. Yang, and H. Pan, *Recent Advances in Electrocatalysts for Efficient Nitrate Reduction to Ammonia*, Adv. Funct. Mater., vol. 33, no. 43, pp. 1–31, Oct. 2023, doi: 10.1002/adfm.202303480.

[66]   J. Zhou, S. Gao, and G. Hu, *Recent Progress and Perspectives on Transition Metal-Based Electrocatalysts for Efficient Nitrate Reduction*, Energy & Fuels, vol. 38, no. 8, pp. 6701–6722, Apr. 2024, doi: 10.1021/acs.energyfuels.4c00415.

[67]   S. Garcia-Segura, M. Lanzarini-Lopes, K. Hristovski, and P. Westerhoff, *Electrocatalytic reduction of nitrate: Fundamentals to full-scale water treatment applications*, Appl. Catal. B Environ., vol. 236, no. May, pp. 546–568, 2018, doi: 10.1016/j.apcatb.2018.05.041.

[68]   D. Anastasiadou, Y. van Beek, E. J. M. Hensen, and M. Costa Figueiredo, *Ammonia electrocatalytic synthesis from nitrate*, Electrochem. Sci. Adv., vol. 3, no. 5, pp. 1–11, Oct. 2023, doi: 10.1002/elsa.202100220.

[69]   Y. Wang, A. Xu, Z. Wang, J. Li, F. Li, J. Wicks, M. Luo, D.H. Nam, C.S. Tan, Y. Ding, J. Wu, Y. Lum, C.T. Dinh, D. Sinton, G. Zheng, and E.H. Sargent, *Enhanced Nitrate-to-Ammonia Activity on Copper-Nickel Alloys via Tuning of Intermediate Adsorption*, J. Am. Chem. Soc., vol. 142, no. 12, pp. 5702–5708, 2020, doi: 10.1021/jacs.9b13347.

[70]   R. Jia, Y. Wang, C. Wang, Y. Ling, Y. Yu, and B. Zhang, *Boosting Selective Nitrate Electroreduction to Ammonium by Constructing Oxygen Vacancies in TiO_2*, ACS Catal., vol. 10, no. 6, pp. 3533–3540, 2020, doi: 10.1021/acscatal.9b05260.

[71]   D. Zhao, J. Liang, J. Li, L. Zhang, K. Dong, L. Yue, Y. Luo, Y. Ren, Q. Liu, M.S. Hamdy, Q. Li, Q. Kong, and X. Sun, *A $TiO_{2−x}$ nanobelt array with oxygen vacancies: an efficient electrocatalyst toward nitrite conversion to ammonia*, Chem. Commun., vol. 58, no. 22, pp. 3669–3672, 2022, doi: 10.1039/d2cc00856d.

[72]   Y. Wang, H. Li, W. Zhou, X. Zhang, B. Zhang, and Y. Yu, *Structurally Disordered RuO_2 Nanosheets with Rich Oxygen Vacancies for Enhanced Nitrate Electroreduction to Ammonia*, Angew. Chemie, vol. 134, no. 19, May 2022, doi: 10.1002/ange.202202604.

[73]   Z. Wei, X. Niu, H. Yin, S. Yu, and J. Li, *Synergistic effect of oxygen defects and hetero-phase junctions of TiO_2 for selective nitrate electroreduction to ammonia*, Appl. Catal. A Gen., vol. 636, no. December 2021, p. 118596, Apr. 2022, doi: 10.1016/j.apcata.2022.118596.

[74]   J. Wang, D. Wu, M. Li, X. Wei, X. Yang, M. Shao, and M. Gu, *Bismuth Ferrite as an Electrocatalyst for the Electrochemical Nitrate Reduction*, Nano Lett., vol. 22, no. 13, pp. 5600–5606, Jul. 2022, doi: 10.1021/acs.nanolett.2c02026.

[75]   N. Zhang, J. Shang, X. Deng, L. Cai, R. Long, Y. Xiong, Y. Chai, *Governing Interlayer Strain in Bismuth Nanocrystals for Efficient Ammonia Electrosynthesis from Nitrate Reduction*, ACS Nano, vol. 16, no. 3, pp. 4795–4804, Mar. 2022, doi: 10.1021/acsnano.2c00101.

[76]   Q. Liu, L. Xie, J. Liang, Y. Ren, W. Wang, L. Zhang, L. Yue, T. Li, Y. Luo, N. Li, B. Tang, Y. Liu, S. Gao, A. Alshehri, I. Shakir, P.O. Agboola, Q. Kong, Q. Wang, D. Ma, and X. Sun, *Ambient Ammonia Synthesis via Electrochemical Reduction of Nitrate Enabled by $NiCo_2O_4$ Nanowire Array*," Small, vol. 18, no. 13, pp. 1–8, Apr. 2022, doi: 10.1002/smll.202106961.

[77]   Z. Niu, S. Fan, X. Li, P. Wang, Z. Liu, J. Wang, C. Bai, and D. Zhang, *Bifunctional copper-cobalt spinel electrocatalysts for efficient tandem-like nitrate reduction to ammonia*, Chem. Eng. J., vol. 450, no. P4, p. 138343, 2022, doi: 10.1016/j.cej.2022.138343.

[78]   Q.L. Hong, J. Zhou, J. Zhai, Q.G. Zhai, Y.C. Jiang, M.C. Hu, X. Xiao, S.N. Li, and Y. Chen, *Cobalt phosphide nanorings towards efficient electrocatalytic nitrate reduction to ammonia*, Chem. Commun., vol. 57, no. 88, pp. 11621–11624, 2021, doi: 10.1039/D1CC04952F.

[79]   J. Wang, C. Cai, Y. Wang, X. Yang, X. Wu, Y. Zhu, M. Li, M. Gu, and M. Shao, *Electrocatalytic Reduction of Nitrate to Ammonia on Low-Cost Ultrathin CoO$_x$ Nanosheets*, ACS Catal., vol. 11, no. 24, pp. 15135–15140, 2021, doi: 10.1021/acscatal.1c03918.

[80]   Y. Jia, Y.G. Ji, O. Xue, F.M. Li, G.T. Zhao, P.J. Jin, S.N. Li, and Y. Chen, *Efficient Nitrate-to-Ammonia Electroreduction at Cobalt Phosphide Nanoshuttles*, ACS Appl. Mater. Interfaces, vol. 13, no. 38, pp. 45521–45527, Sep. 2021, doi: 10.1021/acsami.1c12512.

[81]   S. Ye, Z. Chen, G. Zhang, W. Chen, C. Peng, X. Yang, L. Zheng, Y. Li, X. Ren, H. Cao, D. Xue, J. Qiu, Q. Zhang, and J. Liu, *Elucidating the activity, mechanism and application of selective electrosynthesis of ammonia from nitrate on cobalt phosphide*, Energy Environ. Sci., vol. 15, no. 2, pp. 760–770, 2022, doi: 10.1039/D1EE03097C.

[82]   Z. Gong, W. Zhong, Z. He, Q. Liu, H. Chen, D. Zhou, N. Zhang, X. Kang, and Y. Chen, *Regulating surface oxygen species on copper (I) oxides via plasma treatment for effective reduction of nitrate to ammonia"* Appl. Catal. B Environ., vol. 305, no. December 2021, p. 121021, 2022, doi: 10.1016/j.apcatb.2021.121021.

[83]   Y. Shi, S. Xu, and F. Li, *Electrocatalytic nitrate reduction to ammonia via amorphous cobalt boride*, Chem. Commun., vol. 58, no. 62, pp. 8714–8717, 2022, doi: 10.1039/D2CC02261C.

[84]   W.D. Zhang, H. Dong, L. Zhou, H. Xu, H.R. Wang, X. Yan, Y. Jiang, J. Zhang, and Z.G. Gu, *Fe single-atom catalysts with pre-organized coordination structure for efficient electrochemical nitrate reduction to ammonia*, Appl. Catal. B Environ., vol. 317, no. May, p. 121750, Nov. 2022, doi: 10.1016/j.apcatb.2022.121750.

[85]   J. Li, M. Li, N. An, S. Zhang, Q. Song, Y. Yang, J. Li, and X. Liu, *Boosted ammonium production by single cobalt atom catalysts with high Faradic efficiencies*, Proc. Natl. Acad. Sci. U. S. A., vol. 119, no. 29, p. e2123450119, Jul. 2022, doi: 10.1073/pnas.2123450119.

[86]   J. Cheng, W. Sun, G. Dai, X. Yang, R. Xia, Y. Xu, X. Yang, and W. Tu, *Electroreduction of nitrate to ammonia on atomically-dispersed Cu-N$_4$ active sites with high efficiency and stability*, Fuel, vol. 332, no. P2, p. 126106, Jan. 2023, doi: 10.1016/j.fuel.2022.126106.

[87]   J. Yang, H. Qi, A. Li, X. Liu, X. Yang, S. Zhang, Q. Zhao, Q. Jiang, Y. Su, L. Zhang, J.F. Li, Z.Q. Tian, W. Liu, A. Wang, and T. Zhang, *Potential-Driven Restructuring of Cu Single Atoms to Nanoparticles for Boosting the Electrochemical Reduction of Nitrate to Ammonia*, J. Am. Chem. Soc., vol. 144, no. 27, pp. 12062–12071, Jul. 2022, doi: 10.1021/jacs.2c02262.

[88]   X. Cheng, J.H. He, H.Q. Ji, H.Y. Zhang, Q. Cao, W.J. Sun, C.L. Yan, and J.M. Lu, Coordination Symmetry Breaking of Single-Atom Catalysts for Robust and Efficient Nitrate Electroreduction to Ammonia, Adv. Mater., vol. 34, no. 36, pp. 1–10, Sep. 2022, doi: 10.1002/adma.202205767.

[89]   Y.-T. Xu, M.-Y. Xie, H. Zhong, and Y. Cao, *In Situ Clustering of Single-Atom Copper Precatalysts in a Metal-Organic Framework for Efficient Electrocatalytic Nitrate-to-Ammonia Reduction*, ACS Catal., vol. 12, no. 14, pp. 8698–8706, Jul. 2022, doi: 10.1021/acscatal.2c02033.

[90]   X. Zhao, X. Li, H. Zhang, X. Chen, J. Xu, J. Yang, H. Zhang, and G. Hu, *Atomic-dispersed copper simultaneously achieve high-efficiency removal and high-value-added conversion to ammonia of nitrate in sewage*, J. Hazard. Mater., vol. 424, no. PA, p. 127319, Feb. 2022, doi: 10.1016/j.jhazmat.2021.127319.

[91]   X. Zhao, X. Jia, Y. He, H. Zhang, X. Zhou, H. Zhang, S. Zhang, Y. Dong, X. Hu, A. Kuklin, G.V. Baryshnikov, H. Ågren, and G. Hu, *Two-dimensional BCN matrix inlaid with single-atom-Cu driven electrochemical nitrate*

reduction reaction to achieve sustainable industrial-grade production of ammonia, Appl. Mater. Today, vol. 25, p. 101206, Dec. 2021, doi: 10.1016/j.apmt.2021.101206.

[92]   Y. Liu, R. Cheng, H. Ren, T. Sun, and D. Liu, *Ultrasmall Iron Nanoparticle-Decorated Carbon Black for High-Efficiency Nitrate-to-Ammonia Electrosynthesis and Zinc-Nitrate Batteries*, ACS Sustain. Chem. Eng., vol. 12, no. 9, pp. 3780–3789, Mar. 2024, doi: 10.1021/acssuschemeng.3c07969.

[93]   Q. Hu, Y. Qin, X. Wang, Z. Wang, X. Huang, K. Gao, H. Yang, P. Zhang, M. Shao, and C. He, *Reaction intermediate-mediated electrocatalyst synthesis favors specified facet and defect exposure for efficient nitrate–ammonia conversion*, Energy Environ. Sci., vol. 14, no. 9, pp. 4989–4997, 2021, doi: 10.1039/D1EE01731D.

[94]   Y. Zhao, Y. Liu, Z. Zhang, Z. Mo, C. Wang, and S. Gao, *Flower-like open-structured polycrystalline copper with synergistic multi-crystal plane for efficient electrocatalytic reduction of nitrate to ammonia*, Nano Energy, vol. 97, no. February, p. 107124, Jun. 2022, doi: 10.1016/j.nanoen.2022.107124.

[95]   X. Deng, Y. Yang, L. Wang, X. Fu, and J. Luo, *Metallic Co Nanoarray Catalyzes Selective NH$_3$ Production from Electrochemical Nitrate Reduction at Current Densities Exceeding 2 A cm^{-2}*, Adv. Sci., vol. 8, no. 7, pp. 1–9, Apr. 2021, doi: 10.1002/advs.202004523.

[96]   L. He, F. Yao, Y. Zhong, C. Tan, K. Hou, Z. Pi, S. Chen, X. Li, S. Chen, S. Li, and Q. Yang, *Achieving high-performance electrocatalytic reduction of nitrate by N-rich carbon-encapsulated Ni-Cu bimetallic nanoparticles supported nickel foam electrode*, J. Hazard. Mater., vol. 436, no. February, p. 129253, Aug. 2022, doi: 10.1016/j.jhazmat.2022.129253.

[97]   W. He, J. Zhang, S. Dieckhöfer, S. Varhade, A.C. Brix, A. Lielpetere, A. Seisel, J. Junqueira, and W. Schuhmann, Splicing the active phases of copper/cobalt-based catalysts achieves high-rate tandem electroreduction of nitrate to ammonia.," Nat. Commun., vol. 13, no. 1, p. 1129, Mar. 2022, doi: 10.1038/s41467-022-28728-4.

[98]   X. Zhang, C. Wang, Y. Guo, B. Zhang, Y. Wang, and Y. Yu, *Cu clusters/TiO$_{2-x}$ with abundant oxygen vacancies for enhanced electrocatalytic nitrate reduction to ammonia*, J. Mater. Chem. A, vol. 10, no. 12, pp. 6448–6453, 2022, doi: 10.1039/D2TA00661H.

[99]   H. Wang, Q. Mao, T. Ren, T. Zhou, K. Deng, Z. Wang, X. Li, Y. Xu, and L. Wang, *Synergism of Interfaces and Defects: Cu/Oxygen Vacancy-Rich Cu-Mn$_3$O$_4$ Heterostructured Ultrathin Nanosheet Arrays for Selective Nitrate Electroreduction to Ammonia*, ACS Appl. Mater. Interfaces, vol. 13, no. 37, pp. 44733–44741, Sep. 2021, doi: 10.1021/acsami.1c11249.

[100]   T. Feng, J. Wang, J. Wang, Y. Wang, C. Yu, X. Zhou, B. Xu, K. László, F. Li, and W. Zhang, *Selective electrocatalytic reduction of nitrate to dinitrogen by Cu2O nanowires with mixed oxidation-state*, Chem. Eng. J., vol. 433, no. September 2021, p. 133495, Apr. 2022, doi: 10.1016/j.cej.2021.133495.

[101]   L. Cheng, T. Ma, B. Zhang, L. Huang, W. Guo, F. Hu, H. Zhu, Z. Wang, T. Zheng, D. Yang, C. Siu, Q. Liu, Y. Ren, C. Xia, B.Z. Tang, and R. Ye. *Steering the Topological Defects in Amorphous Laser-Induced Graphene for Direct Nitrate-to-Ammonia Electroreduction*, ACS Catal., vol. 12, no. 19, pp. 11639–11650, Oct. 2022, doi: 10.1021/acscatal.2c03219.

[102]   Z. Chen, J. Chen, G. Barcaro, T. Budnyak, A. Rokicińska, R. Dronskowski, S. Budnyk, P. Kuśtrowski, S. Monti, and A. Slabon, *Reaction pathways on N-substituted carbon catalysts during the electrochemical reduction of nitrate to ammonia*, Catal. Sci. Technol., vol. 12, no. 11, pp. 3582–3593, 2022, doi: 10.1039/D2CY00050D.

[103]   S. K. Kaiser, Z. Chen, D. Faust Akl, S. Mitchell, and J. Pérez-Ramírez, *Single-Atom Catalysts across the Periodic Table*, Chem. Rev., vol. 120, no. 21, pp. 11703–11809, Nov. 2020, doi: 10.1021/acs.chemrev.0c00576.

Chapter 2

Experimental Methods
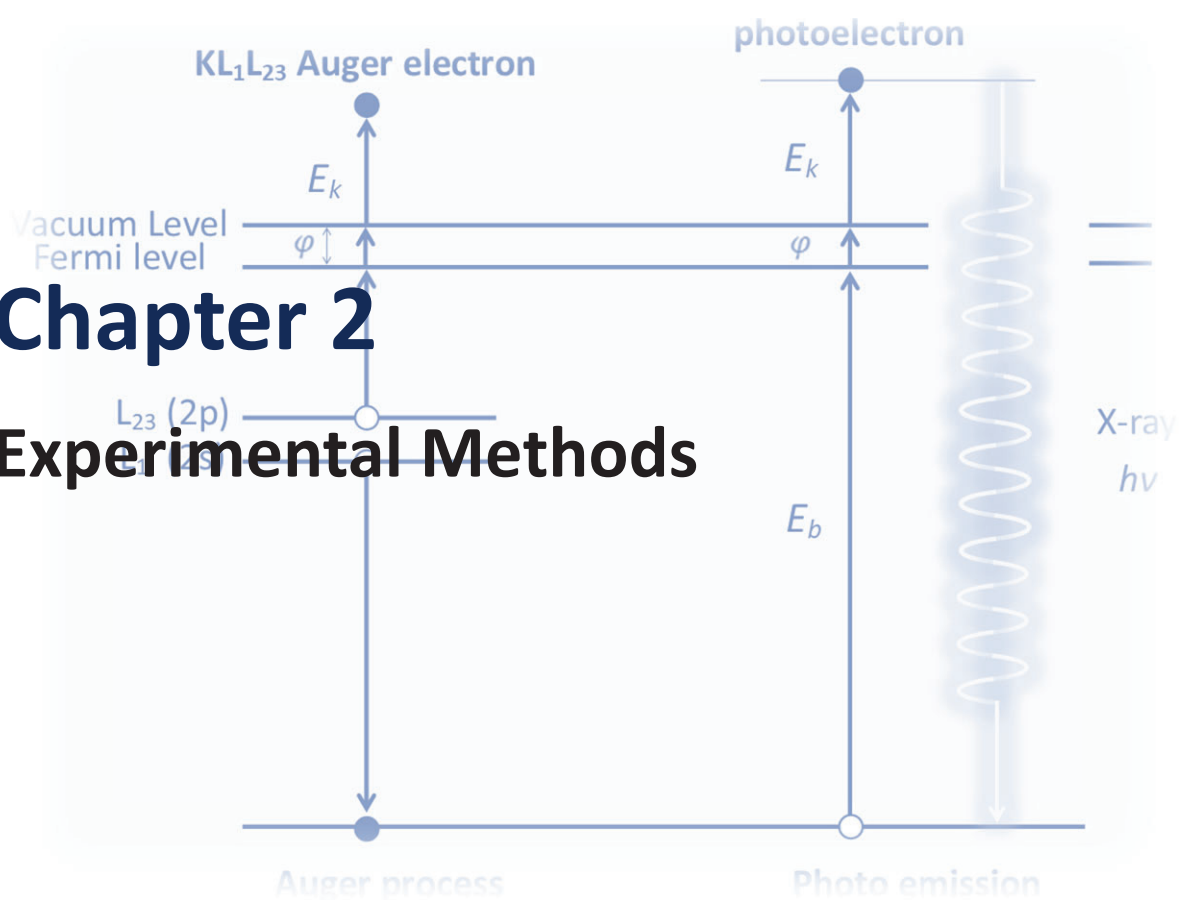
CHAPTER 2 EXPERIMENTAL METHODS

2.1   Introduction to Chapter 2

This chapter describes the experimental techniques used during the development of this work. Section 2.1 describes the catalyst, electrode preparations, and deposition onto the active supports used during NO_x^-RR. **Section 2.2** presents the characterization techniques of the catalyst and full electrodes. **Section 2.3** describes the analytical techniques for determining NOx-RR to the most significant reactants and products. **Section 2.4** details the equipment and methods used for estimating the electrochemical surface area the intrinsic charge transfer coefficient. **Section 2.5** describes the electrochemical techniques used for determining the activity, selectivity, and productivity in terms of final products, along with others encompassing the energy efficiency of the full and half-cell.

2.2 Catalyst and electrode preparation techniques.

Three types of catalysts and three active supports were used during the development of this work. **Chapter 3** describes how Copper-based nanocubes were deposited onto a Titanium substrate, for an electrode defined as Cu_2O-Cu@Ti. In **Chapter 4** TiO_2 nanoparticles show catalytic properties when deposited onto Cu-based supports in a tandem process for NO_3^-RR to NH_3. **Chapter 5** evaluates the effects of cations in the electrolyte and Li in the catalyst structure during NO_3^-RR for the catalysts $NiO+SnO_2$ deposited on a carbon paper. Details of the preparation of electrodes are included in the respective chapters.

2.3 Characterization techniques.

The following characterization techniques were used during the development of this work to understand the electrode-electrolyte interface and look for the key to the activity for NO_3^-RR. The subsections covered the essential information for evaluating results obtained using the technique. Specific details and conditions are included in the respective chapters.

2.3.1 Field Emission - Scanning Electron Microscopy (FE-SEM) and Energy Dispersive X-Ray Spectroscopy (EDX).

SEM is a technique utilized for high-resolution imaging and analysis of materials at the nanoscale level. It operates by employing a focused beam of electrons to generate a magnified image of a sample. The electron beam is systematically scanned in a regular pattern across the surface of the sample, and the electrons emitted from the sample are utilized to create the image. SEM magnifies nanoparticles from about 10 times up to 300,000 times in no-color or artificially colored images, and due to depth of field, images can appear three-dimensional with minimal penetration of the electron beam into the sample. Detectors on SEM can capture two different types of images defined by the type of electrons depending on the energy and inelastic collision (SE) and elastic collisions (BSE). The electron beam consists of high-energy electrons generated by an electron gun, which are then processed by magnetic lenses to focus on the specimen surface. As the beam scans across the specimen surface, it illuminates each point at a time in a regular scanning pattern. The resulting image is formed by the strength of the signal generated from each point, reflecting differences in the sample such as topographical or compositional variations. The viewing screen is scanned synchronously with the beam on the specimen, establishing a one-to-one relationship between points on the specimen and points on the image viewing screen, known as a point-by-point translation. By decreasing the size of the area

scanned on the specimen, increased magnification can be achieved, allowing for a detailed examination of fine features at the nanoscale level[1], [2].

EDX is a technique that allows to explore the chemical composition of the electrode surfaces. By utilizing an EDS X-ray spectrophotometer integrated into SEM setups, this technique enables accurate dimensional and elemental analysis of surfaces. The process involves the generation of characteristic X-rays from a specimen upon electron beam irradiation, with emitted X-rays corresponding to the elemental composition of the sample. This allows for both qualitative and quantitative analysis of elemental constituents. With the help of a detector, the X-ray generates a small current, which is then converted into a voltage pulse dependent on the X-ray energy[3].
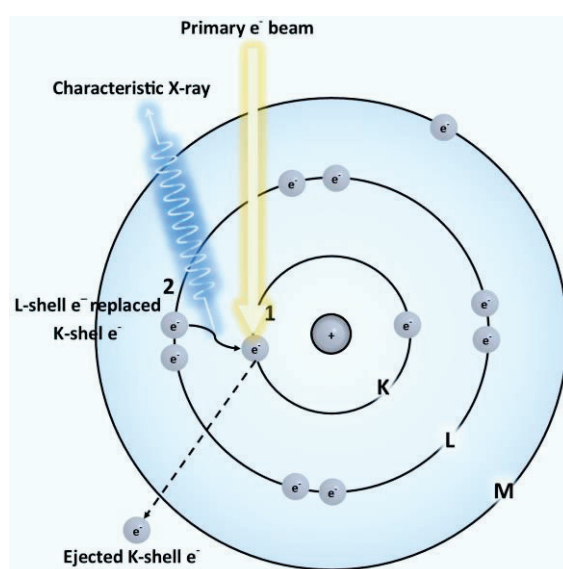
Figure 2.1 EDX spectroscopy schematic representation.

EDX analysis is capable of detecting and quantifying elements with atomic numbers larger than Z = 3, with Bremsstrahlung X-rays and Characteristic X-rays providing valuable insights into sample composition. The low detection limit of EDX analysis in SEM ranges from 0.1 to 0.5 wt.%, making it suitable for major and minor element analysis but less sensitive for trace-element analysis. Despite its non-destructive nature, some materials may experience damage under the electron beam, reason why some electrodes cannot be analyzed by this technique.

2.3.2 X-Ray Diffraction Spectroscopy (XRD)

X-ray diffraction **(Figure 2.2)** is utilized to analyze the crystalline structure of materials. It is based on the constructive interference of monochromatic X-rays and the crystalline conformation of the sample.

Copper (Cu) stands as the most used X-ray source, generating Cu-Kα X-rays with a wavelength of 1.6529 Å. During X-ray diffraction analysis, the incident X-rays interact with the crystalline structure of the sample. At specific angles, X-rays undergo constructive interference after reflecting off repeating crystalline planes, providing valuable information about the material's atomic arrangement. Bragg's law relates the angle of diffraction, or the Bragg angle (θ), and the lattice spacing (*d*) between adjacent identical crystal planes to the incident X-ray wavelength (*λ*) and the diffraction order (*n*) which indicates how many crystalline planes are interacting. The information about the material's crystalline structure can be obtained using Bragg's law, for identifying the specific crystal planes using Miller indices[4].

$$2d \cdot sin(\theta) = n/\lambda$$

For metal nanoparticles, XRD serves as a tool for estimating particle size using the Scherrer equation **(Equation 2.2)**. In this equation, *τ* represents the average size of the crystallite, *K* denotes the shape factor (typically 0.9), *λ* signifies the wavelength of the X-ray, β indicates the full width of the peak at half the maximum, measured in radians, and θ represents the Bragg angle of the peak normally expressed in radians[5].

$$\tau = \frac{K \cdot \lambda}{\beta \cdot \cos(\theta)}$$
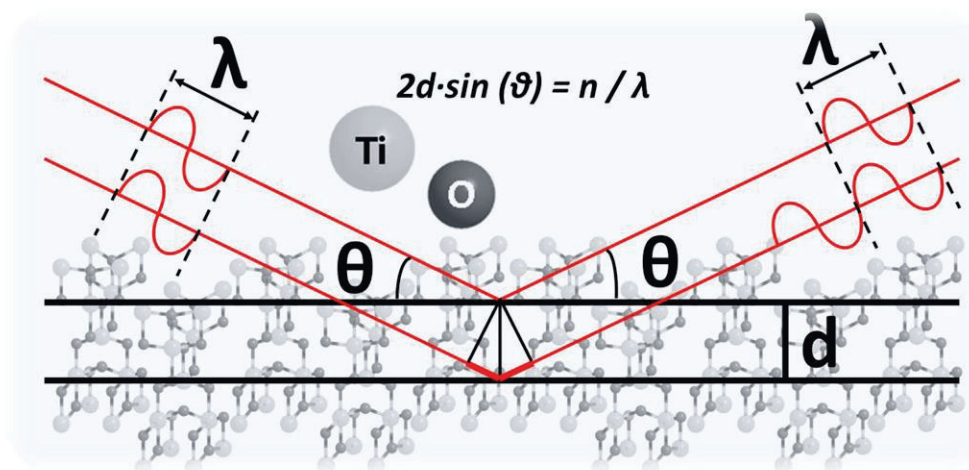
Figure 2.2 Bragg's law for X-ray Diffraction (XRD).

2.3.3 X-Ray Photoelectron Spectroscopy (XPS).

XPS is a technique for studying the elemental composition and chemical state of the surface of a solid material. In the present thesis, it was mainly used to investigate the chemical state of the Cu and Ti-based electrodes used in NO_3^-RR-to NH_3. This technique operates by utilizing X-ray radiation to excite

electrons from the surface of a sample material. As depicted in **Figure 2.3**, an incoming X-ray photon is absorbed by the sample, transferring its energy to a bound electron (photoelectron). This excited photoelectron subsequently leaves the surface with a specific kinetic energy. The relationship between the incoming X-ray energy (hv), the binding energy of the electron in the sample (E_b), and the resulting kinetic energy of the photoelectron (E_k) is described by the following equation[6]:

$$E_k = hv - E_b - \emptyset$$

Where $\emptyset$ represents the work function of the electron energy analyzer. The binding energy of the electron is specific to the element from which it was excited and its chemical state. When an electron from a higher energy level relaxes to fill the hole left by the photoelectron, the energy released can excite an additional electron, a process known as Auger electron emission. The kinetic energy of an Auger electron is element-specific and does not depend on the energy of the incoming X-rays. An example of an XPS survey spectrum corresponding to the TiO_2@Cu electrode used in processes discussed in **Chapter 4** is depicted in **Figure 2.4**[7].
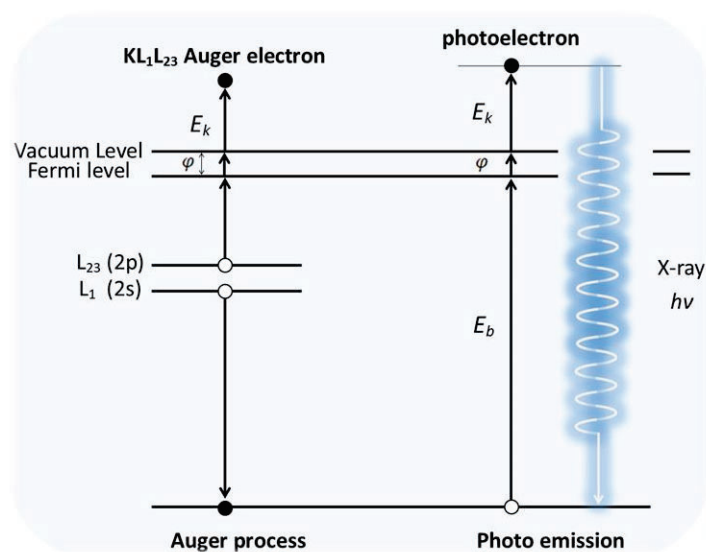
Figure 2.3 Excitation mechanisms occurring during XPS.

The XPS measurements in this thesis were conducted using a SPECS system equipped with a XR50 source operating at 300W and a Phoibos 150 MCD-9 detector, utilizing an AlKα X-ray source. The pass energy of the hemispherical analyzer was set at 20 eV, and the energy step of high-resolution spectra was set at 0.1 eV. Most of the XPS spectra presented in **Chapters 3** and **4** correspond to ex-situ analysis. However, the analysis corresponding to the **Cu₂O-Cu@Ti** electrodes presented in **Chapter 3** is considered semi-in-situ due to the experimental design, which prevented the exposure of the electrode to the atmosphere to conserve the oxidation state of the Cu-based nanoparticles. In the case

of the **TiO₂@Cu** electrodes presented in **Chapter 4**, all measurements were conducted ex-situ before and after electrochemical processes. The specific details of the analysis are shown in the respective chapters.
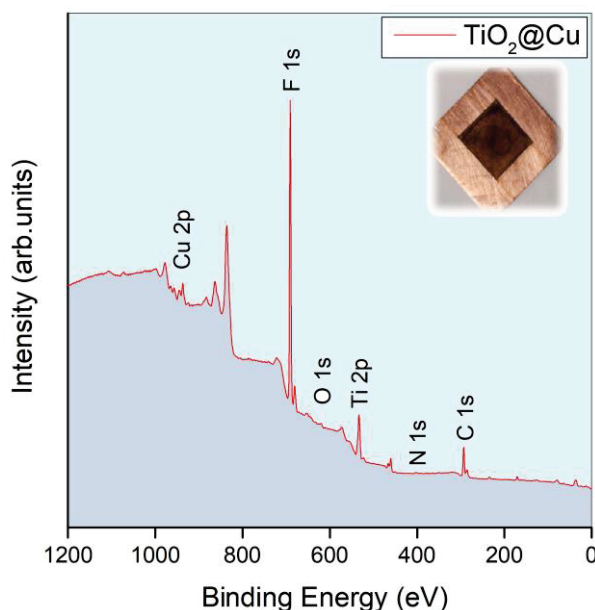
Figure 2.4 XPS Survey of the electrode TiO₂@Cu before electrolysis (Chapter IV)

2.3.4   Raman Spectroscopy

Raman spectroscopy is a non-destructive technique for surface characterization, offering insights into the chemical compositions and structural properties of both liquids and solids. We used it in this work across distinct purposes: discerning the oxidation states of Cu and Ti electrodes in **Chapter 3** and elucidating the crystalline phase of TiO_2 nanoparticles in **Chapter 4,** as well to evaluate the presence of structural defects. One facet of Raman spectroscopy lies in its expansive measurement range spanning from 50 to 4000 cm^{-1}, coupled with the advantage of dispensing with the need for intricate sample preparation protocols. The measurement conditions can be room temperature, cryogenic, and high-temperature observations. Raman spectroscopy entails the analysis of radiation scattered from a sample. Typically, Raman spectra are presented in terms of wavenumber (cm^{-1}) shifts relative to the incident radiation. These shifts in wavenumber signify absolute energy disparities between eigenstates of the molecule. Indirect probing of vibrational transitions is achieved through light scattering in Raman spectroscopy. Notably, the Raman shifts correspond to energy absorptions akin to those observed in infrared spectroscopy, often revealing similar absorptions in both techniques. Hence, Raman scattering finds application in the qualitative identification of ions and organic compounds by leveraging group frequencies and scatter intensities. From a quantum mechanical standpoint, the

scattering of incident electromagnetic waves is construed as perturbation of the molecule's eigenstates. This perturbation induced by the incident radiation engenders a time-dependent virtual state **(Figure 2.5).** When the initial and final states coincide, the perturbation yields Rayleigh scattering, termed as inelastic scatter. Conversely, Raman scattering, arising from transitions between eigenstates $|m\rangle \rightarrow |n\rangle$, is categorized as elastic scatter. In Stoke scattering v_S, no net energy transfer occurs for the molecule, whereas in the Anti-Stoke process v_A, the scatter carries away the excess energy relinquished by the molecule. The intensity ratio of the Stokes Raman lines of the sample depends on the temperature of the sample, the population of molecules in the ground and exited states, according to **Equation 2.4**[8], [9]**.**

$$\frac{I_{Stokes}}{I_{anti-Stokes}} = \frac{(v_0 - \Delta v)^4}{(v_0 + \Delta v)^4} e^{\left(\frac{-hc\Delta v}{kT}\right)}$$

Where h is the Plank's constant, k is the Boltzmann's constant, T is the temperature, Δv is the vibrational energy of the molecule (v_{vib}). The electrodes Cu_2O-Cu@Ti and nanoparticles of TiO_2 were analyzed with a iHR320 spectrometer from HORIBA Scientific with a green laser (λ = 532 nm). Details of the measurements are given in the respective chapters.
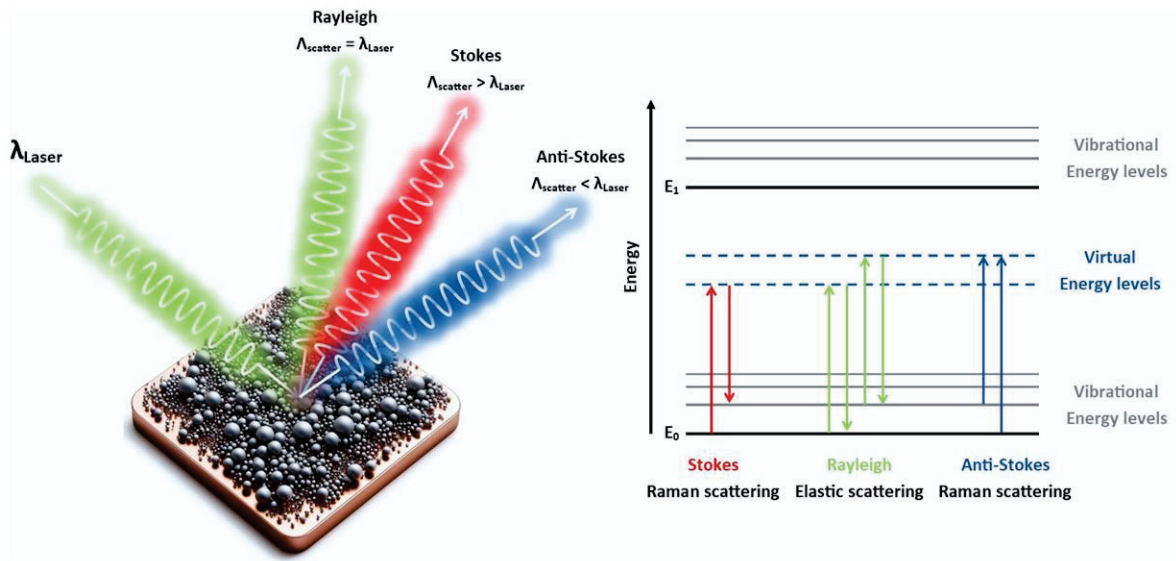
Figure 2.5 Raman scattering.

2.3.5 High-Resolution Transmission Electron Microscopy (HR-TEM).

HR-TEM is a technique of imaging the internal structure of solids using a beam of high-energy electrons transmitted through the solid, that also provides a direct information about the crystallographic structure of materials. This technique allows advanced characterization of materials, allowing the acquisition of information about punctual defects and grain boundaries.

The basic principle of the TEM is that a photographic image is recorded from the electron flux after it has passed through a thin sample of the specimen under study. The TEM image is formed by propagating a bundle of waves onto the sample. Some of the waves interact with the sample after with the resulting image is magnified by a series of lenses.

2.4   Analytical techniques.

2.4.1   Ion Chromatography (IC).

IC is employed for the quantification of ionic reactants and products. By this analytical technique, ions are separated while moving in a mobile phase based on their interaction with a stationary phase within a chromatography column (**Figure 2.6**). The stationary phase typically consists of a resin or gel containing charged functional groups, while the mobile phase is usually a solution of ions or buffers. The separation mechanism primarily relies on ion exchange interactions between the sample ions and the stationary phase. In the chromatography process, ions in the sample solution compete with ions in the mobile phase for binding sites on the stationary phase, leading to separation based on their ionic properties such as charge and size. The quantification process begins with an injector controlling the mixing of the sample liquid with the eluent, which is then passed along for analysis. The dilute sample in the eluent liquid subsequently passes through an auxiliary column to remove unwanted components such as heavy metals or large solid particles. After this pre-column stage, the sample liquid passes through the main column of the IC, coated with the stationary phase described previously. As the sample liquid passes through the column, ions initially adhere to the surface of the resin. However, with the continuous flow of eluent through the column, the ions are gradually washed or pushed off the resin and carried along. Detection occurs after ion separation using various methods such as conductivity, UV-visible spectroscopy, amperometry, or mass spectrometry. Subsequentially, the ion-separated liquid then passes through a suppressor to reduce the background signal of the eluent, which would otherwise exhibit high conductivity by itself. In the case of our equipment, conductivity detection is the method applied for which, the conductivity of the liquid sample is measured, and as charged ions pass through, the conductivity increases, generating a signal that correlates with the number of ions present. The different ions pass the detector at various delayed times due to the chromatography column, enabling independent measurement and quantification[10]–[12].
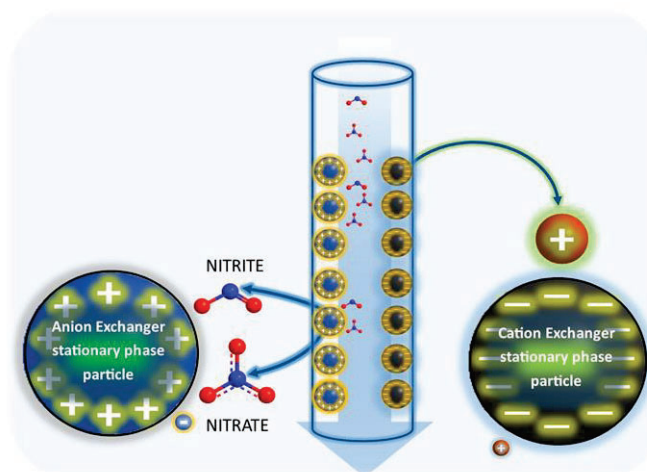
Figure 2.6 Interaction of ions within the column during IC.

In this work, IC was utilized to quantify the concentration of NO_3^- and NO_2^- ions in the electrolyte before and after electrochemical processes. A Thermo-Fisher Dionex 1100 ICS, equipped with a Dionex Ion Pack AS-22 anion exchange column and a chemical suppressor ASR-ultra 4 mm, was employed for this purpose. The mobile phase (eluent) used for anion quantification comprised 4.5 mM sodium carbonate (Na_2CO_3) and 1.4 mM sodium hydrogen carbonate ($NaHCO_3$), with a flow rate of 1.5 mL·min^{-1}[13].
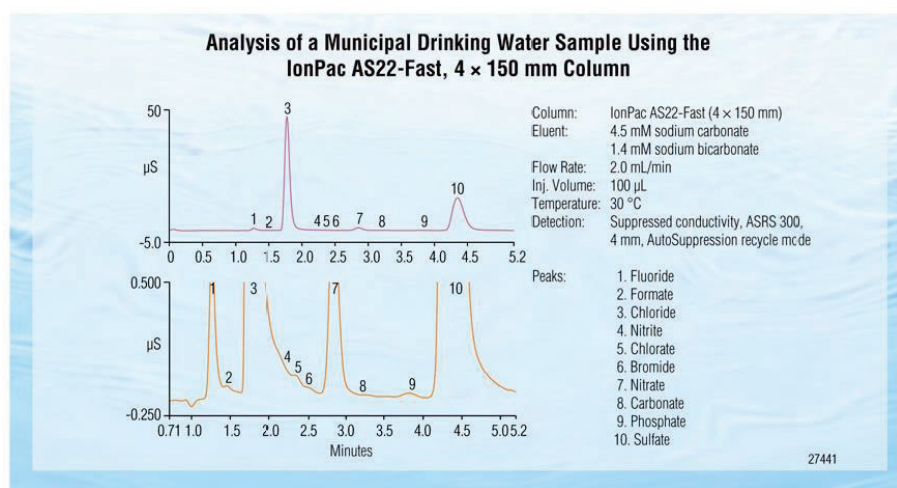
Figure 2.7 IC chromatogram for different ions. Reproduced from Thermo Scientific IonPac AS22 Anion-Exchange Column manual.

Calibration curves for NO_3^- and NO_2^- anions were established by correlating peak areas (µS·min) with the concentration of standard solutions (ranging from 0.0 to 0.6 mM for each ion), as depicted in **Figure**

2.8. To measure the concentration of samples, a 55 µL aliquot of electrolyte was diluted in 10 mL of MilliQ water and subsequently analyzed using IC. The actual ion concentration in the electrolyte was determined by multiplying the measured concentration by the dilution factor (10/0.055).
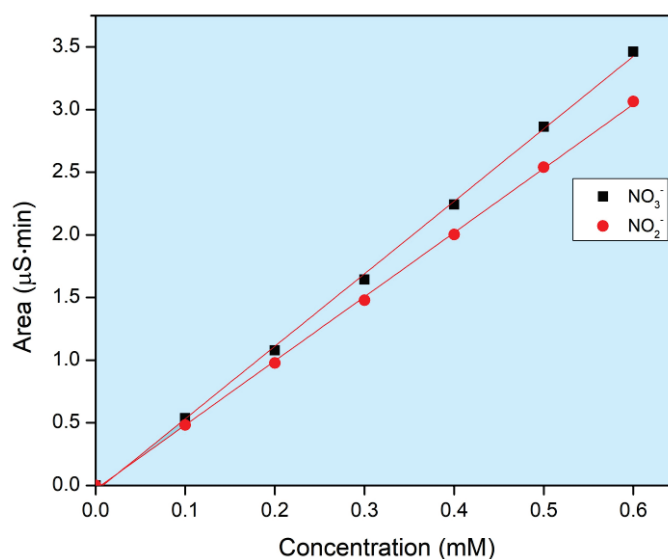
Figure 2.8 calibration curves for NO_2^- and NO_3^- ions constructed using standard solutions. The concentrations of these ions in the electrolyte were determined by analyzing a 55 µL aliquot with the IC and then multiplying the measured concentration by the dilution factor.

2.4.2   Gaseous products

Gas Chromatography (GC) is an analytical technique used to separate and analyze compounds that can be vaporized without decomposition. In this process, a sample is injected into a chromatograph and carried by a mobile phase (typically an inert gas) through a column containing a stationary phase (often a polymer film). The various compounds in the sample interact differently with the stationary phase, causing them to exit the column at different times and enabling individual detection. The principle of GC is based on the distribution of components between the mobile and stationary phases. The interaction strength between a compound in the sample and the column depends on factors such as size (with Van der Waals interactions), polarity, and other forces. Compounds that are weakly retained in the column exit the column first, while those that interact more strongly take longer to elute. A key parameter for detecting gases in GC is the retention time, which is the interval between sample injection and the appearance of a specific product's signal in the detector.

The elements of a Gas Chromatography (GC) system include the **injector**, which introduces the sample into the chromatograph, and the **mobile phase**, typically composed of an inert gas such as argon, helium, or nitrogen, which transports the sample. **The column**, where the separation of sample

components occurs, is usually a long, coiled tube containing the stationary phase, often made of high molecular weight polymers like polysiloxane derivatives (dimethylpolysiloxane, diphenyl-dimethylpolysiloxane) or polyethylene glycol. **The detector**, located at the end of the column, identifies and quantifies the separated components as they elute.

GC data is represented on a chromatogram, a plot of the detector signal against the time of analysis, where each peak corresponds to a specific component of the sample at a distinct retention time, and the area of each peak indicates the quantity of the corresponding component.

An on-line 490 Micro GC, Agilent Technologies equipped with three columns, a first molecular sieve (CP-Molsieve 5 A, Ar) for H2 analysis; a second molecular sieve (CP-Molsieve 5 A, He); and a porous polymer (CP PoralPlot U, He) for the analysis of CO2 and C2+ products. The specific conditions of the analysis were: Injector temperature: 100°C; Column temperature: 70°C, and Column pressure: 150 kPa.

2.4.3   UV-Vis spectroscopy.

UV-Vis spectroscopy is technique used for determining the concentration of compounds in liquid solutions. It involves directing a beam of light with wavelengths in the UV-Vis range (170 – 1200 nm) onto a sample held in a cuvette. A detector then collects the signal representing the light intensity passing through the sample. Specific light wavelengths are absorbed by the sample, and the difference between the signal with and without the sample is known as the absorbance. This absorbance is directly proportional to the concentration of UV-Vis absorbing species and follows Beer's law, as defined in **Equation 2.1**, where A represents absorbance, ε is the molar extinction coefficient, 1 is the path length of the sample (normally defined by the cuvette width), C is the concentration of the UV-Vis active species, I_0 is the incident light intensity, and I is the light intensity after passing through the sample. The absorption scales linearly with the concentration, so a calibration curve can be made and used for quantification of for example NH_3/NH_4^+ in the solution.

$$A = \varepsilon \cdot 1 \cdot C = \log\left(\frac{I_0}{I}\right) \hspace{4cm} 2.1$$

Factors such as solvent and dissolved salts can influence the adsorption profiles, and there might be interferences due to the presence of certain species in solution. One way of avoiding many of these issues is diluting the species to be determined before the measurement[14], [15].
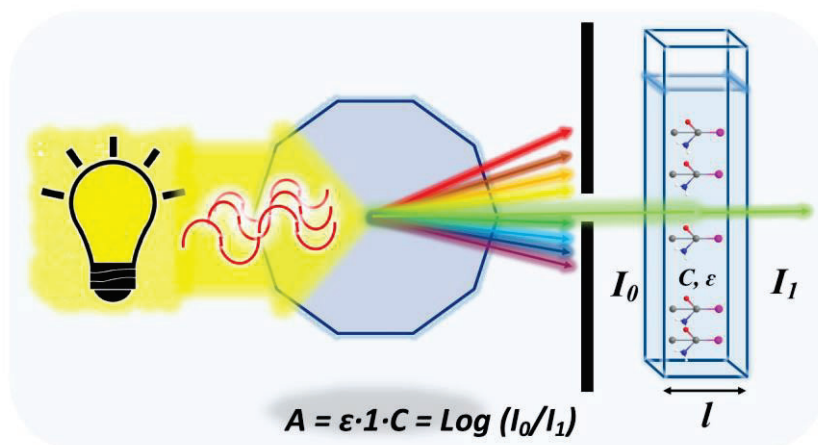
Figure 2.9 Beer's law for Ultraviolet-Visible (UV-Vis) spectrophotometry.

The quantification of NH_3/NH_4^+ species resulting from electrochemical processes in Chapters 3, 4 and 5, was performed using a PerkinElmer Lambda-950 double beam UV-Vis spectrophotometer. A quartz cuvette with a 1 cm path length was used, and absorbance was measured in the visible wavelength range (390 to 500 nm), leveraging the expected transparency of quartz materials in both the visible and UV ranges. Although NH_3/NH_4^+ is not UV-Vis active, it is possible to utilize this technique after complexing these species with the assistance of Nessler reagent ($K[Hg(H_2O)I_3]$) and measuring the absorbance in the visible range as described below.

NH_3/NH_4^+ measurements.

For NH_3/NH_4^+ quantification, a calibration curve was constructed using five standard concentrations of ammonium chloride (NH_4Cl): 0, 0.06, 0.11, 0.17, and 0.22 mM (0 to 4 mg L^{-1} of NH_4^+ respectively). Each sample's NH_3/NH_4^+ concentration was determined by diluting an aliquot 100 to 200 times (0.050 to 0.100 mL up to 10 mL) with Milli-Q water to match the calibration curve's concentration range. To each diluted sample, two drops of Polyvinyl alcohol dispersing agent (Hach) and two drops of a mineral stabilizer solution (Hach) were added. Subsequently, 200 µL of Nessler reagent (Sigma-Aldrich) was added. The formation of the complex compound **Hg_2ONH_2I (reaction below)** was observed within 10 to 30 minutes following the addition of the Nessler reagent, and its absorbance was measured at 420 nm. Figure 2.10 displays the calibration curve derived from NH_4Cl[16], [17].

$$2[HgI_4]^{2-} + NH_3 + 3OH^- \rightarrow Hg_2ONH_2I + 7I^- + 2H_2O$$
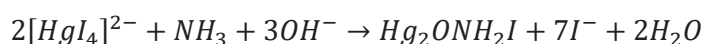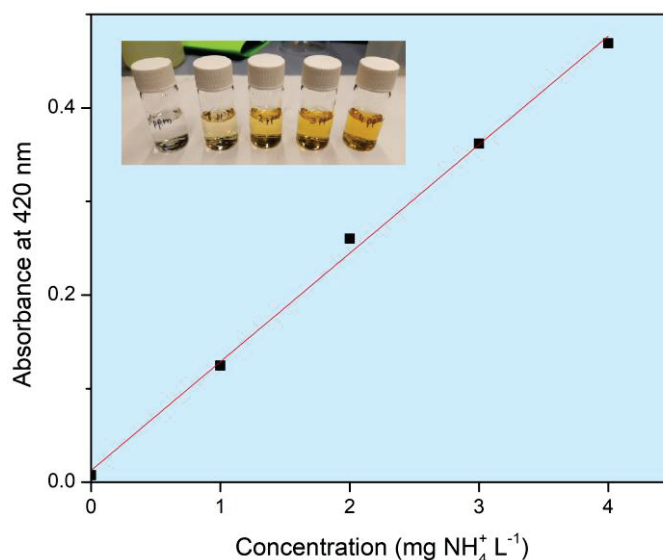
Figure 2.10 UV-Vis absorbance calibration curve constructed with the standard NH₄Cl solutions. Concentrations shown reflect the concentration in the cuvette during the spectrophotometry. The actual concentration of NH₃/NH₄⁺ was obtained by correcting the measured cuvette concentrations with dilution factor.

The obtained concentrations of NH_3 were further used for determining faradaic efficiencies and selectivity.

2.5   Catalyst synthesis.

2.5.1   Electrodeposition

Electrochemical deposition or electrodeposition is a technique utilized in both laboratory and industrial settings for metal plating. In this section some fundamental aspects of the process are presented, particularly those important for the fabrication of structures for composite electrodes, as it will be presented in **Chapter 3**.

The principle of electrodeposition lies in the transfer of electrons between the electrode and electroactive species in solution, alongside the transformation of discharged metal ions into a crystalline state. The initiation of electrochemical deposition occurs with the reduction of species within a solution[18]. From the thermodynamic point of view, this reduction process is characterized by the standard electrode potential (E°), which represents the equilibrium potential at which the rates of reduction and oxidation reactions are equal under standard conditions of concentration, pressure, and temperature. The Nernst equation provides a mathematical framework to relate standard

electrode potential (E^0) to the electrode potential (E), incorporating factors such as temperature, number of transferred electrons, and the ratio of activities of oxidized and reduced species[19].

$$E = E^0 + \frac{RT}{nF} ln \frac{\{Ox\}}{\{Red\}}$$ 2.2

Here, R represents the gas constant (8.314 J·mol⁻¹·K⁻¹), T denotes the absolute temperature (K), n signifies the number of transferred electrons, and F is Faraday's constant (96485.31 C·mol⁻¹). This equation elucidates the dynamic relationship between electrode potential and the redox processes occurring at the electrode interface.

The mass of material deposited during electrodeposition is a direct consequence of Faraday's law, which states that the mass (m) is directly proportional to the total electric charge (Q) and the molar mass (M) of the deposited material, and inversely proportional to the n and F[20].

$$m = \frac{Q \cdot M}{n \cdot F}$$ 2.3

The electrochemical deposition can be controlled by adjusting either the current or the potential. In constant current mode, a specific current is applied through the electrochemical cell, while in constant potential mode, a desired potential is maintained, with the accompanying current being monitored. By manipulating E relative to the E^0 for an electrochemical reaction influences the reduction current. When the electrode potential is more negatively polarized, the reduction current increases due to an acceleration in the rate of electron transfer[21]. This phenomenon, known as the Tafel linearity, manifests as a linear relationship between the potential and the logarithm of the deposition current in the electron transfer-controlled region. However, it's important to note that factors such as mass transfer limitations, chemical processing steps, and crystallization processes can also influence the deposition current, potentially deviating from the ideal Tafel behavior[22].

The optimum current density applied to the WE in the deposition of metals from aqueous electrolytes depends on the desired coating or nanostructure. Hence, the final structure of the deposited metal is correlated with the end of the Tafel linearity range and, nucleation increases with more negative potentials, but mass-transport limitations can lead to irregular growth or particle formation[21]. In the case of metal oxide deposition, nanostructures can be formed by the reduction of metal ions that form stable oxides on the surface of the cathode or by depositing a metallic coating and subsequently partially oxidizing this deposited metal with the application of an anodic potential. This partial oxidation allows for controlled reduction, facilitating the development of desired nanostructures[23].

In our specific case, electrochemical deposition conditions have been developed for allowing the synthesis of nanocrystalline Cu₂O-Cu particles by using a pulsed electrodeposition (PED). Details of the

specific conditions and applied potentials are presented in **Chapter 3**. However, the basics of PED are discussed here:

PED is a type of electrodeposition where nanocrystals are deposited onto a substrate by applying periodic charge pulses in the electric potential or current[24]:

1) Application a of a cathodic potential (E_C) for nucleation and initial growth: During this phase, a cathodic potential is applied to the substrate, which serves as WE. At this potential, metal ions from the electrolyte solution are reduced and deposited on the substrate, forming nuclei of nanoparticles. This phase as well initiates the growth process and the period in which the cathodic potential is applied can define the size and distribution of the nanoparticles.
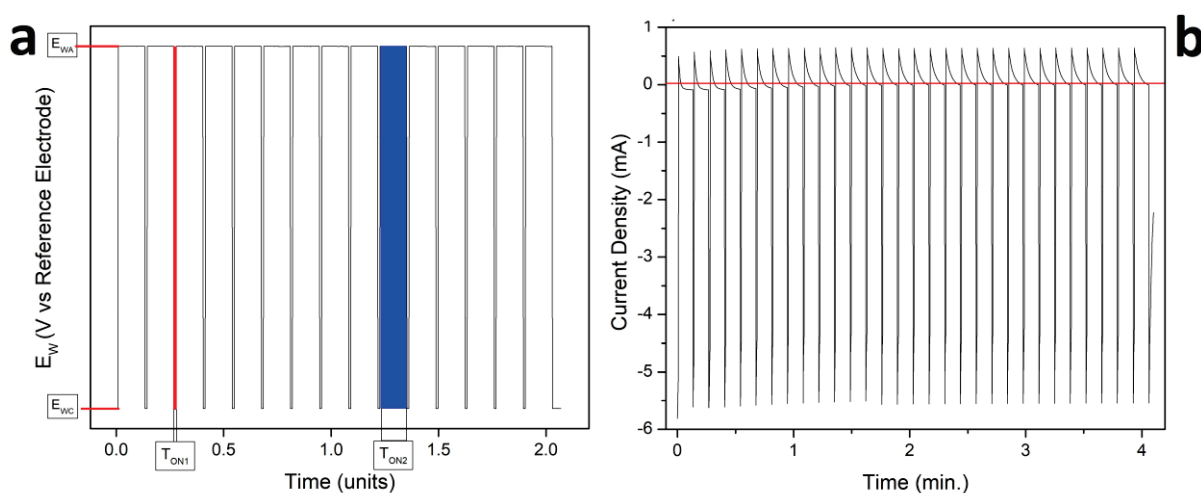
Figure 2.11 a) PED waveform E_w vs time b) CA applied to a 5mM $CuCl_2$ + 5mM KCl electrolyte using a Ti as WE.

2) Anodic potentials (E_A) for partial oxidations: After nucleation and initial growth phase, an anodic potential is applied. E_A allows the deposited nanoparticles to undergo partial oxidation. This oxidation process can alter the composition and catalytic properties of the nanocrystals, tailoring the surface towards the specific electrochemical reaction to be further conducted. The process is schematized in **Figure 2.11a,** whereby alternating cathodic and anodic potentials at defined periods, the synthesis of nanoparticles offers control over size, shape, composition, and surface properties of the structures. **Figure 2.11b** shows an example chronoamperometry of the synthesis of Cu_2O-Cu nanoparticles deposited by PED over a Ti substrate.

The electrochemical cell used for electrodeposition processes is presented in **section 3.8**.

2.5.2   Pulsed Laser ablation in Liquids (PLAL).

PLAL is a technique used for the synthesis of nanostructures in the colloidal state depending on the target employed. This technique has been widely employed in the ablation of titanium dioxide TiO_2 nanomaterials with different shapes, sizes and phases depending on the laser parameters employed such as lased wavelength, laser pulse energy and the type of liquid medium employed. The process begins with laser ablation, which involves focusing a high-energy pulsed laser beam onto a solid target material immersed in a liquid. The intense energy from the laser pulse vaporizes or ablates a portion of the target material, creating a plasma plume above the target surface. The ablation of the target material generates a plasma plume consisting of atoms, ions, and clusters of the target material, as well as the surrounding liquid molecules. The plasma plume expands rapidly into the surrounding liquid medium due to the high energy imparted by the laser pulse. The third stage consists of the nucleation and formation of the nanoparticles by the occurrence of several simultaneous processes. (1) Rapid cooling, the high temperature plasma plume rapidly cools upon contact with the liquid, causing the vaporized species to condense. (2) nucleation, the condensed species in the plasma plume undergo nucleation, forming small nuclei or clusters. (3) Growth, these nuclei then grow further as more atoms and clusters in the plasma plume are deposited onto their surfaces. (4) Stabilization, nanoparticles formed in the liquid medium may undergo surface modifications or stabilization through interaction with the surrounding solvent molecules or by surface functionalization. The last step corresponds to the nanoparticle collection, in which the nanoparticles synthesized are collected from the liquid medium by filtration, centrifugation or precipitation. TiO_2 nanoparticles synthesized by PLAL are used for NO_3-RR to NH_3. Specific details of the synthesis of nanoparticles and preparation of electrodes are given in **Chapter 4**[25].

2.6   Electrochemical methods.

In this section we provide a description of the electrochemical methods employed during the thesis. All measurements were recorded using a BioLogic electrochemical workstation, which offers capabilities for controlling and measuring potentials and currents arising from the electrochemical processes.

2.6.1   Open circuit voltage (OCV)

In OCV measurements, the electrochemical cell is allowed to reach equilibrium with no external bias applied. This means that no current flows between the electrodes, indicating that reactions proceed forward and backward at the exact same rate. In this state, the electrodes are disconnected from the

power source, but potential measurements between the reference and working electrodes are still conducted. The recorded data thus reflects the rest-potential, providing valuable insights into the redox state of species involved in the electrochemical system. OCV measurements serve as a baseline reference point, indicating the equilibrium potential of the system when no current is passing through it. They are often used to assess the thermodynamic properties of electrochemical systems and to monitor changes in the composition of the system or state over time[19].

2.6.2   Linear Sweep Voltammetry (LSV) and Cyclic Voltammetry (CV).
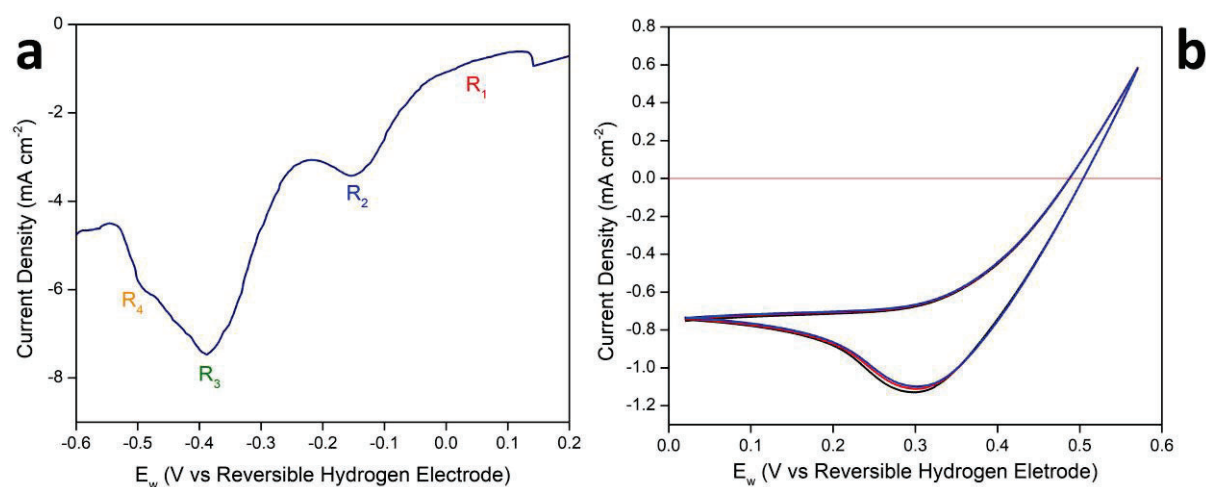
Figure 2.12 (a) LSV applied to a 0.1M KNO3+1M KOH using a Cu plate WE at 20 mV s^{-1}. (b) CV applied to a 5mM $CuCl_2$ + 5mM KCl using a TiO_2 substrate as WE, a scan rate of 10 mV s^{-1}.

For NO_3^-RR to NH_3 processes, the WE must be adequately cathodic for producing enough overpotential. The determination of the cathodic potential of current required for this reduction was initiated with linear scan of the applied potential of the cathode. This allowed monitoring the specific range of cathodic potentials at which the electrochemical reaction is conducted at the electrode surface. Since, when reactions occur, charges are transferred resulting in a current, with the LSV it was possible to determine an optimal range of applied potentials for NO_3^-RR towards different products related to the different materials described in the next chapters. After a cathodic LSV, the WE potential can be scanned in the anodic direction, completing a cycle. This scanning back and forth of the potentials is called CV and an example is given in **Figure 2.13** [26]**.** It shows the two first cyclic scans on a Cu electrode in a 5mM CuCl+5mM KCl electrolyte, measured vs a Pt mesh counter and a Ag/AgCl reference electrodes, respectively.

2.6.3   Potentiostatic Electrochemical Impedance Spectroscopy (PEIS).

PEIS involves studying the electrochemical response of a system to a low-amplitude sinusoidal electrical perturbation applied at varying frequencies. This technique allows for the measurement of the system's impedance, which is the opposition to the flow of electrical current[27]. As the frequency of the applied field is altered, the response in current is measured, providing insights into the electrochemical behavior of the system. Depending on the characteristics of the system under study, there may be a delay between the application of the potential and the response in current. This delay results in a phase shift, along with a certain amplitude, in the measured impedance. By analyzing these phase shifts and amplitudes across a range of frequencies, valuable information about the kinetics and mechanisms of electrochemical processes within the system can be obtained[27], [28].

By varying the frequency in PEIS, processes occurring over different time periods can be probed. For instance, the ohmic resistance, which is a fast process, is predominantly observed at high frequencies[28]. On the other hand, charge transfer processes, being slower, are more discernible at low frequencies. Due to the similar nature of ionic and electric charge transfers, it is possible to infer an equivalent electrical circuit diagram from the electrochemical PEIS measurements. An analysis of PEIS data requires a high understanding of the characteristic of the system. However, in this thesis, the PEIS technique was only employed to determine the ohmic resistance within the setup.

According to Ohm's law, a current (I) is generated by a potential difference (E) across a resistor (R). When conducting measurements on an electrochemical cell, a portion of the applied potential is attributed to the resistance of the cell. To account for this resistance-induced potential loss, the measured potential can be compensated using **Equation 2.4** defining the actual potential at the electrode for reactions[29].

$$U_{measured} = U_{actual} - I \cdot R \hspace{4cm} 2.4$$

While *IR* compensation helps to isolate and analyze specific electrochemical processes, the un-compensated cell potential reflects the total energy input into the system, including contributions from both the desired electrochemical reactions and any resistive losses within the cell.

2.6.4   Chronoamperometry (CA) and chronopotentiometry (CP) tests.

An electrochemical system can be controlled, eighter by defining the WE potential or setting the current between the electrodes. In CA tests, the current is recorded over time at a specified potential. In a three-electrode setup, it is the potential of the WE that is defined. Depending on the experimental

conditions, a certain current can be generated, and the potential of the counter electrode (CE) may adjust accordingly. For example, if a cathodic potential applied to the WE facilitate a significant amount of reaction, a high current will be generated. In response, the potential of the CE may shift to maintain appropriate electrochemical conditions. Similarly, depending on the availability of oxidation reactants, the potential of the anode may need to be adjusted to a more anodic value to increase the reaction rate in accordance with the current drawn. This dynamic interplay between the potentials of the WE and CE ensures the proper progression of electrochemical reactions and facilitates the desired experimental outcomes. On the other hand, in a CP it is the current between the WE and CE what is defined, while recording the electrode potentials over the time. Like CA, the electrode potentials must be adjusted to have reaction rates set by the current[29].

In this thesis, both techniques have been used for NO$_3^-$RR experiments. Whether CA or CP is used, depends on what parameters need to be controlled. From both cases, the accumulated charge passed during an experiment, Q can be calculated by integrating the current over time. This data is also proportioned by the software of the system.

By knowing the applied potential, current, and total charge transferred, different parameters can be calculated for evaluating the performance of the process or materials. For NH$_3$ synthesis, FE towards the different products (NH_3, NO_2^-, H_2) needs to be evaluated. The FE refers to how efficient the charge passed in the system goes toward the product formation. During NH_3 synthesis from NO_3^-, the formation of each mole requires a total of 8 electrons While the formation of NO_2^- requires the transference of 2 charges per molecule. FE is defined as follows in **Equation 2.5**.

$$FE_i(\%) = \frac{\alpha \cdot C_i \cdot F}{M \cdot Q} \cdot 100 \qquad\qquad 2.5$$

Where, C_i (M) is the obtained molar concentration of a target product; M (g/mol) is the molar mass; α is the number of transferred charges for producing a target product; F is the Faraday constant, and Q is the total charge transferred to the system.

For the H$_2$ produced during CA and CP processes the FE is calculated with **Equation 2.6**

$$FE_{H_2}(\%) = \frac{j_{H_2}}{j_{Total}} \cdot 100 \qquad\qquad 2.6$$

Where j_{H_2} is the partial current of the GC-measured concentration of H$_2$, and j_{Total} is the measured current density in case of potentiostatic electrolysis or the applied current density during galvanostatic processes.

In the same line, another efficiency parameters calculated in this work are Global Cell Energy Efficiency (EE_{CELL}) and the half-cell Energy Efficiency ($EE_{Half-Cell}$), parameters rarely reported in the literature for the synthesis of NH_3 from NO_3^-. EE_{CELL} and $EE_{Half-Cell}$ refers to the electrical energy input compared to the chemical energy output from the products. It is less agreed upon, what energy should be included (chemical, mechanical energy such pumps, and others). However, here it was defined that only the chemical energy of the products will be considered for *EE* calculations. The *EE_CELL* would involve the energy input, chemical energy output, and losses due to inefficiencies in the electrochemical processes[30].

$$EE_{CELL} = \frac{E_{OUT}}{E_{IN}} \cdot 100 = \frac{\Delta G_{NH_3}}{\int_0^t I(t) \cdot E_{CELL}(t)dt} \cdot 100 = \frac{EC_{NH_3}}{\int_0^t I(t) \cdot U(t)dt} \cdot 100 \qquad 2.7$$

where the numerator is the theoretical energy consumption in absolute terms, defined as the Gibbs free energy of the reaction (ΔG_{NH_3})[29]:

$$\Delta G_{NH_3} = EC_{NH_3} = \left[\Delta G^0_{NH_3} + R \cdot T \cdot \text{Ln} \left(\frac{C_{NH_3\,t} \cdot C_{OH^-\,t}^9}{C_{NO_x^-\,t}} \right) \right] \cdot C_{NH_3\,t} \cdot V \qquad 2.8$$

The standard Gibbs Free Energy ($\Delta G^0_{NH_3}$) is calculated from the standard cell potential (E^0_{CELL}) of the involved reaction, the Faraday constant (F), and the number of transferred charges (n)[29]:

$$\Delta G^0_{NH_3} = -n \cdot F \cdot E^0_{CELL} \qquad 2.9$$

The integral presented in the denominator, $E_{in} = \int_0^t I(t) \cdot U(t)dt$ of the time dependent current $I(t)$, and the total cell potential $(U)(t)$ respectively, gives the electrical energy input to the cell[31].

The $EE_{Half-Cell}$ measures how efficiently the electrical energy input is converted into the chemical energy stored in *NH₃* only considering the half-cell reaction at the cathode[32].

$$EE_{half-cell}(\%) = \frac{EC_{NH_3}}{(0.4 - U_w) \cdot \int_0^t I(t)dt} \cdot 100 \qquad 2.10$$

The EC_{NH_3} in the numerator corresponds to the same energy consumption used for the EE_{CELL}, calculated from the ΔG_{NH_3}. However, the denominator includes only the cell potential of the semi reaction in the cathode, being 0.4V vs SHE the Standard Reduction Potential of water at pH 14, and U_W the applied potential in the cathode[33].

2.6.5   Electrochemical active surface area (ECSA).

In all interfaces between solids and liquids, liquid molecules interact with the solid surface, and this interaction is ruled by the electrostatic field present. In electrochemical systems, this electrostatic field is manipulated by applying a potential gradient between two electrodes. This manipulation alters the distribution of molecules or ions on the surface of the solid material. Similar to a capacitor, the surface of an electrode undergoes electrostatic changes, leading to the formation of a double layer with molecules and ions. The resulting current arising from electrostatic surface charging is known as non-Faradaic current. In contrast, Faradaic current results from the transfer of electrons[34].
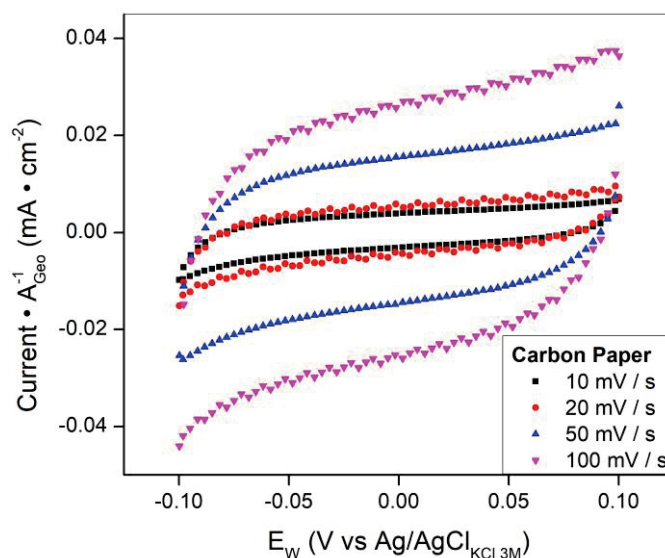
Figure 2.13 Cyclic Voltammetry applied at four different scan rates using a gas diffusion electrode (carbon paper) with 1M KOH electrolyte in a region where only non-faradaic currents are observed.

For materials which act close to ideal capacitors (where the capacitance is constant across applied potentials), the charge associated with the double layer can be related to the ECSA. Using a cyclic voltammetry, if the electrode is cycled across the non-Faradaic region at different scan rates (*v*). The current at the midpoint potential is linearly related to the scan rates and the slope is the differential capacitance. Using the specific capacitance of the material the electrochemical surface area is obtained. The charging of the C_{DL} during the experiment is assumed to match the conditions used to obtain the specific capacitance.

The electrochemical surface area is commonly used for normalizing the measured current and identify intrinsic activity values for catalysts. Most materials do not act as ideal capacitors and, therefore, using the specific capacitance is a first approximation for estimating the ECSA. Some limitations of estimating ECSA only from specific capacitance can be 1) non-faradaic and faradaic currents can be difficult to deconvolute; 2) high surface area or porous structures can have non-linear relationship between

surface-charging and scan rate; 3) the capacitance contributions of the active metals of supported catalyst are not easily separated from total capacitance; 4) and the distribution of species at the double-layer might not be identical for each scan rate within the potential range. The determination of C_{DL} and ECSA are defined in Equations 2.11 and 2.12[35], [36].

$$i = C_{DL} \cdot v \qquad\qquad 2.11$$

$$ECSA = \frac{C_{DL}}{C_S} \qquad\qquad 2.12$$

Where, i represents the measured current or current density by geometric surface area, C_{DL} is the double layer capacitance, v is the scan rate of the CV, and C_S corresponds to the specific capacitance for a material, a value standardized in 40 $\mu F \cdot cm^2$ in most of the cases. During CV, in the non-faradaic region, there is a linear correlation between the i and v.

2.6.6   Intrinsic charge transfer coefficient determination.

Reaction kinetic measurements play a critical role in making sense of catalyst activity, elucidating both reaction rates and mechanisms in simple and complex reactions. The exchange of electrons between the electrode and an active species can be tracked through the measurement of current. Specifically, the current resulting from this electron exchange is defined as faradaic current. In electrocatalytic reactions, the faradaic current serves as a correlation to the reaction rate, as it effectively monitors the movement of electrons during the catalytic reaction.

The primary objective of studying reaction kinetics is to distinguish the parameters controlling the catalytic activity. However, experimental conditions can introduce some errors, potentially causing the observed reaction rate to deviate from the intrinsic reaction rate, particularly if mass transport processes are slower than the intrinsic kinetics. A prevalent challenge encountered in reactions transpiring in liquid phases pertains to the sluggish movement of reactants and products within the medium. Such transport limitations can significantly influence the observed reaction rate by altering reactant concentrations at the electrode surface as they are consumed by the reaction, thereby potentially give a false idea of the true reaction rate under desired conditions.
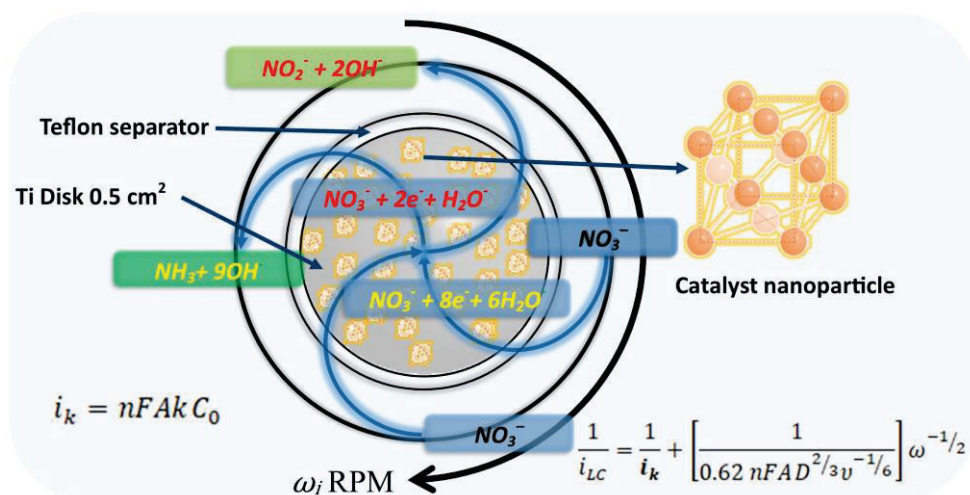
Figure 2.14 Rotating Disk Electrode (RDE) for Koutecky-Levich analysis.

To reduce the restrictions imposed by mass transport limitations and facilitate the movement of species within a solution towards the electrode surface, some strategies can be used. These include the utilization of stir bars to induce mixing, employing flow devices where the electrolyte is actively drive through a channel, or employing a **rotating disk electrode (RDE)** capable of rotating at high speeds to conduct the active species in the solution towards the electrode surface. These techniques serve to enhance mass transport and minimize concentration gradients[37]. The **Koutecky-Levich** analysis is a method for discerning the intrinsic kinetic and mass transport limiting currents within electrocatalytic systems[38]. This analysis, elaborated upon in **Chapter 3**, facilitates the separation of the observed current into its intrinsic kinetic and mass transport limited components. Specifically, in **Chapter 3**, the intrinsic current coefficients for three individual catalysts employed in NO_3^-RR are used to understand the synergy and the kinetic advantages observed for one composite electrode.

The Koutecky-Levich analysis is defined by **Equation 2.13** and the kinetic current is determined using **Equation 2.14**. The analysis of the synergistic performance of the catalytic materials is detailed in **Chapter 3**[39].

$$\frac{1}{i_{LC}} = \frac{1}{i_k} + \left[\frac{1}{0.62\,nFAD^{2/3}v^{-1/6}}\right]\omega^{-1/2} \qquad 2.13$$

$$i_k = nFAkC_0 \qquad 2.14$$

Where i_{LC} is the limiting current (normally expressed in mA), n is the number of transferred electrons for a defined reaction, F is the Faraday constant (96485.33 C mol^{-1}), D is the NO_3^- diffusion coefficient (2×10^{-5} cm^2 s^{-1}), v is the kinematic viscosity (0.0088 cm^2 s^{-1})[40], i_k **is defined as the kinetic current**, C_0

is the initial concentration of electrolyte, and **k is the electrochemical rate constant or intrinsic charge transfer coefficient**.

2.7   Experimental electrochemical NO_x^-RR set-up.

The cell design and configuration for NO_x^-RR-to-NH_3 play a role in the electroreduction performance, particularly when the final objective aligns with industrial applications of the process. The major influenced parameters of cell designing correspond to the maximum contact between the reactants and the active sites in the catalyst, which aims to address the mass transport limitations and reduce the cell resistance and the kinetic of the catalytic process. Align with these, the type of ion exchange membrane, electrolytes, and reactant feeding modes would be as well influential. For NOx^-RR in general terms, the most employed electrochemical cells are the undivided three-electrode cell, the H-type cell and the flow cell. H-type cells typically serve for assessing novel materials and fundamental studies, whereas flow cells are employed to derive scaling-up parameters, particularly with materials in advanced stages of development or for well-established processes.

2.7.1   Undivided three electrode cell.

The preliminary studies in this project on NO_3^-RR were conducted using a glass three-electrode undivided cell with a volume of 50 mL electrolyte. This cell was utilized for experiments requiring a high degree of control over the environment and conditions, such as electrodeposition for preparing electrodes, as well as the initial evaluation of reduction and oxidation potentials in NO_3^- with different materials and electrolyte conditions. Additionally, experiments with the Rotating Disk Electrode (RDE) were carried out in another undivided glass cell capable of accommodating a larger volume of electrolyte. Both glass cells are constructed from borosilicate and enable bubbling of inert gases for the removal of other dissolved reactive gases. These cells provided the necessary experimental platforms for investigating various aspects of the NO_3^-RR process under controlled conditions. **Figure 2.15** shows the electrochemical cell where electrodeposition processes of Cu_2O nanoparticles were carried out for studies in **Chapter 3**.
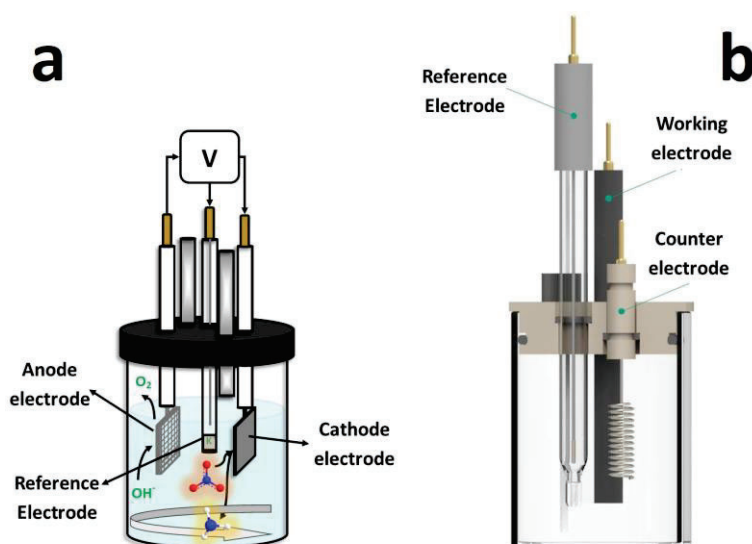
Figure 2.15 a) Three electrode undivided electrochemical cell (b) Redox-me electrochemical cell used in electrodeposition processes and basic electrochemical measurements in Chapter 3.

2.7.2   H-Type cell

H-type cells are commonly utilized for investigating various types of reactions, including CO_2RR, alcohol oxidations, and notably NO_x^-RR, among others (**Figure 2.16 a**). These cells comprise two compartments separated by an ion exchange membrane. Each compartment houses an electrode immersed in an electrolyte solution. Electrochemical reactions take place at the electrode surfaces, with ions capable of traversing between compartments via the membrane. The design of H-type cells facilitates selective product generation, rendering them suitable for exploring reactions involving gases like hydrogen and those resulting from NO_3^- electrochemical reductions (such as N_2 and nitrogen oxides). The configuration of compartments and membranes affords precise control over reaction conditions, encompassing pH, temperature, and reactant concentrations. However, certain drawbacks are associated with this cell type. These include mass transport limitations of electrochemically active species to the electrode surfaces, as well as the accumulation of products hindering the global reaction toward equilibrium, according to Le Chatelier's principle. Additionally, limitations may arise from the poor transport of ions across the membrane, potentially leading to excessively high cell potentials and diminishing overall energetic efficiency.
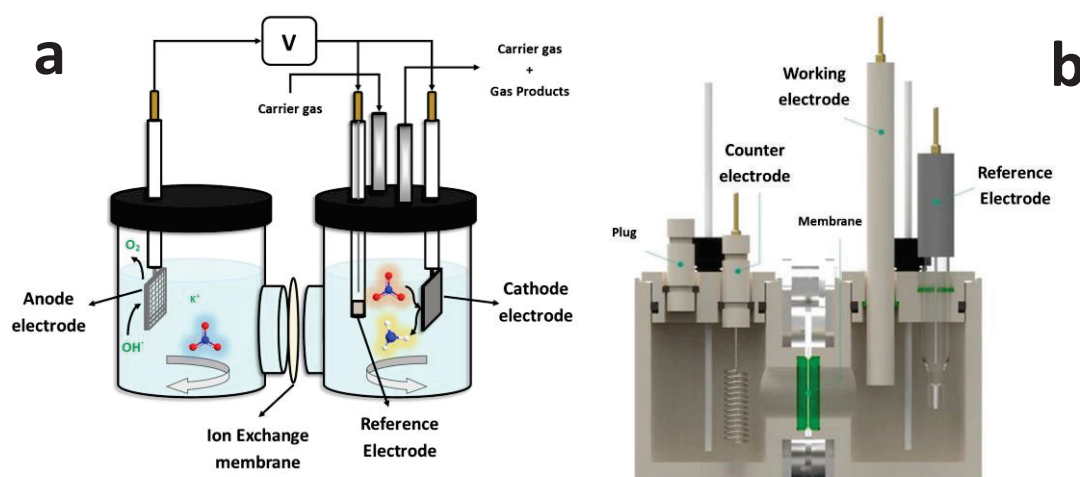
Figure 2.16 (a) H-type electrochemical cell (b) Redox-me electrochemical h-type cell used in Chapter 3.

The first studies developed in **Chapter 3** were performed using an H-Type cell (**Figure 2.16 b**) Redox-me (EC H-CELL 2X15 ML- SCREW MOUNT ELECTROCHEMICAL H-CELL) with a nominal exposure area of the ion exchange membrane of 1cm^2 and 15 milliliters for the electrolyte compartments. For NO$_3^-$RR the cathode corresponds to the working electrode (WE) and it is situated in the catholyte compartment along with the reference electrode (RE; Ag/AgCl$_{3.5M\ KCl}$). The anode compartment contains the counter electrode (CE) constituted by a Platinum mesh (Pt) where the oxidation of water is carried out as counter-reaction. The presence of a membrane in between the two compartments prevents products from transferring to the opposing catalyst and thereby performing the reverse redox reaction, effectively consuming the formed product and reducing the efficiency of the process. In the cathode compartment, the reacting NO$_3^-$, NO$_2^-$ and intermediates react in the cathode surface during electrolysis and NH$_3$ is accumulated as the final product during electrolysis. The cathode compartment should be airtight to prevent gas products to scape, thus affecting the calculations of FE. The gas products, specifically H$_2$ produced during NO$_3^-$RR are removed from the headspace and delivered to the gas chromatography system described in **Section 2.3.2** for detection and quantification. Additionally, the liquid products accumulated in the electrolyte are detected and quantified with the described ion chromatography and colorimetry methods. In the H-type cell, the current density (*j*) was mostly restricted by the mass transport limitations, inherent to the design cell, especially under large overpotentials where the reaction kinetics become relatively fast, and ions cannot reach the active sites faster enough to feed the reaction. Some of these limitations were addressed in **Chapter 4** by using a flow cell for all electrolysis measurements.

2.7.3 Flow cell.

To overcome the mentioned issues presented by H-type cell systems, a flow cell was used in the electrolysis processes for NO_3^--to-NH_3 conversion. Knowledge obtained from H-type cells can be used as a starting point for transferring studies to flow cell experiments looking at parameters that can be enhanced by the changed environment proportioned for the last one. The flow cell consists of compartmentalized sections separated by ion exchange membranes, with electrodes situated at the lowest possible distance. The continuous flow of electrolyte solution containing NO_3^- ions enables to reduce mass transport limitations and ensures better results in terms of productivity. Advantages include continuous operation, controlled environments, and high-throughput screening capabilities, while challenges include complexity, maintenance requirements, and cost. The filter-press flow cell consists of an assembly of gaskets that are pressed together, forming two or three flow channels: one or two for the catholyte and one for the anolyte. A CEM separates the anode and cathode chambers allowing the interchange of ionic charges to keep the potential difference between electrodes. The electrolytes are transported to the containers and recirculated to the cell with the assistance of a peristaltic pump.
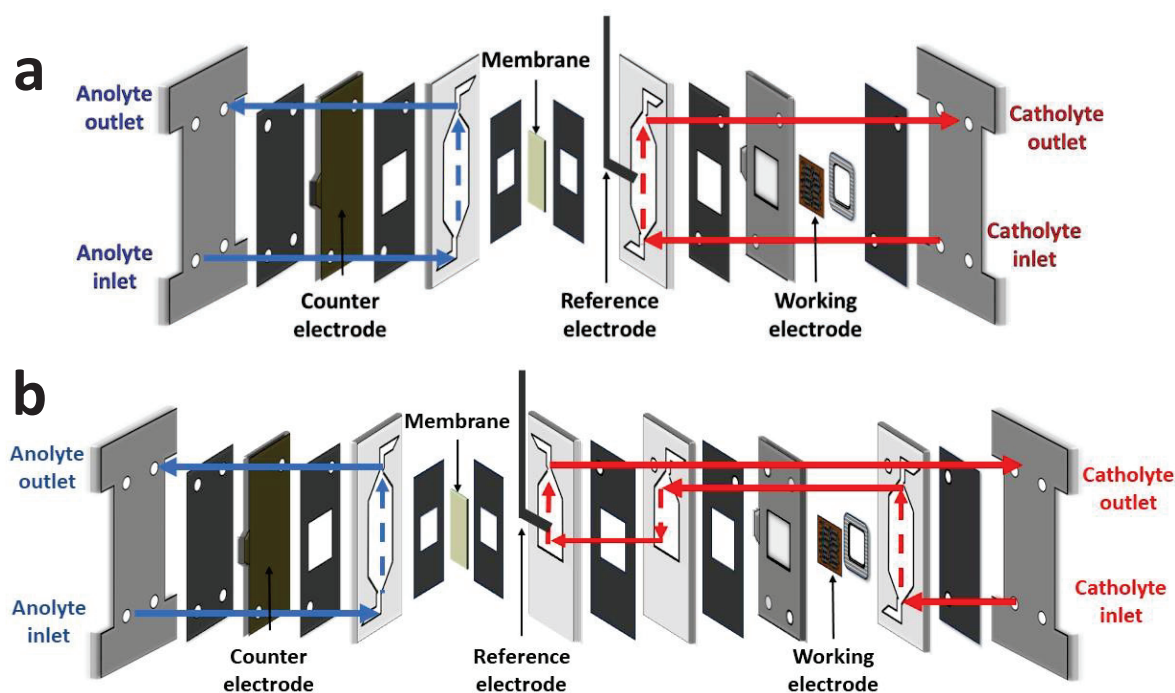
Figure 2.17 (a) Two channels electrolyte flow cell (b) Three channels electrolyte flow cell.

The electrochemical flow cell utilized in the electrolysis process is an ELECTROCELL adapted to accommodate two or three flow channels for the electrolyte. The cell has two separated compartments: one for the WE and RE, and another for the CE, as illustrated in **Figure 2.17 a**, and comprises two end plates constructed with **POM** and **INOX**. Two current collectors facilitate the placement of the working and counter electrodes, enabling connection to the potentiostat. Additionally, the flow cell incorporates multiple gaskets and flow conductors. These current collectors facilitate the installation of electrodes (e.g. planar or porous electrodes) for the electrolysis processes outlined in **Chapters 4** and **5**. Like the H-type cell, a CEM is deployed to provide separation between the compartments.

Cell type	Advantages	Disadvantages
H-Type	- Easy operativity - Low electrolyte volume required. - Used for first stages of materials evaluation.	- Relative low maximum current densities. - Fixed ion exchange membrane area. - Mass transport issues
Flow Cell	- Higher current densities. - Reduced mass transport limitations. - Lower ohmic losses. - Higher energy efficiency. - Easier interchange of charges across the membrane.	Complexity in number of components

Table 2.1 Comparison of electrochemical systems.

Several variables necessitate consideration during flow cell operation due to their impact on process efficiency: (1) The electrolyte flow rate, which determines the operational regime and is regulated using a peristaltic pump. (2) The electrode area, defined by the type of current collector. (3) The distance between the WE and counter electrode CE, alongside other parameters influencing the final measured cell potentials. Low flow rates may manifest as current and mass transport limitations. Contrarily, excessively high flow rates can induce turbulent regimes, impeding proper interaction between reactants and active sites. A notable advantage of employing the flow cell lies in its ability to achieve increased productivity compared to H-type cell systems, attributed to higher current densities at lower operation voltages towards the desired product. However, this design also presents certain disadvantages. For instance, there is a heightened risk of leaks occurring through layers of gaskets. Additionally, mechanical instabilities may arise in nanoparticles deposited on an active substrate. Furthermore, the requirement for external pumps for electrolyte recirculation can be comparable to

the requirements of agitation in H-type cells, both impacting the energy efficiency of the processes. **Table 2.1** provides a comparative overview of the two electrochemical setups utilized in this dissertation.

2.7.4   Ion exchange membranes

The ion exchange membranes have the function of separating the electrolytes in the cathode and anode compartments, facilitating the selective transport of ions across the membrane while blocking the passage of other ions. The specific function depends on the type of ion transport that is required by the process. There are three types of ion exchange membranes (1) the cation exchange membrane (CEM) is comprised of a polymer matrix containing fixed negatively charged functional groups, such as sulfonic acid (- SO_3H^-) or carboxylic acid (- COOH) groups, which facilitate the exchange of cations across the membrane. CEM also facilitates the transport of protons (H^+) from the anode to the cathode and ensures that only cations are transported, maintaining the electrochemical potential difference between the anode and cathode electrodes. (2) The anion exchange membranes (AEM) that are composed of a polymer matrix with fixed positively charged functional groups, such as quaternary ammonium (- NR_3^+) or quaternary phosphonium (PR_3^+) groups, which facilitate the selective transport of anions across the membrane. AEM facilitates the transport of hydroxide ions (OH^-) from the cathode to the anode compartments. The ion exclusion only allows the transport of anions ensuring the potential is maintained during the electrochemical process. (3) The third type corresponds to bipolar membranes (BPM) which are membranes that possess both cation and anion exchange functionalities within the same membrane structure. BPM are composed of one cation exchange one anion exchange layer and a non-conducting spacer layer between them to create a localized pH gradient when the electric potential is applied across the membrane. When the electrodes are polarized, water molecules are electrolyzed at the junction of the cation and anion exchange layers., resulting in the formation of H^+ and OH^- ions.

The most used membrane for NO_3^-RR processes is the CEM (**Figure 2.18**), such as the Nafion-117 in both H and Flow-cells under a variety of electrolyte conditions (pH and ions concentration). Nafion membranes are extensively applied in processes that requires proton exchange such as NO_3^-RR because of their excellent stability and easy availability. When the electrolyte employed is KOH, Nafion CEM are supposed to transfer K^+ ions via ion exchange mechanism, while reject OH^- because of exclusion effect between the negatively charged groups and OH^- anions. The utilization of Nafion CEM alongside high electrolyte concentrations under alkaline conditions facilitates the equilibration of OH^- concentrations between chambers and mitigates crossover of NO_3^- and NO_2^- ions during

electrochemical reduction. Following protonation and formation of ammonium ion (NH_4^+), NH_3 molecules possess the capability to traverse from the cathode chamber to the anode chamber. However, the concentrations of NH_3 measured as consequence of this crossover in the anolyte are 10 times lower than those measured in the catholyte where the reduction process takes place. Nafion 117 CEM was utilized in all chronoamperometry and chronopotentiometry processes presented in **Chapters 3**, **4** and **5**.
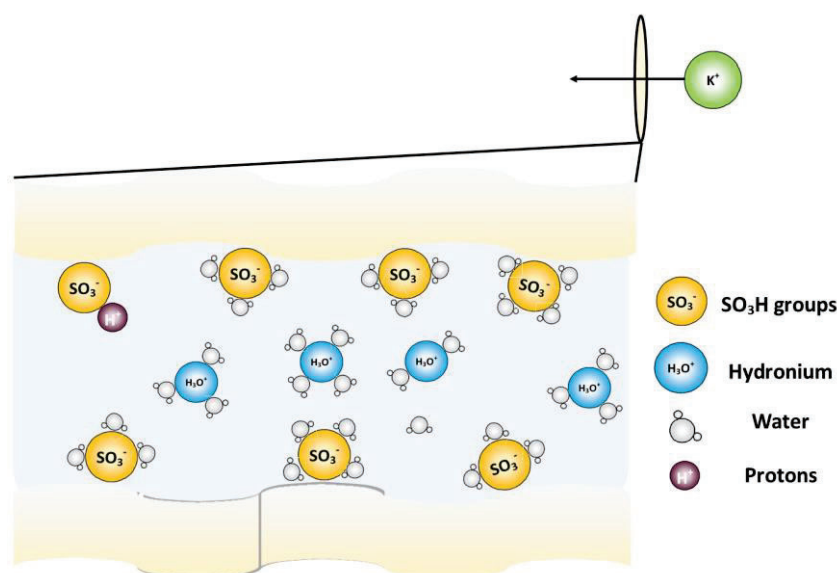
Figure 2.18 Transport of ions through an CEM.

2.7.5   Porous electrodes application.

Porous electrodes are conductive substrate with an extended surface, such as carbon paper, carbon cloth, or metallic porous material, onto which catalyst materials can be deposited in various structural configurations. The porous nature of these electrodes facilitates ion diffusion while offering a large surface area for electrochemical reactions to take place. When combined with the catalyst layer, they effectively enhance the target reaction. In **Chapter 5**, a carbon paper is utilized, featuring a porous carbon substrate serving as both the structural support and conductive medium for the electrode. This substrate is coated with NiO_2+SnO_2 nanoparticles catalyst, facilitating the investigation of cation effects during NO_3^-RR. The chemical stability of carbon paper substrates enables operation under harsh alkaline conditions and supports long-term experiments with minimal catalytic effects, particularly when assessing only the performance of the catalyst or effects of the electrolyte for the defined reaction.

2.8   Summary of equations.

Beer's law

$$A = \varepsilon \cdot 1 \cdot C = \log\left(\frac{I_0}{I}\right)$$

2.1

Nernst equation

$$E = E^0 + \frac{RT}{nF} \ln \frac{\{Ox\}}{\{Red\}}$$

2.2

Electrodeposition

$$m = \frac{Q \cdot M}{n \cdot F}$$

2.3

PEIS IR correction

$$U_{measured} = U_{actual} - I \cdot R$$

2.4

Faradaic Efficiency

$$FE_i(\%) = \frac{\alpha_i \cdot C_i \cdot F}{M \cdot Q} \cdot 100$$

2.5

H$_2$ Faradaic Efficiency

$$FE_i(\%) = \frac{j_{H_2}}{j_{Total}} \cdot 100$$

2.6

Cell energy efficiency

$$EE_{CELL} = \frac{EC_{NH_3}}{\int_0^t I(t) \cdot U(t) dt} \cdot 100$$

2.7

Theoretical Energy consumption

$$EC_{NH_3} = \left[\Delta G^0_{NH_3} + R \cdot T \cdot \text{Ln}\left(\frac{C_{NH_3\,t} \cdot C_{OH^-\,t}^{\,9}}{C_{NO_x^-\,t}}\right)\right] \cdot C_{NH_3\,t} \cdot V$$

2.8

Standard Cell Gibbs Free reaction energy

$$\Delta G^0_{NH_3} = -n \cdot F \cdot E^0_{CELL}$$

2.9

Half-cell Energy Efficiency

$$EE_{half-cell}(\%) = \frac{EC_{NH_3}}{(0.4 - U_w) \cdot \int_0^t I(t) dt} \cdot 100$$

2.10

Double Layer Capacitance

$$i = \boldsymbol{C_{DL}} \cdot v$$

2.11

Electrochemical Active surface Area

$$ECSA = \frac{C_{DL}}{C_S}$$

2.12

Koutecky-Levich analysis

$$\frac{1}{i_{LC}} = \frac{1}{\boldsymbol{i_k}} + \left[\frac{1}{0.62\,nFAD^{2/3}v^{-1/6}}\right]\omega^{-1/2}$$

2.13

Limiting current

$$i_k = nFAkC_0$$

2.14

2.9   Bibliography.

[1]   C. Scheu and W. D. Kaplan, *Introduction to Scanning Electron Microscopy*, in In-Situ Electron Microscopy, Wiley, 2012, pp. 1–37.

[2]   J. Cazaux, *Recent developments and new strategies in scanning electron microscopy*, J. Microsc., vol. 217, no. Pt 1, pp. 16–35, Jan. 2005, doi: 10.1111/j.0022-2720.2005.01414.x.

[3]   A. V. Girão, G. Caputo, and M. C. Ferro, *Application of Scanning Electron Microscopy–Energy Dispersive X-Ray Spectroscopy (SEM-EDS)*, Compr. Anal. Chem., vol. 75, pp. 153–168, 2017, doi: 10.1016/bs.coac.2016.10.002.

[4]   A. Ali, Y. W. Chiang, and R. M. Santos, *X-ray Diffraction Techniques for Mineral Characterization: A Review for Engineers of the Fundamentals, Applications, and Research Directions*, Minerals, vol. 12, no. 2, p. 205, Feb. 2022, doi: 10.3390/min12020205.

[5]   H. Khan, A. S. Yerramilli, A. D'Oliveira, T. L. Alford, D. C. Boffito, and G. S. Patience, *Experimental methods in chemical engineering: X-ray diffraction spectroscopy (XRD)*, Can. J. Chem. Eng., vol. 98, no. 6, pp. 1255–1266, Jun. 2020, doi: 10.1002/cjce.23747.

[6]   G. Greczynski and L. Hultman, *X-ray photoelectron spectroscopy: Towards reliable binding energy referencing*, Prog. Mater. Sci., vol. 107, no. July 2019, p. 100591, 2020, doi: 10.1016/j.pmatsci.2019.100591.

[7]   D. N. G. Krishna and J. Philip, *Review on surface-characterization applications of X-ray photoelectron spectroscopy (XPS): Recent developments and challenges*, Appl. Surf. Sci. Adv., vol. 12, no. November, p. 100332, 2022, doi: 10.1016/j.apsadv.2022.100332.

[8]   A. Orlando, F. Franceschini, C. Muscas, S. Pidkova, M. Bartoli, M. Rovere, and A. Tagliaferro, *A comprehensive review on Raman spectroscopy applications*, Chemosensors, vol. 9, no. 9, pp. 1–28, 2021, doi: 10.3390/chemosensors9090262.

[9]   J. J. Leani, J. I. Robledo, and H. J. Sánchez, *Energy dispersive inelastic X-ray scattering (EDIXS) spectroscopy – A review*, Spectrochim. Acta - Part B At. Spectrosc., vol. 154, no. October 2018, pp. 10–24, 2019, doi: 10.1016/j.sab.2019.02.003.

[10]   D. Walls and S. Loughran, *Methods in Molecular Biology: Protein Chromatography*, vol. 1485. 2017.

[11]   R. Michalski, *Ion chromatography applications in wastewater analysis*, Separations, vol. 5, no. 1, 2018, doi: 10.3390/separations5010016.

[12]   M. R. Ganjali, M. Rezapour, P. Norouzi, and F. Faridbod, *Principles and applications of ion chromatography in environmental analysis*, no. Lc. 2015.

[13]   Dionex, *IonPac AS22 Anion-Exchange Column Datasheet*, pp. 1–8, 2010, [Online]. Available: http://www.dionex-france.com/library/literature/data_sheets/DS_IonPac_AS22_LPN1816-01.pdf.

[14]   M. Picollo, M. Aceto, and T. Vitorino, *UV-Vis spectroscopy*, Phys. Sci. Rev., vol. 4, no. 4, pp. 1–14, 2019, doi: 10.1515/psr-2018-0008.

[15]   F. S. Rocha, A. J. Gomes, C. N. Lunardi, S. Kaliaguine, and G. S. Patience, *Experimental methods in chemical engineering: Ultraviolet visible spectroscopy—UV-Vis*, Can. J. Chem. Eng., vol. 96, no. 12, pp. 2512–2517, Dec. 2018, doi: 10.1002/cjce.23344.

[16]   Y. Zhao, R. Run, X. Bian, C. Zhou, Y. Zhao, S. Zhang, F. Wu, G. Waterhouse, L.Z. Wu, C.H. Tung, and T. Zhang, *Ammonia Detection Methods in Photocatalytic and Electrocatalytic Experiments: How to Improve the Reliability of NH$_3$ Production Rates?*, Adv. Sci., vol. 6, no. 8, Apr. 2019, doi: 10.1002/advs.201802109.

[17]   H. Jeong, J. Park, and H. Kim, *Determination of NH+ in environmental water with interfering substances using the modified nessler method*, J. Chem., vol. 2013, 2013, doi: 10.1155/2013/359217.

[18]   M. L. Munford, *Electrodeposition*, pp. 821–832, 2006, doi: 10.1081/E-ECHP-120037171.

[19]   N. Elgrishi, K. J. Rountree, B. D. McCarthy, E. S. Rountree, T. T. Eisenhart, and J. L. Dempsey, *A Practical Beginner's Guide to Cyclic Voltammetry*, J. Chem. Educ., vol. 95, no. 2, pp. 197–206, Feb. 2018, doi: 10.1021/acs.jchemed.7b00361.

[20]   I. Page, *Exploring Faraday's Law Using Inexpensive Screen-Printed Electrodes*, vol. 10009, no. Ii, pp. 1–5, 2019.

[21]   M. Aliofkhazraei, F.C Walsh, G. Zangari, H. Köçkar, M. Alper, C. Rizal, L. Magagnin, V. Protsenko, R. Arunachalam, A. Rezvanian, A. Moein, S. Assareh, and M. Allahyarzadeh, *Development of electrodeposited multilayer coatings: A review of fabrication, microstructure, properties and applications*, Appl. Surf. Sci. Adv., vol. 6, 2021, doi: 10.1016/j.apsadv.2021.100141.

[22]   Y.-H. Fang and Z.-P. Liu, *Tafel Kinetics of Electrocatalytic Reactions: From Experiment to First-Principles*, ACS Catal., vol. 4, no. 12, pp. 4364–4376, Dec. 2014, doi: 10.1021/cs501312v.

[23]   M. S. Chandrasekar and M. Pushpavanam, *Pulse and pulse reverse plating-Conceptual, advantages and applications*, Electrochim. Acta, vol. 53, no. 8, pp. 3313–3322, 2008, doi: 10.1016/j.electacta.2007.11.054.

[24]   P. Grosse, A. Yoon, C. Rettenmaier, S. W. Chee, and B. Roldan Cuenya, *Growth Dynamics and Processes Governing the Stability of Electrodeposited Size-Controlled Cubic Cu Catalysts*, J. Phys. Chem. C, vol. 124, no. 49, pp. 26908–26915, 2020, doi: 10.1021/acs.jpcc.0c09105.

[25]   G. W. Yang, *Laser ablation in liquids: Applications in the synthesis of nanocrystals*, Prog. Mater. Sci., vol. 52, no. 4, pp. 648–698, 2007, doi: 10.1016/j.pmatsci.2006.10.016.

[26]   L. K. Bieniasz, J. González, Á. Molina, and E. Laborda, *Theory of linear sweep/cyclic voltammetry for the electrochemical reaction mechanism involving a redox catalyst couple attached to a spherical electrode*, Electrochim. Acta, vol. 56, no. 1, pp. 543–552, 2010, doi: 10.1016/j.electacta.2010.09.014.

[27]   J. R. Macdonald and a J. Wiley, *Impedance Spectroscopy Theory, Experiment, and Applications*.

[28]   N. Meddings, M. Heinrich, F. Overney, J.S. Lee, V. Ruiz, E. Napolitano, S. Seitz, G. Hinds, R. Raccichini, M. Gaberšček, and J. Park*, Application of electrochemical impedance spectroscopy to commercial Li-ion cells: A review*, J. Power Sources, vol. 480, no. May, 2020, doi: 10.1016/j.jpowsour.2020.228742.

[29]   A. J. B. Larry and L. R. Faulkner, *ELECTROCHEMICAL METHODS*, in *BIOS Instant Notes in Analytical Chemistry*, Taylor & Francis, 2002, pp. 71–75.

[30]   S. Z. Andersen, M.J. Statt, V.J. Bukas, S.G. Shapel, J.B. Pedersen, K. Krempl, M. Saccoccio, D. Chakraborty, D. Kibsgaard, J. Kibsgaard, P. Vesborg, J. Nørskov, I. Chorkendorff, *Increasing stability, efficiency, and fundamental understanding of lithium-mediated electrochemical nitrogen reduction*, Energy Environ. Sci., vol. 13, no. 11, pp. 4291–4300, 2020, doi: 10.1039/D0EE02246B.

[31]   N. Lazouski, Z. J. Schiffer, K. Williams, and K. Manthiram, *Understanding Continuous Lithium-Mediated Electrochemical Nitrogen Reduction*, Joule, vol. 3, no. 4, pp. 1127–1139, 2019, doi: 10.1016/j.joule.2019.02.003.

[32]   J. Zhang, Y. Wang, Z. Li, S. Xia, R. Cai, L. Ma, T. Zhang, J. Ackley, S. Yang, Y. Wu, and J. Wu, *Grain Boundary-Derived Cu^+/Cu^0 Interfaces in CuO Nanosheets for Low Overpotential Carbon Dioxide Electroreduction to Ethylene*, Adv. Sci., vol. 9, no. 21, pp. 1–11, Jul. 2022, doi: 10.1002/advs.202200454.

[33]   R. M. Choueiri, S. W. Tatarchuk, A. Klinkova, and L. D. Chen, *Mechanism of ammonia oxidation to dinitrogen, nitrite, and nitrate on β-Ni(OH)$_2$ from first-principles simulations,*" Electrochem. Sci. Adv., vol. 2, no. 6, pp. 1–10, 2022, doi: 10.1002/elsa.202100142.

[34]   P. Sharma and T. S. Bhatti, *A review on electrochemical double-layer capacitors*, Energy Convers. Manag., vol. 51, no. 12, pp. 2901–2912, 2010, doi: 10.1016/j.enconman.2010.06.031.

[35]   M. Lukaszewski, M. Soszko, and A. Czerwiński, *Electrochemical methods of real surface area determination of noble metal electrodes - an overview*, Int. J. Electrochem. Sci., vol. 11, no. 6, pp. 4442–4469, 2016, doi: 10.20964/2016.06.71.

[36]   D. M. Morales and M. Risch, *Seven steps to reliable cyclic voltammetry measurements for the determination of double layer capacitance*, JPhys Energy, vol. 3, no. 3, 2021, doi: 10.1088/2515-7655/abee33.

[37]   R. Guidelli, R.G. Compton, J.M. Feliu, E. Gileadi, J. Lipkowski, W. Schmickler, and S. Trasatti, *Defining the transfer coefficient in electrochemistry: An assessment (IUPAC Technical Report)*, Pure Appl. Chem., vol. 86, no. 2, pp. 245–258, 2014, doi: 10.1515/pac-2014-5026.

[38]   S. Xu, Y. Kim, D. Higgins, M. Yusuf, T. F. Jaramillo, and F. B. Prinz, *Building upon the Koutecky-Levich Equation for Evaluation of Next-Generation Oxygen Reduction Reaction Catalysts*, Electrochim. Acta, vol. 255, pp. 99–108, 2017, doi: 10.1016/j.electacta.2017.09.145.

[39]   J. Masa, C. Batchelor-McAuley, W. Schuhmann, and R. G. Compton, *Koutecky-Levich analysis applied to nanoparticle modified rotating disk electrodes: Electrocatalysis or misinterpretation*, Nano Res., vol. 7, no. 1, pp. 71–78, 2014, doi: 10.1007/s12274-013-0372-0.

[40]   D. Reyter, D. Bélanger, and L. Roué, *Study of the electroreduction of nitrate on copper in alkaline solution*, Electrochim. Acta, vol. 53, no. 20, pp. 5977–5984, 2008, doi: 10.1016/j.electacta.2008.03.048.

Chapter 3

Cu and Ti-based materials with synergistic effects in NO$_3^-$RR to NH$_3$
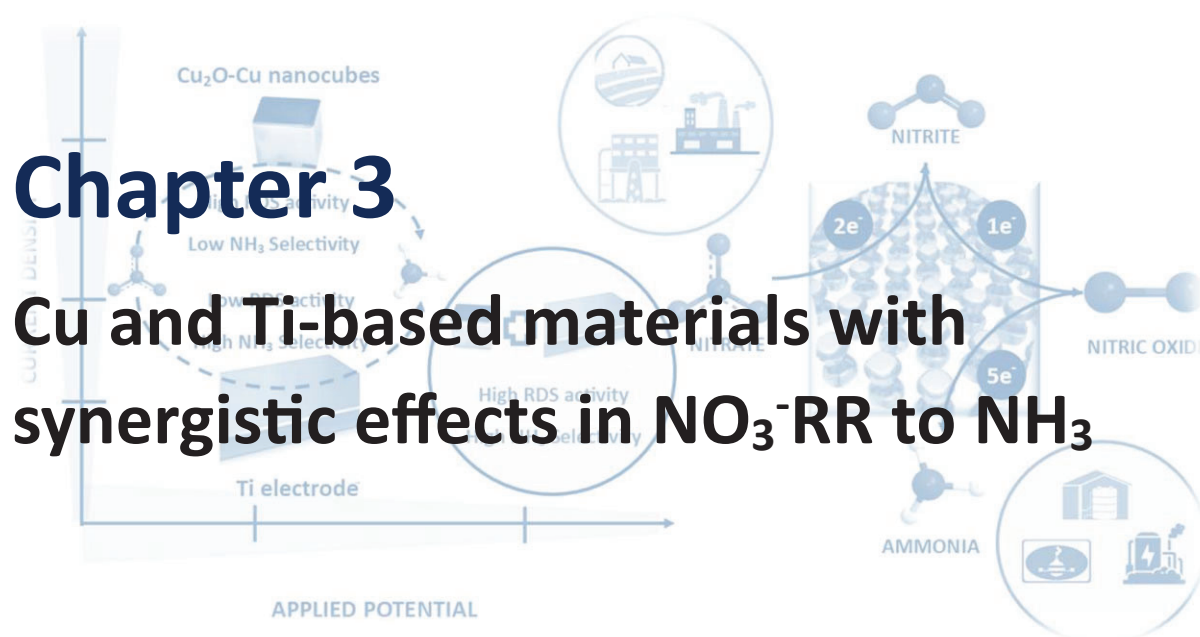
CHAPTER 3 Cu AND Ti-BASED MATERIALS WITH SYNERGISTIC EFFECTS IN NO_3^-RR TO NH_3

3.1 Abstract

This chapter investigates the synergistic effects of titanium (Ti) and copper (Cu) composite electrodes for the NO_3^-RR to NH_3. By integrating Cu_2O-Cu nanocubes on a Ti substrate, the study aims to leverage the high catalytic activity of Cu and the excellent faradaic efficiency of Ti. Optimal electrochemical conditions, such as pH and NO_3^- concentration, were identified to maximize NH_3 generation. The composite electrode demonstrated enhanced performance, combining the strengths of both materials, resulting in improved kinetic behavior and stability over multiple cycles. These findings highlight the potential of using composite materials with differing intrinsic properties to significantly enhance NO_3^- reduction efficiency and productivity.

3.2   Introduction to Chapter 3.

NO_3^-RR has been studied using several noble metals such as silver, gold, palladium, and ruthenium[1], [2]. However, the prohibitive costs of these materials make them less competitive for applications further than fundamental studies at the laboratory scale[3]. Other pure and combined transition metals have been also studied, among which copper (Cu) and Iron (Fe) at different oxidation states [4]–[7] stand out as highly active materials for nitrate electroreduction by modification of shape, crystallographic orientation, and oxidation state, being either use as single catalyst or in composite electrodes. Fu et al. have synthesized Cu nanosheets to maximize the efficiency of NO_3^-RR towards NH_3, reaching a faradaic efficiency to ammonia (FE_{NH3}) of 99.7% and studied the effects of changing catalyst shape in FE_{NH3}[8]. Oxidized forms of Cu have demonstrated to enhance activity for NiRR. Fu et al have studied how the interface Cu_2O-Cu alleviates the adsorption energy of NO_2^- and improves its diffusion[9]. Chen et al. have incorporated Cu nanoparticles onto an organic semiconductor busting the NiRR towards NH_3 reaction by regulating the proton/electrons flow to Cu centers[10]. Shih et al. have reported the effects on selectivity towards different nitrogen-based products of crystalline morphology of Cu nanoparticles on composite electrodes[11]. In fact, Cu selectivity is not limited to ammonia generation. Several studies have been carried out with Cu-based materials, demonstrating its potential for water denitrification (NO_3^- to N_2) and achieving N_2 selectivity values close to 100% [12]–[14] due its high ability of promoting the rate determinant step (RDS) NO_3^- to NO2- of the overall NO_3^-RR. This intrinsic property of Cu make it an excellent primary catalyst if it is combined with other materials that can conduct NiRR towards ammonia generation after surpassing the RDS.

Ti-based electrodes have also recently attracted attention of researchers due their high efficiency and stability under extreme electrochemical conditions. McEnaney et al. have reached a 90% FE_{NH3} and 80% of selectivity (SE_{NH3}) with a pure Ti electrode applying electrolyte engineering[15]. Meantime, oxidized forms of Ti have also shown catalytic properties. Jia et al. busted selectivity towards NH_3 by using TiO_2 nanotubes with rich oxygen vacancies[16]. Consequently, the high selectivity of Ti electrodes for NiRR towards NH_3 makes them suitable active support for other more active materials. In this case, fulfilling the role of a secondary electrocatalyst increasing selectivity toward desired products, while maintaining the catalytic properties of the primary catalyst.

In the present Chapter we aim to study the role of Ti and Cu (primary components of electrodes) in NO_3^-RR towards NH_3 and establish the optimal electrochemical conditions for maximizing its generation. Under those circumstances, electrochemical activity (NO_3^- reduction rate) and kinetic rate constants were evaluated in first place for the Ti electrode (Ti as the primary catalyst). In the second place, for the Cu (I) oxide-copper titanium-modified electrode (Cu_2O-Cu@Ti), studying the synergistic

effects on efficiency parameters of having Ti as active support for more active materials such as Cu_2O-Cu.

3.3 Copper-based materials as active catalysts for NO_3^-RR to NH_3.

Cu has been widely studied in the field given its high active performance for NO_3^-RR, mostly due to its ability to undergo structural transformations that create polycrystalline surfaces, enhancing mass transfer and thus the overall catalytic activity of the material. The morphology and structure of Cu-based catalysts can expose different crystal planes. Gao et al.[17] used DFT calculations to show that both Cu (1 0 0) and Cu (1 1 1) crystal planes are thermodynamically favorable. Similarly, Hu et al.[18] confirmed with DFT that Cu (1 0 0) and Cu (1 1 1) planes exhibit superior catalytic activity compared to Cu (1 1 0). Notably, Cu (1 1 1) is particularly effective at converting NO_3^- to NH_3 in neutral or alkaline electrolytes, while Cu (1 0 0) excels in strongly acidic electrolytes. Copper's effective interaction with reaction intermediates and its synergistic effects when combined with other materials make it an excellent catalyst for driving reactions toward desired products. This section examines the factors contributing to Cu-based catalysts' efficiency, selectivity, and stability, providing context for the results obtained for electrodes used in **Chapters 4** and **5**.

3.3.1 Adsorption and activation of NO_3^-

Commonly to most electrochemical reactions, the initial step in the NO_3^- reduction involves the adsorption of the ions onto the surface of the Cu active sites. According to several DFT calculations, this adsorption, which has been found especially on specific facets like Cu (1 1 1) and neutral/alkaline conditions, is thermodynamically favorable. Therefore, the interaction between the NO_3^- and Cu active centers involves the formation of a $Cu - O$ bond, stabilizing the intermediates and facilitating further reductions[19], [20]. Gibbs Free Energy (ΔG) diagrams illustrate the potential energy landscape of the NO_3^-RR on Cu **Figure 3.1.** They show the energy changes associated with each reaction step, highlighting the most thermodynamically favorable pathways. For Cu, the key steps with relatively low energy barriers include the reduction of NO_3^- to NO_2^- and the subsequent hydrogenation steps leading to NH_3 formation. The diagrams also indicate that Cu surfaces have lower energy barriers for *NH_2 hydrogenation, a critical step for NH_3 production. The electronic structure of Cu, particularly the position of the d-band center, plays a role in its catalytic activity. Shifting the d-band center closer to the Fermi level enhances the adsorption strength of intermediates like *NO and *NH_2, optimizing the reaction kinetics according to the study presented by Wang et al.[20], [21]

Understanding several studies, the high activity of Cu-based materials for NO_x^- reduction to NH_3 results from its optimal electronic structure, favorable adsorption properties, and the ability to form various reactive intermediates efficiently. These properties can be further enhanced by nano-structuring, alloying, and creating composite materials which synergistically enhances the already favorable aptitude of Cu-based for NO_3^-RR.
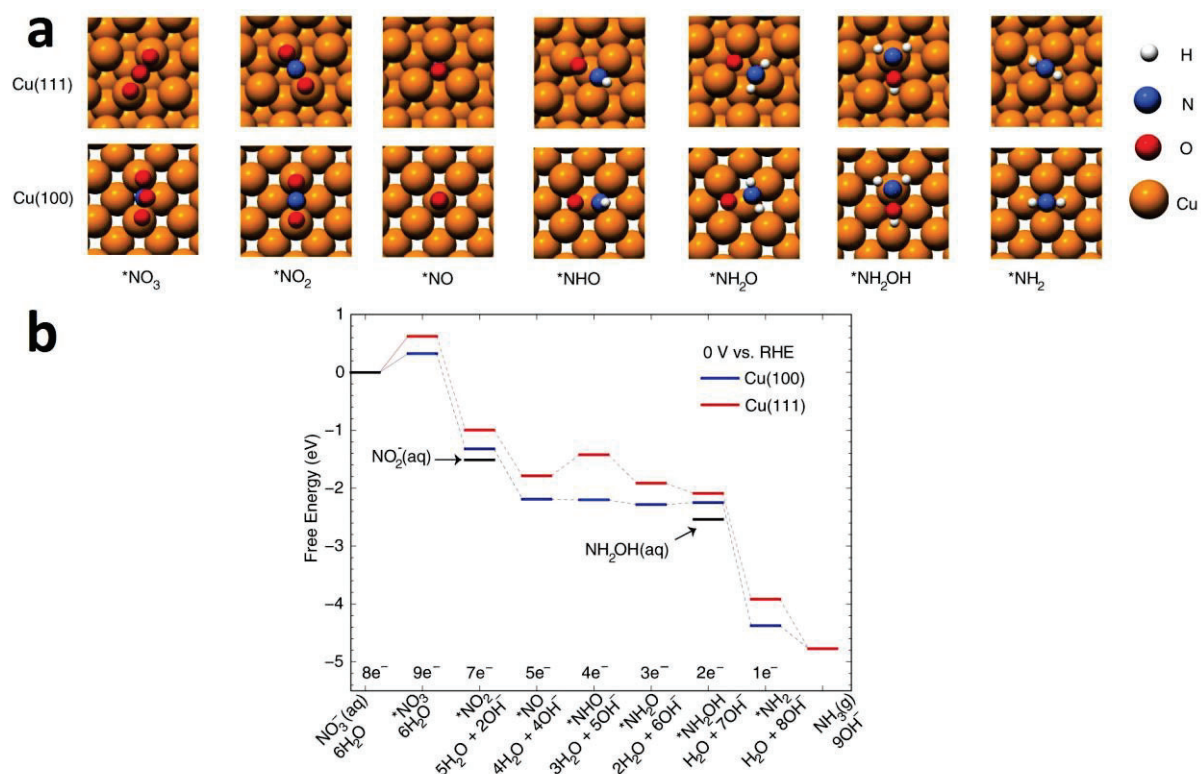
Figure 3.1 a) Adsorption configurations of reaction intermediates (Cu: orange-red, N: blue, O: red, H: gray). b Free energy profiles of NH₃ formation from NO₃⁻ reduction on Cu (1 0 0) and Cu (1 1 1) at 0 V vs. RHE from grand-canonical DFT calculations. Reproduced from "Breaking adsorption-energy scaling limitations of electrocatalytic nitrate reduction on intermetallic CuPd nanocubes by machine-learned insights"[17].

3.4   Titanium-based materials as active catalyst/support for NO₃⁻RR to NH₃.

To understand how Ti-based materials can act as the principal catalyst or as an active support for other more active materials, we explore some fundamental aspects at the molecular level that explain their activity for NO_3^-RR in this section. Ti-based materials offer several advantages, including corrosion resistance, stability across various pH conditions, and relatively poor activity for HER, making them suitable for various reactions[15]. It is important to stablish that in the electrochemical studies conducted in **this chapter**, a Ti foil was used as an active support. However, XPS measurements, discussed in **Section 3.7.4**, revealed the presence of a thin layer of TiO_2 on the Ti substrate, part of the native oxides remaining on the surface after chemical pre-treatment. This layer is the actual surface in contact with the electrolyte, and for instance the one showing catalytic activity during NO_3^- reduction.

Therefore, the activity of TiO$_2$-based catalysts is explored here, with Ti-based materials referring specifically to this oxide.

3.4.1   Adsorption and activation of NO$_3^-$ and structural defects of TiO$_2$.

Several studies revealed that the NO$_3^-$RR mechanism on TiO$_2$ proceeds in a similar way to that for Cu-based catalysts, however, differences in its active sites can modify the catalytic activity in terms of efficiency and selectivity toward desired intermediates and products. Furthermore, structural defects introduced to the TiO$_2$ structure change the catalytic activity and location of the active sites within the catalyst. Defects including Oxygen Vacancies (OV) and Titanium Vacancies (TiV) that enhance adsorption and kinetic properties during NO$_3^-$RR to NH$_3$.

The OVs in TiO$_2$ disrupt the regular lattice structure of the catalyst, creating localized states that facilitate stronger binding of NO$_3^-$ molecules to the catalyst surface. According to Ranran Jia et al., the Ovs introduce local states within the band gap of TiO$_2$, which can act as electron donors, a property that enhances the electron transfer necessary for the activation of NO$_3^-$. This presence of OVs lowers the activation energy for breaking the N – O bonds, making the reduction process more efficient. In addition, another property attributed to the presence of OV corresponds to the suppression of side reactions such as HER, enhancing the whole efficiency of the process[16], [22].

In the case of the TiVs, like OVs, introduce defects that alter the electronic structure of TiO$_2$ that reduce the band gap of the structure that enhances among others the photocatalytic properties by allowing a better adsorption of visible light and improved electron-hole separation. According to the study presented by Xi Zhang et al.[22], the presence of TiVs can also create unsaturated coordination sites, which can act as active sites for NO$_3^-$ adsorption, enhancing the overall activity of TiO$_2$ by providing additional pathways for electron transfer and reaction intermediate stabilization.

3.5   Methods.

Experimental methods were outlined in Chapter 2. However, here we briefly highlight the most important information related to this chapter.

3.5.1   Electrode preparation:

Cu Foil. Purchased from Alfa Aesar (0.5 mm tick, 99.99% metal basis) is defined here as an electrode and active support. Before the electrolysis process, the foil underwent a pre-treatment process aimed at eliminating native oxides present on the surface. For that, initially, the Cu foil was subjected to a 15-minute sonication process in a solution comprising acetone, isopropyl alcohol, and ethanol in a ratio

of 1:1:1. This step effectively removed both organic and inorganic oils from the surface. Subsequently, the material underwent a second treatment involving immersion in an acidic solution (10% H_2SO4 + 36 g L^{-1} $C_6H_8O_7$) while being sonicated for 5 minutes. Finally, the material was thoroughly rinsed with Milli-Q water for 10 minutes.

Ti Foil. Purchased from Alfa Aersar Titanium foil, 0.127mm (0.005in) thick, annealed, 99% - metals basis. The electrode preparation consisted of the chemical removal of impurities present on the Ti surface. First, the Ti foil was sonicated for 15 min in a solution of acetone, isopropyl alcohol, and ethanol in a proportion (1:1:1) for the removal of organic and inorganic oils. Then, it was submerged in the acidic solution under sonication for 5 min; and finally rinsed in milli-Q water for 10 min.

Gr Foil. Purchased from Alfa Aesar (Graphite foil, 0.5mm thick, 99.8% metal basis). The electrode preparation consisted of removal of impurities with milli-Q water and sonication for 15 minutes.

Cu_2O-Cu@Ti electrode. Cu_2O-Cu nanoparticles were plated by PED on a 1x1.5 cm² Ti foil treated as previously described. This technique has been reported to allow for the direct growth of shape controlled Cu_2O-Cu nanocubes[23]. During the alternating potential conditions, Cu nuclei form with further material deposition, while non-cubic particles are preferentially dissolved during the anodic cycles. A CV measurement was performed with an electrolyte containing 5 mM $CuCl_2$ and 5 mM KCl (pH 5) to determine the optimal parameters for Cu electrodeposition and its partial oxidation to Cu_2O onto Ti substrate using a three-electrode undivided cell (Figure 3.1a). Figure 3.1b shows the CV curve performed at a scan rate of 10 mV·s⁻¹. The peaks situated at -0.26 V and 0.24 V vs. RHE are associated with the reduction of Cu^{2+} to Cu^{1+} and the reduction of Cu^{1+} to Cu^0, respectively[24].

Figure 3.2 Schematic representation of the electrode Cu_2O-Cu@Ti synthesized by electrodeposition from a Cu precursor solution.

From the CVs the applied potentials for PED were **$E_{W,C}$= -0.25V** vs RHE, during a duty time of 0.625 s, and **$E_{W,A}$ = 0.3V vs RHE**, during 7.5s for a defined number of cycles (N = 30) (**Figure 3.3c**). The optimum pH value for the PED and Cu nanoparticles stability was fixed in a range of 5.5-6, before the formation of copper hydroxide Cu(OH)$_2$ in the electrolyte[25]. **Figure 3.3d** shows the waveform of the chronoamperometry, and the currents reached during the PED, with a cathodic current peak of -5.5 mA where the Cu nanoparticles were expected to be deposited on the Ti support, and a later anodic peak current of 0.1 mA where the nanoparticles are expected to partially oxidize to Cu$_2$O onto the Cu surface. After PED, the electrodes were rinsed with Milli-Q water (18.2 MΩ·cm^{-1}) to remove the rest of electrolyte.
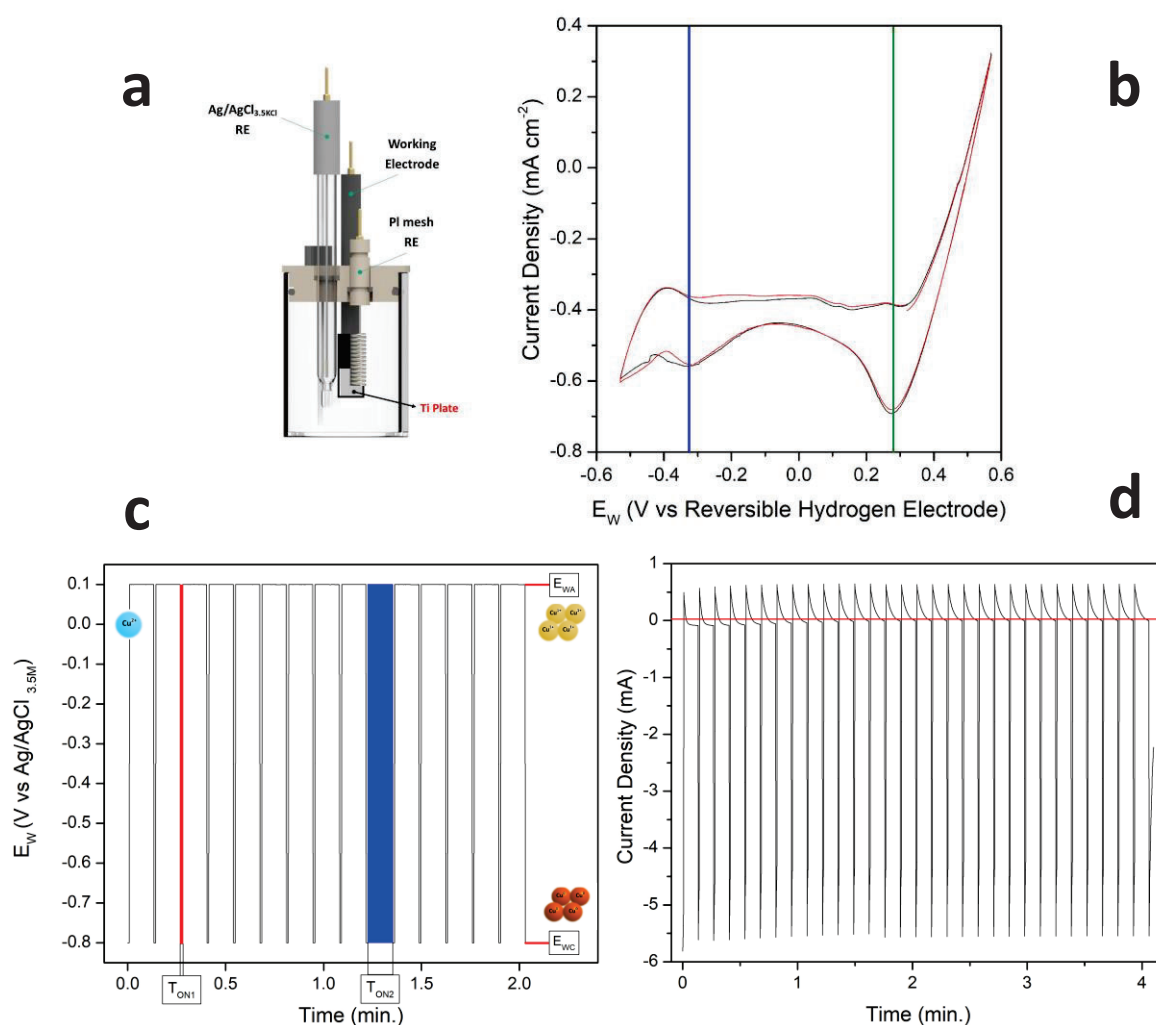
Figure 3.3 a) Electrochemical three electrode undivided cell b) CV of Ti substrate for CuCl$_2$ 5mM + KCl 5mM. c) PED CP scheme d) PED chronoamperometry Ti substrate for CuCl$_2$ 5mM + KCl 5mM.

The resulted Cu$_2$O-Cu nanoparticles acquired a cubic-like shape as shown in the SEM images of **Figure 3.4**. A further XPS ex-situ analysis of nanoparticles synthesized under controlled Ar atmosphere revealed a potential core-shell structure of the nanoparticles.
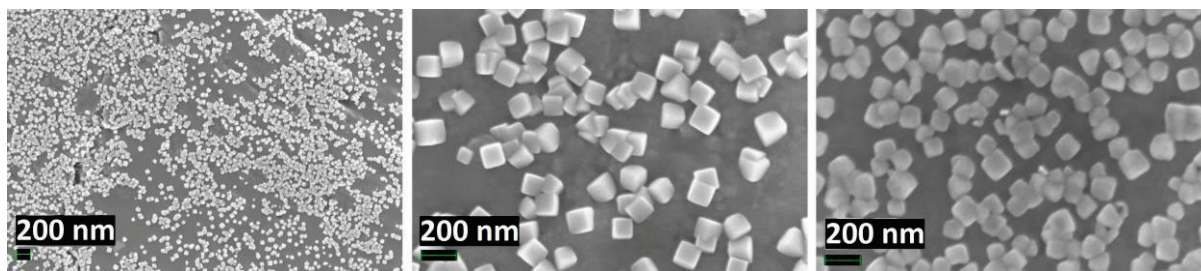
Figure 3.4 SEM images of Cu2O-Cu@Ti electrode

Cu$_2$O-Cu@Gr electrodes. These electrodes were prepared following the procedure described for Cu$_2$O-Cu @Ti electrodes, after an electrochemical evaluation of the required applied potentials.

3.5.2   Electrochemical measurements:

As mentioned in **Chapter 2** all electrochemical measurements were performed with a BioLogic electrochemical workstation. For the NO_3^-RR to NH_3 electrolysis experiments, a three-electrode ***H-cell*** was used. A Nafion-117 CEM divided the cathode and anode. A gas absorption liquid chamber was connected to the cathode compartment. A flow of Ar was passed through the cathode chamber (but not through the catholyte) dragging gaseous products and a solution of 5 mM H_2SO_4 was used to capture the NH_3 passed to the gas phase of the chamber. For the calculations, the total produced ammonia was the addition of the ammonia present in the electrolyte and that in the acidic trap. **Figure 3.5** shows the electrochemical setup for all measurements.

The prepared Cu$_2$O-Cu deposited on Ti and Gr Foils (1x1 cm^2 in all cases) were used as working electrodes, Ag/AgCl$_{3.5M\ KCl}$ as reference electrode, and a Pt mesh served as the counter electrode. All potentials in chronoamperometry tests in this study are reported in V vs Reversible Hydrogen Electrolyte (RHE) and the potential interconversion between electrodes is defined by $E_{RHE}= E_{Ag/AgCl\ 3.5M\ KCl}$ + 0.205V + 0.059·pH.

For NO_3^-RR studies, two electrolyte conditions were prepared with two extreme pH values. For acidic conditions, the electrolyte was 0.3M KNO_3 + 0.1M HNO_3 (final [NO_3^-] of 0.4M and pH 1). While for the alkaline conditions, a solution consisting of 0.1M KNO_3 and 1M KOH was prepared, with a final pH 14. The electrolyte for the electrochemical rate constant determination with the RDE consisted of 0.01M KNO_3 + 1M KOH. The double layer capacitances were determined for Ti and Cu$_2$O-Cu/Ti electrodes using a 0.1 M K_2SO_4 electrolyte. Before the experiments, Ar was bubbled through the electrolyte solution for 15 min to remove all the dissolved gasses.
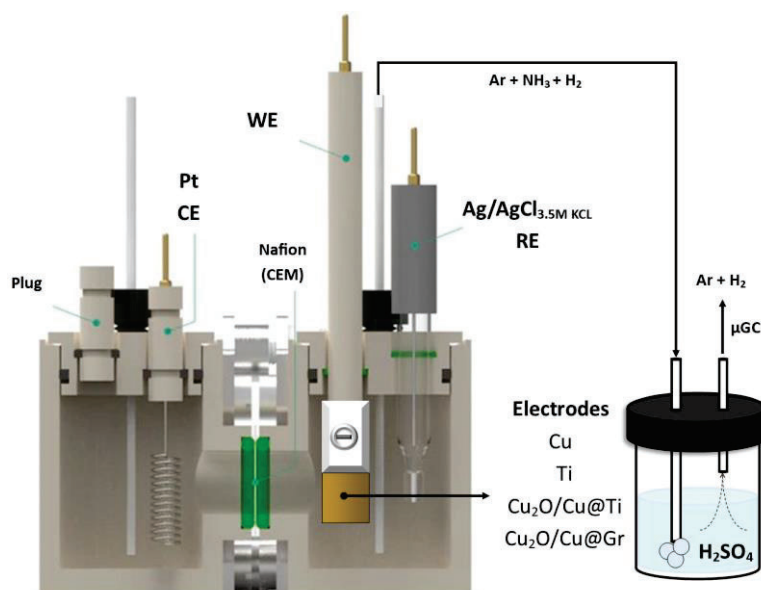
Figure 3.5 H-type cell electrochemical set up including the acidic trap.

Chronoamperometry tests were conducted with all previously cited electrodes. The acidic electrolyte conditions were applied only for pure Ti electrodes due the low stability of Cu-based nanoparticles under those conditions. *FE$_i$* towards NH$_3$, NO$_2^-$, and H$_2$, *SE$_i$* towards NH$_3$, and NO$_2^-$ and productivity (NH$_3$ Yield) were evaluated by electrolysis at -0.3, -0.4, -0.5, -0.6, -0.7 and -0.8 V vs RHE working potentials. These efficiency parameters were calculated as presented in **Chapter 2**.

$$FE_i(\%) = \frac{\alpha \cdot C_i \cdot F}{M \cdot Q} \cdot 100$$

$$NH_3\ Yield = \frac{C_{NH_3} \cdot V \cdot M}{A \cdot t}$$

$$SE_i(\%) = \frac{C_i}{C_{NO_3^-}{}_0 - C_{NO_3^-}} \cdot 100$$

C_i (M) is the obtained molar concentration of a target product; V (L) is the volume of electrolyte in the cathode chamber; M (g/mol) is the molar mass of the target product; A (cm^2) is the geometric surface area of the electrode; α is the number of transferred electrons for producing a target product; F is the Faraday constant, Q is the total charge transferred to the system; C_{NH3} (M) is the measured NH$_3$ concentration for the reaction; t (h) represents the duration of chronoamperometry tests; and $C_{NO_3^-{}_0}$ and $C_{NO_3^-}$ (M) represent the initial and final concentration of nitrates in the electrolyte

3.5.3   Electrochemical rate constant (k_i) determination:

RDE - LSV measures were performed at 0.5 V to -0.88 V vs RHE potential window for 0.01M KNO$_3$ + 1M KOH with a scan rate of 10 mV s^{-1} under the rotating rates 100, 300, 600, 1000, 1500, 2000 RPM. The kinetic currents of NO$_3^-$RR for the different electrode materials were determined by the Koutecky–Levich (K–L) analysis and the electrochemical rate constants by the equations[26].

$$\frac{1}{i_C} = \frac{1}{i_k} + \left[\frac{1}{0.62 \, nFAD^{2/3}v^{-1/6}C_0} \right] \omega^{-1/2} \qquad 3.1$$

$$i_k = nFAkC_0 \qquad 3.2$$

n is the number of transferred electrons for a defined reaction; D is the NO$_3^-$ diffusion coefficient (2×10^{-5} cm^2 s^{-1})[27]; v is the kinematic viscosity (0.0088 cm^2 s^{-1}); i_C is the current at a defined working potential E$_W$; i_k is defined as the kinetic current; C$_0$ is the initial concentration of electrolyte and, k is the electrochemical rate constant.

3.5.4   Analytical instrumentation and measurements:

From **Chapter 2**. A gas chromatography equipment (GC, Agilent technologies 490 Micro GC) was used for quantification of H$_2$, as major gas product. The concentration of NO$_3^-$ and NO$_2^-$ anions were measured by an Ion Chromatograph (Dionex 1100) equipped with a Dionex Ion Pac AS-22 anion exchange column and a chemical suppressor (ASR-ultra 4mm), using 4.5 mM Na$_2$CO$_3$ + 1.4 mM NaHCO$_3$ as eluent at 1.5 mL min^{-1}. The NH$_3$/NH$_4^+$ concentration was determined by visible spectroscopy (after complexing NH$_4^+$ ions by Nessler reagent)[28], [29] on a PerkinElmer Lambda-950 spectrometer.

3.6   Cu and Ti-based electrodes characterization.

Cu$_2$O-Cu@Ti electrodes correspond to the most important catalyst used for the study presented in **this chapter** and the characterization by SEM, EDX, XRD, XPS and Raman is presented in further sections, correlating the structure parameters with the catalytic activity observed during electrolysis of NO$_3^-$.

3.6.1   Cu$_2$O-Cu@Ti. SEM and EDX analysis.

The morphology of Cu$_2$O-Cu nanoparticles and the Ti support was studied using FE-SEM before and after electrolysis experiments. The images, presented in **Figure 3.6 a-e**, show that the irregular surface of the Ti support is homogeneously covered by Cu$_2$O-Cu nanocrystals after PED. At high magnification, a layer of cubic-like nanocrystals, ranging in size from 40-80 nm (edge-to-edge), is observed. When

these nanoparticles are subjected to NO$_3^-$RR to NH$_3$, extensive changes in the oxidation state and morphology can be seen, especially at high cathodic potentials. The initially well-defined nanocubes transform into more aggregated and particulate forms. This transformation becomes evident when comparing **Figures 3.6 e** and **f**, with the latter showing the nanoparticles after 90 minutes of electrolysis, an effect observed in similar studies[30]. Regarding the oxidation state changes of nanoparticles, Lichen Bai et al. [31] studied the activity of isolated Cu-based nanoparticles for NO$_3^-$RR, finding correlations between the morphology and crystalline phases of the nanoparticles and their selectivity toward different products.
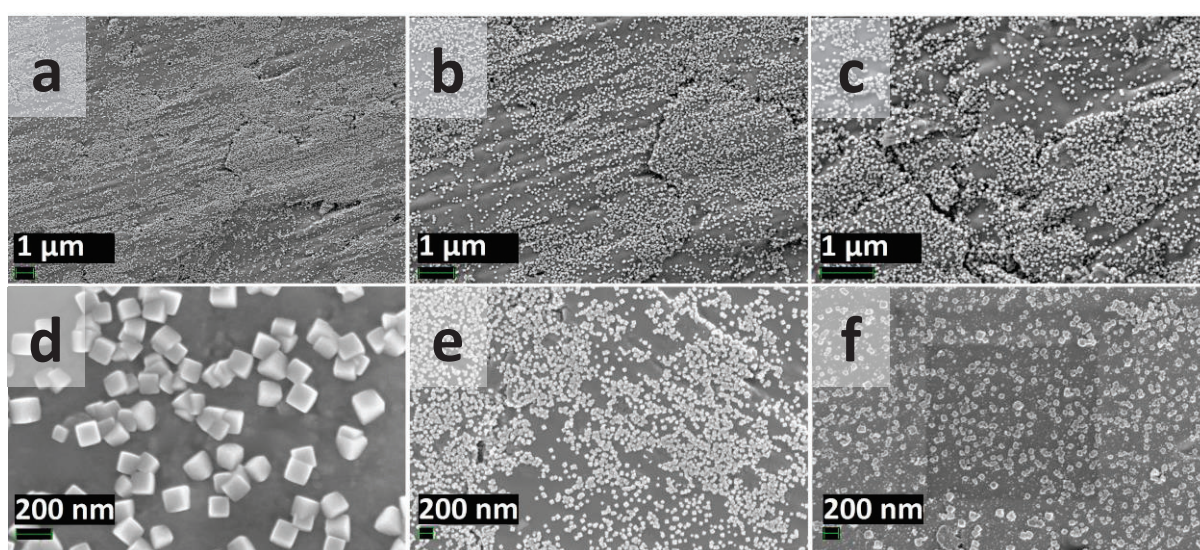
Figure 3.6 SEM images of Cu$_2$O/Cu@Ti electrode a-e) before electrolysis and f) after electrolysis.

By recording EDX spectrum **Figure 3.7**, the Cu$_2$O-Cu@Ti electrode was estimated to have an average atomic composition of 1.2% Cu, 86.5% Ti and 12.2% C, before electrolysis **(Figure 3.7a-b)**. The electrode composition shows that a low percentage of Cu-based nanoparticles on the Ti active support can highly impact in the catalytic activity of the electrode for NO$_3^-$RR. In the other hand, the EDX study performed to the electrode after electrolysis (**Figure 3.7 c-d**), showed a similar atomic composition of 1.25% Cu, 87.3% Ti and 11.3% C.
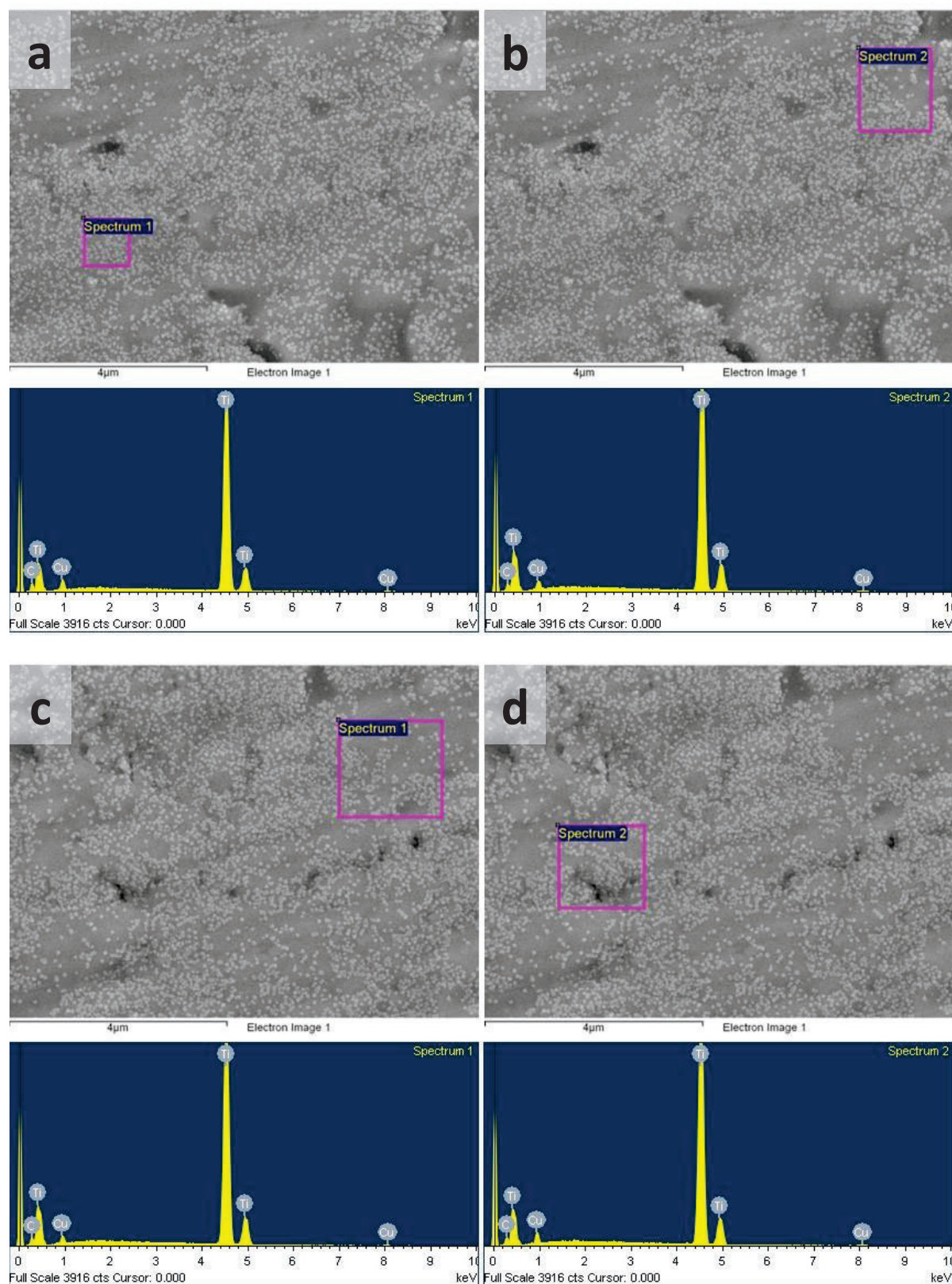
Figure 3.7 EDX analysis for the Cu_2O-Cu@Ti electrode a-b) before electrolysis c-d) after electrolysis.

3.6.2 Cu₂O-Cu@Ti. XRD.

The phase composition of the Cu_2O-Cu@Ti electrodes was studied by XRD, and the results are displayed in **Figure 3.8 a.** A set of diffraction peaks at different positions can be seen, indexed to the (1 0 0), (0 0 2), (1 0 1), (1 0 2), (1 1 0), (1 0 3), (2 0 0), (1 1 2), (2 0 1), (0 0 4), (2 0 2) and (1 0 4) lattice planes of Ti (JCPDS 00-044-1294). No peaks corresponding to TiO_2 can be observed by XRD.
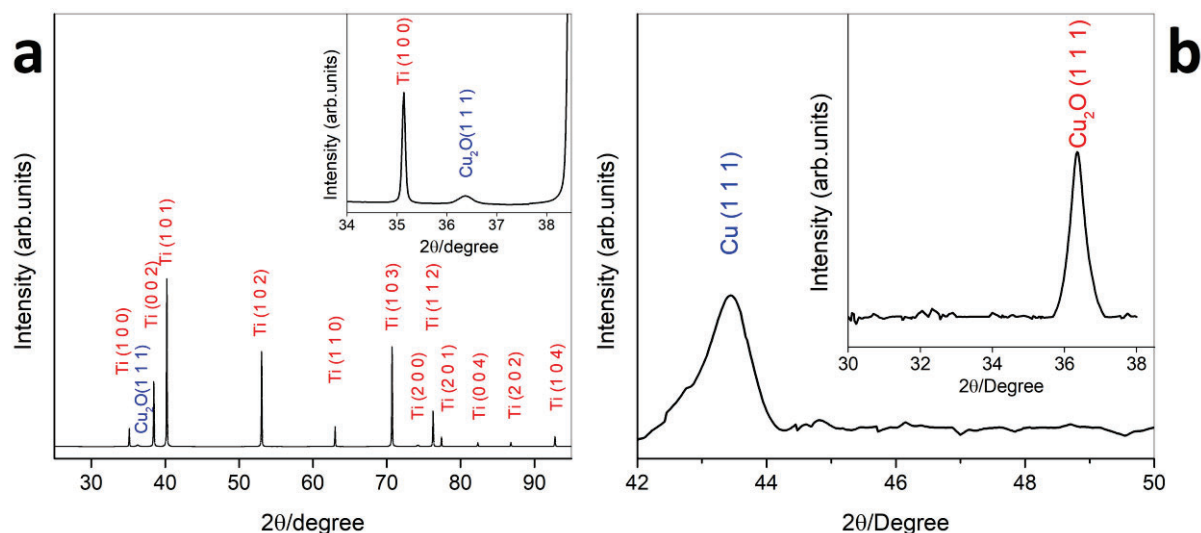
Figure 3.8 XRD spectrum a) for Cu₂O-Cu@Ti electrode and inset graph for the 2Θ range 34° to 38°. b) for the auxiliary electrode Cu₂O-Cu@Gr electrode.

Additionally, a small diffraction peak corresponding to cuprite Cu_2O (JCPDS 005-0667) can be also found in **Figure 3.8 a**. The corresponding peaks of Cu^0 resulted imperceptible owing to the small amount of deposited Cu nanoparticles (charge equivalent to 0.055C) and the overlapping with high intensity peaks associated to Ti. However, an alternative route was employed for identifying the peaks of Cu_2O-Cu nanoparticles depositing them onto a Gr foil support. **Figure 3.8 b** shows the XRD diffraction patterns for the Cu_2O-Cu@Gr electrode in which it was possible identifying two peaks at 36.7° and 43.3°associated with the lattice planes of Cu_2O (1 1 1) and Cu (1 1 1), respectively (JCPDS 005-0667 and 004-0836). These results indicate the partial oxidation of the Cu nanoparticles during the PED. Meanwhile, no other impurity peaks were observed on the XRD patterns of both electrodes. Contributing to both, activity for NO_3^-RR and selectivity towards NH_3, the presence of Cu and Cu_2O phases in the structure of a single nanocube is highly desirable for the catalyst. Different chemical states of Cu catalyze specific stages of NO_3^-RR as studied by Lichen Bai et al., whereby different in-situ applied techniques, identified that Cu is mostly in metallic form during the selective reduction of NO_3^- or NO_2^- to NH_3, while Cu(I) species are predominant when NO_3^- is reduced to NO_2^- (the RDS)[3][31].

3.6.3   Cu$_2$O-Cu@Ti. Raman Spectroscopy.

Raman spectroscopy measurements were also conducted on a Cu$_2$O-Cu/Ti electrode, as shown in **Figure 3.9**. As seen, peaks corresponding to several modes of Cu$_2$O, CuO and rutile TiO$_2$ can be found, in agreement with the results obtained by XRD.
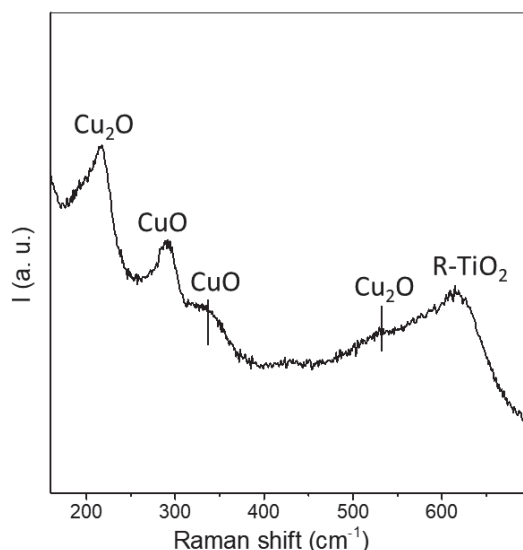
Figure 3. 9 Raman analysis of Cu2O-Cu@Ti electrode.

3.6.4   Cu$_2$O-Cu@Ti. XPS.

In **Figure 3.10 a** is presented the XPS spectrum of the Cu$_2$O-Cu@Ti electrode in the Cu 2p sub-level. The spectrum shows the two peaks corresponding to the 2p$_{3/2}$ and 2p$_{1/2}$ spin orbitals, along with the satellite peaks at 940-948 eV. The presence of these satellite peaks and their binding energy both confirm the existence of oxidized Cu forms on the Cu$_2$O-Cu/Ti electrode. The peak Cu 2p$_{3/2}$ was deconvoluted into three peaks, indicating the co-existence Cu$^+$ at 932.39 eV, Cu^{2+} at 934.48 eV and Cu^0 at 931.0 eV in the nanocubes[32]. The ratios Cu$^+$/total-Cu and Cu^{2+}/total-Cu were determined to be 78% and 20%, respectively. However, the presence of Cu^{2+} can be correlated with oxidation process of the nanocubes by exposition to air prior to the XPS analysis (this will be discussed in section 3.10). **Figure 3.10 b** shows the Ti 2p spectrum. Two strong peaks appear at 458.4 and 464.1 eV that can be correlated with Ti^{4+}, indicating the presence of superficial TiO$_2$ in the Cu$_2$O-Cu/Ti electrode. A deconvolution of the peaks situated at 453-457 eV indicates the minor presence of other oxidized forms as well of Ti (Ti^{2+}, and Ti^{3+} 454.4 and 456.6 eV respectively)[32]. The Ti peak is situated at 453.71 eV. The Auger LMM spectrum for the Cu$_2$O-Cu/Ti electrode in **Figure 3.10** c also suggests the presence of copper in the form of Cu$^+$ rather than as metallic Cu^0, as observed by the signal at 570 eV, associated to Cu$^+$[32].
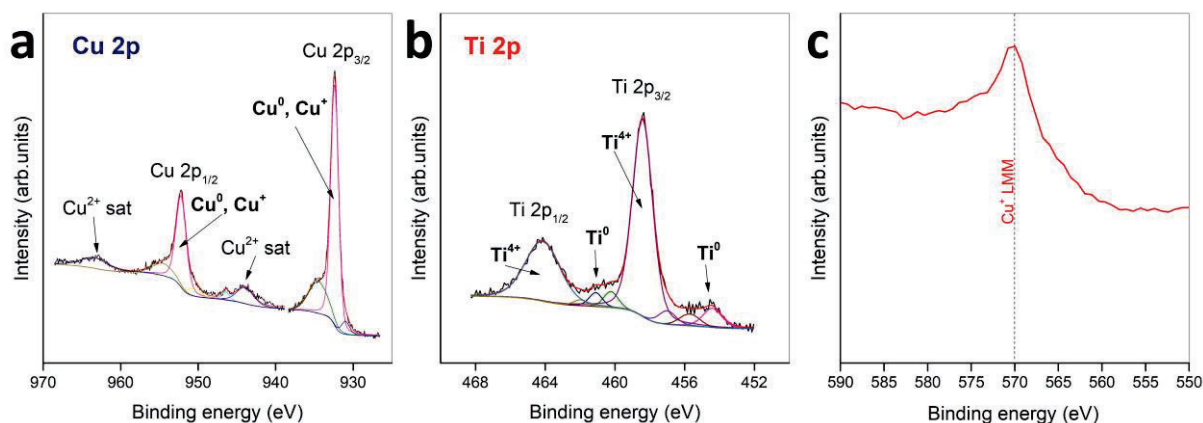
Figure 3.10 HR-XPS spectrum for Cu$_2$O-Cu@Ti electrode a) Cu 2p region b) Ti 2p region and c) The Auger LMM spectrum for the Cu$_2$O-Cu/Ti electrode.

3.7   Ti-base materials as efficient and selective active support.

3.7.1   Effects of pH in NO$_3^-$RR catalyzed by Ti-based electrodes.

The catalytic activity for NO$_3^-$RR was evaluated using Ti-based and Cu-based materials by introducing pH changes and different NO$_3^-$ concentrations, aiming to identify the optimal conditions for directing the reaction towards the generation of NH$_3$. The Ti plate used in all studies in the chapter will be referred to as Ti-based materials, indicating the presence of Ti^0 and Ti^{4+} species.

Several studies have correlated extreme pH conditions with higher nitrate conversion rates, FE or SE, or with higher NH$_3$ productivities [15], [24], [27]. LSV curves obtained with the Ti-base plate electrodes were recorded at pH 14 (0.4 M KNO$_3$ + 1M KOH) and pH 1 (0.3M KNO$_3$ +0.1M HNO$_3$) using a scan rate of 10 mV s^{-1} as illustrated in **Figure 3.11**. Lower polarization values (0 to -0.3V vs RHE) showed low current densities for both electrolyte conditions. However, a sustained increment can be seen in the current density at alkaline conditions from -0.4V to more negative potentials. A different behavior is observed under acidic conditions, where HER is highly suppressed by the high availability of NO$_3^-$ ions that compete for the active sites with protons, conducting the reaction towards NH$_3$ [34]. In the case of the alkaline electrolyte, HER is limited by the low proton concentrations in the electrolyte along with the high concentration of K$^+$ ions in solution**.** Monteiro et al. have observed a reduction in activity of HER at a high concentration of weakly hydrate ions such K$^+$ in high alkaline solutions. This effect is mainly due to the blockage effect caused by the cation accumulation on the interface catalyst-solution [35], [36]. Additionally, the high concentration of cations in solution can reduce the repulsive forces between cathode and NO$_3^-$ enhancing NO$_3^-$RR to nitrogen-based products generation.
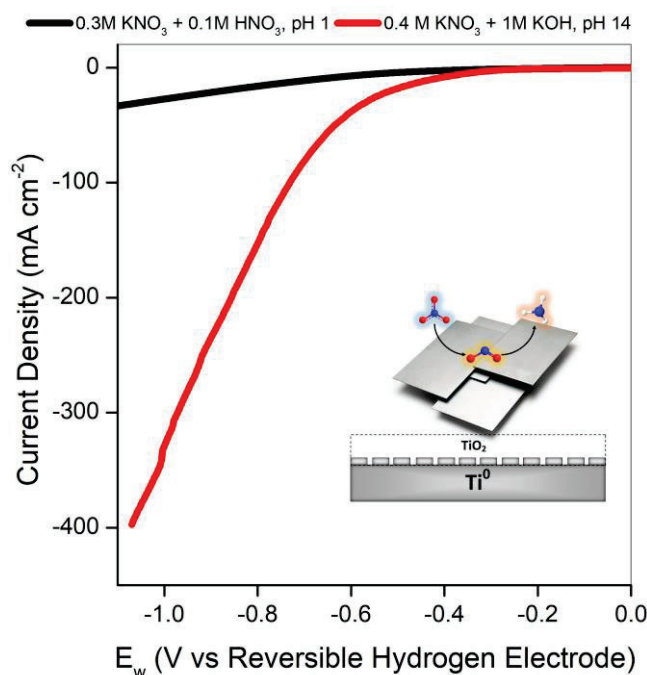
Figure 3.11 LSV curves obtained with the Ti-base plate electrodes recorded at pH 14 (0.4 M KNO_3 + 1M KOH) and pH 1 (0.3M KNO_3 +0.1M HNO_3) using a scan rate of 10 mV s^{-1}

The observed higher current densities at alkaline conditions are correlated with a higher activity of pure Ti-based electrodes in NO_3^-RR, **favored by the presence of OH$^-$ ions what makes the dissociation of water more favorable, ensuring a sufficient supply of protons necessary for the hydrogenation of NO_3^- reduction intermediates to NH_3** [37], [38]**.** Something later corroborated in chronoamperometry tests.

LSVs revealed a higher electrochemical activity at alkaline conditions. However, the information about the efficiency of NO_3^-RR-to-NH_3 is provided by the chronoamperometry tests. **Figure 3.12** displays the NH_3 yield and the faradaic efficiencies of NO_3^-RR to NH_3 after 90 min. **Figure 3.12 a**, corresponds to a chronoamperometry tests carried out with 0.3 M KNO_3 + 0.1M HNO_3 for the Ti-based electrode. The results agree with those already observed by McEnaney et al. under identical conditions where a peak of more than 90% of FE_{NH3} was observed at -0.7V vs RHE. Additionally, under those conditions, 12% of NO_3^- conversion and NH_3 Yield of 0.096 mmol·cm^{-2}·h^{-1} were reached. **Figure 3.12 b** corresponds to the chronoamperometry tests performed with 0.1M KNO_3 + 1M KOH and the Ti electrode. In this case, the peak of FE_{NH3} was observed at -0.4V vs RHE reaching out 86%, and the productivity peak was situated at -0.8V vs RHE (NH_3 Yield 0.37 mmol·cm^{-2}·h^{-1}).

On one hand, the high FE_{NH3} observed at acidic conditions complements the information obtained in LSV curves. While the high KNO_3 concentration significantly suppresses the HER making possible to

obtain a higher FE_{NH3} [39], [40], the low current densities reflected low productivities at all compared working potentials. Chen et al. have observed a lower interaction between NO_3^- molecules and Ti active sites if compared with that observed for Cu active sites. This low interaction could be reflected in low current densities, compensated by the high concentration that limits parasite reactions such the HER. On the other hand, the low concentration of protons in solution at alkaline conditions limits the competition for the active sites with NO_3^- ions, increasing the FE_{NH3} at lower potential values, while the higher currents observed in both LSV and CA were reflected in higher productivities.
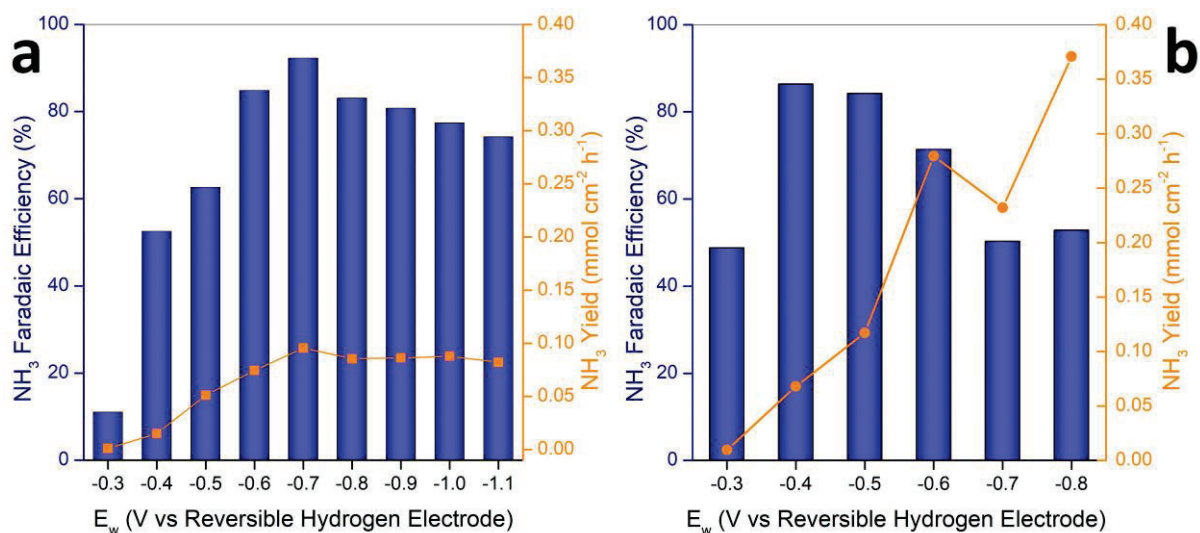
Figure 3.12 FE and productivities to NH_3 for the Ti-based electrode at different E_w a) at pH 1 b) at pH 14.

3.8 Boosting NO_3^-RR to NH_3 with Cu-based catalyst. Performance of Cu_2O-Cu on different supports:

Figure 3.13 shows a LSVs applied to KNO_3 0.1M + KOH 1M using the electrode Cu_2O-Cu@Ti; a peak is observed between the potentials -0.5 to -0.4 V vs RHE. Previous studies with Cu-base electrodes correlated this peak with the reduction of NO_2^- to NH_3 [8], [27]. Meanwhile, NO_3^- reduction to NO_2^- is expected to occur at less negative potentials, which agrees with the results of chronoamperometry tests.
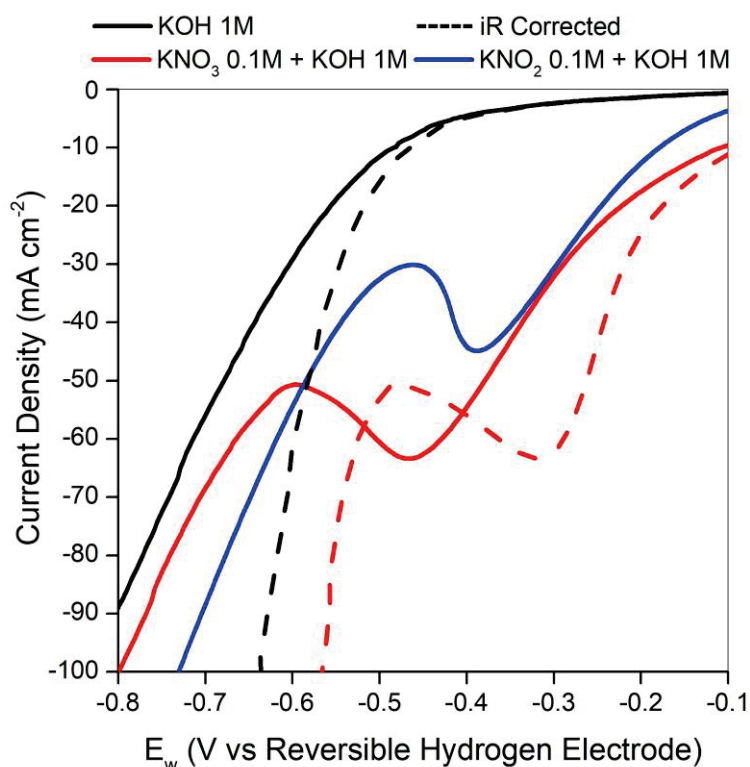
Figure 3.13 LSVs applied to KNO_3 0.1M + KOH 1M using the electrode Cu_2O-Cu@Ti with IR-corrections of E_w.

Since the pure Ti-based electrodes have demonstrated catalytic properties for efficiently conducting the NO_3-RR-to-NH_3 process under alkaline conditions, although with limited productivity at low cathodic potentials, additional strategies were needed to enhance the performance. As mentioned previously, incorporating Cu_2O-Cu nanocubes into a composite electrode, such as the synthesized Cu_2O-Cu/Ti-based, can significantly improve the reaction. In this configuration, Cu_2O-Cu can promote the RDS (i.e. NO_3^- to NO_2^-), while Ti-based material can preserve its intrinsic NH_3 selectivity.

A similar behavior has been observed by Hernandes et al., who reported a synergistic effect between components of a Cu-Pt bimetallic 3D-electrocatalyst, demonstrating enhanced activity and selectivity. This synergistic effect between Cu_2O-Cu and Ti-based in the composite electrode offered improved catalytic performance by combining the strengths of both materials, thereby achieving higher overall productivity and efficiency in the NO_3^-RR-to-NH_3 conversion process [41]. **Figure 3.14 a** shows the FE values for the different products (in the liquid phase) for a series of chronoamperometries carried out at different working potentials during a reaction times of 90 min at each potential. The observed trend for FE_{NH3} followed a volcano shape with a maximum value of 96% at -0.4V vs RHE, after which the FE_{NH3} began to descend as the potential decreased to -0.7 V vs RHE.

Figure 3.14 FE towards different products for CA in H-type cell using the Cu$_2$O-Cu@Ti electrode a) NH$_3$, NO$_2^-$ and Other N-products and b) H$_2$.

In general, the decline in FE$_{NH3}$ is closely associated with the increased FE towards other reaction products (e.g., NO$_2^-$, H$_2$), as observed at low and higher polarization values. The evolution of H$_2$ was followed by gas chromatography and the results are illustrated in **Figure 3.14 b** for a 90 min chronoamperometry. At -0.4V vs RHE, the average FE$_{H2}$ value remains relatively constant around 4% during the electrolysis time. These values are consistent with the measured FE for other products observed in the liquid phase. In the case of FE$_{NO2-}$, the maximum values were reached at less negative potentials. As mentioned previously, several authors situate the first electron transfer of the NO$_3^-$-to-NO$_2^-$ reaction as the RDS in the overall NO$_3^-$RR to any product, in which NO$_2^-$ is the first stable intermediate [42]. This implies that at low polarization values, the lower kinetics of NO$_3^-$RR limits further NO$_2^-$ reductions allowing its desorption from the catalyst surface into the bulk electrolyte. The accumulation of NO$_2^-$ ions in the bulk continues as long as the concentration of NO$_3^-$ ions in the solution remains high.

In the case of productivity, expressed as yield (mmol$_{NH3}$·cm^{-2}·h^{-1}); the values were gradually increased at more negative potentials as shown in **Figure 3.15**, reaching up to 0.38 at -0.7 V vs RHE. Considering FE (92%), SE (80%) and yield (0.28 mmol·cm^{-2} h^{-1}) to NH$_3$, it is possible to stablish an optimum potential around -0.5V vs RHE, which can offer a balance between efficiency and productivity of the process, maximizing NH$_3$ generation.
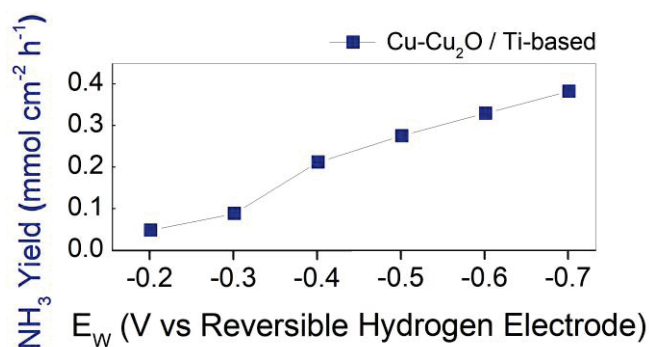
Figure 3.15 NH_3 Productivity at different E_w for the electrode Cu_2O-Cu@Ti.

Also related to the applied potential changes, as observed in **Figure 3.16**, the SE_{NH3} showed a gradual increase with the cathodic potential. The peak value of 82% was observed at -0.4V vs RHE. However, a slight decline was observed at more negative potentials in the range of -0.5V to -0.7V vs RHE, achieving an average value of 80% in most cases. Less negative potentials (E_w= -0.2 to -0.3V vs RHE) have shown higher NO_2^- selectivity, with a maximum value of 60% obtained at -0.2V vs RHE. The accumulation of nitrite ions in the bulk electrolyte at these potential values is a consequence of the nature of the NO_3^-RR with the Cu-Cu_2O/Ti-based electrode. This region presents the optimal electrochemical conditions for the conversion of NO_3^- to NO_2^-, in with the slow kinetics for the further reduction of NO_2^- into NH_3 allows its accumulation [27], [43].

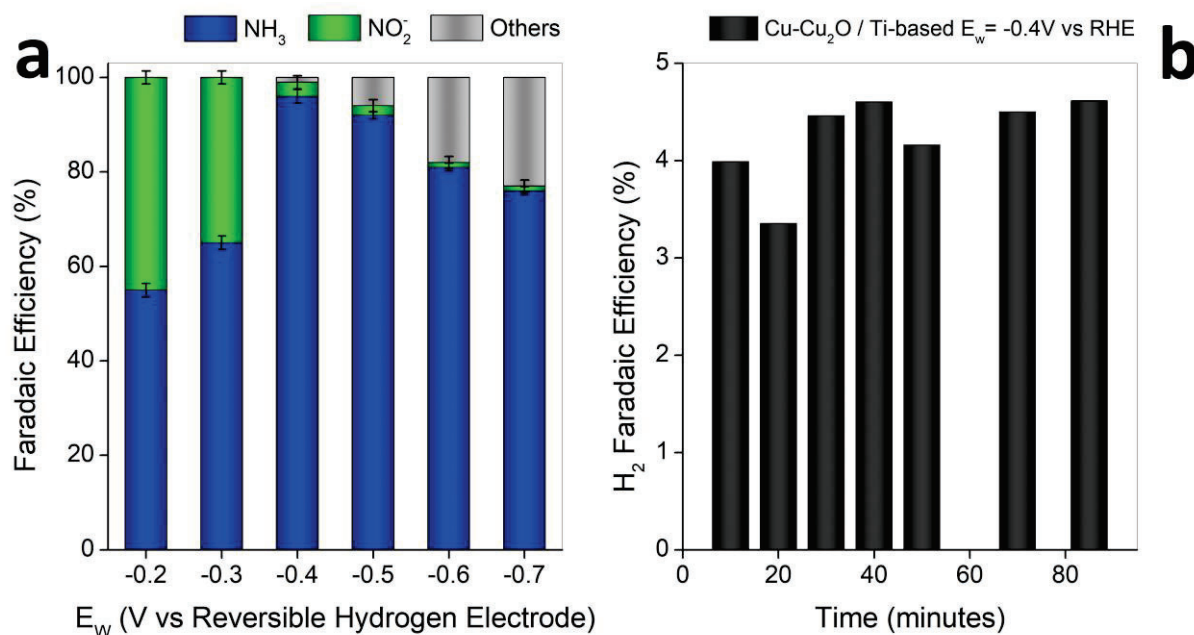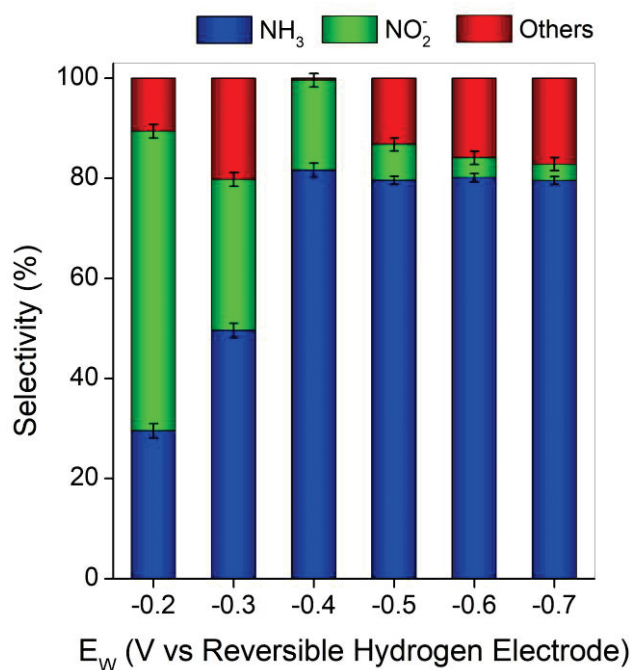*Figure 3.16 SE towards different products for CA in H-type cell using the Cu_2O-Cu@Ti electrode a) NH_3, NO_2^- and Other N-products.*

NO$_3^-$ conversion and specific conversion rates are presented in **Figure 3.17**. The percentage of removed nitrate was increased at more negative potentials up to 75% (-0.8V vs RHE) for both electrodes. However, the specific rate expressed in mg$_{NO3-}$·C^{-1}, which indicates the amount of nitrate removed by unit of charge, decreased progressively at more negative potentials due the contribution of HER. A value of 0.093 mg$_{NO3-}$·C^{-1} was observed at the optimum potential (-0.5V vs RHE) for the electrode Cu$_2$O-Cu/Ti-based. The specific NO$_3^-$ degradation can give information regarding which type of material can offer better properties for water denitrification. While Ti-based electrodes showed better nitrate specific degradation (another way of measuring its efficiency), the composite electrodes showed higher activity in terms of absolute NO$_3^-$ degradation. Cu$_2$O-Cu nanoparticles showed the property of increasing the activity of the Ti-based electrodes with a slight sacrifice of the efficiency in terms of specific degradation and selectivity to NH$_3$ at lower polarization values.
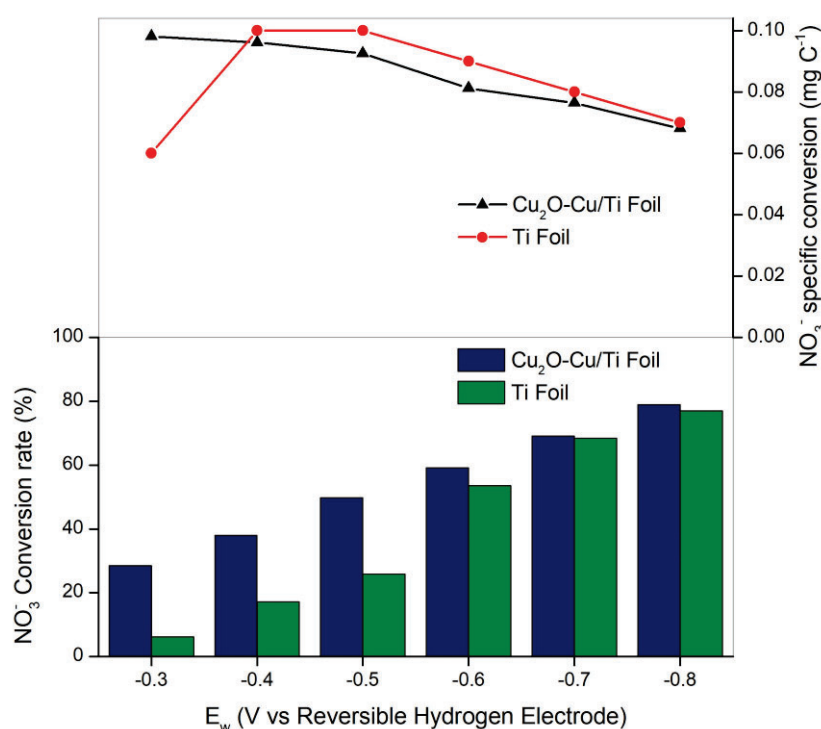
Figure 3.17 NO$_3^-$ absolute and specific conversion rates for the electrodes Ti-based and Cu$_2$O-Cu@Ti.

3.9 Quasi-in-situ XPS analysis of Cu$_2$O-Cu@Ti electrode.

The HR-XPS spectrum of the Cu$_2$O-Cu@Ti electrode in **Figure 3.10a** corresponds to an ex-situ measurement taken after PED synthesis. Satellite peaks in the 2p sub-level indicate a CuO layer on the Cu-based nanoparticles, formed due to air exposure between synthesis and the XPS measurement. Although CuO has limited catalytic activity for reducing NO$_3^-$ ions to NH$_3$, it can enhance NH$_3$ selectivity when combined with other materials in composite electrodes. Recent studies corroborated this,

showing that during nitrate electroreduction, CuO can prevent the full reduction of Cu$_2$O to metallic Cu, maintaining Cu$_2$O active sites and providing longer electrode stability [14]. Additionally, CuO can generate superficial defects like oxygen vacancies that act as active sites for absorbing NO$_3^-$ molecules, as demonstrated by Zhu H. et al. [44].

The effects of air exposure on the electrode can be minimized by performing PED in a controlled, air-free environment. To achieve this, Cu$_2$O-Cu@Ti electrodes were prepared inside an argon atmosphere glovebox (**Figure 3.18**) and analyzed by XPS. This quasi-in-situ XPS process involves conducting both PED synthesis and CA measurements within the glovebox to prevent oxidation of Cu-based nanoparticles and to observe changes in their oxidation state during nitrate electroreduction.
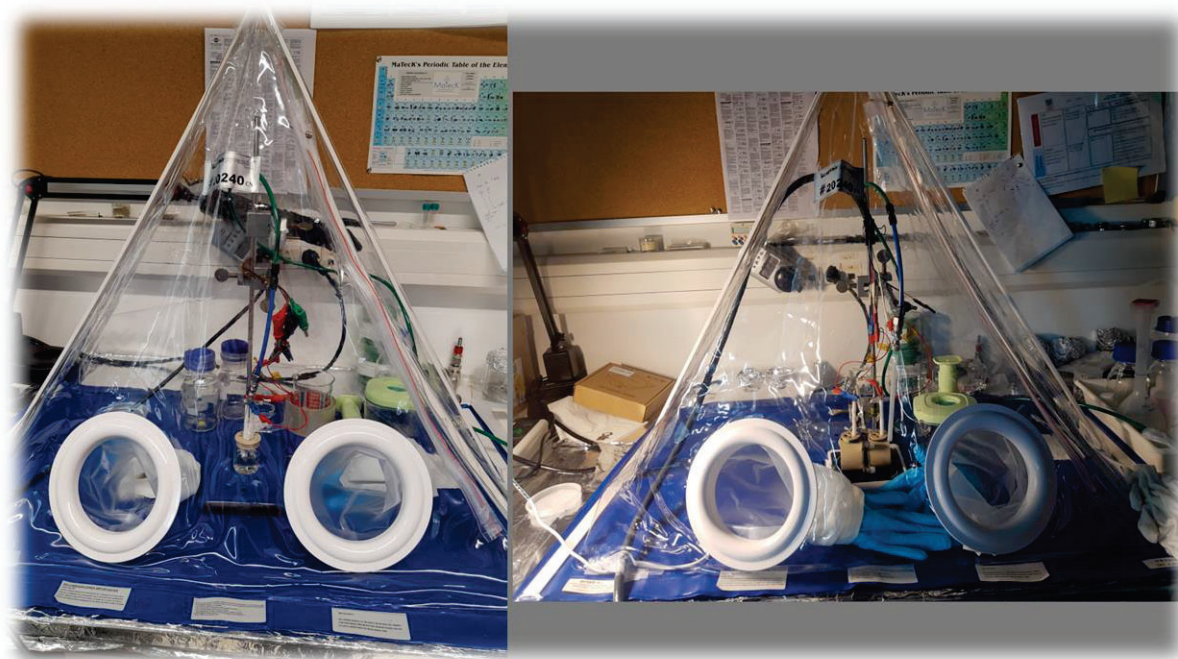
Figure 3.18 Glovebox used to perform PED synthesis and NO$_3^-$RR previous semi-in-situ XPS analysis.

The quasi-in situ XPS measurements were conducted on pre-electrolysis electrodes and after 40 minutes of electrolysis to evaluate the active states of both Cu and Ti-based catalysts. Before, XRD analysis revealed that the preferential phases of the nanoparticles are Cu$_2$O (111) and Cu (111) in the Cu$_2$O-Cu@Ti electrode and it was expected to see the same by XPS. **Figure 3.19** shows the **(a)** Cu 2p and **(b)** Cu Auger spectrums before and after reaction at applied potentials of -0.1, -0.5, and -1V vs RHE.

Before the reaction (blue spectrum), both the Cu 2p$_{3/2}$ and Cu 2p$_{1/2}$ showed contributions corresponding to Cu^0 and Cu$^+$, similar to ex-situ measurements and also according to XRD analysis, but

no notable Cu^{2+} satellite peaks were observed. The Cu LMM Auger peak in **Figure 3.19b** indicates that the catalyst's oxidation state is Cu$^+$ and not Cu^0, confirming that the initial surface of the nanoparticles after PED synthesis is primarily composed of Cu$_2$O, possibly with a metallic Cu core.
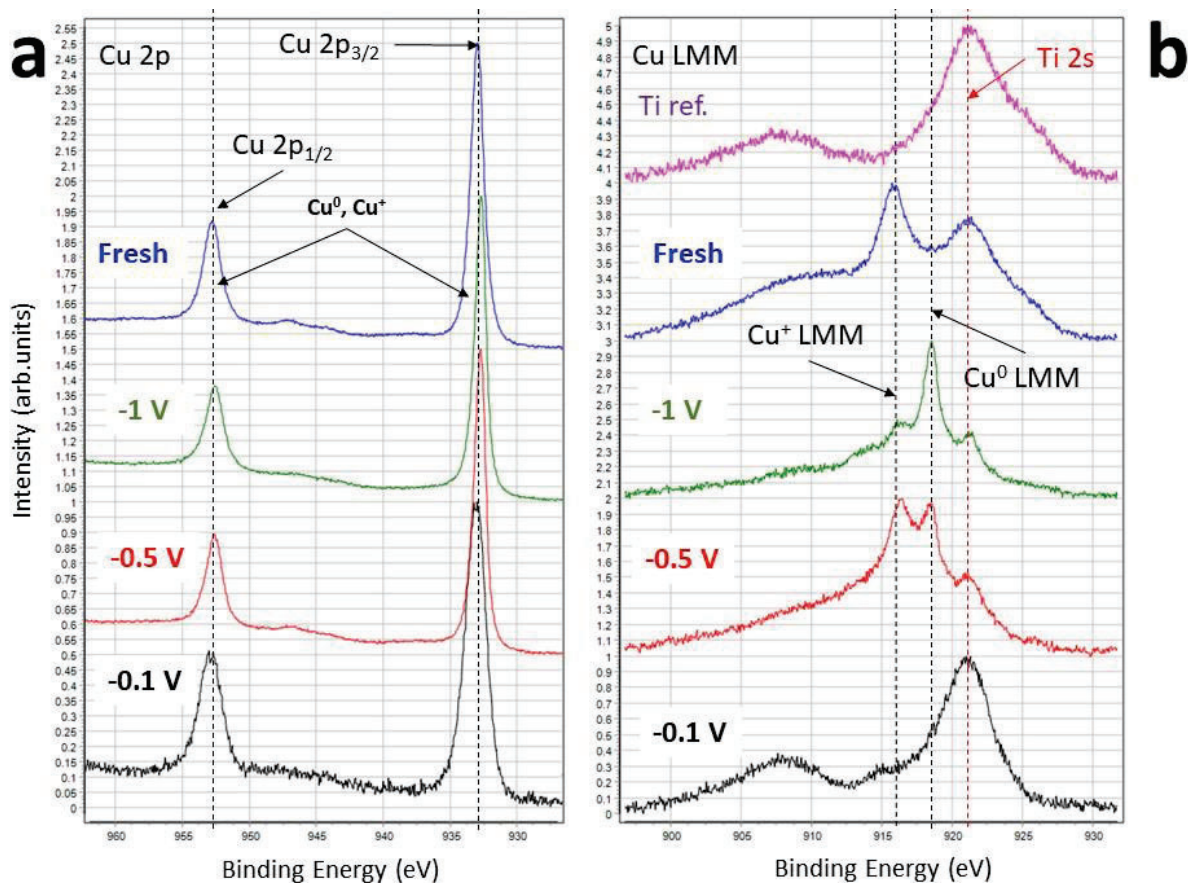
Figure 3.19 a) Cu 2p sub-level and b) Auger Cu LMM spectrums for the Cu$_2$O-Cu@Ti electrode pre- and post-40 minutes NO$_3^-$RR at different applied potentials.

The XPS spectrums recorded before and after 40 minutes of NO$_3^-$RR at applied potentials of -0.5 and -1V vs RHE show a small shift of the main Cu 2p$_{3/2}$ feature to lower binding energies, indicating Cu reduction during NO$_3^-$RR. The Cu LMM Auger line, with its main feature at approximately 918 eV, confirms the formation of Cu^0 as NO$_3^-$RR progresses. And notoriously the metallic Cu LMM peak is more intense at more cathodic potentials (-1.0 V vs RHE). By analyzing these changes in the oxidation state of Cu in the nanoparticles, along with the FE and SE obtained during CA experiments, it is evident that a balanced Cu$_2$O-Cu (predominantly Cu$_2$O) is the efficient surface for NH$_3$ formation at -0.5V vs RHE, where both oxidation states are necessary. Additionally, the increased proportion of metallic Cu can be correlated with a decline in FE at more negative potentials (referred to **Figure 3.15**).

For the Cu 2p sub-level XPS spectrum taken after 40 minutes of NO$_3^-$ electrolysis at -0.1V vs RHE, low-intensity 2p$_{3/2}$ and 2p$_{1/2}$ signals are observed. Similarly, the Auger spectrum is almost entirely composed of the reference Ti 2s signal (purple spectrum). This indicates the detachment of nanoparticles from the Ti substrate surface, leading by their oxidation to Cu^{2+} and eventual dissolution into the electrolyte. For instance, the volcano-shaped FE observed in **Figure 3.15** can be correlated with the proportional increase in metallic Cu at more negative potentials from -0.2 to -0.5V vs RHE. Encountering the optimal Cu$_2$O/Cu proportion between -0.4 and -0.5V vs RHE. Beyond this range, an increase in the proportion of metallic Cu, along with changes in the nanoparticle shape, leads to a reduction in FE.
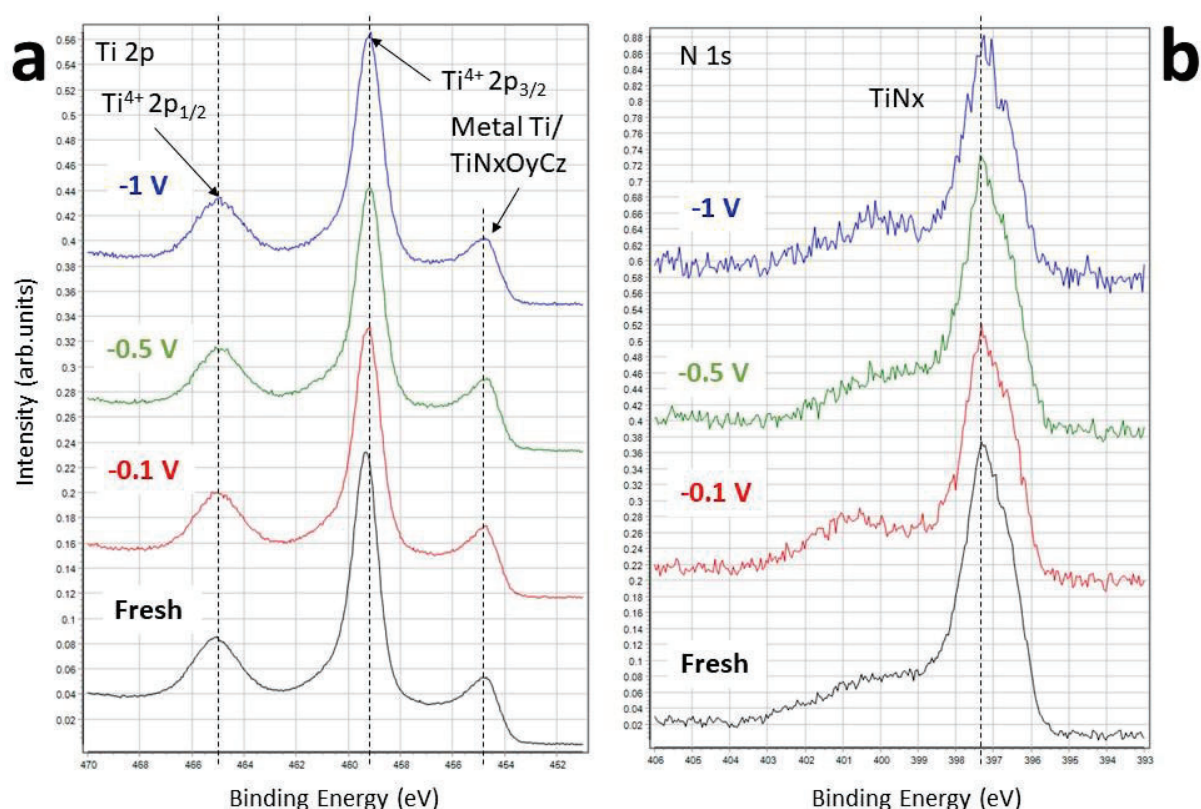
Figure 3.20 a) Ti 2p sub-level and b) Ti 1s core level spectrums for the Cu$_2$O-Cu@Ti electrode pre- and post-40 minutes NO$_3^-$ RR at different applied potentials.

Focusing on the Ti 2p sub-level of the Cu$_2$O-Cu@Ti electrode (**Figure 3.20a**), the quasi-in-situ XPS study reveals peaks at 458.4 and 464.1 eV, corresponding to Ti^{4+} and indicating a TiO$_2$ layer on the surface, similar to the ex-situ analysis shown in **Figure 3.6b**. The third peak at 454.8 eV is associated with various oxidized forms of Ti (Ti^{2+}, Ti^{3+}), as well as metallic Ti^0 [32].

The N 1s core-level peak (**Figure 3.6b**) remains complex in determining the exact chemical composition and states. However, its semi-Gaussian shape, with the full width of about 1.6–1.9 eV, has been

correlated in some studies to titanium nitride (TiN$_x$) on the surface, among other chemical states. Regardless of the applied potential during electrochemical NO$_3^-$ reduction, the surface species appear to remain unchanged. For instance, the catalytic selectivity towards NH$_3$ shown by Ti substrates can be then correlated to its various oxidation states, particularly TiO$_2$ as main component of the surface.
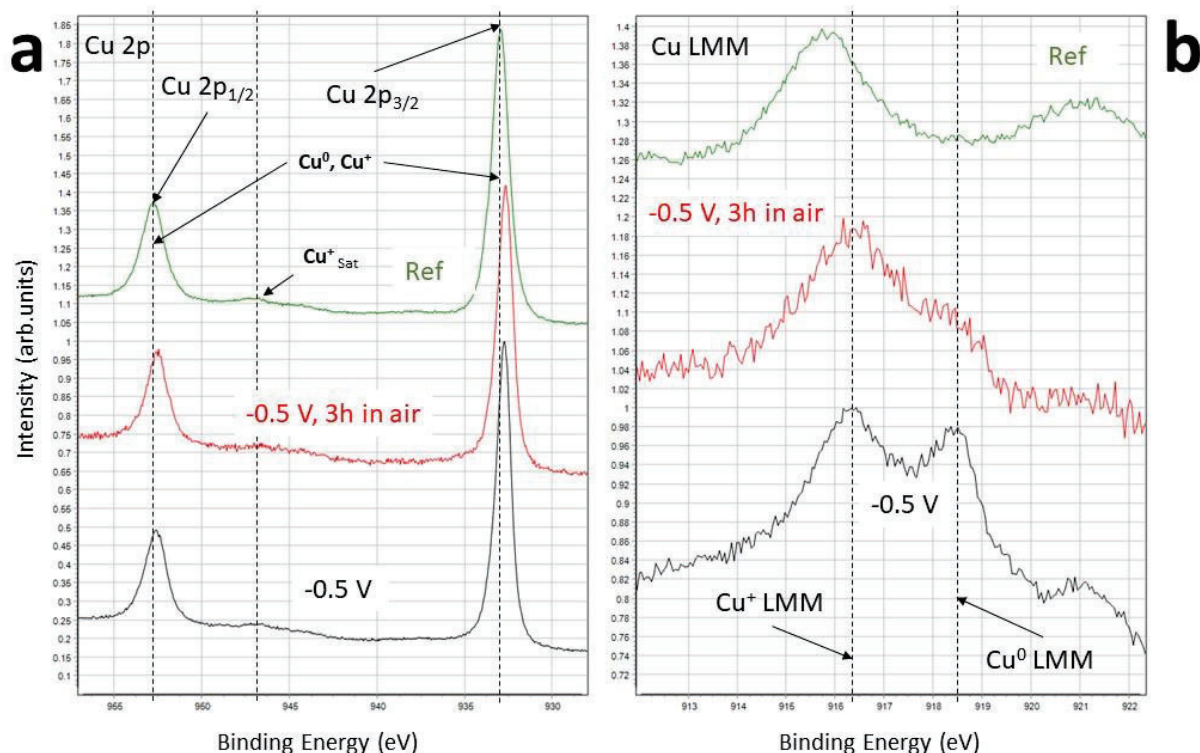
Figure 3.21 a) Cu 2p sub-level and b) Auger Cu LMM spectrums for the Cu$_2$O-Cu@Ti electrode pre- and post-3hs of air exposition.

Finally, the idea that the Cu-based nanoparticles deposited by PED have an encapsulated metallic Cu structure covered by Cu$_2$O on the Ti support is supported by both ex-situ XRD and XPS results, where both Cu and Cu$_2$O are present. Further evidence comes from quasi-in-situ XPS measurements. **Figure 3.21a** shows the spectrum of a reference Cu material (black signal), the Cu$_2$O-Cu@Ti electrode after 40 minutes of NO$_3^-$RR (blue signal), and the same electrode after 3 hours of air exposure (red signal). The peaks attributed to Cu$^+$ and Cu^0 are observed in the Cu 2p region, consistent with previous measurements.

In the Cu LMM Auger measurements, the peaks recorded in the black signal (after NO$_3^-$RR) confirms the formation of metallic Cu, as observed before. After a 3-hour air exposure, the electrode was analyzed again by XPS. The red signal indicates that only part of the metallic Cu^0 re-oxidizes to Cu$_2$O,

while some metallic Cu remains detectable. This suggests that part of the metallic copper is passivated by the Cu$_2$O layer after air exposure, a behavior also expected for freshly PED-synthesized electrodes.

3.10 Evaluating the effect of a different substrate:

Figure 3.22 compares different cathode materials at −0.5 V vs RHE for NO$_3^-$RR to NH$_3$ with 0.1 M KNO$_3$ + 1 M KOH electrolyte. Pure Cu, Ti, and composite Cu$_2$O-Cu@Ti-based and Cu$_2$O-Cu@Gr electrodes were analyzed for FE$_{NH3}$, SE$_{NH3}$, and productivity. Pure Ti-based high selectivity for reducing NO$_3^-$ to NH$_3$ makes it an excellent support for Cu-based NO$_3^-$RR catalysts. FE and SE decrease in electrodes lacking Ti. The Cu$_2$O-Cu@Ti electrode shows a synergistic effect, leveraging the intrinsic properties of both components to enhance ammonia generation.
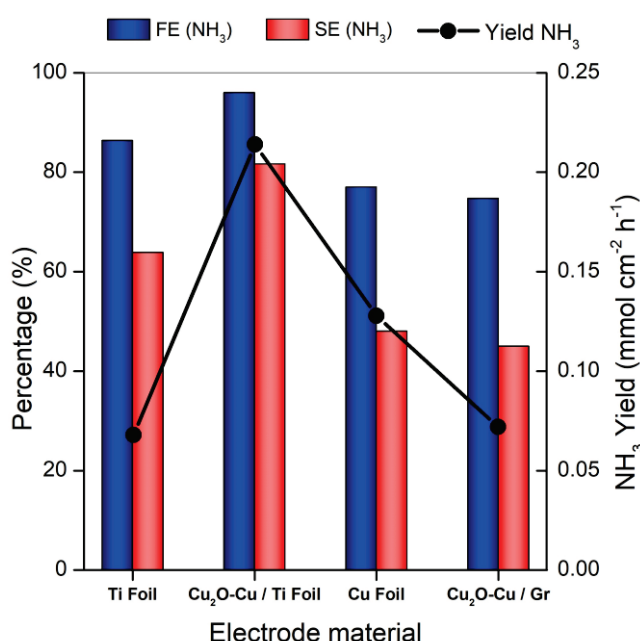
Figure 3.22 FE towards NH$_3$ for different cathode materials at −0.5 V vs RHE.

3.11 Determining the electrochemical rate constant (k): Why do we have synergy between Cu and Ti-based materials.

A RDE was used to determine the k for NO$_3^-$RR using the different materials in this Chapter. Pure Ti-based, pure Cu-based, and electrodeposited Cu$_2$O-Cu@Ti-based disks were analyzed to explain the different performances. Hg/HgO$_{KOH\ 1M}$ and Pt wire were used as reference and counter electrodes, respectively. LSVs were recorded on the disks at various rotating rates (ω).
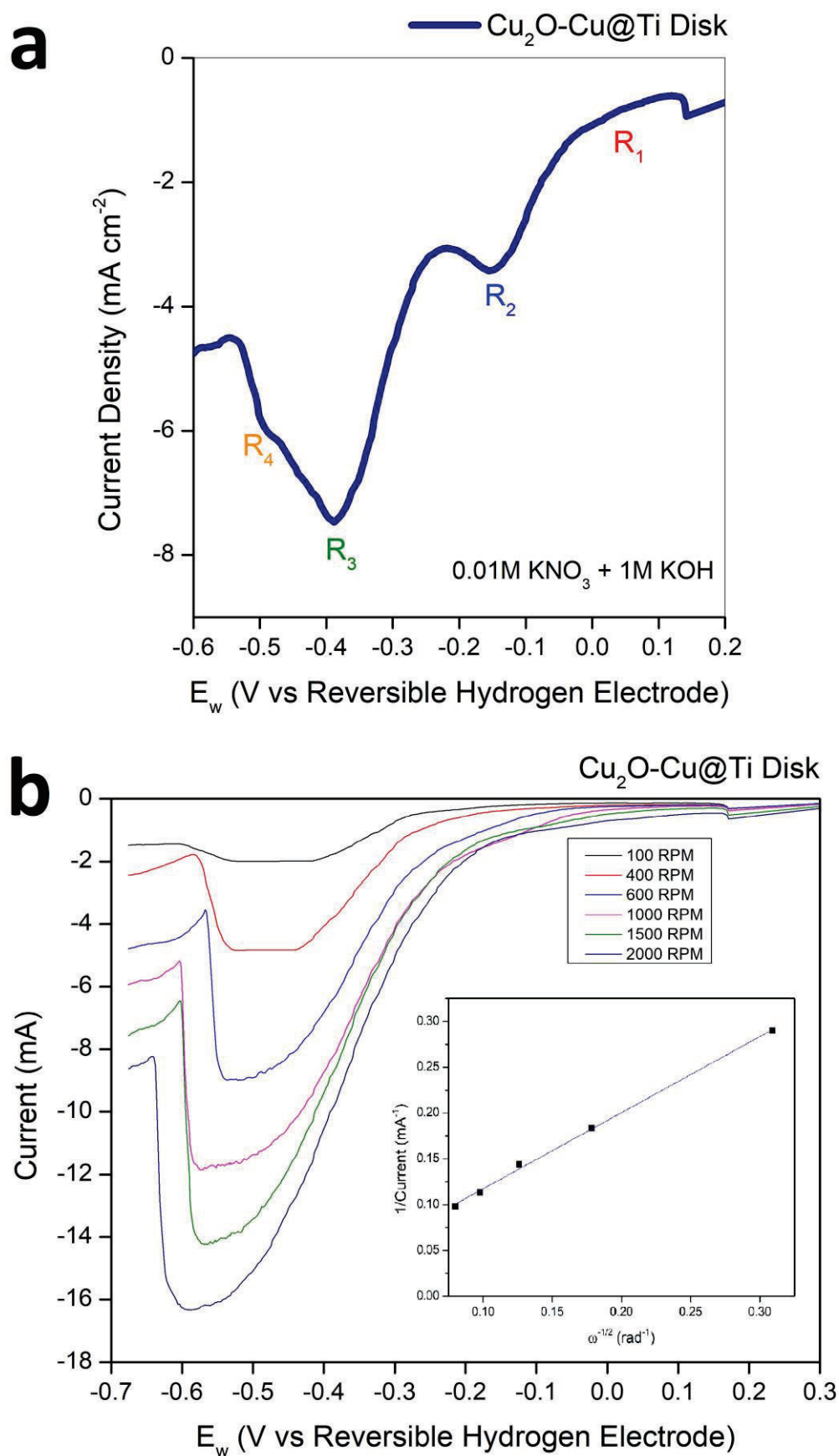
Figure 3.23 a) LSV under static conditions with Cu_2O-Cu/Ti disk RDE. R1 CuO to Cu_2O reduction; R2 NO_3^- to NO_2^- reduction; R3 NO_3^- to NH_3 reduction;1 from R4 HER (b) LSV curves with RDE under different rotation speeds.

Figure 3.19 shows LSVs at **(a)** 0 RPM and **(b)** rotating rates of 100, 400, 600, 1000, 1500, and 2000 RPM for the composite electrode, starting from the OCP to the expected potential. The recorded current densities j exhibited a linear dependency on the $\omega^{-1/2}$ value. The distortion of the sigmoidal shape in the initial stages of rising j (between 0.2 and -0.1 V vs RHE) indicates that NO_3^-RR on the Cu_2O-Cu@Ti electrode is limited by both the mass transport of NO_3^- ions to the electrode surface and the sluggish kinetics of the first electron transfer during the RDS. Limiting currents (I_L) were observed between -0.5 and -0.6 V vs RHE, indicating mass transport limitations in that region. Therefore, the potential range between -0.3 to -0.5 V was used to determine the k, where contributions from limited mass transport and limited first electron transfer can be separated according to the **Koutecky-Levich** analysis as described in **Chapter 2**.

Also, in **Figure 3.19 b** the Koutecky-Levich plot obtained with currents measured is presented in the voltammograms at -0.45 V vs RHE. From the intercept with the y-axis, the reciprocal of the kinetic current (i_k) was extracted as indicated in **Equation 3.1**. Once the i_k was determined, the k, also known as the **intrinsic charge transfer rate constant**, was obtained according to **Equation 3.2**, resulting in $3.91 \cdot 10^{-4}$ cm·s^{-1} for the Cu_2O-Cu@Ti disk electrode. A previous study reported a k for NO_3-RR for a Cu-Pt electrode in $2.48 \cdot 10^{-4}$ cm·s^{-1} under neutral pH at 0.15V vs RHE [41], a value in the same order of magnitude as determined four our electrode. The k for individual Cu and Ti-based disk were determined using the same procedure, resulting in values of $3.88 \cdot 10^{-4}$ cm·s^{-1} and $3.02 \cdot 10^{-6}$ cm·s^{-1}, respectively. The Cu_2O-Cu@Ti electrode at low potential values (-0.4 to -0.6 V vs RHE) maintained some characteristics of the pure Ti electrode, such as high FE and SE to NH_3, while exhibiting the high activity typical of Cu-based electrodes.

3.12   Double Layer capacitance determination (C_{DL}).

Previous studies found synergistic effects when Cu surfaces/particles were partially oxidized to Cu(I), where metallic Cu accelerates the reaction rate of the RDS, and Cu(I) particles conduct further reductions selectively to NH_3 [7], [41]. As well with the k, the double layer capacitances (C_{DL}) of Cu_2O-Cu/Ti and Ti electrodes were determined to study the influence of surface area variation on k and its effects on efficiency parameters.

For C_{DL} measurements, CVs at different scan rates were obtained in 0.1 M Na_2SO_4 electrolyte in the non-faradaic region (-0.15 to 0.15 V vs Ag/AgCl$_{3.5M\ KCl}$) [47]. **Figure 3.20** shows the CV for Cu_2O-Cu@Ti electrode at four different scan rates, with the average current plotted against scan rates. The slope of the current vs. scan rate gives the capacitance for the specific electrode.
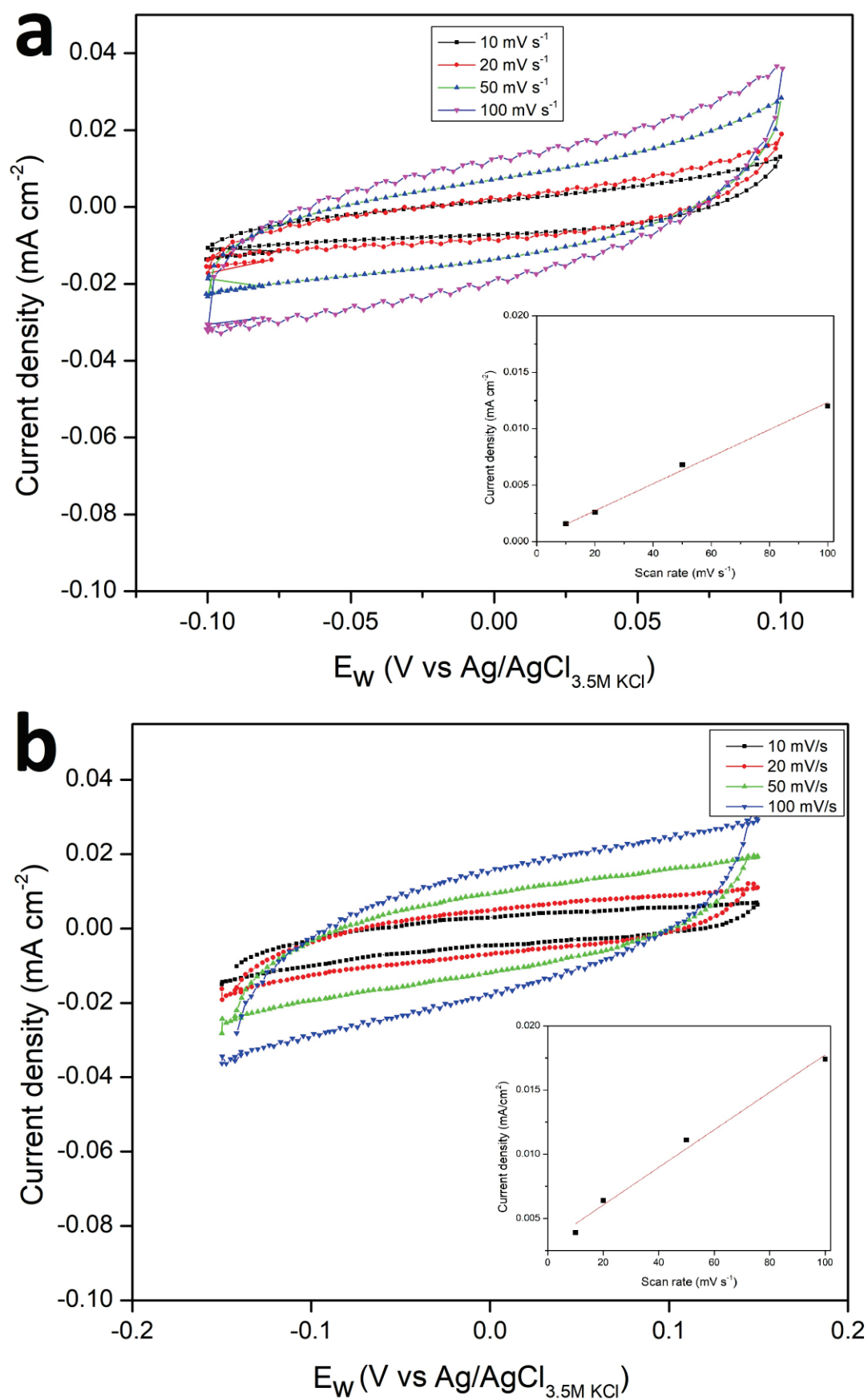
Figure 3.24 Double layer capacitance CDL for 1 cm² a) Ti and b) Cu₂O-Cu/Ti electrodes (0.1M Na₂SO₄ electrolyte).

The C_{DL} values for 1 cm^2 geometric area electrodes were 120 and 150 μF for Cu$_2$O-Cu@Ti and Ti electrodes, respectively. An additional parameter Ψ was introduced into Equation 2.13 as a correction factor for the geometric area of the Ti disk to calculate a new ki for NO$_3^-$RR with the Cu$_2$O-Cu@Ti disk electrode [45]. This theoretical calculation attempts to determine the real k_i of the composite electrode by reducing errors caused by using a geometric flat area when the surface is fully covered by nanoparticles. The new k_i was calculated as follows:

Under these conditions, the new k_i for the Cu$_2$O-Cu/Ti disk electrode reached 4.77·10^{-4} cm·s^{-1}, approximately 15% higher than that of the pure Cu disk. This partially explains the observed higher activity and efficiency of the composite electrodes for reducing NO$_3^-$ to NH$_3$.

Finally, the increased k_i demonstrated that combining Cu$_2$O-Cu nanoparticles with Ti surfaces offers better kinetic behavior for NO$_3^-$RR-to-NH$_3$ than the pure components. While the Cu$_2$O-Cu interface improves the diffusion of adsorbed NO$_3^-$ ions, Cu accelerates the first electron transfer process, and Ti provides stability, limits HER, and efficiently conducts NO$_3^-$RR to NH$_3$ as the final product.

3.13 Conclusions:

Electrochemical reduction of nitrate toward ammonia using Ti, electrodeposited Cu$_2$O-Cu/Ti, and Cu$_2$O-Cu/Gr cathodes have been investigated in an H-type divided and with rotating disk electrodes in a series of electrolyte conditions. In general, pristine Ti electrodes showed excellent properties as supporting active material for NO$_3^-$RR, being highly sensitive to the NO$_3^-$ concentration and pH of the electrolyte. Higher current densities were obtained under alkaline conditions, which was translated into higher catalytic activity for NO$_3^-$RR. Acidic conditions showed higher FE toward NH$_3$ (90%) than alkaline conditions (82%) at their respective optimal working potential, with lower productivities. Cu$_2$O-Cu/Ti electrodes efficiently conduct the NO$_3^-$RR-to- NH$_3$ process allowing working at an optimum potential of −0.5 V vs RHE, attaining FE_{NH_3} and SE_{NH_3} values of 92 and 80%, respectively. The composite electrode showed synergistic properties with respect to individual components (high faradaic efficiency toward NH$_3$ of pristine Ti and high NO$_3^-$RR activity of copper and copper oxide nanoparticles). The estimated electrochemical rate constants (k) resulted in similar values for pure Cu and Cu$_2$O-Cu/Ti disk electrodes (3.88 × 10^{-4} and 3.91 × 10^{-4} cm·s^{-1} respectively). However, the correction of the disk geometric areas with the ψ factor increased the k_i of the composite electrode up to 4.77 × 10^{-4} cm·s^{-1} pointing to an improved kinetic performance of combined Cu$_2$O and Ti. In this sense, the present work shows that combining materials with different intrinsic activities is a good strategy to boost productivity, while preserving the efficiency toward the desired product.

3.14 Highlights of the chapter.

Synergistic Effect of Cu and Ti-based Electrodes:

The study demonstrates that combining Cu and Ti materials in composite electrodes enhances the NO_3^-RR. The Cu_2O-Cu@Ti showed improved activity and selectivity due to the synergistic effects of both materials.

High Faradaic Efficiency and Productivity:

Cu_2O-Cu@Ti electrode achieved a faradaic efficiency of 92% and a NH_3 productivity of 0.28 mmol·cm^{-2}·h^{-1} at -0.5 V vs. RHE, showcasing the potential of this approach in comparison to direct N_2RR methods.

Optimal Electrochemical Conditions:

Optimal conditions for maximizing NH_3 generation were defined, including the pH and applied potential for Ti and Cu_2O-Cu@Ti materials. Alkaline conditions (0.1M KNO_3 + 1M KOH) were found to be favorable for achieving higher current densities and productivity.

Electrochemical Rate Constants:

The electrochemical rate constants for different electrodes were determined using the RDE analysis. The values for Ti, Cu, and Cu_2O-Cu@Ti electrodes were $3.02 \cdot 10^{-6}$, $4.77 \cdot 10^{-4}$, and $3.88 \cdot 10^{-4}$ cm·s^{-1}, respectively, indicating the higher kinetic performance of the composite electrode as consequence of synergies in the kinetics.

Bibliography.

[1]   F. Calle-Vallejo, M. Huang, J. B. Henry, M. T. M. Koper, and A. S. Bandarenka, *Theoretical design and experimental implementation of Ag/Au electrodes for the electrochemical reduction of nitrate*, Phys. Chem. Chem. Phys., vol. 15, no. 9, pp. 3196–3202, 2013, doi: 10.1039/c2cp44620k.

[2]   F. A. Marchesini, V. Aghemo, I. Moreno, N. Navascués, S. Irusta, and L. Gutierrez, *Pd and Pd,In nanoparticles supported on polymer fibres as catalysts for the nitrate and nitrite reduction in aqueous media*, J. Environ. Chem. Eng., vol. 8, no. 2, p. 103651, 2020, doi: 10.1016/j.jece.2019.103651.

[3]   A. S. Fajardo, P. Westerhoff, C. M. Sanchez-Sanchez, and S. Garcia-Segura, *Earth-abundant elements a sustainable solution for electrocatalytic reduction of nitrate*, Appl. Catal. B Environ., vol. 281, no. June 2020, p. 119465, 2021, doi: 10.1016/j.apcatb.2020.119465.

[4]   J. Wang, L. Ling, Z. Deng, and W. Zhang, *Nitrogen-doped iron for selective catalytic reduction of nitrate to dinitrogen*, Sci. Bull., vol. 65, no. 11, pp. 926–933, 2020, doi: 10.1016/j.scib.2020.02.015.

[5]   Z. A. Jonoush, A. Rezaee, and A. Ghaffarinejad, *Electrocatalytic nitrate reduction using Fe^0/Fe_3O_4 nanoparticles immobilized on nickel foam: Selectivity and energy consumption studies,* J. Clean. Prod., vol. 242, p. 118569, 2020, doi: 10.1016/j.jclepro.2019.118569.

[6]   Y. Lan, J. Chen, and H. Zhang, *Fe/Fe$_3$C nanoparticle-decorated N-doped carbon nanofibers for improving the nitrogen selectivity of electrocatalytic nitrate reduction*, J. Mater. Chem. A Mater. energy Sustain., vol. 00, pp. 1–11, 2020, doi: 10.1039/D0TA02317E.

[7]   M. Marcos-Hernández, G. Antonio Cerrón-Calle, Y. Ge, S. Garcia-Segura, C.M. Sánchez, A. Fajardo, and V. Villagrán, *Effect of surface functionalization of Fe$_3$O$_4$ nano-enabled electrodes on the electrochemical reduction of nitrate*, Sep. Purif. Technol., vol. 282, no. July 2021, 2022, doi: 10.1016/j.seppur.2021.119771.

[8]   X. Fu, X. Zhao, X. Hu, K. He, Y. Yu, T. Li, Q. Tu, X. Qian, Q. Yue, M. Wasielewski, and Y. Kang, *Alternative route for electrochemical ammonia synthesis by reduction of nitrate on copper nanosheets*, Appl. Mater. Today, vol. 19, p. 100620, 2020, doi: 10.1016/j.apmt.2020.100620.

[9]   W. Fu, Z. Hu, Y. Zheng, P. Su, Q. Zhang, Y. Jiao, and M. Zhou, *Tuning mobility of intermediate and electron transfer to enhance electrochemical reduction of nitrate to ammonia on Cu$_2$O/Cu interface*, Chem. Eng. J., vol. 433, no. October, p. 133680, 2022, doi: 10.1016/j.cej.2021.133680

[10]   G. Chen, Y. Yuan, H. Jiang, S. Ren, L. Ding, L. Ma, T. Wu, J. Lu, and H. Wang, *Electrochemical reduction of nitrate to ammonia via direct eight-electron transfer using a copper–molecular solid catalyst*, Nat. Energy, 2020, doi: 10.1038/s41560-020-0654-1.

[11]   Y. J. Shih, Z. L. Wu, C. Y. Lin, Y. H. Huang, and C. P. Huang, *Manipulating the crystalline morphology and facet orientation of copper and copper-palladium nanocatalysts supported on stainless steel mesh with the aid of cationic surfactant to improve the electrochemical reduction of nitrate and N$_2$ selectivity*, Appl. Catal. B Environ., vol. 273, no. May, p. 119053, 2020, doi: 10.1016/j.apcatb.2020.119053.

[12]   W. Gao, L. Gao, D. Li, K. Huang, L. Cui, J. Meng, and J. Liang, *Removal of nitrate from water by the electrocatalytic denitrification on the Cu-Bi electrode*, J. Electroanal. Chem., vol. 817, no. April, pp. 202–209, 2018, doi: 10.1016/j.jelechem.2018.04.006.

[13]   Y. Zhang, Y. Zhao, Z. Chen, L. Wang, P. Wu, and F. Wang, *Electrochemical reduction of nitrate via Cu/Ni composite cathode paired with Ir-Ru/Ti anode: High efficiency and N$_2$ selectivity*, Electrochim. Acta, vol. 291, pp. 151–160, 2018, doi: 10.1016/j.electacta.2018.08.154.

[14]   T. Feng, J. Wang, Y. Wang, C. Yu, X. Zhou, B. Xu, K. László, F. Li, and W. Zhang, *Selective electrocatalytic reduction of nitrate to dinitrogen by Cu$_2$O nanowires with mixed oxidation-state,*" Chem. Eng. J., vol. 433, no. September 2021, 2022, doi: 10.1016/j.cej.2021.133495.

[15]   J. McEnaney, S. Blair, A. Nielander, J. Schwalbe, D. Koshy, M. Cargnello, and Thomas F. Jaramillo, *Electrolyte engineering for efficient electrochemical nitrate reduction to ammonia on a titanium electrode*, ACS Sustain. Chem. Eng., vol. 8, no. 7, pp. 2672–2681, 2020, doi: 10.1021/acssuschemeng.9b05983.

[16]   R. Jia, Y. Wang, C. Wang, Y. Ling, Y. Yu, and B. Zhang, *Boosting Selective Nitrate Electroreduction to Ammonium by Constructing Oxygen Vacancies in TiO₂*, ACS Catal., vol. 10, no. 6, pp. 3533–3540, 2020, doi: 10.1021/acscatal.9b05260.

[17]   Q. Gao, h.s. Pillai, y. Huang, S. Liu, Q. Mu, X. Han, Z. Yan, H. Zhou, Q. He, H. Xin, and H. Zhu, *Breaking adsorption-energy scaling limitations of electrocatalytic nitrate reduction on intermetallic CuPd nanocubes by machine-learned insights*, Nat. Commun., vol. 13, no. 1, pp. 1–12, 2022, doi: 10.1038/s41467-022-29926-w.

[18]   T. Hu, C. Wang, M. Wang, C. M. Li, and C. Guo, *Theoretical Insights into Superior Nitrate Reduction to Ammonia Performance of Copper Catalysts*, ACS Catal., vol. 11, no. 23, pp. 14417–14427, 2021, doi: 10.1021/acscatal.1c03666.

[19]   O. Q. Carvalho, R. Marks, H. Nguyen, M. Vitale-Sullivan, S. Martinez, L. Árnadóttir, and K. Stoerzinger, *Role of Electronic Structure on Nitrate Reduction to Ammonium: A Periodic Journey*, J. Am. Chem. Soc., vol. 144, no. 32, pp. 14809–14818, 2022, doi: 10.1021/jacs.2c05673.

[20]   J. Wei, Y. Li, H. Lin, X. Lu, C. Zhou, and Y. yun Li, *Copper-based electro-catalytic nitrate reduction to ammonia from water: Mechanism, preparation, and research directions*, Environ. Sci. Ecotechnology, vol. 20, 2024, doi: 10.1016/j.ese.2023.100383.

[21]   Y.Wang, A. Xu, Z. Wang, L. Huang, J. Li, F. Li, J. Wicks, M. Luo, D. Nam, C. Tan, Y. Ding, J. Wu, Y. Lum, C. Dinh, D. Sinton, G. Zheng, and Edward H. Sargent, *Enhanced Nitrate-to-Ammonia Activity on Copper-Nickel Alloys via Tuning of Intermediate Adsorption*, J. Am. Chem. Soc., vol. 142, no. 12, pp. 5702–5708, 2020, doi: 10.1021/jacs.9b13347.

[22]   X. Zhang, C. Wang, Y. Guo, B. Zhang, Y. Wang, and Y. Yu, *Cu clusters/TiO₂₋ₓ with abundant oxygen vacancies for enhanced electrocatalytic nitrate reduction to ammonia*, J. Mater. Chem. A, vol. 10, no. 12, pp. 6448–6453, 2022, doi: 10.1039/D2TA00661H.

[23]   P. Grosse, A. Yoon, C. Rettenmaier, S. W. Chee, and B. Roldan Cuenya, *Growth Dynamics and Processes Governing the Stability of Electrodeposited Size-Controlled Cubic Cu Catalysts*, J. Phys. Chem. C, vol. 124, no. 49, pp. 26908–26915, 2020, doi: 10.1021/acs.jpcc.0c09105.

[24]   D. Reyter, D. Bélanger, and L. Roué, *Elaboration of Cu-Pd films by coelectrodeposition: Application to nitrate electroreduction*, J. Phys. Chem. C, vol. 113, no. 1, pp. 290–297, 2009, doi: 10.1021/jp805484t.

[25]   L. Hidmi and M. Edwards, *Role of temperature and pH in Cu(OH)₂ solubility*, Environ. Sci. Technol., vol. 33, no. 15, pp. 2607–2610, 1999, doi: 10.1021/es981121q.

[26]   Y. Sun, S. Li, ZP. Jovanov, D. Bernsmeier, H. Wang, B. Paul, X. Wang, S. Kühl, and P. Strasser, *Structure, "Structure, Activity, and Faradaic Efficiency of Nitrogen-Doped Porous Carbon Catalysts for Direct Electrochemical Hydrogen Peroxide Production*, ChemSusChem, vol. 11, no. 19, pp. 3388–3395, 2018, doi: 10.1002/cssc.201801583.

[27]   D. Reyter, D. Bélanger, and L. Roué, *Study of the electroreduction of nitrate on copper in alkaline solution*, Electrochim. Acta, vol. 53, no. 20, pp. 5977–5984, 2008, doi: 10.1016/j.electacta.2008.03.048.

[28]   Y. Zhao, R. Shi, X. Bian, C. Zhou, Y. Zhao, S. Zhang, F. Wu, G. Waterhouse, L. Wu, C. Tung, and T. Zhang, "Ammonia Detection Methods in Photocatalytic and Electrocatalytic Experiments: How to Improve the Reliability of NH₃ Production Rates?, Adv. Sci., vol. 6, no. 8, 2019, doi: 10.1002/advs.201802109.

[29]   H. Jeong, J. Park, and H. Kim, *Determination of NH₄⁺ in environmental water with interfering substances using the modified nessler method*, J. Chem., vol. 2013, 2013, doi: 10.1155/2013/359217.

[30]   D. Anastasiadou, Y. van Beek, W. Chen, T. Wissink, A. Parastaev, E. Hensen, M. Costa-Figueiredo, *Morphology Changes of Cu2O Catalysts During Nitrate Electroreduction to Ammonia*, ChemCatChem, vol. 15, no. 10, 2023, doi: 10.1002/cctc.202201503.

[31]   L. Bai, F. Franco, J. Timoshenko, C. Rettenmaier, F. Scholten, H. Jeon, A. Yoon, M. Rüscher, A. Herzog, F.T. Haase, S. Kühl, S.W. Chee, A. Bergmann, and B. Roldan, *Electrocatalytic Nitrate and Nitrite Reduction toward Ammonia Using Cu2O Nanocubes: Active Species and Reaction Mechanisms*, J. Am. Chem. Soc., vol. 146, no. 14, pp. 9665–9678, 2024, doi: 10.1021/jacs.3c13288.

[32]   M. C. Biesinger, L. W. M. Lau, A. R. Gerson, and R. S. C. Smart, *Resolving surface chemical states in XPS analysis of first row transition metals, oxides and hydroxides: Sc, Ti, V, Cu and Zn*, Appl. Surf. Sci., vol. 257, no. 3, pp. 887–898, 2010, doi: 10.1016/j.apsusc.2010.07.086.

[33]   C. Zhu, A. Osherov, and M. J. Panzer, *Surface chemistry of electrodeposited Cu2O films studied by XPS*, Electrochim. Acta, vol. 111, pp. 771–778, 2013, doi: 10.1016/j.electacta.2013.08.038.

[34]   P. M. Krzywda, A. Paradelo Rodríguez, L. Cino, N. E. Benes, B. T. Mei, and G. Mul, *Electroreduction of NO3− on tubular porous Ti electrodes*, Catal. Sci. Technol., pp. 3281–3288, 2022, doi: 10.1039/d2cy00289b.

[35]   M. C. O. Monteiro, A. Goyal, P. Moerland, and M. T. M. Koper, *Understanding Cation Trends for Hydrogen Evolution on Platinum and Gold Electrodes in Alkaline Media*, ACS Catal., vol. 11, no. 23, pp. 14328–14335, 2021, doi: 10.1021/acscatal.1c04268.

[36]   A. Goyal and M. T. M. Koper, *Understanding the role of mass transport in tuning the hydrogen evolution kinetics on gold in alkaline media*, J. Chem. Phys., vol. 155, no. 13, 2021, doi: 10.1063/5.0064330.

[37]   E. Murphy, Y. Liu, I. Matanovic, M. Rüscher, Y. Huang, A. Ly, S. Guo, S. Zang, X. Yan, A. Martini, J. Timoshenko, B. Roldan, I.V Zenyuk, X. Pan, E. Spoerke, and, P. Atanassov, *Elucidating electrochemical nitrate and nitrite reduction over atomically-dispersed transition metal sites*, Nat. Commun., vol. 14, no. 1, p. 4554, Jul. 2023, doi: 10.1038/s41467-023-40174-4.

[38]   W. Liao, J. Wang, G. Ni, K. Liu, S. Chen, Q. Wang, Y. Chen, T. Luo, X. Wang, Y. Wang, W. Li, T.-S. Chan, C. Ma, H. Li, Y. Liang, W. Liu, J. Fu, B. Xi, and M. Liu, *Sustainable conversion of alkaline nitrate to ammonia at activities greater than 2 A cm⁻²*, Nat. Commun., vol. 15, no. 1, pp. 1–12, 2024, doi: 10.1038/s41467-024-45534-2.

[39]   Z.Cui, F. Ge, Y. Lin, L. Wang, L. Lei, H. Tian, M. Yu, and X. Wang, *Corrosion behavior of AZ31 magnesium alloy in the chloride solution containing ammonium nitrate*, Electrochim. Acta, vol. 278, no. 3, pp. 421–437, 2018, doi: 10.1016/j.electacta.2018.05.059.

[40]   M. T. De Groot and M. T. M. Koper, *The influence of nitrate concentration and acidity on the electrocatalytic reduction of nitrate on platinum*, J. Electroanal. Chem., vol. 562, no. 1, pp. 81–94, 2004, doi: 10.1016/j.jelechem.2003.08.011.

[41]   G. A. Cerrón-Calle, A. S. Fajardo, C. M. Sánchez-Sánchez, and S. Garcia-Segura, *Highly reactive Cu-Pt bimetallic 3D-electrocatalyst for selective nitrate reduction to ammonia*, Appl. Catal. B Environ., vol. 302, no. July 2021, 2022, doi: 10.1016/j.apcatb.2021.120844.

[42]   M. Duca and M. T. M. Koper, *Powering denitrification: The perspectives of electrocatalytic nitrate reduction*, Energy and Environmental Science, vol. 5, no. 12. pp. 9726–9742, 2012, doi: 10.1039/c2ee23062c.

[43]   Y. Wang, C. Wang, M. Li, Y. Yu, and B. Zhang, *Nitrate electroreduction: Mechanism insight,: In situ characterization, performance evaluation, and challenges*, Chem. Soc. Rev., vol. 50, no. 12, pp. 6720–6733, 2021, doi: 10.1039/d1cs00116g.

[44]   H. Zhu, S. Dong, X. Du, H. Du, J. Xia, Q. Liu, Y. Luo, H. Guo, and T. Li, *Defective CuO-rich CuFe$_2$O$_4$ nanofibers enable the efficient synergistic electrochemical reduction of nitrate to ammonia*, Catal. Sci. Technol., vol. 12, no. 16, pp. 4998–5002, 2022, doi: 10.1039/D2CY00910B.

[45]   J Li, G. Zhan, J. Yang, F. Quan, C. Mao, Y. Liu, B. Wang, F. Lei, L. Li, A. Chan, L. Xu, Y. Shi, Y. Du, W. Hao, P. Wong, J. Wang, S. Dou, L. Zhang, and J. Yu, *Efficient Ammonia Electrosynthesis from Nitrate on Strained Ruthenium Nanoclusters*, J. Am. Chem. Soc., vol. 142, no. 15, pp. 7036–7046, 2020, doi: 10.1021/jacs.0c00418.

Chapter 4

Increasing the Energy Efficiency of NO$_3^-$RR to NH$_3$

CHAPTER 4 ENERGY EFFICIENCY OF FLOW-CELL PROCESS

4.1 Abstract

Reducing NO$_3^-$ to NO$_2^-$ is considered the rate-determining step of the NO$_3^-$RR process, allowing the formed NO$_2^-$ intermediate to follow two possible routes. The first route follows the direct electrochemical reduction of NO$_3^-$ to NH$_3$. This necessitates the simultaneous acceleration of NO$_3^-$RR and NO$_2^-$RR to NH$_3$, presenting a challenging yet promising approach for efficient ammonia generation. This study introduces a tandem NO$_3^-$RR process, involving sequential electrochemical processes converting NO$_3^-$ to NO$_2^-$ and then NO$_2^-$ to NH$_3$, with a composite electrode with Cu and TiO$_2$/Cu faces, in an optimized flow-cell configuration. The results demonstrate a Faradaic Efficiency of 97%, selectivity of 80%, and a productivity yield of 0.45 mmol·h^{-1}·cm^{-2}. The cooperative approach of intrinsic properties of the electrode composition and cell configuration enables high full-cell energy efficiencies of 29%.

In summary, our tandem NO$_3^-$RR process represents a significant advancement in addressing the challenges of sustainable ammonia production, providing a promising approach for efficient and environmentally friendly energy applications.

4.2   Introduction to Chapter 4.

In this chapter, we extend the use of Cu-based electrocatalysts for NO$_3^-$RR to NH$_3$ by utilizing flow-cells aiming to enhance energy-related parameters such as energy efficiencies and consumption. A novel cell configuration is introduced, which improves energy efficiency compared to other simpler configurations also presented here and achieves values comparable to those with high-efficiency studies conducted in the field.

During NO$_3^-$RR, the NO$_2^-$ ion appears as the most stable intermediate no-matter the electrocatalysts is in use, including Cu-based ones, which are particularly selective for producing NO$_2^-$ ions at less negative applied potentials. This selectivity can be exploited by coupling Cu-based catalysts with others that have a better affinity for converting NO$_2^-$ to NH$_3$. Notably, as already observed in Chapter 3, and according to other studies, Ti-based materials have a high adsorption capability for the *NO$_2^-$ intermediate [11], [12] and exhibit high selectivity towards NH$_3$. Therefore, a tandem system combining Cu-based and Ti-based catalysts in a proper configuration is predicted to synergistically enhance NO$_3^-$RR, maximizing NH$_3$ generation.

To differentiate the study in this chapter from the one conducted in **Chapter 3**, which focuses on similar materials, we introduce TiO$_2$ nanoparticles as the Ti-based material while maintaining Cu-based catalysts as the more active one for the reaction. Although the studies are not directly comparable, **Chapter 4** represents an evolution that builds on established optimal parameters for NO$_3^-$RR to NH$_3$ and aims to increase ammonia productivity and the Energy Efficiency at global and semi-cell levels.

In summary, Chapter **4** presents a tandem approach for the NO$_3^-$RR-to-NH$_3$. That involves the development of a cascade reduction system, which incorporates TiO$_2$ nanoparticles as a catalyst deposited on a Cu-based support. Offering insights into various aspects of the electrochemical cell configurations, including Faradaic efficiencies, selectivity towards different N-based products, and preliminary scaling-up values for NO$_3^-$RR under alkaline conditions at ambient temperature. By integrating cell engineering principles, utilizing materials with diverse intrinsic properties, and optimizing operating conditions, we have achieved notable results [20].

4.3 Copper and TiO₂ electrocatalysts for NO₃⁻RR to NH₃:

Summarizing the key points of catalytic activity of Cu and Ti-based catalysts defined in **Chapter 3.**

Copper-based Catalysts:

Adsorption: NO₃⁻ ions adsorb onto Cu active sites, particularly on Cu (1 1 1) facets, in neutral and alkaline conditions.

Energy Barriers: Low energy barriers for key steps like NO₃⁻ to NO₂⁻ reduction and subsequent hydrogenation to NH₃.

Electronic Structure: The d-band center position optimizes adsorption strength of intermediates, enhancing reaction kinetics.

Titanium-based Catalysts:

Defects: Oxygen Vacancies (OV) and Titanium Vacancies (TiV) in TiO₂ enhance catalytic activity.

OV Benefits: By creating localized states, NO₃⁻ binding and electron transfer improves, lowering the activation energy for N-O bond breaking, and suppressing side reactions like HER.

4.4 Methods.

The experimental methods used were outlined in **Chapter 2**. Briefly, using a flow cell, electrolysis experiments were carried out using two electrolytes (1) 0.1M KNO₃ + 1M KOH for NO₃⁻RR and (2) 0.1M KNO₂ + 1M KOH for NO₂⁻RR. A series of different applied potentials and current densities have been used for evaluating the effects in different efficiency parameters. IC has been used for quantification of ions in the liquid phase (NO_3^- and NO_2^-) and UV-vis spectroscopy for NH₃. Gas chromatography was used for quantifying H₂ produced during electrolysis. From the concentrations, we calculate charge, products and reactants related parameters, FE, SE and Yield productivity. With these values and the electrochemical performance indicators, we calculate energy related parameters EE_{CELL} and $EE_{Half-Cell}$. The electrolysis processes were run at each E_W (-0.4 to -0.8 V vs RHE) and j (-35, -50, -70, 90, 110 mA·cm⁻²) for different cell configurations and electrodes. Details of the electrode preparation are described below.

Cu. Foil purchased from alfa Aesar (0.5 mm tick, 99.99% metal basis) is defined here as an electrode and active support. Before electrolysis process, the foil underwent a pre-treatment process aimed at eliminating native oxides present on the surface. For that, initially, the Cu foil was subjected to a 15-minute sonication process in a solution comprising acetone, isopropyl alcohol, and ethanol in a ratio of 1:1:1. This step effectively removed both organic and inorganic oils from the surface. Subsequently, the material underwent a second treatment involving immersion in an acidic solution (10% H_2SO4 + 36 g L^{-1} $C_6H_8O_7$) while being sonicated for 5 minutes. Finally, the material was thoroughly rinsed with Milli-Q water for 10 minutes.

TiO$_2$ NPs. Titania nanoparticles (defined here as the catalyst) were fabricated through pulsed laser ablation in liquid (PLAL method) as it offers catalytic enhancement due to the formation of defect-rich NPs [6], [7]. A titanium target was ablated using a 1064 nm neodymium-doped yttrium aluminum garnet (Nd:YAG) laser, with pulse duration of 10 ps, repetition rate of 1000 kHz, and laser power of 43 W. The laser was coupled with a galvanometer scanner with (scanning speed 20 m/s) and an f-theta lens (focal length 167 mm) to steer and focus the laser beam into an Archimedean spiral pattern. The PLAL was performed in a flow chamber[8]–[10] and ethanol was chosen as the liquid carrier due to capability to act as capping agent to hinder the growth of TiO$_2$ NPs (size quenching)[11]. The colloidal dispersion of TiO$_2$ NPs in ethanol was partially evaporated until it reached a concentration of 0.125 mg·mL^{-1}.

TiO$_2$@Cu electrode. Schematically represented in **Figure 4.1**. To prepare this electrode, Cu Foil served as an active support, after being subjected to the same pre-treatment described above. The catalyst ink was formulated utilizing the TiO$_2$ NPs solution outlined in the previous section. To achieve the desired concentration, the solution was diluted to 0.0625 mg·mL^{-1} using anhydrous ethanol, and a binder solution of 2% wt. Nafion perfluorinated solution was incorporated. The resulting ink composition comprised 0.50 mL of 0.125 mg·mL^{-1} TiO$_2$ NPs, 0.48 mL of ethanol, and 0.02 mL of the binder. This prepared ink was drop-casted onto the Cu support covering a surface area of 1 cm^2 and finally dried for 3 h in a vacuum oven. The resulting composition of the electrode was 0.0625 mg·cm^{-2} TiO$_2$.

Cu Plate + **TiO$_2$ Nanoparticles** = **TiO$_2$@Cu electrode**
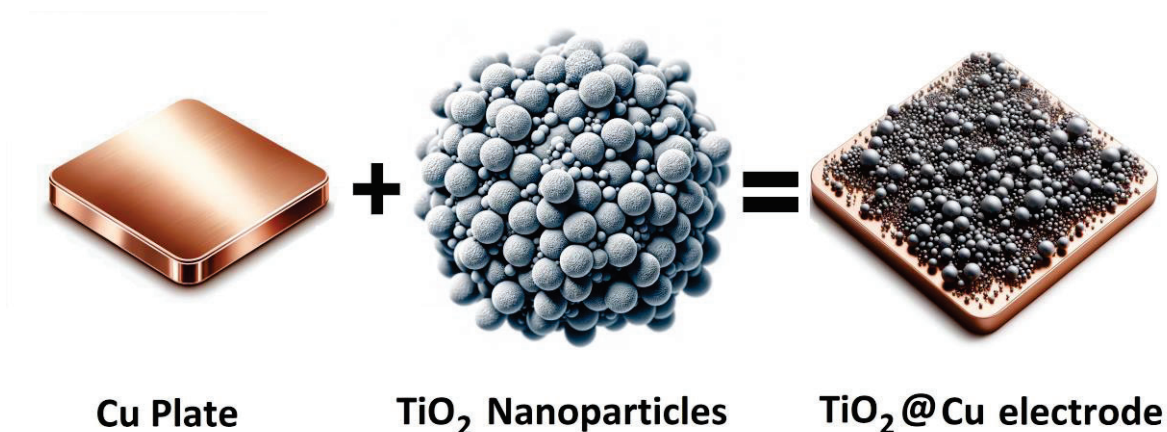
Figure 4.1 TiO$_2$@Cu electrode preparation scheme.

4.5 TiO2@Cu electrode Characterization.

4.5.1 TiO$_2$ NPs HR-TEM.

The HR-TEM images in **Figure 4.2** depict the surface of the PLAL-produced TiO$_2$ nanoparticles. The images reveal anatase tetragonal phases of TiO$_2$, with no evidence of rutile or other crystalline phases. The TiO$_2$ anatase crystalline phase is associated with high electrochemical efficiency for NO_3^-RR-to-NH_3 when combined with Cu-based materials. According with the observations of Wahyu P. et al., the strong interaction between Cu-based nanoparticles and TiO$_2$, particularly with the dominant (101) facet exposure, results in electron-deficient Cu, efficient electron transfer, and stronger binding of the *NO$_2$ intermediate. This interaction enhances the hydrogenation process in the NO_3^- reduction reaction, facilitating selective NH$_3$ synthesis. This robust interaction leads to electron transfer from the Cu nanoparticles to the TiO$_2$ based material, making the Cu-based more effective for NO_3^- reduction [23], [24].
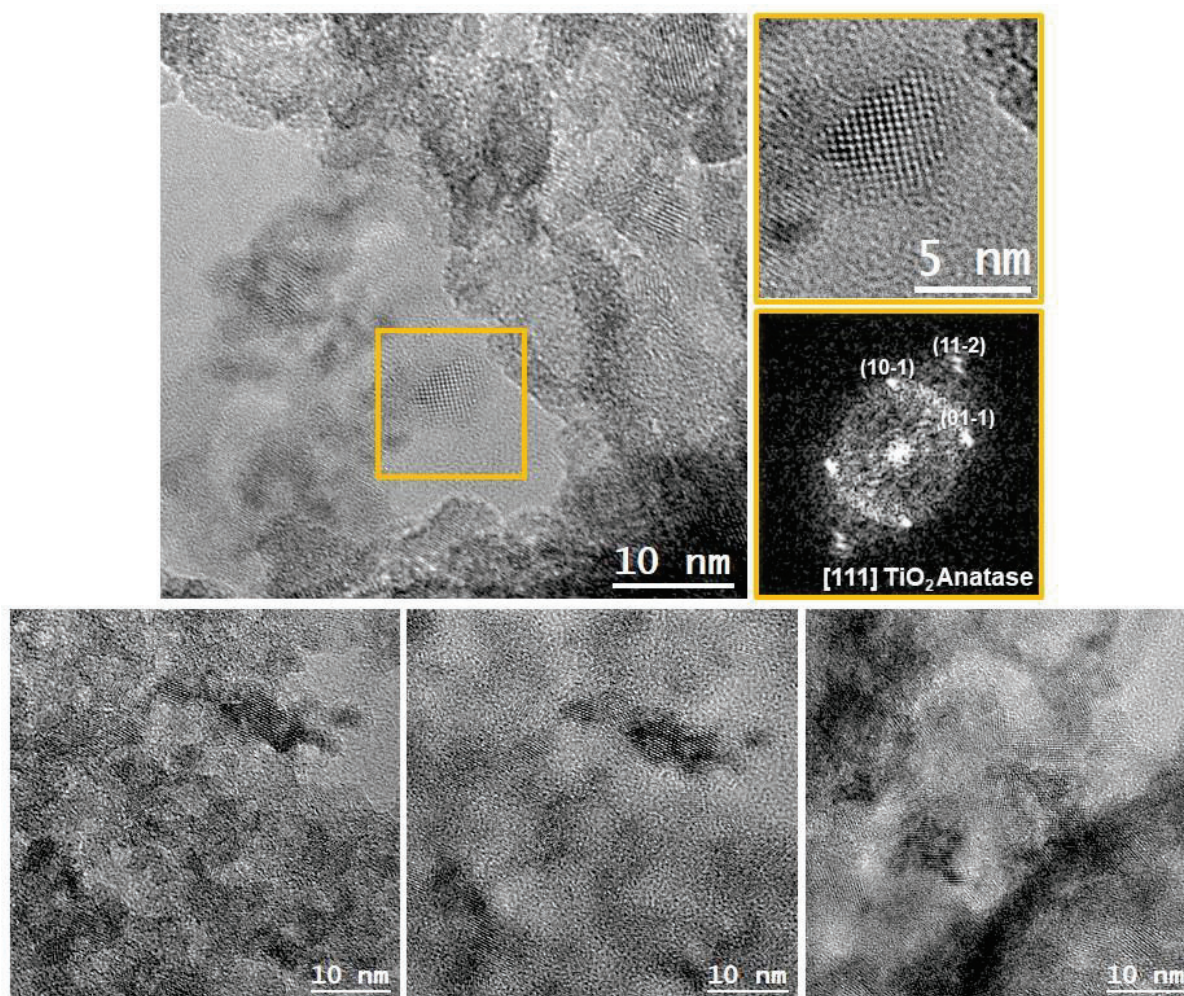
Figure 4.2 TiO_2 HR-TEM images evidencing the anatase tetragonal phases of the nanoparticles.

4.5.2 TiO$_2$@Cu SEM.

The SEM images in **Figure 4.3 a** and **b** illustrate the irregular surface of the Cu substrate, featuring numerous defects that might contribute to the electrode activity. These defects introduce multi-crystalline phases and modify the active surface area (ECSA) of the catalyst, known factors affecting adsorption behavior and catalytic activity [25]. Moving on to the synthesized TiO_2 nanoparticles (**Figure 3.10 c** before and **d** after electrolysis), they adhere to the Cu substrate forming the composite electrode. With the SEM, it is possible to see an aggregated porous structure that increases the active surface area, facilitating the absorption of NO_3^-/NO_2^- ions and intermediates, as well as the subsequent release and diffusion of products [7], [26].
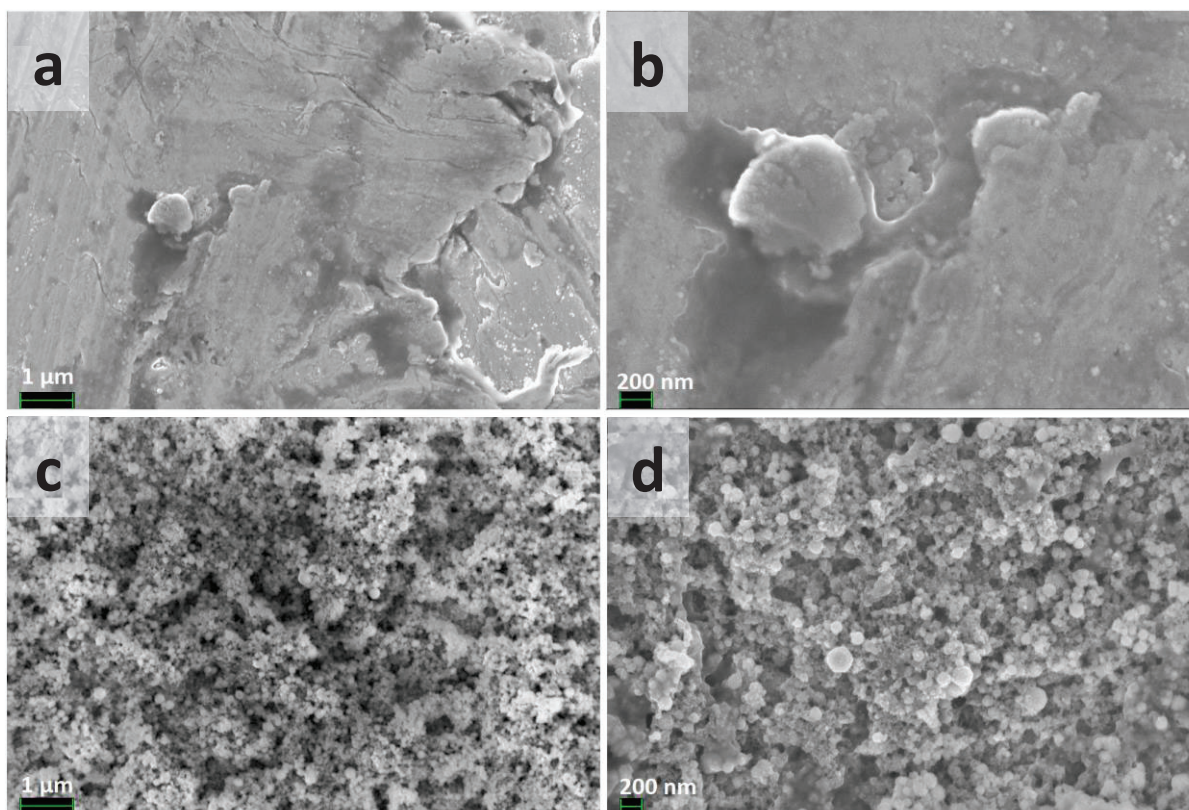
Figure 4.3 SEM images of a-b) Cu active support. c-d) TiO$_2$@Cu

4.5.3   TiO$_2$@Cu EDX analysis.

EDX analysis (**Figure 4.4 a** to **d**) provides insight into the atomic percentage of the primary Ti- and Cu-based materials in the TiO$_2$@Cu electrode. Despite initial aggregation in the ink, the nanoparticles exhibit a uniform distribution. The cyan mapping represents the aggregated TiO$_2$ particles on the electrode surface, while the yellow distribution displays the underlying Cu substrate. According to EDX analysis, the estimated atomic composition is 4.5% Ti, 39% Cu, 21% O, 30% C and 6% F. The notable presence of C in the catalyst structure is attributed to the Nafion-117 binder used during ink preparation.
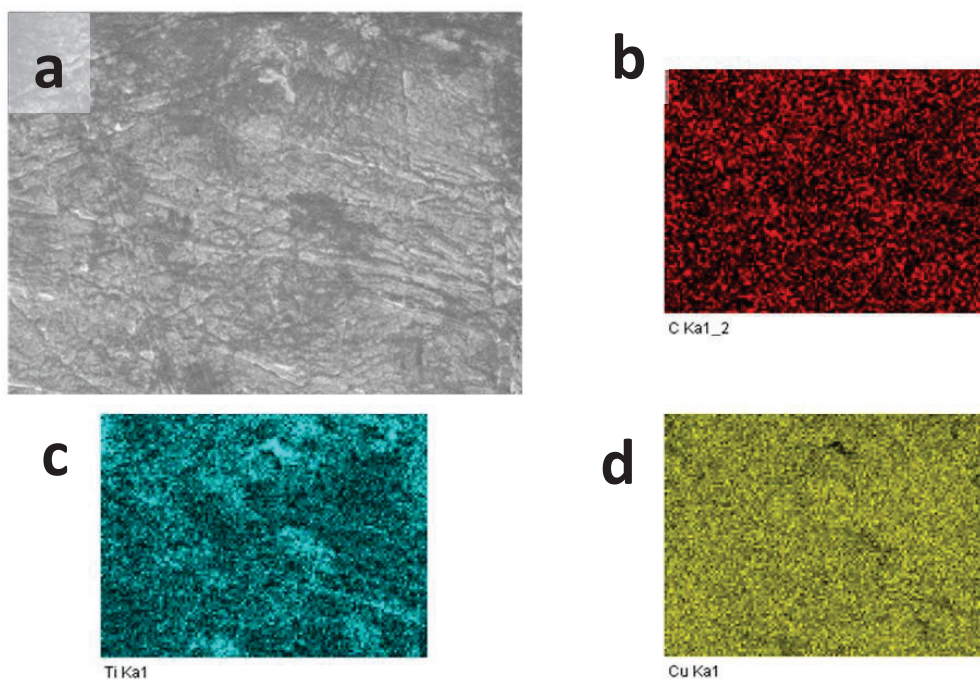
Figure 4.4 EDX analysis of TiO$_2$@Cu electrode.

4.5.4   TiO$_2$@Cu XRD analysis.
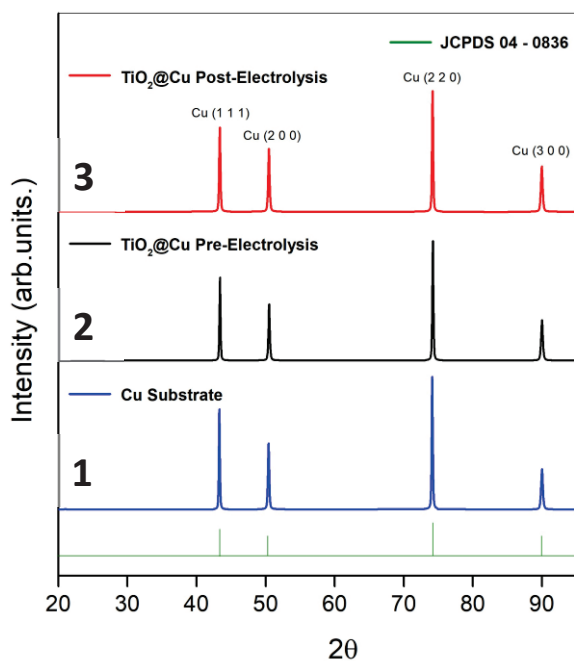
Figure 4.5 XRD patterns obtained from the Cu substrate, and the TiO$_2$@Cu electrode before and after chronoamperometry tests.

Figure 4.5 illustrates the XRD patterns obtained from the Cu substrate (1), and the TiO$_2$@Cu electrode before (2) and after (3) CA tests. In the case of the Cu substrate, the patterns exhibit three highly textured peaks located at the 2θ angles of 43.3° and 73.99°, corresponding to the (111) and (220)

planes of face-centered cubic Cu (JCPDS 04–0836). Additionally, two less pronounced peaks are observed at 50.4° and 90.2°, well correlated with the (200) and (300) planes **[26]**. For the TiO$_2$@Cu electrode, the same peaks have been observed, denoting minimum changes in the structure of the Cu-base component of the electrode. As anticipated, the deposition of nanoparticles did not alter the plane distribution of the support. No peak correlated with the Ti-based materials was observed, as expected by the small size of the TiO$_2$ nanoparticles. In the post electrolysis analysis, the TiO$_2$@Cu electrode did not show signals of oxidation.

4.5.5   TiO$_2$@Cu Raman spectroscopy.
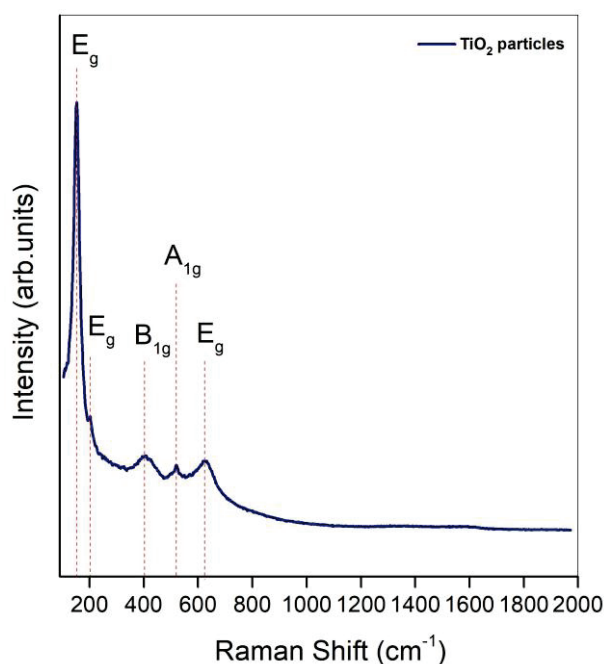
Figure 4.6 Raman spectroscopy analysis of the TiO$_2$@Cu electrode before electrolysis.

Figure 4.6 presents the structural insights derived from Raman spectroscopy. Specifically, five distinct Raman active modes of anatase TiO$_2$ with symmetries E$_g$, E$_g$, B$_{1g}$, A$_{1g}$, and E$_g$ were identified at frequencies of 143, 196, 392, 510, and 639 cm^{-1}, respectively. These characteristic vibrational frequencies and their corresponding ratios are indicative of the anatase phase of TiO$_2$ **[27]**.

4.5.6   TiO₂@Cu HR-XPS analysis.

Figures 4.7 a to d depict the XPS analysis of the main components of the TiO_2@Cu electrodes before and after electrolysis. In the high-resolution spectrum of Cu 2p (a), peaks at 933.2 eV and 955.9 eV correspond to the sub-levels $2p_{3/2}$ and $2p_{1/2}$ of Cu^0 / Cu^+. These are further deconvoluted into their respective constituents: Cu^0 at 932 eV and Cu^+ at 933 and 935 eV for Cu $2p_{3/2}$, and Cu^0 at 951 eV and Cu^+ at 952 and 954 eV for Cu $2p_{1/2}$. Additional peaks at 943.2 eV and 964.2 eV, indicative of satellite peaks typically attributed to the presence of Cu^{2+} on the surface, are also registered. The intensity of these satellite peaks decreased after electrolysis (b), suggesting the electrochemical reduction of superficial Cu^{2+} [28]–[30]. In general, Cu_2O and CuO have also been ascribed to have electrocatalytic properties for the NO_3^- to NH_3 reaction [31], [32].
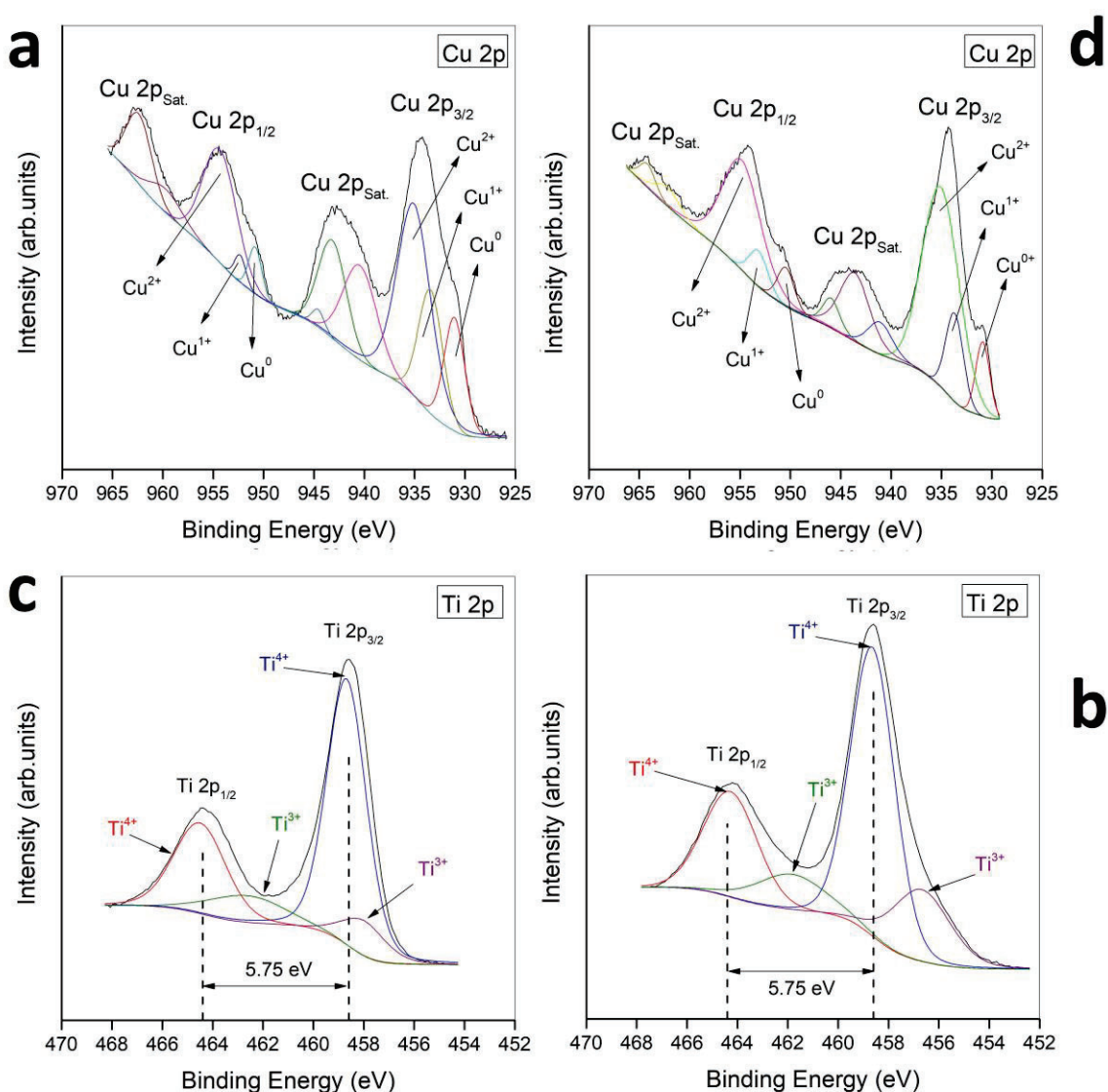
Figure 4.7 HR-XPS analysis of the main components of the TiO₂@Cu electrodes.

Figures 4.7 **c** and **f** present the HR-XPS spectrum for the Ti 2p level of the electrode pre- and post-electrolysis, featuring four discernible peaks corresponding to titanium dioxide (Ti^{4+}) and titanium sub-dioxide (Ti^{3+}) in the 2p$_{3/2}$ and 2p$_{1/2}$ sub-levels, respectively [33]. These peaks are identified as Ti^{4+} 2p$_{1/2}$ at 464.4 eV, Ti^{4+} 2p$_{3/2}$ at 458 eV, Ti^{3+} 2p$_{1/2}$ at 461.8 eV, and Ti^{3+} 2p$_{3/2}$ at 460.2 eV. The separation between peaks of the corresponding sub-levels 2p$_{3/2}$ and 2p$_{1/2}$ is 5.75 eV, consistent with the standard binding energy of TiO$_2$. Notably, the presence of peaks corresponding to Ti^{3+} (2p$_{1/2}$ and 2p$_{3/2}$) might indicate the existence of OV in the surface layers [34]–[36], a result of the synthesis process involving laser ablation for obtaining the TiO$_2$ nanoparticles that is detailed in **Section 5.2**.

4.6 TiO$_2$@Cu. Electrochemical Characterization.

An electrochemical profiling of the electrode for NO$_3^-$RR and NO$_2^-$RR to NH$_3$ was conducted through LSV and is presented in **Figure 4.8 a**. Employing an electrolyte composition of 0.1 M KNO$_3$ + 1 M KOH for NO$_3^-$RR and 0.1 M KNO$_2$ + 1 M KOH for NO$_2^-$RR, the LSVs were executed with a scan rate of 20 mV s^{-1}, spanning a potential window from -0.8 V to 0.15 V vs RHE. LSVs were also conducted in blank electrolyte (1M KOH). The electrode, comprising TiO$_2$ nanoparticles deposited on a 0.2 cm^2 copper disk with a final nanoparticle concentration of 0.0625 mg cm^{-2}, exhibited distinctive peak patterns during NO$_3^-$RR. Four discernible peaks (P$_1$, P$_2$, P$_3$, and P$_4$) manifested within varying potential ranges: P$_1$ emerged between 0 to 0.1 V vs RHE, P$_2$ between -0.2 and -0.1 V vs RHE, P$_3$ between -0.4 and -0.35 V vs RHE, and P$_4$ between -0.55 and -0.5 V vs RHE as observed in **Figure 4.8a**. Notably, peak P$_1$ exclusively appeared during NO$_3^-$RR, corresponding to the RDS involving a two-electron transfer reaction associated with the conversion NO$_3^-$ to NO$_2^-$ [37]. Further scrutiny revealed that peak P$_2$, observed for both NO$_3^-$RR and NO$_2^-$RR, corresponds to a four-electron transfer reaction converting NO$_2^-$ to NH$_2$OH (hydroxylamine). Subsequently, NH$_2$OH may undergo further reduction to NH$_3$, elucidating the observed low concentration of NH$_2$OH for higher overpotentials.

Intriguingly, both NO$_3^-$RR and NO$_2^-$RR exhibited the emergence of Peak P$_3$ within the applied potentials of -0.4 to -0.35 V vs RHE, aligning with prior studies that attribute this peak to the reduction of NO$_2^-$ to NH$_3$ involving a six-electron transfer reaction [38]. Remarkably, the blank electrolyte (1 M KOH) exhibited no discernible peaks, underscoring the specificity of the observed electrochemical responses to the NO$_3^-$ and NO$_2^-$ ions. Importantly, during NO$_3^-$RR, the current densities associated with Peaks P$_2$ and P$_3$ resulted to be higher; this effect can be attributed to the predominant concentration of NO$_2^-$ ions in the interphase between the electrolyte and electrode surface. These NO$_2^-$ ions, formed during the RDS, exhibited limited desorption from the electrode surface in Cu-based electrodes [39], mitigating diffusion limitations, a phenomenon contrary to the NO$_2^-$RR where ions had to traverse from

the bulk to the electrode surface. Aligned with these observations, the increased HER overpotential observed for NO$_3^-$RR can be explained by digging into the process mechanism established by several prior studies. These investigations have delineated that the subsequent deoxygenation and hydrogenation steps in NO$_3^-$RR involve the participation of adsorbed hydrogen (H$_{ads}$), and its consumption can be influenced by the concentration of NO$_3^-$ in the system, given that all N-intermediates generated from NO$_3^-$ undergo reactions with H$_{ads}$ until NH$_3$ is produced. At lower overpotentials (P1), the sluggish rate of H$_{ads}$ generation predominately results in the production of non-hydrogenated N-intermediates, such as NO$_2^-$, irrespective of the $C_{NO_3^-}$. However, at higher overpotentials (P$_3$ or P$_4$), the elevated rate of H$_{ads}$ generation can significantly enhance the N-intermediate further reduction, particularly when $C_{NO_3^-}$ is high. Therefore, the dynamic equilibrium of H$_{ads}$ is maintained and the competitive HER is mitigated [10], [40].
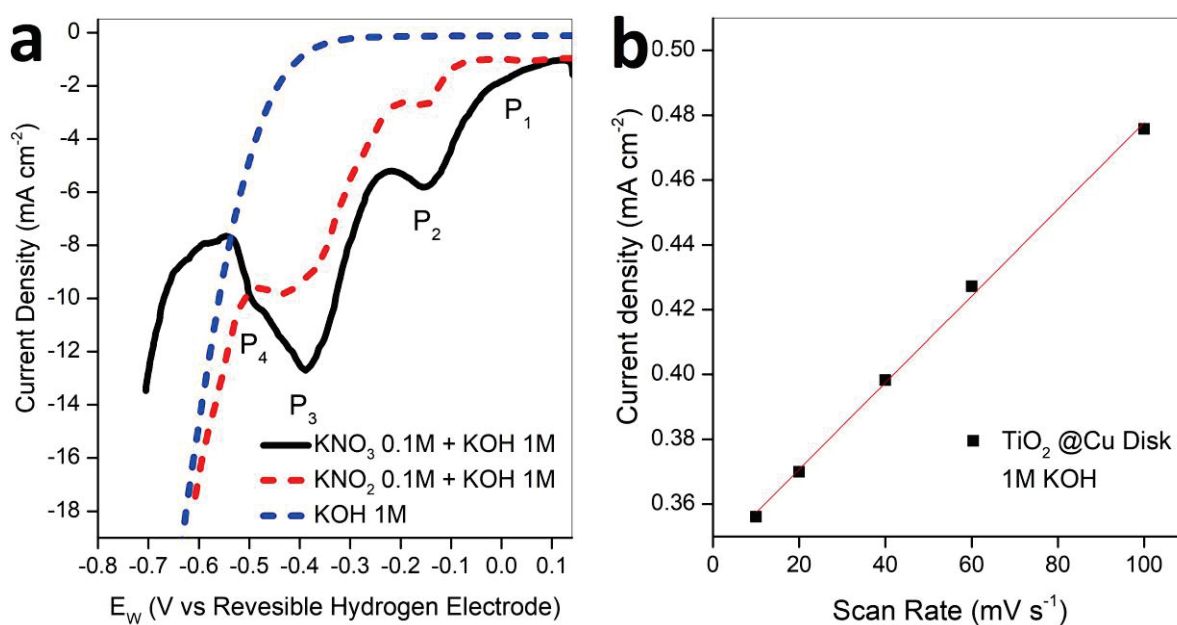
Figure 4.8 a) Linear swept voltammetry for different electrolytes using the TiO$_2$@Cu electrode; b) current density as function of scan rate for determining the double layer capacitance.

When the current density is plotted as a function of the scan rates for the TiO2@Cu electrode, the double layer capacitance (C_{DL}) is determined by correlating it with the slope of the linear region of the capacitive current in a potential range where no faradaic processes take place (-0.1 to 0.1 V vs Ag/AgCl$_{3.5 M KCl}$). This correlation was determined through a series of cyclic voltammetry experiments at various scan rates, as depicted in **Figure 4.8**. Using the standard value of 40 µF/cm² for specific capacitance, the ECSA of the electrode was calculated to be 3.35 cm²/cm²$_{geo}$.

4.7 NO$_2^-$RR and NO$_3^-$RR to NH$_3$ in the two-channels flow cell.

Cell configurations were established in **Chapter 2**, however, here a brief description is presented. The electrochemical two channels flow cell (**Figure 4.9**) was assembled with a current collector that exposes 1 cm^2 geometric area of the WE. A DSA and Ag/AgCl were the CE and RE respectively. The anolyte was circulating through channel 1 and the catholyte trough channel 2. A CEM was placed in the cell to separate the anolyte and catholyte, the electrolysis time was defined in 2 hours and the electrolyte was circulated using a peristaltic pump sending a flow of 170 mL·min^{-1}.
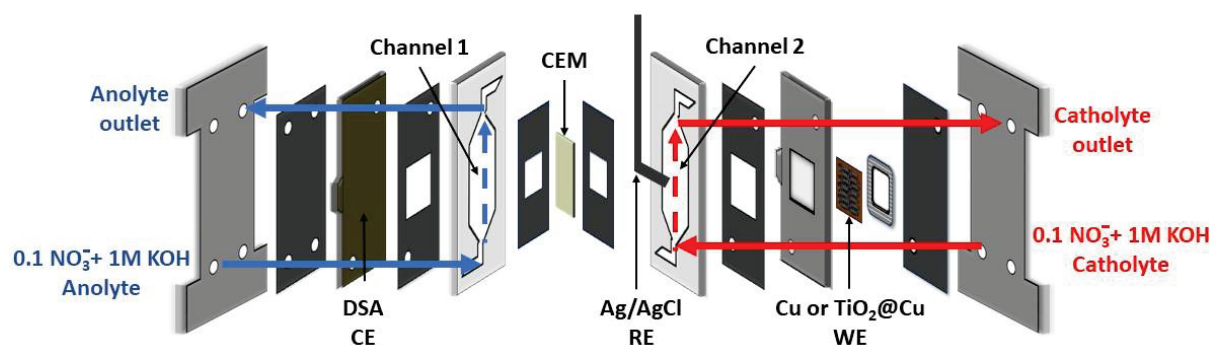
Figure 4.9 Electrochemical two-channels flow cell adapted for a 1 cm^2 working electrode (Configuration 1).

4.7.1 The NO$_3^-$ to NO$_2^-$ reaction. Best electrode for accumulating intermediates.

Cu-based electrodes have already shown a high activity for the RDS of the reaction and a high selectivity for the intermediate NO$_2^-$ during NO$_3^-$RR. For the following results, Cu electrode performance is compared with that observed for the TiO$_2$@Cu electrode under the experimental conditions given in Section 5.3. **Figure 4.10** shows the FE distribution of the NO$_3^-$RR to NO$_2^-$. The green bars represent the percentage in FE of the total NO$_2^-$ produced during 2 hours of chronoamperometry for the Cu electrode, while the black bars represent that for the TiO$_2$@Cu electrode. Cu electrodes have shown a higher FE for all applied potentials if compared with the TiO$_2$@Cu, reaching a maximum value of 65% toward NO$_2^-$ at the higher applied potential of the range (-0.4V vs RHE). For more negative E_W, FE is reduced given the higher generation of N-based products or the HER, reaching values lower than 10%. As explored in the introduction of the chapter, the RDS for the NO$_3^-$RR is the nitrate dissociation ($NO_3^* + * \rightarrow NO_2^* + O^*$) and the mechanism presented in several studies by the following steps.
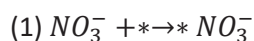
(1) $NO_3^- + * \rightarrow * NO_3^-$ Nitrate adsorption on the active site.
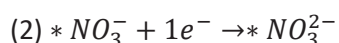
(2) $* NO_3^- + 1e^- \rightarrow * NO_3^{2-}$ First electron transfer to form NO_3^{2-} **intermediate.**

(3) $* NO_3^{2-} + H_2O \rightarrow * HNO_3^- + OH^-$ Water dissociation and formation of $\boldsymbol{HNO_3^-}$ **intermediate.**

(4) $* HNO_3^- + 1e^- \rightarrow * NO_2^- + OH^-$ Second electron transfer and formation of nitrite.

The RDS of the reaction is primarily associated with the conversion of NO_3^- to NO_2^-. However, divergent findings exist in the literature regarding the localization of this crucial step. Some studies suggest that the RDS occurs during the absorption of NO_3^- onto the catalyst surface (1), whereas others, employing density functional theory (DFT) calculations, propose that it takes place during the first electron transfer reaction, leading to the formation of the NO_3^{2-} intermediate (2) [41]. Despite these discrepancies in mechanisms governing the RDS, it is noteworthy that the adsorbed NO_2^- species on the catalyst surface, resulting from the initial reaction, can follow two distinct pathways. It can either undergo further chemical and electrochemical reduction on the surface to yield other products, or it can desorb from the catalyst surface and reintegrate into the bulk electrolyte. Cu-base electrodes have shown a high SE and FE towards NO_2^- at lower overpotentials, and this property can be exploited in the design of processes in tandem or cascade steps applying a different type of active site more specialized in catalyzing the reaction NO_2^- to NH_3. The higher activity of Cu is also observed if the specific NO_3^- conversion by charge unit is compared. This value can give an idea of how efficiently a catalyst material utilizes the transferred charge for reducing the concentration of NO_3^- during electrolysis. For lower overpotential, Cu have shown better activity, something not observed at more cathodic potential.
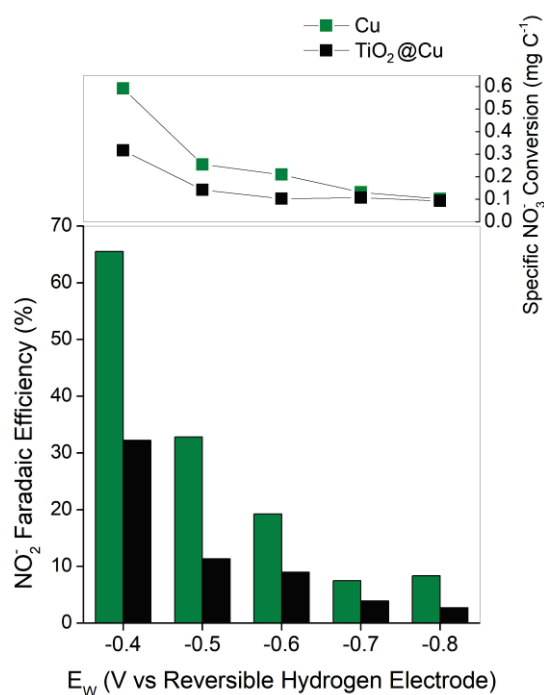
Figure 4.10 FE towards NO_2^- at different applied potentials in a 2 hours chronoamperometry test for the electrodes Cu and $TiO_2@Cu$ in a two-channel electrochemical flow cell.

The propensity of certain materials, such as copper (Cu), to predominantly liberate NO_2^- as the main product at low overpotentials has been the subject of investigation in numerous studies. These investigations have highlighted a correlation between the HER and the applied overpotentials, particularly in materials exhibiting weak hydrogen adsorption. The primary focus has been on mitigating the competitive reaction of NO_3^- reduction by optimizing overpotentials. However, at lower overpotentials, the cleavage of N–O bonds (deoxygenation) in the adsorbed NO_2^- species emerges as a significant determinant in the overall NO_3^-RR process. This is attributed to the insufficient concentration of adsorbed hydrogen at these conditions. Consequently, NO_2^- intermediates are liberated and accumulate in the bulk electrolyte, further influencing the reaction kinetics and product distribution [42], [43]. In the next sections, this property of Cu is addressed and considered for optimizing the generation of NH_3.

4.7.2 The NO_2^- to NH_3 reaction. Defining the order for a cascade/tandem configuration.

According to the electrochemical characterization of the TiO_2@Cu electrodes in **Section 4.8**. The Evaluation of NO_2^-RR can be conducted at the E_W window ranging from -0.4 V to -0.8V vs RHE for potentiostatic studies, similar to the previous section. The results of FE and SE towards NH_3 are shown in **Figure 4.11.** The electrodes evaluated here were the pristine Cu Foil and the TiO_2@Cu, both exposing a 1 cm^2 geometric areas, KNO_2 0.1 M+KOH 1M electrolyte and duration of 2hs.
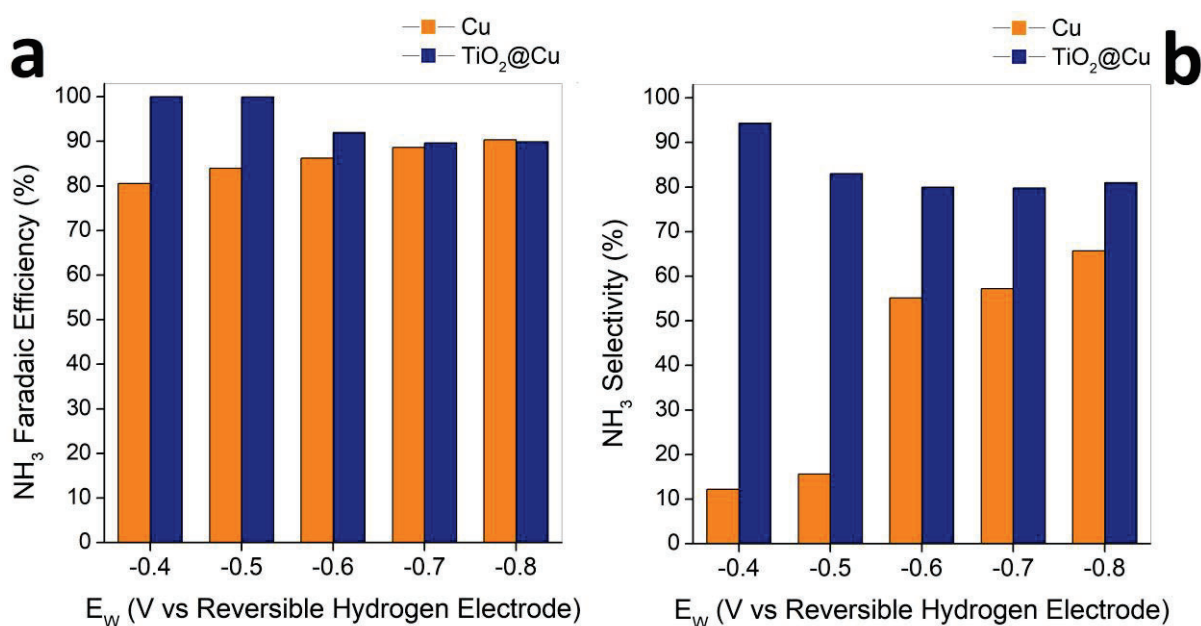
Figure 4.11 a) FE and (b) SE towards NH_3 for Cu and TiO_2@Cu electrodes for the NO_2^-RR and potentiostatic 2 hours electrolysis.

As observed in **Figure 4.11a,** the TiO_2@Cu FE approaches 99% at applied potentials of -0.4 V and -0.5 V vs RHE. As the potential becomes more cathodic, the values gradually decrease and stabilize at approximately 90% for the applied potentials of -0.7 V and -0.8 V vs RHE. Conversely, the Cu electrode exhibits an opposite trend, with FE increasing at more cathodic potentials, ranging between 80% at -0.4 V vs RHE and 90% at -0.8 V vs RHE. Cu electrodes demonstrate lower FE at less negative potentials and the explanation can be found in a similar effect observed during NO_3^-RR, the decrease of hydrogen adsorption, resulting in low hydrogen coverage and slow *NH_x hydrogenation rate [44]. However, the incorporation of TiO_2 NPs on the Cu-support reduces the overpotential requirements for producing NH_3, enabling the achievement of remarkably high FE at high cathodic potentials. The activity of TiO_2 with defects for catalyzing NO_2^-RR has been investigated to understand the behavior of the catalyst. In **Section 4.7.6**, XPS analysis conducted on the TiO_2 NPs revealed peaks indicative of oxygen vacancies (OVs) in the structure. For instance, as introduced in the chapter, these defects have implications in catalytic activity of TiO_2 promoting both NO_2^- and NO_3^- to NH_3 reaction, especially NO_2^-RR when certain crystalline phases are present. NO_2^- ions can undergo adsorption and activation on TiO_2(1 1 1) surfaces containing OVs where one O atom of the NO_2^- molecule occupies the vacancy site, while the other remains exposed to the ambient environment. The process begins with the reduction of the exposed O atom by a H^+ and an $1e^-$, followed by the removal of the resulting O-species by a second proton-electron pair attack. Subsequently, three proton-electron pairs couple with nitrogen to form NH_3, leaving O bound to the vacancy site. Finally, this oxygen species is reduced by two protons to form H_2O. The potential-determining step in this process, denoted as *NO_2 + H^+ + $1e^-$ + eNO_2H, exhibits a positive energy of 0.75 eV. It is worth noting that the HER on the TiO_2(101) surface with oxygen vacancies is also considered due to the competitive nature of NO_2^-RR and HER under reduction conditions. Additionally, the study highlights that H atoms cannot be stably adsorbed on Ti^{3+} atoms, thereby favoring the adsorption of NO_2^- over H on the TiO_2(1 1 1) surface with OVs [16], [45].

In **Figure 4.11 b**, the SE toward NH_3 is depicted. Like the findings observed for the FE, both electrodes exhibit a comparable trend in SE toward NH_3. However, the lower values of SE toward NH_3 observed for Cu electrodes are attributed to the lower conversion of NO_2^- (reflected in a lower NH_3 productivity as observed in **Figure 4.12**) and the higher adsorption of NO_2^- on the electrolyte surface. This increased adsorption can potentially lead to an underestimation of the final concentration of NO_2^- in the electrolyte at the end of the electrolysis, affecting the calculations of SE.
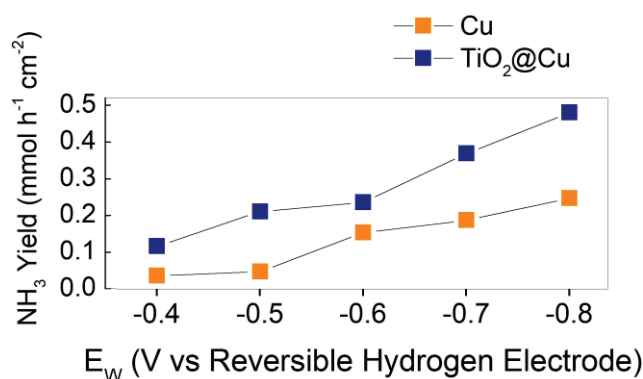
Figure 4.12 Productivity yield towards NH$_3$ during electrolysis for the electrodes Cu and TiO$_2$@Cu.

The findings obtained from the performance assessment of individual catalysts for both NO$_3^-$ and NO$_2^-$ RR offer insights into the potential arrangement of different active sites to facilitate a cascade reaction. Such a cascade reaction could be achieved using a tandem configuration, wherein the first active site is tailored to favor the absorption and reduction of NO$_3^-$ to NO$_2^-$. Subsequently, the desorption of NO$_2^-$ to the bulk electrolyte occurs, leading to the second active site, which is designed to preferentially adsorb and reduce NO$_2^-$ to the final product NH$_3$. This sequential arrangement of active sites in a tandem configuration enables efficient and selective conversion of NO$_3^-$ to NH$_3$, thereby enhancing the overall performance of the electrochemical system.

4.8   Cascade process. The three channels electrochemical cell.

Analyzing the performances of the Cu and TiO$_2$@Cu electrodes in **Section 4.7** we propose a tandem electrocatalytic system to cascade the initial accumulation and final conversion of NO$_2^-$ intermediates to NH$_3$ at lower overpotentials. For this, the electrochemical cell (**Figure 4.13**) was adapted to expose two faces: Cu (**Channel 1**) and TiO$_2$@Cu (**Channel 2**).
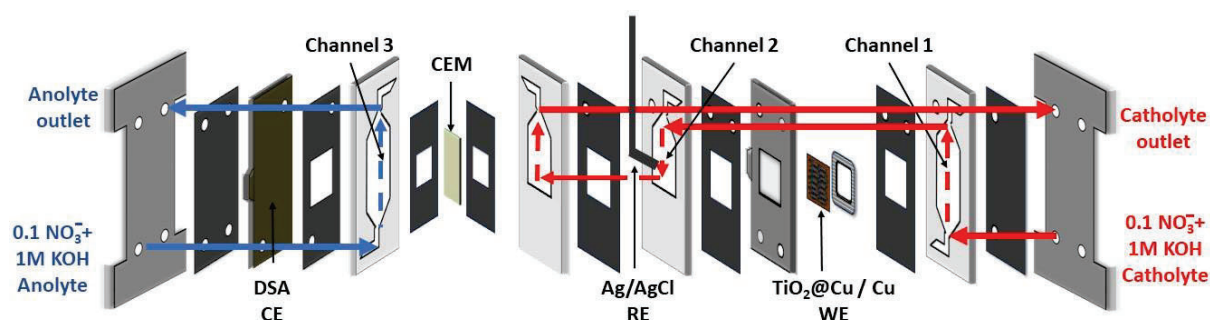
Figure 4.13 Three-channels electrochemical flow-cell adapted with a current collector that exposes a 1 cm^2 geometric area for the WE (Configuration 2).

This tandem approach capitalizes on the strengths of individual catalysts but also addresses the limitations identified in the prior sections. Taking advantage of the superior performance of Cu in the RDS of NO_3^- reduction [46], Surface 1 consisted of a 1 cm^2 Cu electrode, pretreated as described in methods of the chapter, in charge of facilitating the consecution of the RDS and increasing the NO_2^- concentration in the electrolyte for further reductions [38], [47], [48]. Setting the stage for a subsequent reduction to NH_3 in the **Channel 2** of the cell. Surface 2 consisted of a 1 cm^2 TiO$_2$@Cu active area in charge of driving both NO_3^-RR and NO_2^-RR towards NH_3 as the final product, aiming at facilitating NO_2^-RR at lower overpotentials and minimizing the HER. This approach also aims to enhance the global energy efficiency by maximizing the NO_3^- and NO_2^- conversion at lower overpotentials on optimum surfaces. The tandem configuration was studied by chronoamperometry tests conducted across various applied potentials in a common flow cell to assess NO_3^-RR to NH_3 performance. The cathode and anode were supplied with 0.1 M KNO_3 + 1 M KOH aqueous solutions as electrolytes and all the rest of parameters for alkaline conditions already described.

4.8.1 Cascade process. Increased FE and SE towards NH_3

The results for the cascade process are shown in **Figure 4.14 a.** The FE distribution towards NH_3, NO_2^- and H_2 at the applied potential range of -0.4 V to -0.8 V vs RHE. In the tandem setup, NH_3 emerged as the predominant product with an FE consistently exceeding 83% across all applied potentials.
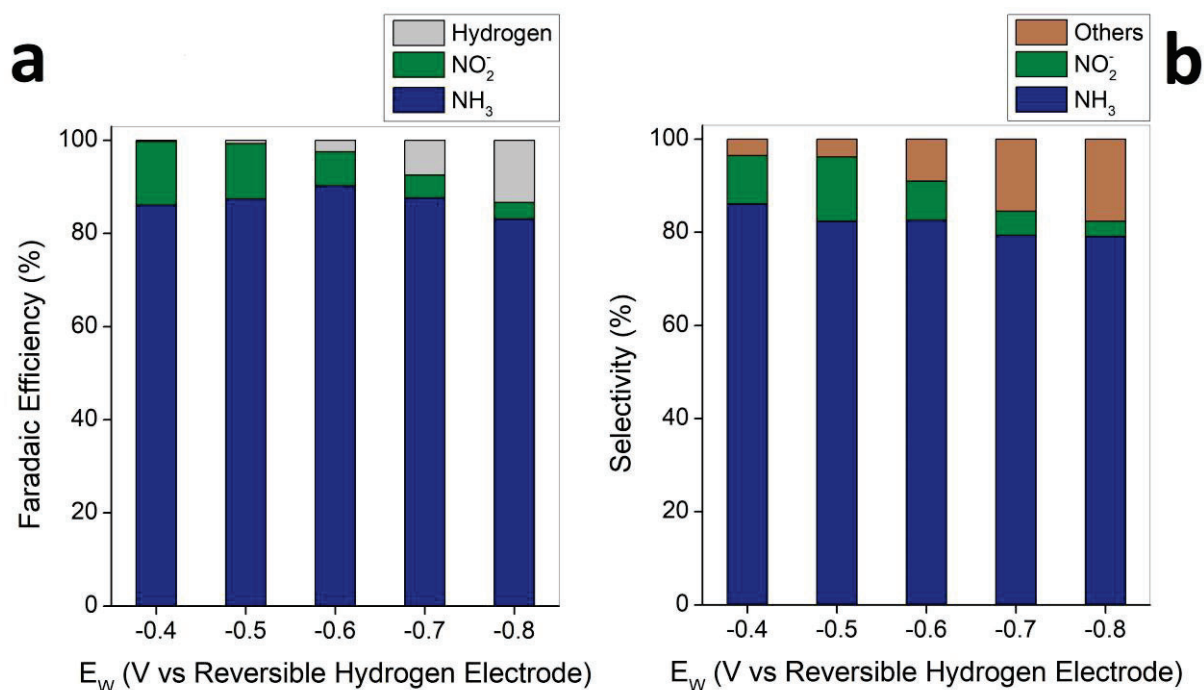
Figure 4.14 a) FE distribution and (b) SE distribution for the products NH_3, NO_2^-, H_2 and other N-based for cascade electrolysis processes.

A volcano-shaped pattern was observed, with the peak FE occurring at -0.6 V vs RHE, registering at 91% toward NH_3. Noteworthy values were sustained above 85% at -0.4 V, -0.5 V, and -0.7 V vs RHE. Conversely, FE toward NO_2^- experienced a gradual decline at higher overpotentials, ranging from 13% at -0.4 V to 3% at -0.8 V vs RHE. The varying FE toward other products aligns with HER trends detected by GC. It is essential to highlight that FE toward H_2 was significantly suppressed by the high bulk concentrations of NO_3^- and K^+ ions, as well by the content of NO_2^- intermediates, which faster reduction kinetics can overcome the H_2O reduction to H_2 [49], [50]. Previous studies have observed more favorable hydrogenation on oxygen for the intermediate of $*NO_2$ in the presence of OV, which can efficiently inhibit the formation of nitrogenated by-products [16], [51].

The performance of the tandem configuration, as depicted in **Figure 4.14 b**, demonstrates the SE to N-base products based on the applied potential. The selectivity focuses solely on N-based products achievable through NO_3^- reduction, while yield productivity is specific to the target NH_3 product. The peak selectivity to NH_3 occurred at -0.4 V vs RHE, reaching 86%. A gradual decrease was noted at more cathodic potentials, although kept at values > 80% in all the potential range. Simultaneously, selectivity toward NO_2^- experienced a gradual decrease, with the maximum value at -0.5 V vs RHE (14%). In the case of NH_3 yield, **Figure 4.15** exhibited a direct correlation with the increase of the applied potential, exhibiting a S-shape curve and almost reaching a plateau at -0.8 V vs RHE, with a 0.45 mmol $h^{-1} \cdot cm^{-2}$ value. While higher yield productivity was attainable at higher overpotentials, the volcano-shaped FE toward NH_3 indicates a lower efficiency in transforming NO_3^- to NH_3 due to the growing importance of other side reactions, such as HER.
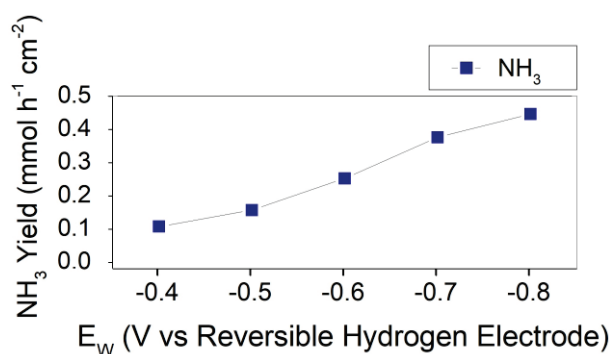
Figure 4. 15 NH_3 productivity yield or the cascade/tandem process.

The FE serves as an important parameter for evaluating the efficiency of the supplied charge to the system. Notably, values exceeding 90% at intermediate working electrode potentials within the range signify an effective utilization of the charge to maximize the generation of the target product, particularly in the proposed cascade tandem system.

Energy efficiency (EE) and FE are directly correlated. However, the fact that a FE exceeding 90% does not equate to an equivalent value in terms of EE is given several factors such overpotential losses, side reactions, and others that reduce this value. In the next section, the EE of various configurations of the cell are explored, understanding how a cascade/tandem process affects the efficiency at global and semi-cell levels.

4.9   Energy efficiency calculations. The effects of cascading NO$_3^-$RR.

From Chapter 2.

The EE_{CELL} and EC_{NH_3} are calculated from the next equations.

$$EE_{CELL} = \frac{EC_{NH_3}}{\int_0^t I(t) \cdot U(t) dt} \cdot 100$$

$$EC_{NH_3} = \left[\Delta G^0_{NH_3} + R \cdot T \cdot \text{Ln} \left(\frac{C_{NH_3\,t} \cdot C_{OH^-\,t}^9}{C_{NO_x^-\,t}} \right) \right] \cdot C_{NH_3\,t} \cdot V$$

$$\Delta G^0_{NH_3} = -n \cdot F \cdot E^0_{CELL}$$

In this section, an energy analysis is presented by comparing the cascade NO$_3^-$RR in tandem configuration and a configuration that exposes TiO$_2$@Cu in Channels 1 and 2. In this comparison, the 2 cm^2 TiO$_2$@Cu electrode follows the same configuration than the tandem system (**Figure 4.13**), but with both surfaces 1 and 2 covered by TiO$_2$@Cu. **Figure 4.16** illustrates the EE_{cell} distribution, forming a distinctive volcano shape. Notably, the highest values are achieved with the tandem system at -0.5 V and -0.6 V vs RHE, reaching high values of 28.7% and 28.5%, respectively. This distribution underscores the efficient utilization of supplied energy in the conversion of NO$_3^-$ to NH$_3$. However, as we move to more cathodic potentials, the EE_{cell} gradually diminishes, hitting a minimum of 23% at -0.8V vs RHE, an effect strongly influenced by the HER and other side reactions. The cathode configurations of 1 and 2 cm^2 TiO$_2$@Cu exhibit lower EE_{cell}, also forming a volcano shape with peak values centered at -0.5V vs RHE. For the 1 cm^2 configuration, this peak corresponds to 22% EE_{cell}, with lower values observed at lower cathodic potentials: 18% for the -0.8V vs RHE applied potential. A similar distribution of EE_{cell} is observed for the 2 cm^2 TiO$_2$@Cu electrode, with the peak at -0.5V vs RHE reaching 20.5% of EE_{cell} and lower values for all other applied potentials within the studied range. It is noteworthy that the higher values of EE_{cell} recorded at all applied potentials observed for the 1 cm^2 TiO$_2$@Cu electrode, compared to the 2 cm^2 one, can be attributed to the cell disposition (two or three channels), with both surfaces polarized with respect to the reference electrode, only facing surface 2.
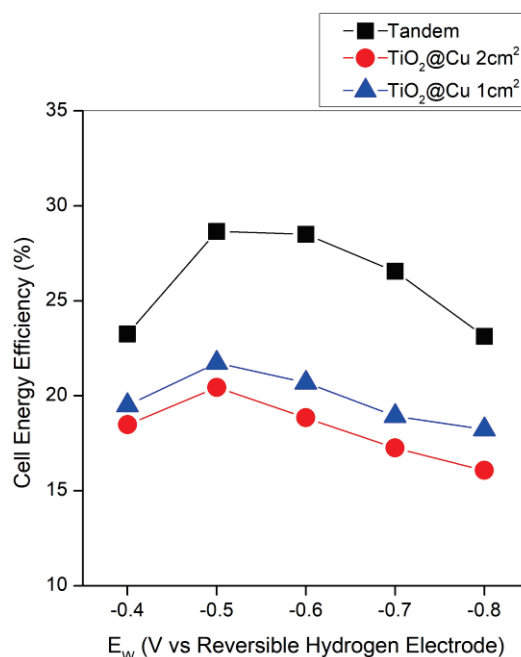
Figure 4.16 Energy Efficiency comparison for the three systems as function of the applied potential.

Figure 4.17 illustrates the relationship between EC_{NH_3} and EE_{cell} for the proposed systems. EC_{NH_3}, quantified in kWh·kg^{-1}, measures the energy required to produce 1 kg of NH_3 for the three specified cathode configurations. The data points, gathered over the applied potential range (-0.4 V to -0.8 V vs RHE), form a curved trend line shaped by all calculated values of EC_{NH_3} as a function of EE_{cell}. As anticipated, an increase in EE_{cell} results in a reduction of the total EC_{NH_3}, enhancing the efficiency of NH_3 production. For the two TiO_2@Cu configurations with 1 and 2 cm^2, the EC_{NH_3} varies between 43 kWh·kg^{-1} at the lower EE_{cell} value (16%) and 30 kWh·kg^{-1} at the highest (20%), with intermediate overlapping points. Values corresponding to the tandem configuration fall within the limits of 29 kWh·kg^{-1} for EE_{cell} at 23% and 23 kWh·kg^{-1} for 28% EE_{cell}. This underscores the impact of implementing a tandem configuration for NO_3^-RR to NH_3. Considering that the Low Heating Value or minimum energy requirement for producing NH_3 is situated in 5.92 kWh·kg^{-1} and the minimum required for the Haber-Bosch process ranges between 16.7 and 8.8 kWh·kg^{-1} depending on the used technology [54], the tandem system demonstrates to be an advantageous approach for the NO_3^-RR to NH_3. The lower activation energy for the NO_3^- to NO_2^- reaction facilitated by the Cu surface in the tandem configuration confers kinetic advantages, yielding superior outcomes in the overall NO_3^-RR to NH_3 process.
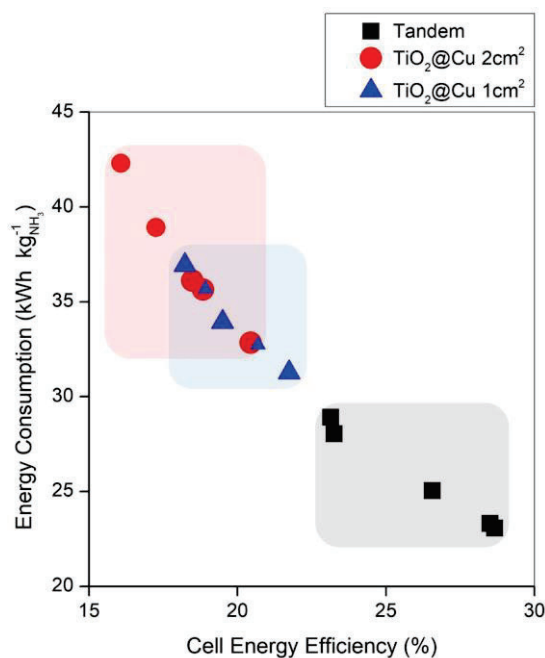
Figure 4.17 Energy Consumption evolution with the Energy efficiency for three different systems.

The decrease in EC_{NH_3} also affects the requirements for reaching higher productivities. As depicted in **Figure 4.18**, lower EC_{NH_3} are associated to similar productivities with the tandem system in comparison to the 1 and 2 cm^2 TiO$_2$@Cu cathodes. For instance, to obtain productivities close to 0.1 mmol h^{-1} cm^{-2}, the tandem system only requires 22.10 kWh·kg^{-1}, while the 1 and 2 cm^2 TiO$_2$@Cu configurations need 30-32 kWh·kg^{-1}. Notably, with the increase of the E_W from -0.4 to -0.7 V vs RHE, the productivity observed for the tandem configuration increased approximately 3.5 times (up to 0.38 mmol h^{-1} cm^{-2}) with a minimum variation of EC_{NH_3} of only 2.5 kWh·kg^{-1}. This agrees with the behavior observed for EE_{cell} as a function of E_W. However, for increasing productivity up to 0.44 mmol h^{-1} cm^{-2} (reached at -0.8 V vs RHE), the EC_{NH_3} increases up to 29 kWh·kg^{-1}, a value that agrees with the energy efficiency decrease at high overpotentials, correlated with HER and other competitive reactions. On the other hand, 39 and 43 kWh·kg^{-1} are required to elevate the productivity to 0.41 mmol h^{-1} cm^{-2} for the configurations of 1 and 2 cm^2 TiO$_2$@Cu, respectively, which represents more than 40% increase in the energy consumption with respect to the tandem system.

The EE_{Cell} provides an assessment of the efficiency achievable while considering losses within the cell for both anodic and cathodic reactions. However, calculating the EE solely for the semi-reaction occurring at the cathode offers valuable insights as well. This calculation represents the maximum efficiency attainable for an electrochemical reduction process, wherein any disparity with the global energy efficiency can indicate losses generated in the anode or other components of the cell. Thus,

analyzing the energy efficiency of the cathodic semi-reaction in isolation helped pinpointing specific areas where improvements or optimizations may be necessary to enhance the overall efficiency of the electrochemical system. From **Chapter 2** the definitions of $EE_{Half-Cell}$.
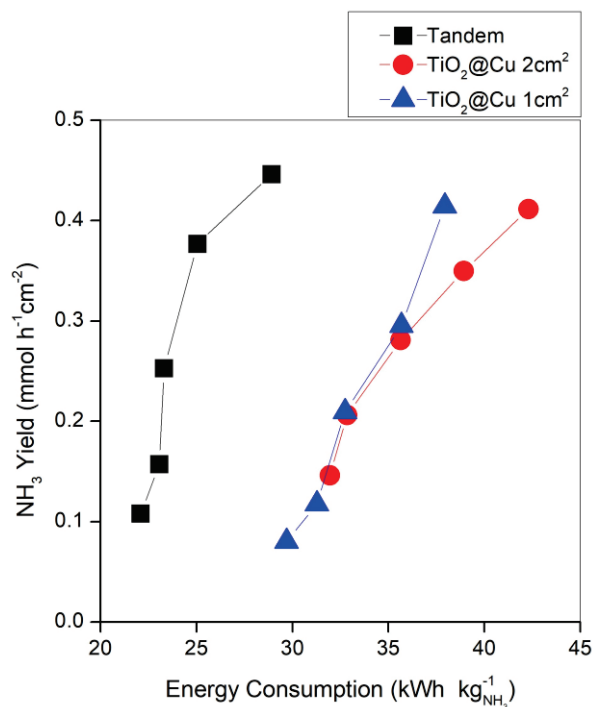
Figure 4.18 Effects of Global Energy Efficiency in NH₃ yield productivity.

From **Chapter 2**

The $EE_{Half-Cell}$ is calculated as follows:

$$EE_{half-cell}(\%) = \frac{EC_{NH_3}}{(0.4 - U_w) \cdot \int_0^t I(t)dt} \cdot 100$$

The $EE_{Half-Cell}$ distribution is presented in **Figure 4.19a** for NO₂⁻RR to NH₃ in the **two channels cell**, where the Cu and TiO₂@Cu electrodes are compared at different applied potentials. And **Figure 4.19b** for the NO₃-RR to NH₃ in cascade/tandem configuration (three channels cell).
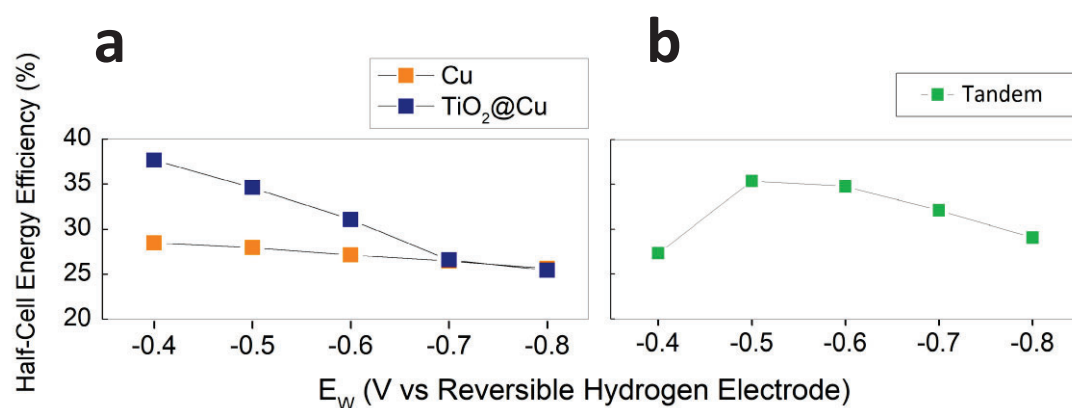
Figure 4.19 Half-Cell Energy Efficiency distribution for (a) NO$_2^-$RR and two channel systems for the electrodes Cu and TiO$_2$@Cu and (b) NO$_3^-$RR for the three-channels system and the tandem configuration.

In **Figure 4.19a**, the results demonstrate that **TiO₂@Cu** exhibits higher $EE_{Half-Cell}$ values across the entire range from -0.4 V to -0.8 V vs RHE in the electrolysis processes of NO$_2^-$ to NH$_3$. Notably, it starts impressively at 38% at -0.4 V vs RHE and gradually decreases to 28% at -0.8 V vs RHE.

In contrast, for the NO$_3^-$RR in cascade reaction, the $EE_{Half-Cell}$ displays the highest values at intermediate applied potentials within the range. This observation directly correlates with the **FE** to NH$_3$ calculated in the previous section.

When comparing the $EE_{Half-Cell}$ values with the overall EE_{Cell}, an average reduction of 5% is observed for all applied potentials. This reduction indicates a low contribution of energy losses in the anode and other components of the cell, suggesting that most of the energy losses occur in the cathodic half-cell during the electrochemical processes under investigation.

4.10 Energy consumption calculations. Scaling up NO$_3^-$ to NH$_3$ conversion.

In industrial processes, particularly in electrochemistry, the choice between galvanostatic and potentiostatic electrolysis depends on several factors, including the desired outcome, process control requirements, and the nature of the reactions involved [57]. Galvanostatic methods are more practical because they ensure that the same current is applied in the system, which helps maintain a steady rate of reaction. In the case of NO$_3^-$ treatments in wastewater treatment plants, it is expected to have large amounts of nitrate polluted waters, and galvanostatic setups can be simpler and more cost-effective to implement compared to potentiostatic setups [58].

By employing a tandem configuration, we conducted experiments using a series of current densities to identify a single parameter that could serve as a valuable starting point for scaling up the process by systematically varying the *j* and calculating efficiency parameters (FE, EE, SE, and conversion rates).

Figure 4.20a illustrates the *FE* distribution as a function of the current density, forming a distinctive volcano shape. The peak is reached at -90 mA with 97% toward NH_3. Subsequently, the FE slightly drops to 85% at the highest applied current of -110 mA cm^{-2}. The potentials corresponding to *j* with the highest FE (-70 and -90 mA cm^{-2}) were -0.7 and -0.8 V vs RHE, differing slightly from observations under potentiostatic conditions, where the highest FE was reached at -0.6 V vs RHE. Like potentiostatic conditions, the FE towards NO_2^- is higher at less negative current densities, reaching a maximum of 16.5% at -35 mA cm^{-2}. FE toward other products remains low for all applied currents, with a significant value observed only at the highest current density (-110 mA cm^{-2}) with a value of 10%.
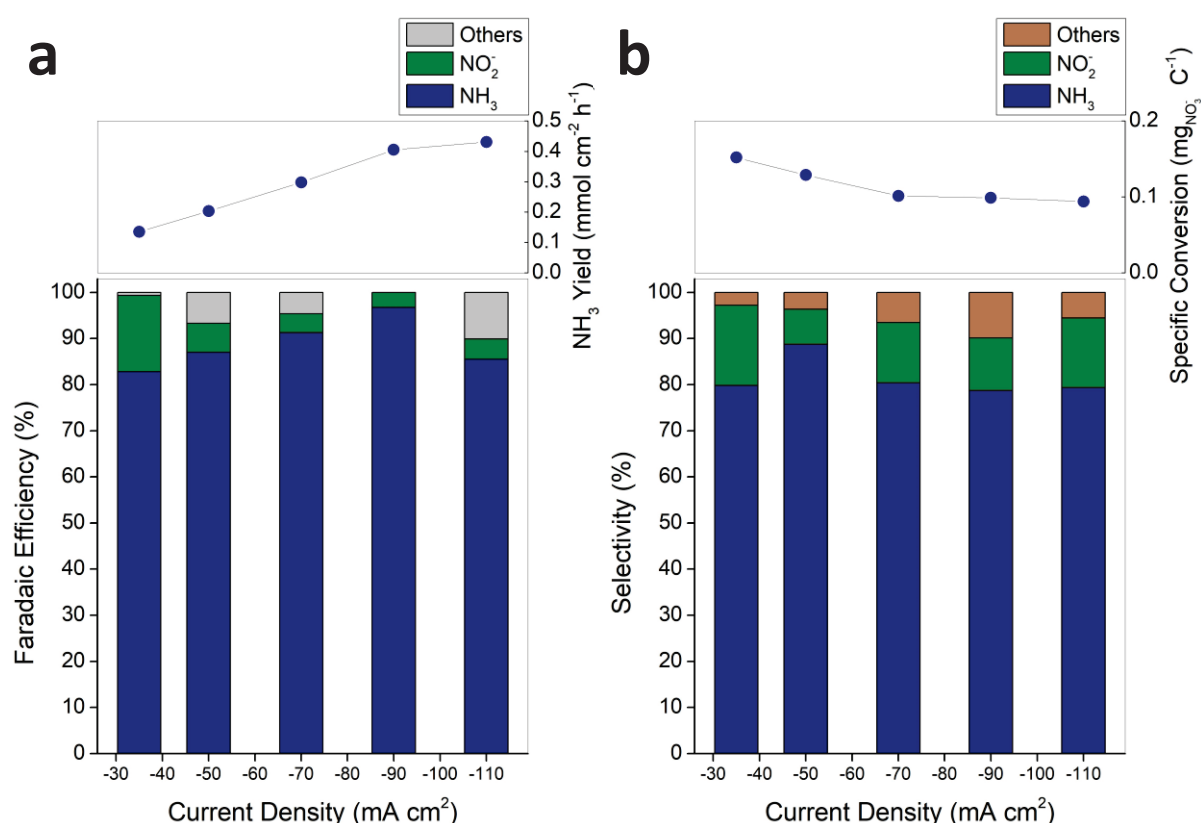
Figure 4.20 a) FE distribution and (b) SE distribution of products for cascade/tandem process under galvanostatic conditions.

Productivity toward NH_3 gradually increases with the rise in current density, mirroring the behavior observed under potentiostatic conditions. Starting at 0.14 mmol h^{-1} cm^{-2} at -35 mA cm^{-2}, it peaks at 0.43 mmol h^{-1} cm^{-2} at -110 mA cm^{-2}, representing the apparent limit of productivity for the system under the evaluated conditions. An explanation for reaching an apparent limit is the transient decrease

on the available NO$_3^-$ species, due to the continuous conversion of up to 45% of the initial NO$_3^-$. **Figure 4.20 b** demonstrates the SE distribution of products across the mentioned range of applied *j*. The highest SE toward NH$_3$ is achieved at -50 mA cm^{-2}, reaching 90%. For other current densities, the SE remains approximately at 80% for the entire studied range. The SE to NO$_2^-$ shows similar values to those observed under potentiostatic conditions, with the maximum SE measured at 16% at -35 mA cm^{-2}. For the rest of the applied currents, the SE toward NO$_2^-$ remains below 10% in all cases. The specific NO$_3^-$ conversion by charge unit decreases at higher applied current densities, ranging from 0.15 down to 0.1 mg C^{-1}, consistent with the lower limit observed in another Cu/Ti-based NH$_3$ generation system in **Chapter 3**.
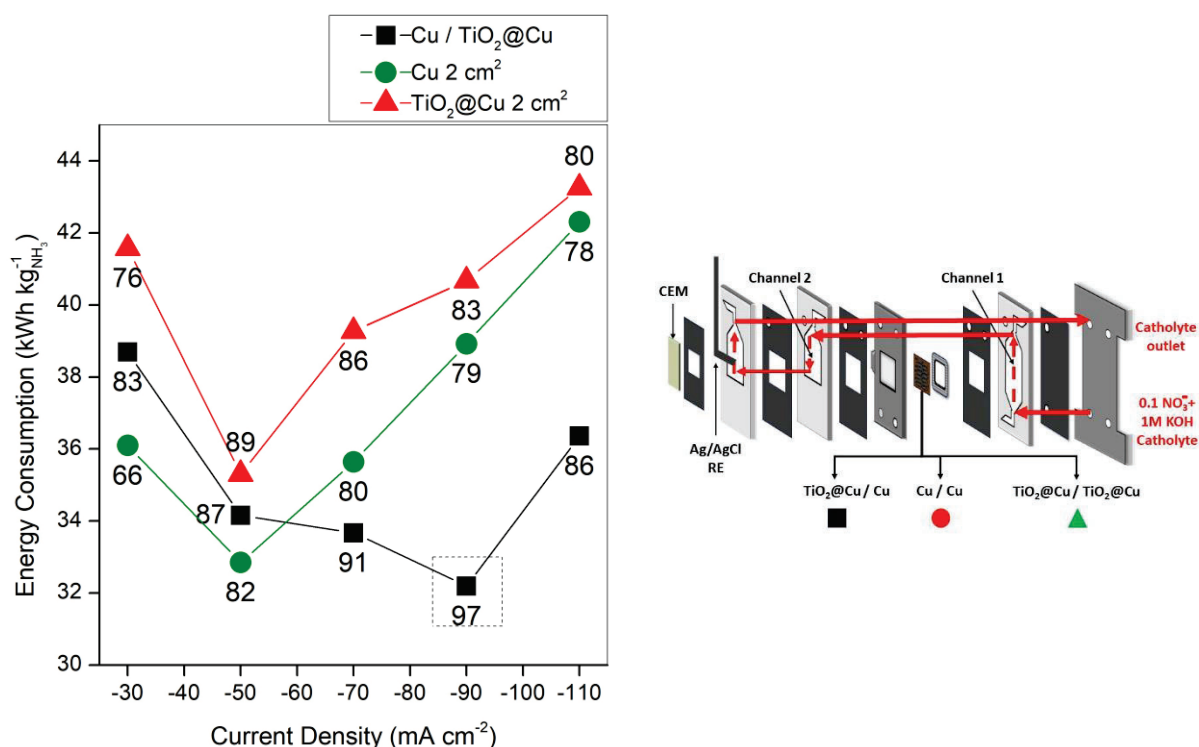
Figure 4.21 Energy Consumption distribution at different current densities for the three channels systems. The FE towards NH$_3$ is included for each point.

For our electrolytic cell we wanted to define one single parameter of NO$_3^-$RR to NH$_3$ process that serves as the preliminary value for scaling up: the energy required to produce 1 kg of NH$_3$, expressed in kWh·kg^{-1}, at a current density that yields at least 90% FE. **Figure 4.21** illustrates the variation in energy consumption (EC) with current density for three different systems, alongside the *FE* at various current densities. Remarkably, for two of the systems (Cu and TiO$_2$@Cu electrodes), the minimum energy consumption is recorded at a *j* of -50 mA·cm^{-2}, coinciding with their maximum FE. Similarly, in the case of the **Cascade/Tandem** system, which achieved a remarkable 97% FE, the lowest energy consumption

among all current densities and systems was observed at a higher current density. This value of **33 kWh·kg** of NH$_3$ represents the primitive scale-up parameter, as it corresponds to the energy required to produce 1 kg of NH$_3$ with a 97% faradaic efficiency. By fixing this parameter, we establish a benchmark for scaling up the electrochemical our process.

4.11   Economic implications of increasing the Energy Efficiency.

Apart of the generation of NH$_3$, NO$_3^-$RR can be used in water treatment systems. For this reason, the energy requirements for converting a define amount of NO$_3^-$ can be used as a starting point for scale up the process, and the implications of increasing the energy efficiency. **Figure 4.22** presents the NO$_3^-$ consumption by charge unit ($\Delta C_{NO_3^-}$) as a function of EC for converting a defined mass of NO$_3^-$ ($EC_{NO_3^-}$), providing insights into the energy required for the conversion of 1 kg of NO$_3^-$. This is a useful parameter that helps to determine and compare the operational costs of energy-dependent water treatment systems [54]. In this case we use this parameter to compare between different materials used in denitrification processes. Among a series of catalyst materials, we determine that the Cu/TiO$_2$@Cu in our tandem configuration reduces the energy consumption down to 2.89 kWh·kg^{-1} at potentiostatic conditions and 4.95 kWh·kg^{-1} under galvanostatic conditions, representing the lowest values for this parameter among different materials found in recent studies. Comparatively, other Cu-based catalysts (Cu:Ni [12] or Cu:Zn) showed better specific NO$_3^-$ conversion at significantly higher energy consumption values [60]. It is important to mention that some of the values collected correspond to systems working under different conditions, such as lower initial NO$_3^-$ concentrations, explaining the wide range of $EC_{NO_3^-}$ values in the figure. However, the excellent values achieved demonstrate the potential of our tandem configuration and serve as primitive scaling-up parameters, offering starting point of the lower energy requirements for systems aiming at denitrification (complete elimination of NO$_3^-$ from waters) or the production of NH$_3$ as the primary product.
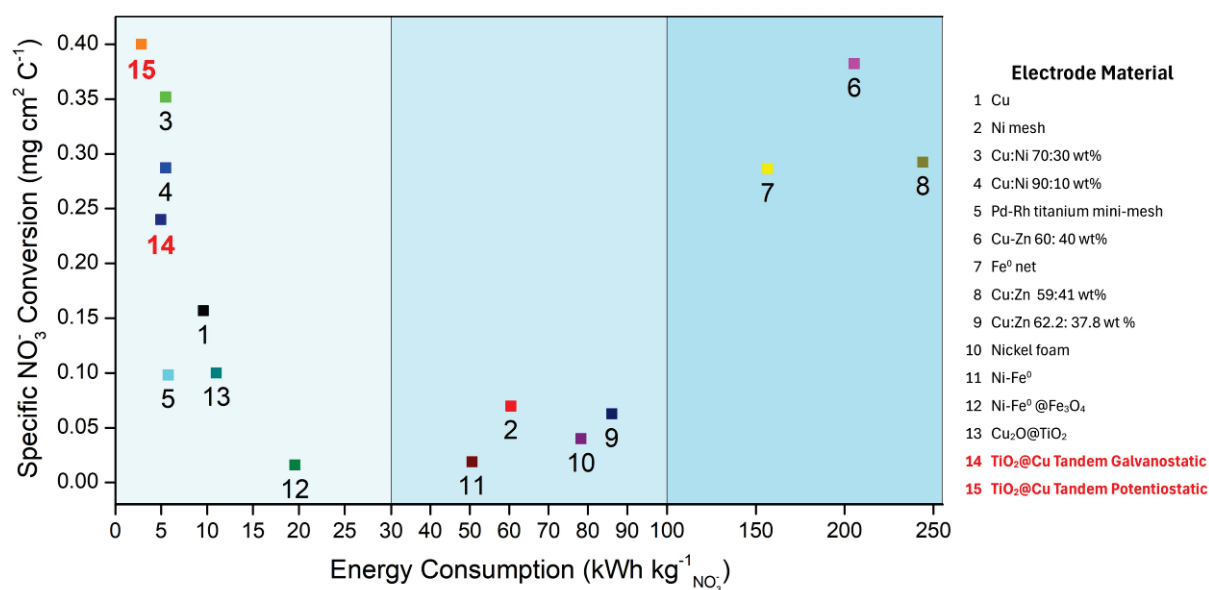
Figure 4.22 Specific NO₃⁻ conversion by charge unit as function of Energy Consumption for similar processes and different electrode materials.

In 2023, the average price of electricity for industrial use in the Euro Zone was $0.2517 \, €\cdot kWh$ [61]. This information allows us to calculate the cost of energy consumption for both producing NH_3 and degrading NO_3^-.

For producing NH_3, considering the energy consumption of $33 \, kWh\cdot kg^{-1}$ as determined from our electrochemical process, the cost of electricity per kilogram of NH_3 produced would be:

$$33 \, \frac{kWh}{kg_{NH_3}} * 0.2517 \, \frac{€}{kWh} = \mathbf{8.3} \, \frac{€}{\boldsymbol{kg_{NH_3}}}$$

Similarly, for degrading NO_3^-, using the energy consumption determined for this process, the cost of electricity per kilogram of NO_3^- degraded would be:

$$2.89 \, \frac{kWh}{kg_{NO_3^-}} * 0.2517 \, \frac{€}{kWh} = \mathbf{0.727} \, \frac{€}{\boldsymbol{kg_{NO_3^-}}}$$

These values provide insight into the economic implications of the electrochemical processes involved in NH_3 production and NO_3^- degradation, helping to assess their feasibility and cost-effectiveness in industrial applications.

4.12 Conclusions.

This **Chapter** presents a cascade electrolysis approach for nitrate conversion to ammonia using a tandem system comprised of two distinct active sites, Cu and TiO$_2$@Cu, operating under alkaline conditions. Our findings reveal significantly enhanced energy efficiencies towards ammonia production, coupled with decreased energy consumption, particularly notable under moderate applied potential conditions even down to −0.7 V. Through individual investigations of Cu and TiO$_2$@Cu active sites, we confirm the higher activity of Cu for NO$_3$$^-$RR to nitrite intermediates, while TiO$_2$@Cu exhibits superior performance for NO$_2$$^-$RR to ammonia, providing insights into the critical transition for reducing the required overpotential for global NO$_3$$^-$RR to ammonia. Energy consumption analysis further indicates that the cascade nitrate electrolysis in tandem configuration offers lower energy requirements compared to similar studies. Our findings underscore the utility of transient cell configurations in electrochemical systems in facilitating tandem catalysis of reactive intermediates within spatially confined different active sites, thereby significantly improving the energy efficiency. Moreover, this study exemplifies an alternative strategy enabled by innovative electrochemical techniques and material design to overcome complex scaling relations in electrocatalysis.

4.13   Highlights of the chapter.

High Faradaic Efficiency and Selectivity:

The tandem NO$_3$$^-$RR process demonstrated a FE of 97% and a selectivity of 80% towards NH$_3$, showcasing the effectiveness of the composite Cu and TiO$_2$@Cu electrodes in an optimized flow-cell configuration.

Enhanced Energy Efficiency:

The cascade electrolysis approach resulted in high full-cell energy efficiencies of 29%, significantly improving the energy consumption metrics for NH$_3$ production.

Effective Use of Cu and TiO$_2$@Cu Electrodes:

Cu electrodes exhibited superior activity for the NO$_3$$^-$RR to NO$_2$$^-$ intermediates, while TiO$_2$@Cu electrodes showed higher performance for the NO$_2$$^-$RR to NH$_3$, highlighting the synergistic benefits of the tandem system.

Innovative Electrochemical Cell Design:

The chapter introduced a three-channel electrochemical cell that effectively facilitated the cascade reaction, optimizing the spatial arrangement of active sites to enhance the overall process efficiency.

Economic Viability and Scalability:

The study's findings underscore the potential for scaling up the tandem system for industrial applications, with a notable reduction in energy consumption for nitrate conversion to ammonia, making it economically viable for large-scale implementation.

4.14 Bibliography.

[1]   Z.Y. Wu, M. Karamad, X. Yong, Q. Huang, D. Cullen, P. Zhu, C. Xia, Q. Xiao, M. Shakouri, M. Shakouri, F.Y. Chen, J.Y. Kim, Y. Xia, K. Heck, Y. Hu, M.S. Wong, Q. Li, I. Gates, S. Siahrostami, H. Wang, *Electrochemical ammonia synthesis via nitrate reduction on Fe single atom catalyst*. Nat. Commun. 12, 1–10 (2021). http://doi.org/10.1038/s41467-021-23115-x

[2]   G.F. Chen, Y. Yuan, H. Jiang, S.Y. Ren, L.X. Ding, L. Ma, T. Wu, J. Lu, H. Wang, *Electrochemical reduction of nitrate to ammonia via direct eight-electron transfer using a copper–molecular solid catalyst*. Nat. Energy 5, 605–613 (2020). http://doi.org/10.1038/s41560-020-0654-1

[3]   X. Fu, X. Zhao, X. Hu, K. He, Y. Yu, T. Li, Q. Tu, X. Qian, Q. Yue, M.R. Wasielewski, Y. Kang, *Alternative route for electrochemical ammonia synthesis by reduction of nitrate on copper nanosheets*. Appl. Mater. Today 19, 100620 (2020). https://doi.org/10.1016/j.apmt.2020.100620

[4]   J. Li, G. Zhan, J. Yang, F. Quan, C. Mao, Y. Liu, B. Wang, F. Lei, L. Li, A.W.M Chan, L. Xu, Y. Shi, Y. Du, W. Hao, P.K. Wong, J. Wang, S.X. Dou, L. Zhang, J.C. Yu, *Efficient Ammonia Electrosynthesis from Nitrate on Strained Ruthenium Nanoclusters*. J. Am. Chem. Soc. 142, 7036–7046 (2020). https://doi.org/10.1021/jacs.0c00418

[5]   T. Zhu, Q. Chen, P. Liao, W. Duan, S. Liang, Z. Yan, C. Feng, Single-Atom Cu Catalysts for Enhanced *Electrocatalytic Nitrate Reduction with Significant Alleviation of Nitrite Production*. Small 16, 1–11 (2020). https://doi.org/10.1002/smll.202004526

[6]   T. Yoshioka, K. Iwase, S. Nakanishi, K. Hashimoto, and K. Kamiya, *Electrocatalytic Reduction of Nitrate to Nitrous Oxide by a Copper-Modified Covalent Triazine Framework*. J. Phys. Chem. C, vol. 120, no. 29, pp. 15729–15734, 2016, doi: 10.1021/acs.jpcc.5b10962.

[7]   W. Teng, N. Bai, Y. Liu, Y. Liu, J. Fan, and W. X. Zhang, *Selective Nitrate Reduction to Dinitrogen by Electrocatalysis on Nanoscale Iron Encapsulated in Mesoporous Carbon*. Environ. Sci. Technol., vol. 52, no. 1, pp. 230–236, 2018, doi: 10.1021/acs.est.7b04775.

[8]   R. Zhao, H. Xie, L. Chang, X. Zhang, X. Zhu, X. Tong, T. Wang, Y. Luo, P. Wei, Z. Wang, X. Sun, Recent progress in the electrochemical ammonia synthesis under ambient conditions. EnergyChem 1, 100011 (2019). https://doi.org/10.1016/j.enchem.2019.100011.

[9]   S. Overa, T. G. Feric, A. H. A. Park, and F. Jiao, *Tandem and Hybrid Processes for Carbon Dioxide Utilization*, *Joule*, vol. 5, no. 1, pp. 8–13, 2021, doi: 10.1016/j.joule.2020.12.004.

[10]   M. H. Guan, T. Wu, and A. H. Lu, *Tandem Synthesis of Valuable Chemicals via Electrocatalysis*. ChemCatChem, vol. 15, no. 24, 2023, doi: 10.1002/cctc.202301311.

[11]   D. E. Kim and D. Pak, *Ti plate with TiO_2 nanotube arrays as a novel cathode for nitrate reduction*," Chemosphere, vol. 228, pp. 611–618, 2019, doi: 10.1016/j.chemosphere.2019.04.071.

[12]   J.M. McEnaney, S. Blair, A.C. Nielander, J.A Schwalbe, D.M. Koshy, M. Cargnello, T.F. Jaramillo, *Electrolyte engineering for efficient electrochemical nitrate reduction to ammonia on a titanium electrode*. ACS Sustain. Chem. Eng. 8, 2672–2681 (2020). https://doi.org/10.1021/acssuschemeng.9b05983

[13]   L. Hong, R. Guo, Y. Yuan, X. Ji, Z. Lin, W. Pan, *Recent Progress of Transition Metal Phosphides for Photocatalytic Hydrogen Evolution*. ChemSusChem 14, 539–557 (2021). https://doi.org/10.1002/cssc.202002454

[14]   C. Liu, X. Guo, Z. Han, Y. Sun, Y. Feng, G. Yu, X. Xi, Q. Zhang, Z. Zou, *Core-shell heterostructured and visible-light-driven titanonio-bate/TiO_2 composite for boosting photodegradation performance*. Nanomaterials 9, 1–15 (2019). https://doi.org/10.3390/nano9101503.

[15]   R. Jia, Y. Wang, C. Wang, Y. Ling, Y. Yu, and B. Zhang, *Boosting Selective Nitrate Electroreduction to Ammonium by Constructing Oxygen Vacancies in TiO_2*. ACS Catal., vol. 10, no. 6, pp. 3533–3540, 2020, doi: 10.1021/acscatal.9b05260.

[16]   D. Zhao, J. Liang, J. Li, L. Zhang, K. Dong, L. Yue, Y. Luo, Y. Ren, Q. Liu, M.S. Hamdy, Q. Li, Q. Kong, and X.

Sun, *A TiO$_{2-x}$ nanobelt array with oxygen vacancies: an efficient electrocatalyst toward nitrite conversion to ammonia*, Chem. Commun., vol. 58, no. 22, pp. 3669–3672, 2022, doi: 10.1039/d2cc00856d.

[17]   B. M. Hunter, J. D. BlakemorAe, M. Deimund, H. B. Gray, J. R. Winkler, and A. M. Múller, *Highly active mixed-metal nanosheet water oxidation catalysts made by pulsed-laser ablation in liquids*, J. Am. Chem. Soc., vol. 136, no. 38, pp. 13118–13121, 2014, doi: 10.1021/ja506087h.

[18]   G. W. Yang, *Laser ablation in liquids: Applications in the synthesis of nanocrystals*. Prog. Mater. *Sci.*, vol. 52, no. 4, pp. 648–698, 2007, doi: 10.1016/j.pmatsci.2006.10.016.

[19]   I. Y. Khairani, M. Spellauge, F. Riahi, H. P. Huber, B. Gökce, and C. Doñate-Buendía, *Parallel Diffractive Multi-Beam Pulsed-Laser Ablation in Liquids Toward Cost-Effective Gram Per Hour Nanoparticle Productivity*. Adv. Photonics Res., vol. 2300290, pp. 1–12, Feb. 2024, doi: 10.1002/adpr.202300290.

[20]   I.Y. Khairani, Q. Lin, J. Landers, S. Salamon, C. Doñate, E. Karapetrova, H. Wende, G. Zangari, B. Gökce, *Solvent Influence on the Magnetization and Phase of Fe-Ni Alloy Nanoparticles Generated by Laser Ablation in Liquids*. Nanomaterials 13, (2023). https://doi.org/10.3390/nano13020227

[21]   I. Y. Khairani, G. Mínguez-Vega, C. Doñate-Buendía, and B. Gökce, *Green nanoparticle synthesis at scale: a perspective on overcoming the limits of pulsed laser ablation in liquids for high-throughput production*," Phys. Chem. Chem. Phys., vol. 25, no. 29, pp. 19380–19408, 2023, doi: 10.1039/d3cp01214j.

[22]   D. Zhang and H. Wada, *Laser Ablation in Liquids for Nanomaterial Synthesis and Applications*. Handb. Laser Micro-and Nano-Engineering, vol. 3, pp. 1481–1516, 2021, doi: 10.1007/978-3-030-63647-0_30.

[23]   W. P. Utomo, H. Wu, R. Liu, and Y. H. Ng, *Tailoring metal-support interaction over faceted TiO$_2$ and copper nanoparticles for electrocatalytic nitrate reduction to ammonia*. Green Chem., vol. 26, no. 3, pp. 1443–1453, 2023, doi: 10.1039/d3gc02018e.

[24]   Q. Song, S. Zhang, X. Hou, J. Li, L. Yang, X. Liu, and M. Li. *Efficient electrocatalytic nitrate reduction via boosting oxygen vacancies of TiO$_2$ nanotube array by highly dispersed trace Cu doping*. J. Hazard. Mater., vol. 438, no. May, p. 129455, 2022, doi: 10.1016/j.jhazmat.2022.129455.

[25]   B. Garlyyev, J. Fichtner, O. Piqué, O. Schneider, A. S. Bandarenka, and F. Calle-Vallejo, *Revealing the nature of active sites in electrocatalysis*, *Chem. Sci.*, vol. 10, no. 35, pp. 8060–8075, 2019, doi: 10.1039/C9SC02654A.

[26]   P. Xu, K. Ye, M. Du, J. Liu, K. Cheng, J. Yin, G. Wang, D. Cao, *One-step synthesis of copper compounds on copper foil and their supercapacitive performance*. RSC Adv. 5, 36656–36664 (2015). https://doi.org/10.1039/C5RA04889C.

[27]   W. Su, J. Zhang, Z. Feng, T. Chen, P. Ying, and C. Li, *Surface Phases of TiO$_2$ Nanoparticles Studied by UV Raman Spectroscopy and FT-IR Spectroscopy*. J. Phys. Chem. C, vol. 112, no. 20, pp. 7710–7716, May 2008, doi: 10.1021/jp7118422.

[28]   J. A. Torres-Ochoa, D. Cabrera-German, O. Cortazar-Martinez, M. Bravo-Sanchez, G. Gomez-Sosa, and A. Herrera-Gomez, *Peak-fitting of Cu 2p photoemission spectra in Cu^0, Cu^{1+}, and Cu^{2+} oxides: A method for discriminating Cu^0 from Cu^{1+}*. Appl. Surf. Sci., vol. 622, no. December 2022, p. 156960, 2023, doi: 10.1016/j.apsusc.2023.156960.

[29]   M. Yurderi, A. Bulut, I. E. Ertas, M. Zahmakiran, and M. Kaya, *Supported copper-copper oxide nanoparticles as active, stable and low-cost catalyst in the methanolysis of ammonia-borane for chemical hydrogen storage*. Appl. Catal. B Environ., vol. 165, pp. 169–175, 2015, doi: 10.1016/j.apcatb.2014.10.011.

[30]   I. Platzman, R. Brener, H. Haick, and R. Tannenbaum, *Oxidation of polycrystalline copper thin films at ambient conditions*. J. Phys. Chem. C, vol. 112, no. 4, pp. 1101–1108, 2008, doi: 10.1021/jp076981k.

[31]   L. Fang, S. Wang, C. Song, S. Lu, X. Yang, X. Qi, H. Liu, *Boosting nitrate electroreduction to ammonia via in situ generated stacking faults in oxide-derived copper*. Chem. Eng. J. 446, 1–10 (2022). https://doi.org/10.1016/j.cej.2022.137341.

[32]   M. E. Chavez, M. Biset-Peiró, S. Murcia-López, and J. R. Morante, *Cu$_2$O–Cu@Titanium Surface with Synergistic Performance for Nitrate-to-Ammonia Electrochemical Reduction*. ACS Sustain. Chem. Eng., vol. 11, no. 9, pp. 3633–3643, Mar. 2023, doi: 10.1021/acssuschemeng.2c05885.

[33]   R. H. Temperton, A. Gibson, and J. N. O'Shea, *In situ XPS analysis of the atomic layer deposition of aluminium oxide on titanium dioxide*. Phys. Chem. Chem. Phys., vol. 21, no. 3, pp. 1393–1398, 2019, doi: 10.1039/C8CP06912C.

[34]   B. Bharti, S. Kumar, H.-N. Lee, and R. Kumar, *Formation of oxygen vacancies and Ti^{3+} state in TiO$_2$ thin film and enhanced optical properties by air plasma treatment*. Sci. Rep., vol. 6, no. 1, p. 32355, Aug. 2016, doi: 10.1038/srep32355.

[35]   S. Guan, Y. Cheng, L. Hao, H. Yoshida, C. Tarashima, T. Zhan¸ T. Itoi, T. Qiu, and Y. Lu, *Oxygen vacancies induced band gap narrowing for efficient visible-light response in carbon-doped TiO$_2$*. Sci. Rep., vol. 13, no. 1, pp. 1–9, 2023, doi: 10.1038/s41598-023-39523-6.

[36]   L. Ren, W. Zhu, X. Li, X. Lin, H. Xu, F. Sun, C. Lu, and J. Zou, *Oxygen Vacancy-Rich 2D TiO2 Nanosheets: A Bridge Toward High Stability and Rapid Hydrogen Storage Kinetics of Nano-Confined MgH$_2$*. Nano-Micro Lett., vol. 14, no. 1, pp. 1–16, 2022, doi: 10.1007/s40820-022-00891-9.

[37]   E. Pérez-Gallent, M. C. Figueiredo, I. Katsounaros, and M. T. M. Koper, *Electrocatalytic reduction of Nitrate on Copper single crystals in acidic and alkaline solutions*. Electrochim. Acta, vol. 227, pp. 77–84, Feb. 2017, doi: 10.1016/j.electacta.2016.12.147.

[38]   M. Karamad, T. J. Goncalves, S. Jimenez-Villegas, I. D. Gates, and S. Siahrostami, *Why copper catalyzes electrochemical reduction of nitrate to ammonia*. Faraday Discuss., vol. 243, pp. 502–519, 2023, doi: 10.1039/D2FD00145D.

[39]   E. Murphy, Y. Liu, I. Matanovic, M. Rüscher, Y. Huang, A. Ly, S. Guo, W. Zang, X. Yan, A. Martini, J. Timoshenko, B. R. Cuenya, I.V. Zenyuk, X. Pan, E.D. Spoerke, P. Atanassov, *Elucidating electrochemical nitrate and nitrite reduction over atomically-dispersed transition metal sites*. Nat. Commun. 14, 4–6 (2023). https://doi.org/10.1038/s41467-023-40174-4.

[40]   K. Fan, W. Xie, J. Li, Y. Sun, P. Xu, Y. Tang, Z. Li, M. Shao, *Active hydrogen boosts electrochemical nitrate reduction to ammonia*. Nat. Commun. 13, 1–13 (2022). https://doi.org/10.1038/s41467-022-35664-w.

[41]   S. Meng, Y. Ling, M. Yang, X. Zhao, A.J. Osman, A. Al-Muhtaseb, D. Rooney, and P.-S. Yap, *Recent research progress of electrocatalytic reduction technology for nitrate wastewater: A review*. J. Environ. Chem. Eng., vol. 11, no. 2, p. 109418, 2023, doi: 10.1016/j.jece.2023.109418.

[42]   W. Qiu, X. Chen, Y. Liu, D. Xiao, P. Wang, R. Li, Z. Jin, and P. Li, *Confining intermediates within a catalytic nanoreactor facilitates nitrate-to-ammonia electrosynthesis*. Appl. Catal. B Environ. 315, 121548 (2022). https://doi.org/10.1016/j.apcatb.2022.121548

[43]   J. Yang, H. Qi, A. Li, X. Liu, X. Yang, Q. Zhao, Q. Jiang, Y. Su, L. Zhang, J.F. Li, Z.Q. Tian, W. Liu, A. Wang, T. Zhang, *Potential-Driven Restructuring of Cu Single Atoms to Nanoparticles for Boosting the Electrochemical Reduction of Nitrate to Ammonia*. J. Am. Chem. Soc. 144, 12062–12071 (2022). https://doi.org/10.1021/jacs.2c02262.

[44]   Y. Zhang, X. Chen, W. Wang, L. Yin, and J. C. Crittenden, *Electrocatalytic nitrate reduction to ammonia on defective Au1Cu (111) single-atom alloys*. Appl. Catal. B Environ., vol. 310, no. February, p. 121346, Aug. 2022, doi: 10.1016/j.apcatb.2022.121346.

[45]   H. Hirakawa, M. Hashimoto, Y. Shiraishi, and T. Hirai, *Selective Nitrate-to-Ammonia Transformation on Surface Defects of Titanium Dioxide Photocatalysts*. ACS Catal., vol. 7, no. 5, pp. 3713–3720, 2017, doi: 10.1021/acscatal.7b00611.

[46]   Z. Ren, K. Shi, and X. Feng, *Elucidating the Intrinsic Activity and Selectivity of Cu for Nitrate Electroreduction*. *ACS Energy Lett.*, vol. 8, no. 9, pp. 3658–3665, Sep. 2023, doi: 10.1021/acsenergylett.3c01226.

[47]   E. Murphy, Y. Liu, I. Matanovic, S. Guo, P. Tieu, Y. Huang, A. Ly, S. Das, I. Zenyuk, X. Pan, E. Spoerke, P.

Atanassov, *Highly Durable and Selective Fe and Mo-Based Atomically Dispersed Electrocatalysts for Nitrate Reduction to Ammonia via Distinct and Synergized NO₂⁻ Pathways*. ACS Catal. 12, 6651–6662 (2022). https://doi.org/10.1021/acscatal.2c01367

[48] H. Liu, J. Park, Y. Chem, Y. Chen, Y. Qiu, Y. Cheng, K. Srivastava, S. Gu, B.H. Shanks, L.T. Roling, W. Li, *Electrocatalytic nitrate reduction on oxide-derived silver with tunable selectivity to nitrite and ammonia*. ACS Catal. 11, 8431–8442 (2021). https://doi.org/10.1021/acscatal.1c01525

[49] J. M. Barlow, J. W. Ziller, and J. Y. Yang, *Inhibiting the Hydrogen Evolution Reaction (HER) with Proximal Cations: A Strategy for Promoting Selective Electrocatalytic Reduction*. ACS Catal., vol. 11, no. 13, pp. 8155–8164, Jul. 2021, doi: 10.1021/acscatal.1c01527.

[50] J.T. Bender, A.S. Petersen, F.C. Østergaard, M.A. Wood, S.M.J. Heffernan, D.J. Milliron, J. Rossmeisl, J. Resasco, *Understanding Cation Effects on the Hydrogen Evolution Reaction*. ACS Energy Lett. 8, 657–665 (2023). https://doi.org/10.1021/acsenergylett.2c02500

[51] X. Zhang, C. Wang, Y. Guo, B. Zhang, Y. Wang, and Y. Yu, *Cu clusters/TiO₂₋ₓ with abundant oxygen vacancies for enhanced electrocatalytic nitrate reduction to ammonia*," *J. Mater. Chem. A*, vol. 10, no. 12, pp. 6448–6453, 2022, doi: 10.1039/D2TA00661H.

[52] S. Z. Andersen, M.J. Statt, V. Bukas, S. Shapel, J. Pedersen, K. Krempl, M. Saccoccio, D. Chakraborty, J. Kibsgaard, P. Vesborg, J. Nørskov, and I. Chorkendorff, *Increasing stability, efficiency, and fundamental understanding of lithium-mediated electrochemical nitrogen reduction*. Energy Environ. Sci., vol. 13, no. 11, pp. 4291–4300, 2020, doi: 10.1039/D0EE02246B.

[53] A. J. B. Larry and L. R. Faulkner, "*ELECTROCHEMICAL METHODS*," in *BIOS Instant Notes in Analytical Chemistry*, Taylor & Francis, 2002, pp. 71–75.

[54] C. Smith, A. K. Hill, and L. Torrente-Murciano, *Current and future role of Haber-Bosch ammonia in a carbon-free energy landscape*. Energy Environ. Sci., vol. 13, no. 2, pp. 331–344, 2020, doi: 10.1039/c9ee02873k.

[55] J. Zhang, Y. Wang, Z. Li, S. Xia, R. Cai, L. Ma, T. Zhang, J. Ackley, S. Yang, Y. Wu, and J. Wu, *Grain Boundary-Derived Cu⁺/Cu⁰ Interfaces in CuO Nanosheets for Low Overpotential Carbon Dioxide Electroreduction to Ethylene*. Adv. Sci., vol. 9, no. 21, pp. 1–11, Jul. 2022, doi: 10.1002/advs.202200454.

[56] R. M. Choueiri, S. W. Tatarchuk, A. Klinkova, and L. D. Chen, *Mechanism of ammonia oxidation to dinitrogen, nitrite, and nitrate on β-Ni(OH)₂ from first-principles simulations*," Electrochem. Sci. Adv., vol. 2, no. 6, pp. 1–10, 2022, doi: 10.1002/elsa.202100142.

[57] M. Duca and M. T. M. Koper, *Powering denitrification: The perspectives of electrocatalytic nitrate reduction*. Energy and Environmental Science, vol. 5, no. 12. pp. 9726–9742, 2012, doi: 10.1039/c2ee23062c.

[58] C. Schotten, T. P. Nicholls, R. A. Bourne, N. Kapur, B. N. Nguyen, and C. E. Willans, *Making electrochemistry easily accessible to the synthetic chemist*. Green Chem., vol. 22, no. 11, pp. 3358–3375, 2020, doi: 10.1039/d0gc01247e.

[59] D. Reyter, D. Bélanger, and L. Roué, *Optimization of the cathode material for nitrate removal by a paired electrolysis process*. J. Hazard. Mater., vol. 192, no. 2, pp. 507–513, Aug. 2011, doi: 10.1016/j.jhazmat.2011.05.054.

[60] Z. A. Jonoush, A. Rezaee, and A. Ghaffarinejad, *Electrocatalytic nitrate reduction using Fe⁰/Fe₃O₄ nanoparticles immobilized on nickel foam: Selectivity and energy consumption studies*," *J. Clean. Prod.*, vol. 242, p. 118569, 2020, doi: 10.1016/j.jclepro.2019.118569.

[61] MINTUR, *Precio Neto De La Electricidad Para Uso Doméstico Y Uso Industrial*. no. 1, p. 1, 2023, [Online]. Available: http://www.minetad.gob.es/es-ES/IndicadoresyEstadisticas/DatosEstadisticos/IV. Energía y emisiones/IV_12.pdf.

Chapter 5

Li-rich catalyst effects
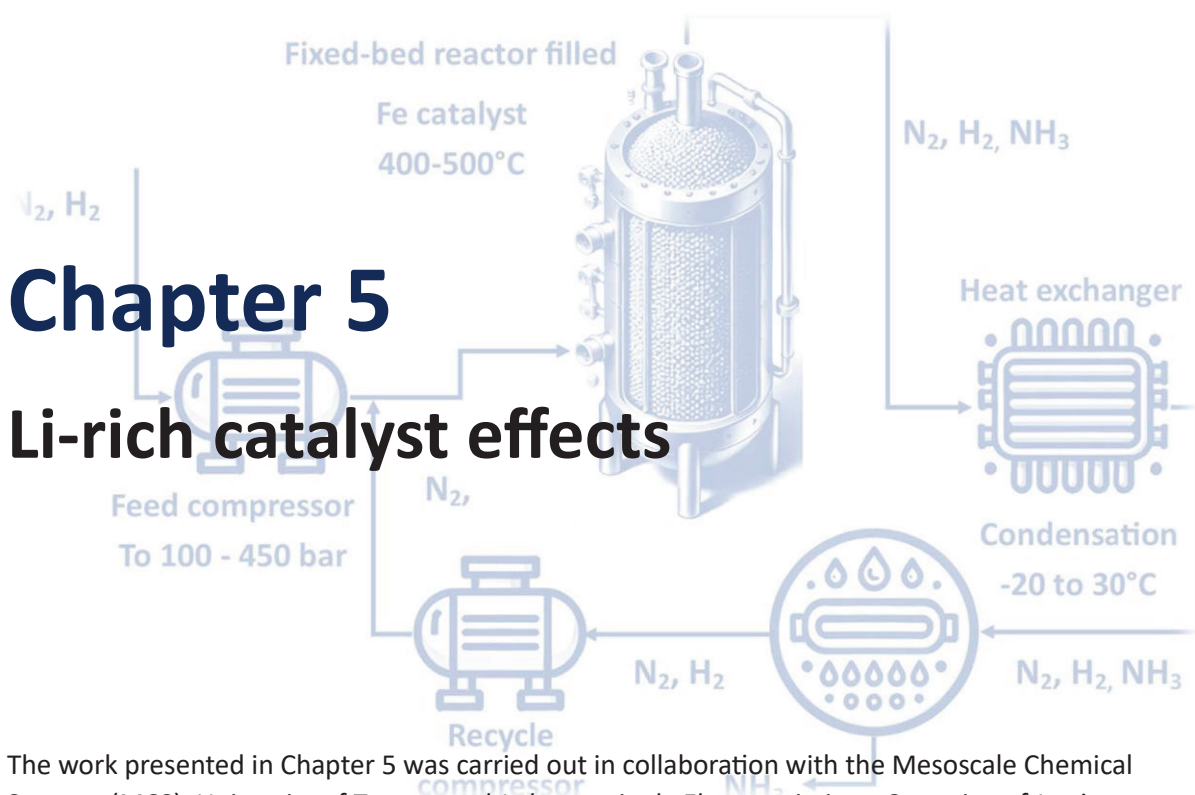
The work presented in Chapter 5 was carried out in collaboration with the Mesoscale Chemical Systems (MCS), University of Twente and *Laboratorio de Electroquimica y Corrosion* of *Instituto Politecnico Nacional*.

CHAPTER 5 LI-RICH CATALYST EFFECTS

5.1 Abstract

Chapter 5 explores the impact of lithium (Li) enrichment on the performance of mixed nickel oxide (NiO) and tin oxide (SnO_2) catalysts for nitrate reduction reactions (NO_3^-RR). The study assesses if 10% Li incorporation can enhance selectivity and catalytic activity for NO_3^-RR, aiming to increase ammonia (NH_3) production while suppressing the competing hydrogen evolution reaction (HER). Initial findings indicate that lithium enrichment improves both the selectivity and efficiency of NO_3^-RR, providing valuable insights for the design of more effective catalysts for sustainable ammonia production.

5.2 Introduction to Chapter 5.

In the preceding chapters, we have explored optimal conditions and strategies to enhance energy efficiency for NH_3 electrosynthesis from NO_3^-. Specifically, Chapter 3 focused on the combination of materials such as Cu and Ti-based, including titanium dioxide (TiO_2)), to optimize the conversion of nitrate to ammonia (NH_3). Chapter 4 examined the energy efficiency of various electrochemical cell configurations using these and other materials to achieve high performance.

Building upon these findings, **Chapter 5** shifts focus to a novel approach in catalyst modification by introducing lithium (Li) enrichment into the structure of a mixed oxide catalyst composed of nickel oxide (NiO) and tin oxide (SnO_2). The objective is to evaluate whether the incorporation of lithium can influence the catalytic behavior, specifically in promoting reactions that compete with the hydrogen evolution reaction (HER).

The materials investigated in this chapter include a baseline $NiO+SnO_2$ catalyst and a lithium-enriched variant (10% $Li-NiO+SnO_2$). To set the stage for this investigation, we will first provide a brief bibliography overview of SnO_2-based and NiO-based electrocatalysts used for NO_3^-RR, and the effects of alkali cations on NO_3^-RR and the HER, establishing a foundation for our subsequent interpretations and analysis.

Through systematic electrochemical testing and characterization, this chapter aims to provide insights into the role of lithium in modifying the catalytic properties of these mixed oxides. The goal is to determine if lithium enrichment can enhance NO_3^-RR efficiency by suppressing HER and thereby improving the overall selectivity and productivity of NH_3 under optimized electrochemical conditions.

The findings from this chapter could offer valuable guidance for the design of more effective catalysts, highlighting the potential of lithium-enriched materials in achieving selective and efficient nitrate reduction, thus contributing to the broader objective of sustainable ammonia production.

5.3   Catalyst dopping.

From **Chapter 1**, **Figure 5.1** illustrates the possible reaction pathways of NO_3^-RR under acidic and alkaline conditions.
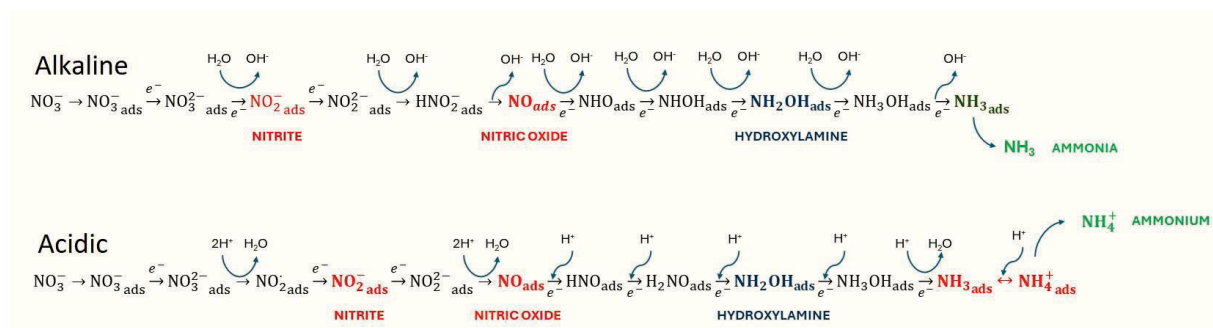
Figure 5.1 NO_3^-RR-to-NH_3 pathways.

NiO and SnO_2 are not commonly known materials used as electrocatalysts for the conversion of NO_3^- to NH_3. However, their low activity in this reaction makes them interesting candidates for investigating the role of material doping and its impact on competitive reactions. Before delving into this, a brief overview of the use of these materials in NO_3^-RR and the impact of cations in the solution on this reaction and the competitive HER is provided.

5.3.1 NO_3^-RR with NiO-based catalysts overview.

Pure NiO-based catalysts have not been extensively explored for NO_3^-RR to NH_3. However, some studies have investigated its performance, either by testing different structures of NiO or by using it as an active support for other materials:

The study by Y. Zhang [13] highlights the role of proton-coupled electron transfer (PCET) in the catalytic function of Nb-doped-NiO for the electrochemical reduction of NO_2^- to NH_3. As shown in **Figure 5.1**, NO_2^- reduction to NH_3 follows PCET steps. NiO facilitates PCET through electronic and protonic conductivity, with Ni^{2+} and Ni^{3+} sites enabling electron transfer and surface hydroxyl groups and OVs aiding proton transfer. Adsorbed NO_2^- interacts with Ni sites and OVs, undergoing activation and becoming receptive to protonation and electron transfer.

Another study conducted by Pengyu Liu et al. [14] explores the catalytic performance of NiO nanosheets on titanium mesh for NO reduction to NH_3. Notably, in this study, the reaction starts from NO as the initial state, not the NO_3^- molecule. As mentioned in previous chapters and as evident in

Figure 5.1, nitrous oxide is one of the semi-stable reaction intermediates of NO_3^-RR towards any final product. The findings correspond to NO molecules preferentially adsorbed onto the (200) plane of NiO, with the end-on adsorption (N atom binding to Ni site) showing the most negative binding energy. The reduction pathway follows that for acidic conditions given the presence of EDTA in the electrolyte, with the protonation of **NO to HNO being the potential rate determining step**. It is interesting to mention the poor performance of NiO-based electrodes for HER in this study, which ensures high selectivity for NORR. Looking into the specific role of NiO active sites, the study highlights that primarily the Ni atoms on the (200) plane, play a role in the adsorption and activation of NO molecules. These sites provide strong binding interactions, facilitating the initial adsorption step where NO binds end-on to the Ni site, polarizing the NO molecule and weakening the N=O bond, thus making it more susceptible to reduction.

Among other studies conducted with NO_3^-, Y. Wang et al. [15] investigated the synthesis and performance of Co_3O_4@NiO hierarchical nanotubes with NiO porous nanosheets for NO_3^- reduction to NH_3. They identified nickel atoms as the primary active sites, responsible for the initial adsorption and activation of NO_3^- molecules. DFT calculations showed that the hierarchical structure of NiO enhances the binding energy and stability of NO_3^- and intermediates, lowers activation barriers, and improves charge transfer.

5.3.2 NO_3^-RR with SnO_2-based catalysts overview.

Similar to NiO-based electrocatalysts, few studies have been conducted with SnO_2-based materials. G. Zhang et al. [16] investigated the catalytic performance of Mo-doped SnO_2 with enriched OVs (Mo-SnO_{2-x}) for NO_3^- reduction to NH_3. In this study, SnO_2 serves as the primary structural framework for the catalyst. The introduction of Mo and OVs creates new active sites and enhances existing ones, boosting the adsorption and activation of NO_3^-. **The electronic structure analysis revealed significant electronic coupling between Mo and Sn atoms, enhancing Mo-d and Sn-p orbital hybridization, which promotes NO_3^- adsorption and activation**. However, SnO_2 alone shows low NO_3^- conversion and FE to NH_3, making it a poor electrocatalyst for NO_3^-RR.

5.3.3   Supporting electrolyte effects in NO_3^-RR

NO_3^-RR conversion to NH_3 is a dissociative (N–O bond breaking) and associative (hydrogenation) process. Under alkaline conditions, hydrogen is sourced from water dissociation, forming active hydrogen species (H^* or H^+) simultaneously with N–O bond breaking[17]. All NO_3^-RR processes,

including NO_3^- adsorption, N–O breaking, hydrogenation, and water dissociation, can be influenced by the composition and concentration of the supporting electrolyte. This electrolyte aims to minimize unaccounted potential drops and, in some cases, stabilize reaction intermediates. The following sections will explore recent studies on the effects of cations in the electrolyte on various steps of NO_3^- RR.

5.3.4   Cation effects in NO_3^-RR

The study carried out by Y. Zhang et al. [18] investigates the role of alkali cations K^+ and Na^+ in the photocatalytic reduction of NO_3^- to NH_3 using a Ni single-atom catalyst supported on TiO_2**.** According with mechanistic studies the K^+ cations from KNO_3 bonds with two oxygen atoms around the Ni site, forming a K-O-Ni moiety during the reaction, a structure not observed with Na^+ cations. **The K-O-Ni moiety induced charge accumulation on Ni sites by weakening the Ni-O covalency, promoting the adsorption and activation of NO_3^- and stabilizing intermediates during the hydrogenation process.** DFT calculations showed that the presence of K^+ cations reduced the protonation barrier for the rate-determining step from 0.21 eV to -0.45 eV. The K atom also bonded with the *NO intermediate, stabilizing it and facilitating protonation processes. In other experiments **with $LiNO_3$ and $CsNO_3$ solutions, there is an indication that the ionic radius of K^+ is optimal for forming the K-O-Ni moiety.** The incorporation of K species did not significantly alter the energy band structures of the catalysts but significantly influenced the electronic properties, leading to decreased Ni-O covalency and lower valence states of Ni sites.

In the recent study performed by A. Fajardo et al. [19], it was investigated how different alkali cations (Li^+, Na^+, K^+, and Cs^+) in the electrolyte influence the selectivity and kinetics of NO_3^-RR to NH_3 on a Sn electrode. **The Sn electrodes, known for poor NH_3 selectivity from nitrates, showed significant variation in performance depending on the cations present.** According with the findings, NO_3^- conversion rates followed the order: $Li^+ < Na^+ \approx K^+ < Cs^+$, with Cs^+ showing the highest NO_3^- conversion rate and NH_3 production. **The larger cations like Cs^+ create a stronger local electric field at the electrode/electrolyte interface, enhancing the stabilization of reaction intermediates and promoting NH_3 formation.** The presence of different cations influences the stabilization of negatively charged intermediates (*NO_2^-, *NO^-), with Cs^+ generating a stronger local electric field.

And one last study that can help us to understand our experimental observations corresponds to a very recent one presented by J. Fan et al. [20]. This work examines the effects of various alkali cations (Li^+, Na^+, K^+, Cs^+) on the NO_3^-RR to NH_3. The findings highlight that cations within the electric double layer (EDL) affect electrostatic interactions between NO_3^- and the cathode, stabilizing reaction intermediates and influencing water dissociation activity. According to their results, NO_3^- removal

efficiency decreases with increasing cation size: $Li^+ < Na^+ < K^+ < Cs^+$. This is because cations form ion pairs with NO_3^-, affecting its transport towards the cathode. However, larger cations form more stable contact ion pairs (CIPs), which also enhances the reduction rate. Among both effects, the formation of CIPs seems to be stronger.

Another observed effect is that higher concentrations of cations lead to increased shielding effects, diminishing ionic diffusion coefficients and constraining ion motion. Alkali cations can competitively adsorb onto the catalyst surface, reducing active sites for NO_3^- reduction, and can also precipitate, blocking the catalyst surface and disrupting the EDL structure. As in the previously highlighted study, cations stabilize negatively charged intermediates (NO_2^-, NO^-) through electrostatic interactions, with larger cations generating stronger local electric fields that enhance stabilization and promote NH3 formation.

The three studies summarized in this section explore the effects of alkali cations Li^+, Na^+, K^+, Cs^+ in NO_3^- RR, revealing both complementary insights but also some potential contradictions. Y. Zhang et al. finds Na^+ less effective in NO_3^-RR, with no significant interaction with the catalyst, however, this is something specific of the catalyst composition and not correlative to the other studies. On the other hand, Fajardo et al. reports that Na^+ moderately enhances NO_3^-RR. Additionally, along with Fan et al. study both indicate that bulky cations like Cs^+ improve NH_3 selectivity. Nevertheless, the three studies consistently highlight K cation as very effective for enhancing NO_3^-RR, something that agrees with the larger number of studies conducted using K^+ as supporting cation.

5.3.5 Effects of cations on HER.

In this section we will give an overview of some studies that are focused on the effects of alkali cations in HER, trying to understand the possible implication on the water dissociation, as the source of hydrogen during NO_3^-RR to NH_3.

The study presented by S. Ringe et al. [21] reviews the impact of various cations on the HER. According with the findings, **the concentration of hydrated cations at the solid-liquid interface increases at more negative potentials, enhancing double-layer capacitance and surface charge density.** Cations influence the structure of interfacial water by breaking hydrogen bonds and reorienting water molecules, with larger cations creating a stronger electric field that stabilizes reaction intermediates. **This stabilization is crucial for the Volmer step under alkaline conditions, where water acts as the proton donor.**
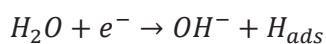
$$H_2O + e^- \rightarrow OH^- + H_{ads}$$
<div align="right">Volmer Step</div>

Cations affect the HER rate by polarizing water and increasing the proton transfer rate, with higher interfacial concentrations creating a stronger electric field. Specific adsorption of larger cations like Cs^+ is enhanced at very negative potentials, and can competitively be adsorb onto the electrode surface, reducing active sites for HER.

And another study in the field corresponds to J. Bender et al. [22], that investigates the influence of alkali metal cations (Li^+, Na^+, K^+, Cs^+) on HER across various metal electrodes (Cu, Ag, Au, Ir, Pd, Pt) in acidic and alkaline media. The findings indicate no significant cation effects on HER in acidic media. However, in alkaline, the impact varies with cation size. For HER-active metals (Ir, Pd, Pt), activity decreases with increasing cation size ($Li^+ > Na^+ > K^+ > Cs^+$). In these cases, water dissociation is not kinetically limited, but larger cations stabilize the transition state and products (OH^-) on the electrode-electrolyte interphase, blocking active sites. While for less HER-active metals (Cu, Ag, Au), HER activity increases with increasing cation size ($Li^+ < Na^+ < K^+ < Cs^+$). Here, cations enhance the HER rate by stabilizing and aiding the diffusion of water dissociation products (OH^-), with larger cations providing a greater enhancement.

5.4   Methods.

5.4.1   Electrode materials.

TW-DC and TW-DC-Li10% WE. To prepare the WE, the NPs were deposited on the carbon paper. The electrocatalyst consisted of a mixture of Vulcan carbon and the NiO-SnO_2 particles (DC and DC-Li10%) dispersed in 970 µL of anhydrous ethanol and 30 µL of a 5% Nafion solution. The mixture was then sonicated for 1 hour, drop-casted onto the support (geometric area: 1 x 1 cm^2), and finally dried in a vacuum oven at 60°C for 3 hours.

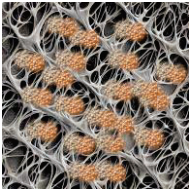| TW - DC	TW-DC-Li10%
2.7 mg NiO-SnO$_2$ DC 0.3 mg Vulcan 970 µL Ethanol 30 µL Nafion (5%)	2.7 mg NiO-SnO$_2$ (Li 10%) DC 0.3 mg Vulcan 970 µL Ethanol 30 µL Nafion (5%)

Figure 5. 2 Electrodes composition and name designation.

5.4.2 TW-DC and TW-DC-Li10%. SEM

Figure 5.3 shows the HR-SEM images of the NiO and SnO_2 nanoparticles where polycrystal structures are observed. No changes in morphology and oxidation state of the components were observed during the Li-enrichment.
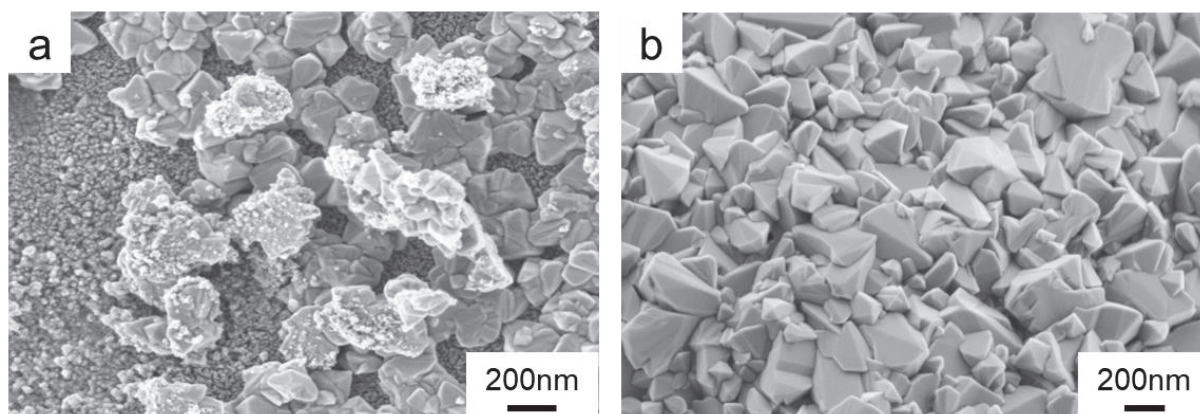

Figure 5.3 SEM images a) NiO-SnO_2 oxide nanoparticles. b) NiO-SnO_2-Li10% nanoparticles.

5.4.3 Electrochemical Characterization.

CVs for C_{DL} determination were recorded within the range with minimal faradaic currents at υ 10, 20, 50, and 100 mV s^{-1} using a 1M KOH electrolyte. And CV test with 0.1M KNO3 and 1M KOH was conducted at υ 15 mV s^{-1}.

The C_{DL} values measured were 265 μF for the Carbon Paper, 273 μF for TW-DC-Li10% and 321 μF for TW-DC electrodes. This non-significant difference in C_{DL} values (**Figure 5.4 a-c**), indicating similar ECSA, is insufficient to explain the different behaviors of TW-DC and TW-DC-Li10% electrodes. Therefore, a different electrochemical response must be a result of the structural modification of the TW-DC-Li10% electrode with lithium species. CV curves in **Figure 5.4d** show that the TW-DC electrode exhibits a higher current density (red line) compared to the TW-DC-Li10% electrode (blue line). TW-DC produces more hydrogen, as confirmed by Differential Electrochemical Mass Spectroscopy (DEMS) results (**Figure 5.4e-f**), which show three times higher HER currents for this electrode than for the TW-DC-Li10%. In the case of having Li$^+$ in the electrolyte instead of in the structure, DEMS results (**Figure 5.4g**) the reduction in the current density assigned to HER is also observed, but less effective than if it is in the structure.

Li species added to the oxide nanoparticles limit HER. This effect can be understood by correlating it with studies on Li$^+$ in the electrolyte. According to J. Bender et al. [22], for less HER-active metals (Cu, Ag, Au), HER activity increases with cation size (Li$^+$ < Na$^+$ < K$^+$ < Cs$^+$). In these metals, water dissociation

is the rate-limiting step of HER, and larger cations stabilize and transport OH⁻ products away from the active sites, increasing HER kinetics. One possibility is that the TW-DC electrode behaves similarly to these less HER-active metals, where HER is favored by the high concentration of K⁺ but slowed down by the Li-species in TW-DC-Li10%. However, a thorough evaluation of the Li effects requires considering product and reactant changes of NO_3^-RR, something discussed in next sections.
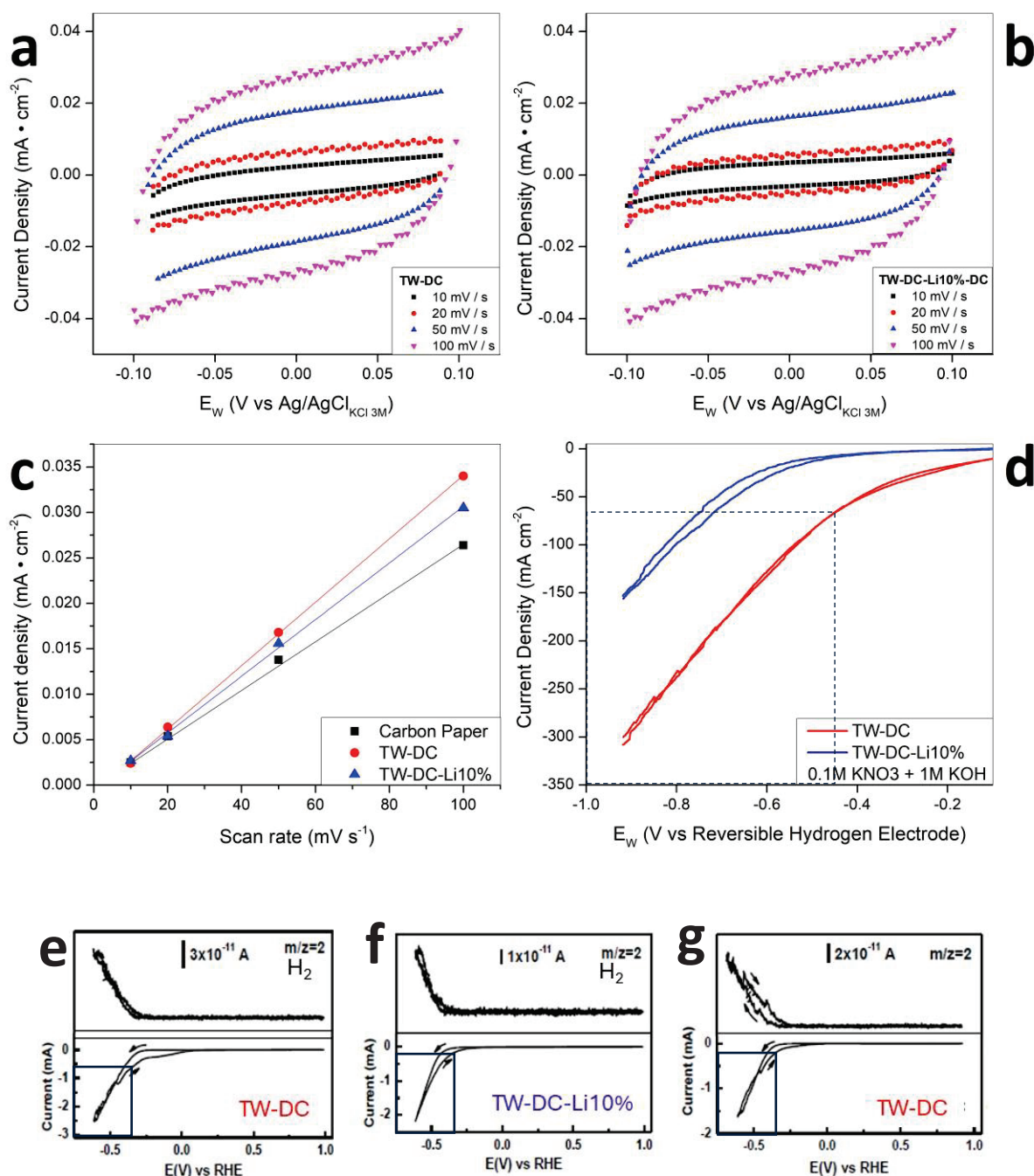
Figure 5. 4 CV with KOH electrolyte at different scan rates a) for TW-DC electrode b) TW-DC-Li10% electrode. C) Current density in the non-faradaic region vs scan rate for Carbon Paper, TW-DC and TW-DC-Li10% electrodes for determining C_{DL} d) CVs with 0.1M KNO₃+1M KOH electrolyte for TW-DC and TW-DC-Li10% electrodes. e-g) DEMS results of NO_3^-RR for H_2 product. The DEMS studies were performed in the Instituto Politecnico Internacional-Mexico.

5.5   Li effects on NO_3^-RR and HER using a Flow-Cell.

The incorporation of Li-species into the NiO and SnO_2 structure modifies the active sites in the catalyst, apparently to those linked to HER. This is mainly observed by the reduction on the current density in the TW-DC-Li10% electrode. To understand the full impact of Li incorporation, we conducted a series of CA using a flow cell, focusing on NO_3^- specific-conversion, FE, and nitrogen-based products Yield.

5.5.1   Electrochemical Set-up:

CA experiments were carried out using a 0.1M KNO_3 + 1M KOH electrolyte. IC has been used for quantification of ions in the liquid phase (NO_3^- and NO_2^-), UV-vis spectroscopy for NH_3, and GC quantifying H_2. Evaluated E_W were -0.3, -0.4, -0.5, -0.6, -0.7, and -0.8 V vs. RHE for 180 minutes.

In the flow-cell (**Figure 5.4**). A CEM (Nafion 117) separated the cathode and anode compartments, both filled with the same electrolyte, and DSA and Ag/AgCl$_{3M\ KCl}$ were the CE and RE respectively.
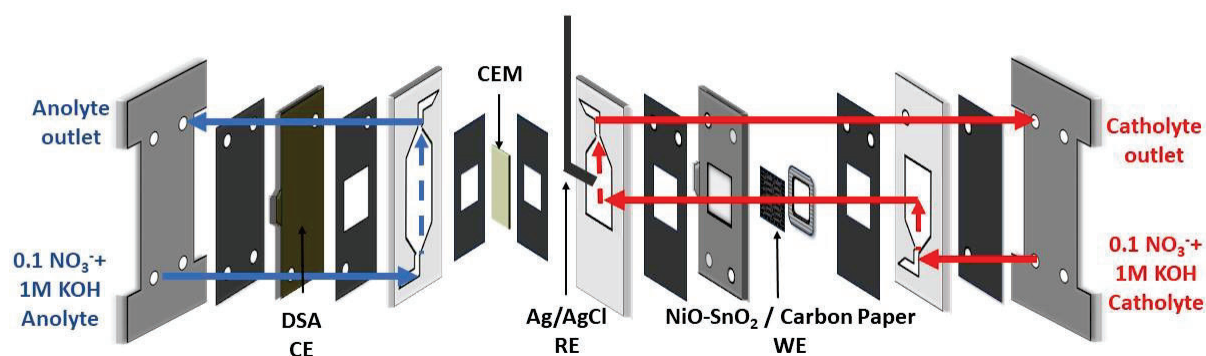
Figure 5.5 Electrochemical flow-cell configuration 3.

5.5.2 NO_3^- specific conversion (ΔNO_3^-) during CA in flow cells:

The ΔNO_3^- corresponds the specific mass (mg) of nitrate converted by charge; a parameter already used in previous chapters. As observed in **Figure 5.6**, ΔNO_3^- was evaluated for TW-DC-Li10% and TW-DC electrodes across various E_W. The TW-DC-Li10% electrode demonstrated higher NO_3^- conversion, peaking at 0.25 mg C^{-1} at E_W = -0.4 V vs RHE among the range. The efficiency decreased when more negative potentials are applied, reaching 0.14 mg C^{-1} at -0.7 V vs RHE, but increased again -0.8 V, indicating non-linear behavior. Conversely, the TW-DC electrode showed lower and more stable efficiency, decreasing from 0.10 mg C^{-1} at -0.3 V to a minimum of 0.05 mg C^{-1} at -0.5 V, with slight increases at more negative potentials up to 0.11 mg C^{-1} at -0.8 V vs RHE. The superior performance ΔNO_3^- of the TW-DC-Li10% electrode can be attributed to a synergistic contribution of K$^+$ and Li-species

effects. Although the oxidation state of Li in the catalyst structure remains undetermined, its presence is evident from the electrochemical effects observed. Lithium in the structure can act similarly to smaller cations like Li^+ in solution, facilitating better access and interaction of NO_3^- with the cathode due to less steric hindrance and stronger electrostatic attraction. Additionally, the presence of K^+ in the electrolyte, forms stable contact ion pairs with NO_3^-, which enhances the reduction rate by stabilizing intermediates and lowering activation barriers. These interpretations are based on the effects of cations as described by J. Fan et al [20]. Nevertheless, it might seem opposite to that provided by A. Fajardo et al. [19], where NO_3^- conversion rates followed the order: $Li^+ < Na^+ \approx K^+ < Cs^+$. However, this study only established an increasing order of cation effects by size in NO_3^- conversion, without limiting a possible synergistic effect if several cations are present in solution. For instance, we can complementarily use both studies to explain our observations.
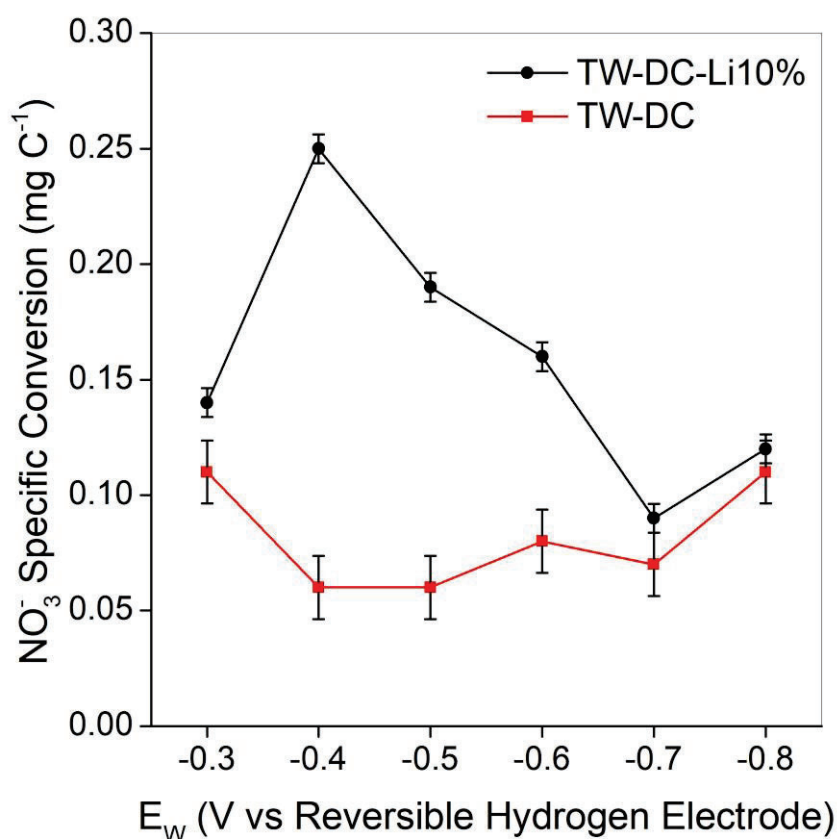

Figure 5. 6 Nitrate specific conversion for the electrodes TW-DC and TW-DC-Li10%

5.5.3   Faradaic Efficiency, and Yield of TW-DC and TW-DC-Li10% electrodes in Flow-cells.

From CA conducted in flow-cell FE, and quantified nitrogen-products yield are represented in **Figure 5.7.**

The analysis of the FE and product yields for the TW-DC and TW-DC-Li10% electrodes reveal distinct trends in their tendencies toward various products. For the TW-DC electrode (**Figure 5.7 a**), H_2 production increases significantly at more negative potentials, reaching 36 at -0.5 V vs RHE, indicating strong competition from the HER. NH_3 production shows a decreasing trend from 50% at -0.3 V to approximately 27% at more negative potentials, suggesting reduced NO_3^- reduction efficiency as HER becomes more competitive. NO_2^- and other products maintain relatively lower and stable percentages across the potentials. Conversely, the TW-DC-Li10% electrode demonstrates a more favorable tendency towards NH_3 production, with the highest FE of 59% at -0.4 V vs RHE, and generally lower H_2 production, indicating less competition from HER. The presence of lithium appears to enhance NO_3^- reduction efficiency, with reduced H_2 production (as low as 8% -0.5 V) and increased production of NH_3 and other nitrogen-based products.
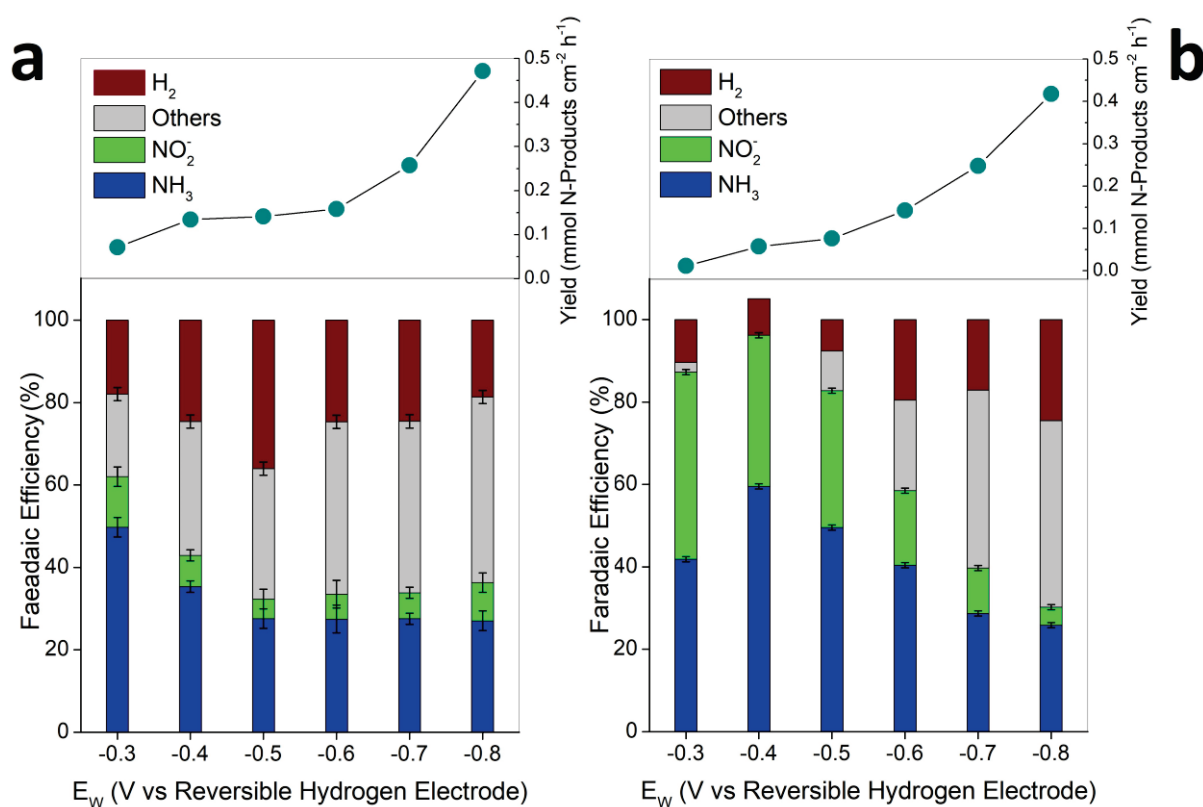
Figure 5.7 Product distribution in terms of Faradaic Efficiency and Yield to N-Products for the electrodes a) TW-DC, and b) TW-DC-Li10% and Yield of Nitrogen-based at different applied potentials.

The results also indicate that the TW-DC-Li10% electrode exhibits significantly lower HER compared to the TW-DC electrode, particularly at −0.4 V vs RHE where the FE for N-based products reaches more than 90% while HER stays at 9%. This suggests that Li-species in the structure limits the evolution of H_2, likely by making water dissociation of the Volmer step more favorable to NO_3^-RR. This means that in the presence of lithium, water dissociation still occurs but the adsorbed hydrogen atoms are more

available for NO_3^- reduction rather than forming H_2 gas. This interpretation aligns with the observations of J. Bender et al. [22], which highlight that smaller cations like Li^+ do not significantly promote HER in alkaline media for **HER-active metals (Ir, Pt, Pd)**. Instead, they stabilize intermediates that favor selective reduction processes. Lithium-species might affect the interfacial water structure and hydrogen bonding network less disruptively than larger cations, leading to reduced competition from HER and more efficient NO_3^- reduction. Specifically, lithium alters surface properties by modifying surface energy and electronic structure, which decreases proton adsorption favorability and hydrogen evolution while stabilizing reaction intermediates.

5.6   Conclusions.

In this chapter, we investigated the impact of Li-enrichment on the catalytic behavior of mixed NiO and SnO$_2$ catalysts for NO$_3^-$RR. By comparing a baseline NiO+SnO$_2$ catalyst with a lithium-enriched variant (10% Li-NiO+SnO$_2$), we aimed to evaluate whether lithium incorporation can enhance the selectivity and efficiency of nitrate electroreduction by limiting the competing HER.

Our study began with an overview of the effects of cations on NO$_3^-$RR and HER, providing a foundation for understanding the role of lithium in these processes. The systematic electrochemical testing and characterization revealed several key findings:

The lithium-enriched NiO+SnO$_2$ catalyst demonstrated improved specific conversion of NO$_3^-$ compared to the baseline catalyst. The presence of lithium appears to modify the electronic properties of the catalyst, making it more favorable for nitrate reduction over HER.

DEMS results showed evidence of a lower current density for HER and a higher Faradaic efficiency for N-based products of the Li-rich catalyst, indicating that lithium helps to steer the reaction pathway towards NO$_3^-$ conversion.

These findings highlight the potential of lithium-enriched catalysts for limiting HER. A strategy that can be used not only for nitrate conversion, but also for other reactions where HER represents a high contributor in reducing the overall efficiency of the process.

The results suggest that lithium enrichment is a promising strategy for enhancing the performance of mixed oxide catalysts. Future research could further optimize the lithium content and explore other cation modifications to continue improving catalyst performance.

5.7   Highlights of chapter 5.

Overview of Cation Effects: The chapter begins with a brief overview of the effects of cations on NO_3^- RR and HER, providing a foundation for interpreting the role of lithium in the catalyst structure.

Material Composition: The materials studied include a baseline $NiO+SnO_2$ catalyst and a lithium-enriched variant (10% Li-$NiO+SnO_2$).

**Suppression of HER**: Effective suppression of HER was observed with lithium incorporation, as evidenced by lower current densities for hydrogen evolution, which favored nitrate conversion.

Experimental Validation: Systematic electrochemical testing and characterization confirmed the role of lithium in modifying the catalytic, providing a strategy for future investigations on other type of reactions where HER represents an issue.

5.8   Bibliography

[1]   Y. Zhang, Y. Wan, X. Liu, K. Chen, and K. Chu, *Nb-doped NiO nanoflowers for nitrite electroreduction to ammonia*. iScience, vol. 26, no. 10, p. 107944, 2023, doi: 10.1016/j.isci.2023.107944.

[2]   P. Liu, J. Liang, J. Wang, L. Zhang, J. Li, L. Yue, Y. Ren, T. Li, Y. Luo, N. Li, B. Tang, Q. Liu, A.M. Asiri, O. Kong, and X. Sun, *High-performance NH_3 production via NO electroreduction over a NiO nanosheet array*. Chem. Commun., vol. 57, no. 99, pp. 13562–13565, 2021, doi: 10.1039/D1CC06113E.

[3]   Y. Wang, C. Liu, B. Zhang, and Y. Yu, *Self-template synthesis of hierarchically structured Co_3O_4@NiO bifunctional electrodes for selective nitrate reduction and tetrahydroisoquinolines semi-dehydrogenation*. Sci. China Mater., vol. 63, no. 12, pp. 2530–2538, Dec. 2020, doi: 10.1007/s40843-020-1365-0.

[4]   G. Zhang, N. Zhang, K. Chen, X. Zhao, and K. Chu, *Atomically Mo-Doped SnO_{2-x} for efficient nitrate electroreduction to ammonia*. J. Colloid Interface Sci., vol. 649, no. June, pp. 724–730, Nov. 2023, doi: 10.1016/j.jcis.2023.06.160.

[5]   X. Zheng, Y. Yan, X. Li, Y. Liu, and Y. Yao, *Theoretical insights into dissociative-associative mechanism for enhanced electrochemical nitrate reduction to ammonia*. J. Hazard. Mater., vol. 446, no. 3, p. 130679, Mar. 2023, doi: 10.1016/j.jhazmat.2022.130679.

[6]   Y. Zhang, Z. Ma, S. Yang, Q. Wang, L. Liu, Y. Bai, D. Rao, G. Wang, H. Li, and X. Zheng, *Element-dependent effects of alkali cations on nitrate reduction to ammonia*. Sci. Bull., vol. 69, no. 8, pp. 1100–1108, Apr. 2024, doi: 10.1016/j.scib.2024.02.011.

[7]   A. S. Fajardo, P. Westerhoff, S. Garcia-Segura, and C. M. Sánchez-Sánchez, *Selectivity modulation during electrochemical reduction of nitrate by electrolyte engineering*. Sep. Purif. Technol., vol. 321, no. April, 2023, doi: 10.1016/j.seppur.2023.124233.

[8]   J. Fan, L.K. Arrazolo, J. Du, H. Xu, S. Fang, Y. Liu, Z. Wu, J.-H. Kim, and X. Wu, *Effects of Ionic Interferents on Electrocatalytic Nitrate Reduction: Mechanistic Insight*. Environmental Science & Technology 2024, doi: 10.1021/acs.est.4c03949.

[9]   S. Ringe, *Cation effects on electrocatalytic reduction processes at the example of the hydrogen evolution reaction*. Curr. Opin. Electrochem., vol. 39, p. 101268, Jun. 2023, doi: 10.1016/j.coelec.2023.101268.

[10]   J.T. Bender, A.S. Petersen, F.C. Østergaard, M.A. Wood, S.M.J. Heffernan, D.J. Milliron, J. Rossmeisl, J. Resasco, *Understanding Cation Effects on the Hydrogen Evolution Reaction*. ACS Energy Lett. 8, 657–665 (2023). https://doi.org/10.1021/acsenergylett.2c02500

[11]   D.-R. Yang, Z.-L. Wu, K. Ren, P. Dong, D. Zhang, B. Yang, and F. Liang, *Recent advances of the thermodynamic behavior of tin species in aqueous solution*. J. Min. Metall. Sect. B Metall., vol. 59, no. 1, pp. 1–15, 2023, doi: 10.2298/JMMB220617001Y.

Conclusions and outlook
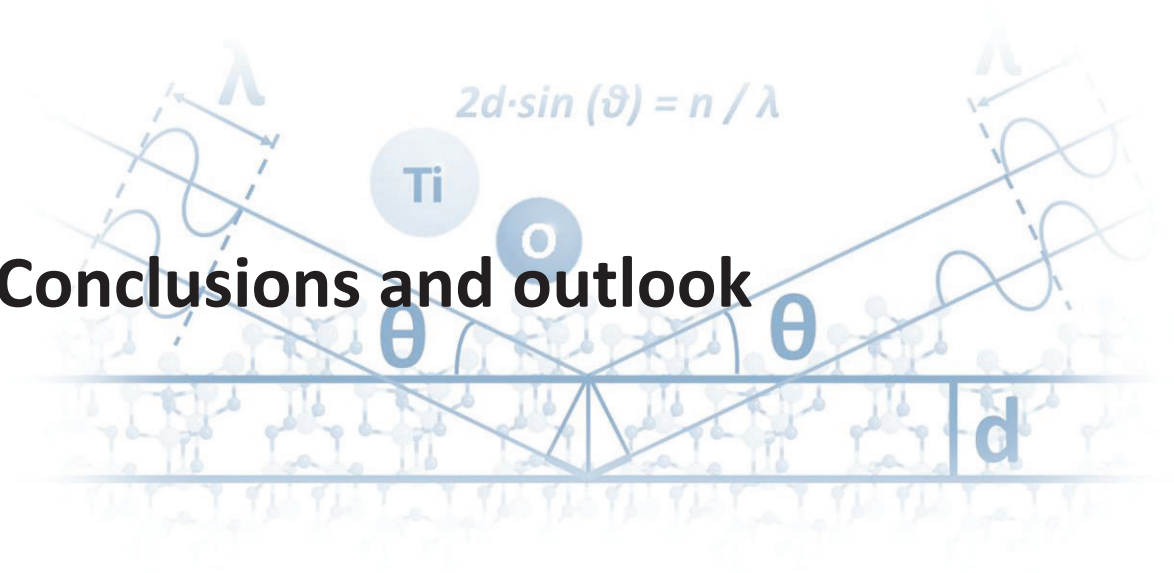
CONCLUSIONS

This doctoral thesis was focused on the development of an optimized electrocatalytic system for generation of ammonia as energy carrier. First, we focused on the integration of the electrocatalyst in electrochemical systems and optimizing conditions for achieving high selectivity and efficiency in the generation of ammonia. Second, we paid attention towards increasing the energy efficiency and scalability of the process. Finally, we evaluated electrocatalyst-doping for reducing competitive reactions to nitrate-to-ammonia.

In that way, the work covered the following specific challenges. 1) Synthesis of an efficient electrocatalyst that simultaneously shows a high current efficiency, selectivity and productivity towards ammonia. 2) Development of a reliable quantification method for ammonia as the primary reaction product. 3) Characterization of oxidation state of nanoparticles Cu-based nanoparticles and defects in TiO_2. Accordingly, the next conclusions are summarized.

Chapter 3

- The integration of Cu_2O-Cu nanocubes on a Ti substrate resulted in significantly enhanced electrocatalytic performance for the NO_3^-RR to NH_3. This combination leveraged the high catalytic activity of Cu and the excellent faradaic efficiency of Ti, leading to improved kinetic behavior and stability over multiple cycles. The Cu_2O-Cu@Ti catalysts achieved a faradaic efficiency of over 90%, selectivity to ammonia of 80%, and an ammonia productivity of 0.45 $mmol \cdot h^{-1} \cdot cm^{-2}$. Additionally, the enhanced kinetic constant (k) was determined to be higher than that of individual components, indicating a better kinetic property for conducting the NO_3^- conversion.

- The quasi in situ analysis underscored the significance of maintaining both Cu_2O and Cu within the nanocube structures during the NO_3^-RR process. The unique structural features contributed to their enhanced catalytic activity for NO_3^- conversion.

Chapter 4

- The introduction of optimized flow-cell configurations significantly enhanced the energy efficiency of the NO_3^-RR to NH_3 process. The tandem system combining Cu-based and TiO_2-based catalysts in a cascade reduction system demonstrated a Faradaic Efficiency of 97%, a 80% Selectivity, productivity of 0.45 $mmol \cdot h^{-1} \cdot cm^{-2}$ towards ammonia. The global energy efficiency and half-cell energy efficiency of the optimized flow-cell configuration were found to be 29% and 58%, respectively, higher than the 22% and 26% respectively for non-tandem configurations.

- The energy consumption for ammonia generation was calculated at 2.2 MJ mol^{-1} NH$_3$, and for nitrate reduction, it was 4.4 MJ mol^{-1} NO$_3^-$. These values are still far from being competitive with traditional ammonia synthesis methods. However, they provide a starting point for optimizing the system, as only the cathodic reaction was studied. Further research and development are needed to enhance the overall efficiency and economic viability of the process.

Chapter 5: Lithium Enrichment and Hydrogen Evolution Reactions

- The incorporation of lithium into mixed nickel oxide (NiO) and tin oxide (SnO$_2$) catalysts effectively mitigated hydrogen evolution reactions (HER) during the NO$_3^-$RR process. The lithium-enriched catalyst demonstrated higher selectivity by suppressing HER, resulting in improved faradaic efficiency for nitrate conversion.
- The results observed in the experimental study can be explained by considering the presence of Li-species in the electrode and Li$^+$ cations in the electrolyte. This offers an approximation of the behavior observed in the literature, where the influence of both NO$_3^-$RR and HER is studied separately. The presence of lithium species in the electrode structure enhances the catalytic properties and stability, while the Li$^+$ cations in the electrolyte help in stabilizing reaction intermediates and suppressing unwanted side reactions.

The research presented in this thesis advances the field of electrocatalytic ammonia synthesis by demonstrating the benefits of synergistic catalyst combinations, optimizing energy-efficient flow-cell processes, and leveraging lithium enrichment to improve reaction selectivity and efficiency. These findings offer promising solutions for sustainable and scalable ammonia production, contributing to global efforts in energy and environmental sustainability.

OUTLOOK AND FUTURE WORK.

Electrogeneration of nitrogen-based energy carriers from nitrates is still an emerging field that necessitates further investigation into catalysts and operating conditions to fully realize its potential. Based on the results of this work and the corresponding state of the art, several key areas can be addressed in future research to advance this promising technology.

- Despite the high Faradaic Efficiencies achieved in recent studies, catalyst stability remains a significant issue. Future research should focus on enhancing the durability and long-term performance of electrocatalysts under harsh operational conditions. This includes the development of more robust catalyst materials, optimizing structure, and fine-tuning the operating parameters that allows conducting efficiently the nitrate conversion under neutral pH, low nitrate initial concentration and the integration of other pollutants.

- The energy efficiency results in this work were primarily based on the optimization of the cathodic reaction. However, to achieve holistic system efficiency, further investigation is required to extend optimization efforts to the anodic reaction. This includes exploring alternative oxidation processes, such as the oxidation of organic components, which can contribute to circular economy principles and Power-to-X concepts by generating valuable byproducts and utilizing renewable energy sources effectively.

- Building on the findings from Chapter 5, there is a need for a deeper understanding of the mechanisms involving lithium-doping affects for both nitrate reduction and hydrogen evolution reactions. Future work should focus on optimizing the lithium content and the structure of catalyst materials to enhance nitrate-to-ammonia conversion. The goal is to develop catalysts that allow for increased applied cathodic potentials or current densities while minimizing the competing HER, thereby improving overall process efficiency.

- Finally, future research should aim at optimizing catalyst materials, operative conditions, and process engineering: first, direct the reaction towards other nitrogen-based carriers such as hydroxylamine and hydrazine. Additionally, coupling nitrate electroreduction with other cathodic reactions, such as CO_2 reduction, can lead to the production of other value-added products like urea. This dual approach can enhance the versatility and economic viability of the technology, also following the power-to-X concept.

Marcelo Eduardo Chavez Blanco

mchavez984@gmail.com

+34 651 93 64 66

08024, Barcelona Spain

WWW: https://py.linkedin.com/in/Marcelo Eduardo Chavez Blanco

Professional Summary

Innovative researcher adapted to developing probing questions, designing experiments, and generating meaningful results. Experienced at identifying and using new technologies and resources in photo-electrocatalysis for N-base compounds. Works effectively and collaboratively with groups and individuals.

Skills

Data Collection and Analysis	Research Program Planning
Interpreting Results of Experimental Data	Data Compilation
	Experiment Design
Scientific Writing	Paper Writing
Electron Microscopes	Research Presentation
Sequence Analysis	Programming

Work History

11/2019 - Present
Doctoral Researcher
Institut De Recerca En Energia De Catalunya (IREC), **Barcelona**

- Developed experimental data collection strategies for nitrogen-based compound valorization.
- Wrote research papers, reports, and summaries regarding nitrogen-based valuable compounds generation.
- Evaluated potential electrocatalysts materials for direct nitrogen-based compound generation from molecular nitrogen.
- Presented obtained research results in international conferences.

04/2023 - 05/2023
Visiting Researcher
University Of Basque Country, **San Sebastian - Spain**

- Learned the use of equipment, data collection, and analysis of semi-in-situ X-ray Photoemission Spectroscopy (XPS) for Cu/Ti-based electrodes used in nitrate-to-ammonia reactions.
- Learned new laboratory techniques and applied expertise in carrying out enhanced experiments under the supervision of senior lab members.

07/2018 - 04/2019
Production Engineer
Ramirez Diaz De Espada ICSA, **Asuncion**

- Led and supervised the entire wine production process and prepared proper documentation for dispatch.
- Performed root cause analysis and implemented corrective actions based on ISO 9001 Quality Management System.
- Performed root cause analysis and implemented corrective actions based on ISO 14001 Environmental Management System.
- Communicated with other team members to enhance process and performance.
- Trained team on best practices to optimize production and improve quality.

02/2013 - 03/2015

Production Supervisor
Tecnomyl S.A., **Villeta**

- Resolved issues quickly to maintain productivity goals.
- Managed a team of 5 production leaders and associates, overseeing productive production processes and meeting all deadlines.
- Coordinated with other departments to maintain smooth and efficient product flow.
- Evaluated team member performance regularly to identify and resolve productivity concerns.
- Evaluated existing production processes and identified areas for improvement.
- Managed internal operational standards and productivity targets.

Education

Expected in 06/2024 | **Ph.D.**, **Engineering and Applied Sciences**, *University of Barcelona*, Barcelona

02/2018 | **Master of Science**, **Chemical Engineering**, *University of Barcelona*, Barcelona - Spain

02/2016 | **Chemical Engineer**, **Engineering Technology**, *National University of Asuncion*, Asuncion - Paraguay

Additional Information

International Conferences:

Material Research Society (MRS) Spring Meeting 2021: Electrode Optimization for Nitrate electroreduction
International Society of Electrochemistry Topical Meeting 2021: Electrolyte and cathode optimization for nitrate to ammonia generation
NanoGe INTEREC Valencia 2021. Ammonia generation by electroreduction of high nitrate content electrolyte
EUROMAT FEMS 2023: Synergistic electrochemical reduction of nitrates to ammonia with Cu/Ti-based materials
MATSUS24 – March 2024: Energy Efficient Nitrate to Ammina Electroreduction in a Tandem configuration

Publications:
M.E. Chavez, M. Biset-Peiró, S. Murcia-López, J.R. Morante; "Cu2O–Cu@Titanium Surface with Synergistic Performance for Nitrate-to-Ammonia Electrochemical Reduction", ACS Sustainable Chem. Eng. 2023, 11, 9, 3633–3643.
https://doi.org/10.1021/acssuschemeng.2c05885

N. López-Vinent, A. Cruz-Alcalde, L.E. Romero, **M.E. Chávez**, P. Marco, J. Giménez, S. Esplugas, Synergies, radiation and kinetics in photo-Fenton process with UVA-LEDs, Journal of Hazardous Materials, Volume 380, 2019, 120882, ISSN 0304-3894, https://doi.org/10.1016/j.jhazmat.2019.120882.

Languages

Spanish
Advanced (C1)

English
Advanced (C1)